

ADVERTIMENT. La consulta d'aquesta tesi queda condicionada a l'acceptació de les següents condicions d'ús: La difusió d'aquesta tesi per mitjà del servei TDX (www.tesisenxarxa.net) ha estat autoritzada pels titulars dels drets de propietat intel·lectual únicament per a usos privats emmarcats en activitats d'investigació i docència. No s'autoritza la seva reproducció amb finalitats de lucre ni la seva difusió i posada a disposició des d'un lloc aliè al servei TDX. No s'autoritza la presentació del seu contingut en una finestra o marc aliè a TDX (framing). Aquesta reserva de drets afecta tant al resum de presentació de la tesi com als seus continguts. En la utilització o cita de parts de la tesi és obligat indicar el nom de la persona autora.

ADVERTENCIA. La consulta de esta tesis queda condicionada a la aceptación de las siguientes condiciones de uso: La difusión de esta tesis por medio del servicio TDR (www.tesisenred.net) ha sido autorizada por los titulares de los derechos de propiedad intelectual únicamente para usos privados enmarcados en actividades de investigación y docencia. No se autoriza su reproducción con finalidades de lucro ni su difusión y puesta a disposición desde un sitio ajeno al servicio TDR. No se autoriza la presentación de su contenido en una ventana o marco ajeno a TDR (framing). Esta reserva de derechos afecta tanto al resumen de presentación de la tesis como a sus contenidos. En la utilización o cita de partes de la tesis es obligado indicar el nombre de la persona autora.

WARNING. On having consulted this thesis you're accepting the following use conditions: Spreading this thesis by the TDX (www.tesisenxarxa.net) service has been authorized by the titular of the intellectual property rights only for private uses placed in investigation and teaching activities. Reproduction with lucrative aims is not authorized neither its spreading and availability from a site foreign to the TDX service. Introducing its content in a window or frame foreign to the TDX service is not authorized (framing). This rights affect to the presentation summary of the thesis as well as to its contents. In the using or citation of parts of the thesis it's obliged to indicate the name of the author

Post-processing Methods for Ocean Monitoring in SAR Images

Author: Mariví Tello

Thesis advisors: Jordi J. Mallorquí, Carlos López-Martínez

Index

INDEX	3
CHAPTER 1. INTRODUCTION.....	7
CHAPTER 2. CHARACTERISTICS OF SAR IMAGERY	13
2.1 NATURE OF THE INFORMATION IMAGED BY A SAR SYSTEM.....	15
2.1.1 BASICS OF SAR DATA ACQUISITION.....	15
2.1.2 BASICS OF SAR DATA PROCESSING.....	17
2.1.2.1. PULSE COMPRESSION	18
2.1.2.2. COMPRESSION IN RANGE	20
2.1.2.3. COMPRESSION IN AZIMUTH	21
2.1.3 APPLICATIONS OF SAR SYSTEMS AND NEEDS OF UNSUPERVISED TECHNIQUES.....	24
2.2 ASSOCIATED DIFFICULTIES FOR AUTOMATIC SAR IMAGE INTERPRETATION	26
2.2.1 SPECKLE	26
2.2.2 SPATIAL CORRELATION DUE TO PROCESSING	29
2.2.3 LARGE DYNAMIC RANGE.....	30
2.3 SAR IMAGING OF THE OCEAN SURFACE	30
2.4 SUMMARY.....	32
CHAPTER 3. A MULTISCALE FRAMEWORK FOR THE EXPLOITATION OF SAR DATA.....	35
3.1 MULTISCALE TIME – FREQUENCY CONCEPT	36
3.1.1 SHORT TIME FOURIER TRANSFORM (STFT)	38
3.1.2 THE WAVELET TRANSFORM	39
3.1.2.1. BASICS OF THE WAVELET TRANSFORM	39
3.1.2.2. PROPERTIES OF THE WT	47
3.1.2.3. THE WAVELET TRANSFORM AS A MULTISCALE DIFFERENTIAL OPERATOR.....	48
3.1.2.4. THE WAVELET TRANSFORM AS AN ESTIMATOR OF LOCAL REGULARITY OF A SIGNAL	50
3.1.2.5. CONE OF INFLUENCE	52
3.1.2.6. INTRASCALE AND INTERSCALE CORRELATIONS.....	54
3.1.2.7. PRACTICAL CONSIDERATIONS WHEN USING WAVELET TOOLS	54
3.1.2.8. SELECTION OF THE TYPE OF WT	54
3.1.2.9. SELECTION OF THE WAVELET FAMILY	55
3.2 A MULTISCALE FRAMEWORK FOR THE INTERPRETATION OF MULTISCALE INFORMATION.....	55
3.2.1 MULTIPLICATIVE MODEL FOR SPECKLE.....	56
3.2.2 PRODUCT MODEL FOR SAR DATA	58
3.3 SUMMARY.....	59
CHAPTER 4. AUTOMATIC SPOT DETECTION IN SAR IMAGERY	61
4.1 MAIN DRAWBACKS OF SPOT ENHANCEMENT.....	63

4.2 SPOTS IN THE MULTISCALE TIME / FREQUENCY PLANE	65
4.3 ALGORITHM DESIGNED FOR SPOT ENHANCEMENT.....	67
4.3.1 THEORETICAL PRINCIPLES	67
4.3.1.1. PRELIMINARY CONSIDERATIONS	67
4.3.1.2. DETAILED EXAMPLE OF OPERATION.....	68
4.3.2 PROPERTIES OF USEA	73
4.3.2.1. PRESERVATION OF THE SPATIAL RESOLUTION	73
4.3.2.2. SPOT TO BACKGROUND CONTRAST ENHANCEMENT.....	74
4.3.2.3. NATURE OF THE STATISTICAL DISTRIBUTION INVARIANT IN THE WAVELET DOMAIN.....	77
4.3.2.4. CAPABILITY OF MANAGING DISCONTINUITIES AT DIFFERENT SCALES	79
4.3.2.5. DETECTION NOT EXCLUSIVELY DEPENDENT ON THE INTENSITY	82
4.3.3 VALIDATION THROUGH SIMULATED DATA	83
4.4 APPLICATION TO SHIP MONITORING WITH SAR SENSORS.....	89
4.4.1 STATE OF THE ART	89
4.4.2 APPLICATION OF THE SPOT DETECTION ALGORITHM DESIGNED TO AUTOMATIC SHIP DETECTION IN SAR IMAGERY	93
4.4.2.1. EXAMPLE OF OPERATION IN A RADARSAT IMAGE.....	93
4.4.2.2. EXAMPLE OF OPERATION IN AN ENVISAT IMAGE.....	98
4.5 EXTENSION TO MULTICHANNEL DATA	101
4.5.1 EXPERIMENTS WITH DUAL POLARIZED DATA	101
4.5.2 EXPERIMENTS WITH FULL-POL DATA.....	106
4.6 CONCLUSIONS.....	116

CHAPTER 5. AUTOMATIC DETECTION OF LINEAR FEATURES IN SAR IMAGERY.....119

5.1 PRELIMINARY CONSIDERATIONS	120
5.1.1 MAIN DRAWBACKS AND STATE OF THE ART	120
5.1.2 APPLICATION OF THE LOGARITHM TRANSFORM	124
5.2 ALGORITHM DESIGNED FOR AUTOMATIC EDGE ENHANCEMENT ON SAR IMAGERY.....	127
5.2.1 THEORETICAL PRINCIPLES	127
5.2.2 DETAILED EXAMPLE OF OPERATION IN A SIMULATED IMAGE	132
5.2.3 PROPERTIES	137
5.2.4 APPLICATION TO COASTLINE ENHANCEMENT IN SAR IMAGERY	138
5.3 EDGE LABELING WITH GEODESIC ACTIVE CONTOUR	143
5.3.1 THEORETICAL PRINCIPLES	143
5.3.2 VALIDATION THROUGH SIMULATED IMAGES.....	149
5.3.2.1. DEFINITION OF QUALITY PARAMETERS	149
5.3.2.2. RESULTS	150
5.3.3 VALIDATION THROUGH REAL DATA	151
5.4 CONCLUSIONS.....	153

CHAPTER 6. AUTOMATIC ANALYSIS OF TEXTURES IN MARITIME SAR IMAGERY157

6.1 MAIN DRAWBACKS	159
6.1.1 TURBULENT NATURE OF THE SEA SURFACE.....	160
6.1.2 SEA SURFACE IN SAR IMAGES	160
6.1.3 MULTISCALE FRAMEWORK FOR THE ANALYSIS OF TEXTURES IN MARITIME SAR IMAGES	162
6.1.3.1. ENERGY SPECTRUM.....	162
6.1.3.2. STRUCTURE FUNCTIONS.....	163
6.1.3.3. SINGULARITY SPECTRUM	164
6.2 ALGORITHM FOR THE ESTIMATION OF THE LIPSCHITZ EXPONENT BASED ON THE WAVELET TRANSFORM	164
6.2.1 WAVELET TRANSFORM MODULUS MAXIMA	165
6.2.2 GRADIENT MODULUS PROJECTION	169

6.2.3 ESTIMATION OF THE FRACTAL DIMENSION BASED ON THE WAVELET TRANSFORM.....	170
6.3 APPLICATION TO OIL SPILL DETECTION IN MARITIME SAR IMAGES.....	171
6.3.1 OIL SPILLS IN SAR IMAGES	172
6.3.2 MAIN DRAWBACKS FOR SEGMENTATION AND STATE OF THE ART	174
6.3.3 EXPERIMENTAL RESULTS	176
6.3.3.1. VALIDATION TROUGH SIMULATED IMAGES	176
6.3.3.2. VALIDATION TROUGH REAL DATA	180
6.4 CONCLUSIONS.....	185
CHAPTER 7. CONCLUSIONS.....	189
REFERENCES	197

Chapter 1. Introduction

Nowadays, there is an increasing interest in civilian remote sensing applications from space. Data produced by space technologies can provide key observables at a global scale, necessary for gaining insight in understanding the Earth's environment. In the long term, monitoring the Earth from space is expected to enable the evaluation of the extent of climate change, which is a major concern in these days. Even more, a communication appeared recently in the European Space Agency (ESA) portal [1] states that space technology may help to mitigate climate change. For example, space observations have proven their usefulness to increase the performance of systems based on renewal energies. Besides, the dissemination of the images derived from space borne sensors is a key element for increasing awareness of society and inducing a change in its lifestyle.

In Europe, Global Monitoring for Environment and Security (GMES) [2], which is a joint endeavor of the ESA and the European Community, remains a valuable proof of the actual rise of space technologies. It plans to establish a global framework involving policy makers and spatial industry agents in order to reach a better management of the environment and a mitigation of the effects of climate change. In the scope of GMES, one of the most encouraged services is maritime ones: state and dynamics of the ocean and coastal zones, ecosystems and sea-ice. The pre-operational marine service of GMES is provided by the FP7 project, called MyOcean which covers: maritime security, oil spill prevention, marine resources management, climate change, seasonal forecast, coastal activities, ice survey and water quality and pollution.

There are different types of spaceborne sensors for Earth observation. They are usually divided into active or passive. Passive sensors provide data through the measurement of radio waves of natural origin. Optical sensors and radiometers are included into this category. Optical sensors measure an amount of light energy, whereas radiometers retrieve an amount of heat energy. Some optical sensors are IKONOS [3], SPOT [4], Quickbird [5], LandSAT [6]. Among the radiometric sensors, it is worth mentioning the recent launch of SMOS [7] which is devoted to measure soil moisture and ocean salinity. In opposition to passive ones, active sensors provide their own illumination. In the scope of this work, Synthetic Aperture Radar (SAR) sensors deserve special attention. The first civilian SAR satellite was the SEASAT [11], launched in 1978 and devoted to image and probe planetary processes involving oceans. Then, the ERS [8], the ENVISAT [9] and the RADARSAT [12] missions were launched for environmental monitoring. In the last years, numerous spaceborne sensors with new technological capabilities based on SAR have been developed all around the world: the Japanese ALOS/PALSAR [13], the RADARSAT-2 [10], the TerraSAR-X [14]. Several missions are planned in the near future, aiming at combining active and passive sensors: SMAP [15], ESA's Sentinel satellites [16] and Aquarius [17].

Since they illuminate the scene they are observing, active sensors and in particular radar ones can offer day and night coverage and they are not affected by meteorological phenomena. Moreover, they can cover large areas and the resolution achieved is high compared to that of actual microwave passive sensors. These distinctive characteristics make them useful in numerous monitoring applications. Nonetheless, the counterpart is that the interpretation of radar data and specifically SAR images is quite troublesome. For a non experienced user, a SAR image is not talkative since it does not correspond to common visual perception. On the one hand, the image does not correspond to the reflection of light on a series of objects but to the response of the scene to an electromagnetic microwaves illumination. On the other hand, the geometry of a SAR system produces differences in the projection of the image acquired with respect to a usual aerial optical image: targets may appear misplaced, slopes effects alter the relative position and the dimensions of elements of the target, etc.

On the contrary, an experienced operator, used to this type of data, is usually able to distinguish structural patterns, in a correct way. However, since a manual treatment is unacceptably slow, unpractical and hardly reproducible, fully or eventually partially computerized schemes are desirable. On the one hand, due to the nature of the data, designing automatic interpretation processes is awkward. Besides, historically, in the SAR domain, the development of processing and post processing techniques has been slower than the technological advances and, most of the times, post processing of SAR data has been performed through traditional image processing methods, resulting in limited performances. In fact, it is worth observing that most of traditional image processing techniques have been conceived to deal with optical data, very different from SAR one. As a consequence, a gap exists between the available technology and the means of exploitation of the data produced by this technology. Hence, in order to increase further usability of SAR images, more specific data mining methods are still to be developed to provide efficient tools for automatic interpretation of SAR data.

Accordingly, the purpose of this work is to develop specific post processing techniques for SAR oceanic scenarios in order to establish a framework for the unsupervised exploitation of SAR

imagery for different maritime applications. Inspired on the operation of the human visual system but adapting it to SAR data, the set of methods proposed, when confronted to a scene, plans extracting first the elements carrying most of the information of the image, i.e. the elements with the highest entropy. Then, once revealed the structural information of the image, analysis will be concentrated on more subtle changes. Besides, the series of techniques developed are inscribed in a multiscale framework permitting, as the human vision, a global analysis and a zooming into different elements at different scales.

Specifically, the framework proposed is structured following three milestones: spot detection, extraction of linear features and texture analysis. Each of these steps is related to a maritime application. Spot detection will be directly applied to vessel detection. Maritime traffic surveillance from space includes fisheries monitoring and control in order to prevent overexploitation of the seas, maritime security, prosecution of ocean pollution responsible agents and border control. The extraction of linear features will be directly applied to coastline monitoring. Monitoring of the coastline involves among others coastal management and planning and the evaluation of coastal flooding and erosion. At last, texture analysis will be applied to oil spill detection in the ocean surface. The detection of pollutants in the ocean surface is necessary to capture the effects of environmental hazards and to help in the management of pollution crisis.

This dissertation is structured as follows. Chapter 2 is devoted to analyze the particularities of SAR images and the difficulties associated to their unsupervised post-processing. The basics of the SAR systems geometry and the principles of SAR data acquisition and image formation are presented in Section 2.1. The most relevant applications of SAR systems are overviewed and, at the end of Section 2.1, the need of unsupervised methods is justified. The coherent nature of SAR imaging generates speckle, which is the major drawback for the treatment of SAR images. Moreover, in the processing of SAR data, the convolution of filters with finite length induces a residual correlation which is the origin of the granular pattern observable in SAR images. Section 2.2 is devoted to analyze the implications of these effects in the automatic interpretation of SAR data. The special case of maritime scenarios is considered in Section 2.3.

From an image processing point of view, speckle and granularity may be considered as discontinuities concentrated at different scales than the information of interest for the applications focused in this work. Hence, it is shown that a multiscale framework may be appropriate for the exploitation of SAR data. Chapter 3 presents the multiscale time – frequency concept and, in particular, the wavelet theory. In Section 3.1, the main properties of the WT are reviewed and a particular attention is given to residual correlations that persist both between subbands within a scale and between different scales. In the literature, the WT is usually imperfectly considered as a whitening process, but it is shown that these residual dependencies may be useful for segmentation purposes since they highlight the presence of structures in front of noise. Section 3.2 introduces the option of using a multiscale framework for the interpretation of SAR data.

Based on the observations raised in previous chapters, Chapter 4 proposes a novel method for unsupervised spot detection in SAR images based on the WT. After setting the concept of spot and analyzing the main difficulties of performing spot detection in SAR images in Section 4.1, Section 4.2 observes how the presence of a spot is translated into the time – frequency space. This leads to the presentation of the algorithm proposed for spot enhancement in Section 4.3. The method is theoretically justified and first tested on simulated data. On a second step, in Section 4.4, the technique is applied to vessel monitoring with SAR sensors. The distinctive features of this technique with respect to existing ones are presented. A rigorous analysis in single channel SAR data of different sensors is carried out. The method is then extended to dual polarimetric imagery. Several options are presented and results on SAR data are employed to empirically justify that polarization channel diversity is favorable for automatic ship detection. At last, the multiscale spot enhancement technique is adapted to be applied to fully polarimetric data and results are compared to that obtained by the polarimetric entropy parameter. It is shown that the consideration of the information produced by the four polarization configurations dramatically increases the target to clutter ratio and, thus, facilitates the automatic detection. Besides, false alarms produced by sea spikes are reduced.

Chapter 5 presents a novel method for the enhancement of linear features in SAR images, based on a multiscale approach. After a discussion on the concept of “edge” and the related difficulties for automatic edge detection, several preliminary considerations and the state of the art are reviewed in Section 5.1. In Section 5.2, the algorithm proposed for automatic edge enhancement on SAR images is presented. The technique is applied on simulated images on a first step. Then, the method is applied to SAR data for coastline extraction purposes. After edge enhancement, edge labeling is addressed in Section 5.3. The use of Geodesic Active Contours is justified and the method is explained. The performance of the overall method of edge extraction, constituted by the technique designed for edge enhancement in SAR images followed by the Geodesic Active Contour, is evaluated. Several quantitative parameters are proposed and estimated on simulated images. Then, qualitative validation is performed on SAR images.

The techniques addressed in Chapter 4 and Chapter 5 reveal the structure of the image. Once the structure of the image extracted, a deeper comprehension requires performing texture analysis. This issue, discussed in Chapter 6, is particularly difficult in SAR images, mainly due to speckle. Chapter 6 aims at providing a technique for the local estimation of the regularity of a signal in order to perform texture analysis and to characterize local discontinuities. This chapter is mainly involved with maritime scenarios. Section 6.1 explores the characteristics of the sea surface and analyzes how they are translated by the SAR imaging process. Through this, the suitability of inscribing the interpretation of textures in a multiscale framework is justified. Section 6.2 presents wavelet tools for the characterization of turbulences and in particular the estimation of local regularity by means of the Lipschitz exponent is considered. In Section 6.3, the algorithm proposed for the automatic retrieval of the local regularity is applied to ocean scenes in order to detect oil spills in the sea surface and to discriminate them from look-alikes.

Chapter 7 presents the global conclusions and discussions of this work. A series of future lines are suggested.

Chapter 2. Characteristics of SAR imagery

A radar image does not correspond to a representation fully comprehensible through common visual perception, as it can be appreciated in the example shown in Figure 1. It displays in parallel a scene corresponding to the area of the city of Barcelona (Spain) as seen by an optical sensor and by a SAR one. The image on the left column in Figure 1 has been acquired by Quickbird, a commercial optical spaceborne sensor. A human observer, assisted by his experience of aerial pictures, may easily identify an urban coastal scenario, clearly distinguishing streets and buildings. Moreover, this interpretation is valid when confronted to the overall scene and persists when zooming into smaller fragments of it, see bottom row in Figure 1. In contrast, the image on the right column represents likewise the same urban scenario as seen by a spaceborne SAR sensor, on board the ERS satellite. This type of data is hardly attractive for a non experienced user. However, a specialist would be able to discriminate not only the presence of buildings, streets and squares, but also additional information such as, for example, quarters occupied by higher buildings or a rough qualitative estimation of wind field in the sea surface. It is worth noting that this information is not inferable from optical imagery. Furthermore, SAR images may appear even less explicit when considering a fragment corresponding to a reduced extension, see bottom row in Figure 1: at small scales, in homogeneous scenarios, just a granular pattern is noticeable. Nonetheless, it is worth mentioning that this feature is less noticeable in images provided by recent SAR sensors such as TERRASAR-X, with very high resolution capabilities.

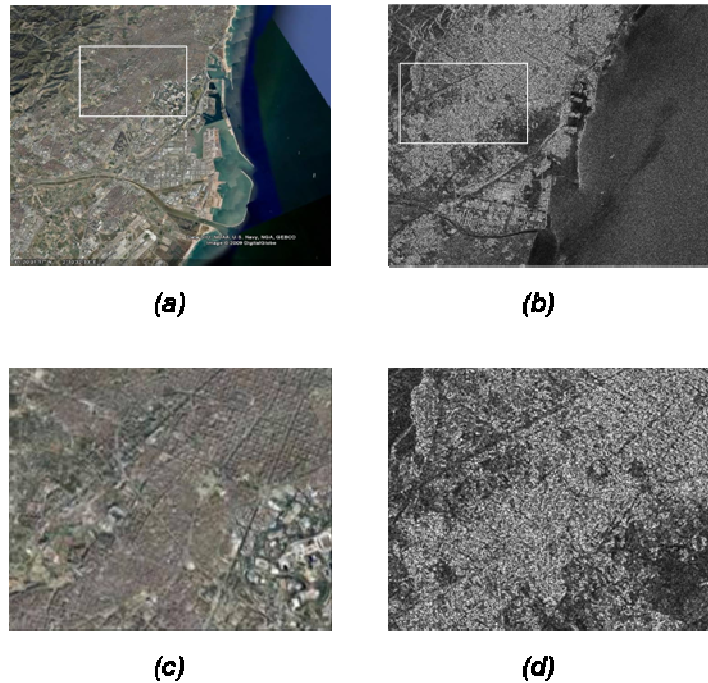


Figure 1. The same coastal urban scene (city of Barcelona, Spain) as observed by Quickbird, an optical spaceborne sensor (source: Google Earth) (a) and by ERS, a SAR one (b). The bottom row, (c) and (d), corresponds to zooms of the area inscribed in the rectangle in the images of the top row.

Images generated by spaceborne optical sensors have better resolution capabilities than those generated by SAR ones. This is obtained at the expense of a narrower coverage. Added to the lower resolution capabilities of radar systems in front of optical ones, these difficulties in interpretation are motivated by the fact that a radar image consists of a representation of the local scattering properties to microwaves illumination of the observed scene. Hence, contrarily to an optical image, it does not purely reflect geometrical aspects of objects, but it also maps their scattering behavior to a microwave electromagnetic illumination. This backscattered energy constitutes a measurable quantity that may be retrieved precisely by means of understanding through electromagnetic theory. However, this inversion process is not straightforward.

As a consequence, the application of conventional techniques for image processing, usually conceived to deal with optical like data, provides very limited efficiency in radar imagery. Due to the lack of robust means of image interpretation, still today, the segmentation of SAR data is often carried out through visual inspection performed by qualified analysts. Nevertheless, manual assimilation does not allow a rapid and massive exploitation of the data and, consequently, an operational use of SAR. Moreover, in recent years, technology to acquire SAR data has been subject to great advances, but the progresses in signal post processing methods to use these data do not follow the same rapid evolution. Therefore, great efforts oriented to design specifically dedicated methods for SAR information extraction are still to be provided.

The objective of this chapter is to present the particular characteristics of SAR images and then to identify the specific difficulties of post processing associated to the nature of the information content in SAR data.

The chapter is structured as follows. Section 2.1 presents the principles of SAR data acquisition in order to analyze the nature of the information imaged by a SAR system. Section 2.2 discusses the drawbacks associated to the unsupervised interpretation of SAR images. The special case of maritime scenarios in SAR images is reviewed in Section 2.3. Then, conclusions and further discussion are presented in Section 2.4.

2.1 Nature of the information imaged by a SAR system

This section aims at bringing some insight on SAR technology, by reviewing the principles of data acquisition in Section 2.1.1 and processing in the sensor in Section 2.1.2. The analysis of the nature of the information imaged by a SAR system allows an identification of the drawbacks associated to its exploitation in Section 2.2. Moreover, through a brief overview of the main applications, involving SAR sensors, the need of automatic tools is justified.

2.1.1 Basics of SAR data acquisition

The basic geometry of a SAR is shown in Figure 2. A platform moving with velocity v , at altitude h carries a side-looking radar antenna that illuminates the Earth's surface with pulses of electromagnetic radiation. The direction of travel of the platform is known as the *azimuth or along track direction*, whereas the distance from the radar track is measured in the *range or across track direction*.

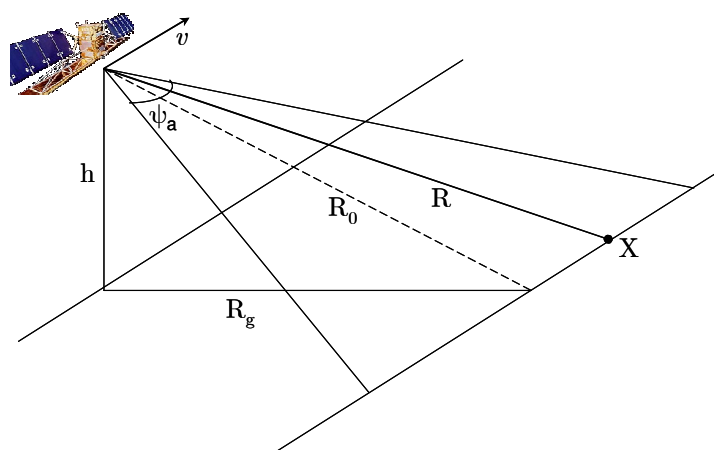


Figure 2. Basic geometry of a SAR system.

Typically, the antenna is rectangular with dimensions $d_a \times d_e$ where a and e denote azimuth and elevation, respectively. These dimensions are significant because they determine the area illuminated by the antenna. The radiation from an antenna of length d spreads out over an angle in radians

$$\psi = \frac{\lambda}{d} \quad (2.1)$$

where λ is the radar wavelength. This relation determines both the azimuth and the elevation beamwidths, ψ_a and ψ_e . Wavelength is related to the radar carrier frequency f_0 (in Hz) by:

$$\lambda f_0 = c \quad (2.2)$$

where c is the speed of light.

While the radar beam sweeps over a fixed scatterer X , the distance R between the scatterer and the platform will vary symmetrically about its minimum value R_0 with zero Doppler. R_g is the distance of the scatterer to the platform track on the Earth's surface and it is known as ground range. Important parameters of the pulses that modulate the carrier signal are the pulse length τ_p , the bandwidth B and the Pulse Repetition Frequency, PRF [18].

In this chapter, the simplest SAR geometry, corresponding to a monostatic configuration, is considered. Nevertheless, it is worth noting that multichannel or multidimensional SAR systems are of great interest for a number of applications. Up to now, the most extended two basic types of multidimensional SAR imagery are interferometry [19] [20] and polarimetry [21] [22]. On the one hand, SAR interferometry is essentially based on the construction of an interferogram by taking into account two complex SAR images of the same area, acquired at slightly different positions, see Figure 3. The small excursion in the angle of sight results in a phase difference between both SAR images that can be used to retrieve the scene's topography.

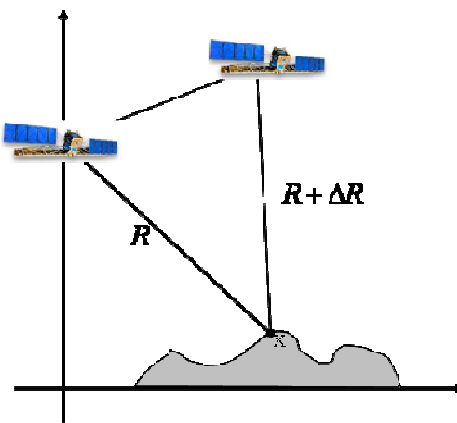


Figure 3. Geometry of an interferometric SAR system.

On the other hand, in the case of polarimetry, multidimensionality is obtained by taking advantage of wave polarization diversity in transmission and in reception. This permits deriving the scatterer response to any wave polarization state from the response to a pair of orthogonal polarization states [23] [24].

2.1.2 Basics of SAR data processing

The operation of a radar system is based on the transmission of electromagnetic pulses and then on the measurement of the characteristics of the echoes of these pulses reflected back to the receiver. Then, in order to determine the contribution in the echoes of the backscattering properties of the illuminated scene, processing is carried out in the receiver. In conventional imaging radar systems, the received signal, which is known as RAW data is usually processed by means of matched filtering [25] in order to obtain the reflectivity image, see Section 2.1.2.1. For SAR systems, this operation is usually performed in two sequential steps: range compression, see Section 2.1.2.2, and azimuth compression, see Section 2.1.2.3 (see Figure 4), in which s_R is the received signal, h_r is the impulse response of the filter in range, h_a is the impulse response of the filter in azimuth, τ and η are the range and azimuth coordinates respectively.

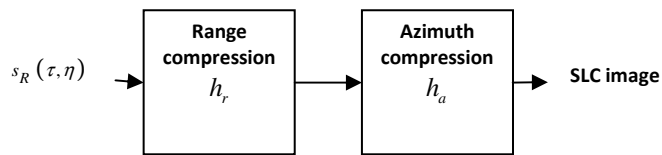


Figure 4. Simplified SAR focusing by means of sequential compression in range and in azimuth.

In this section, the concept of pulse compression through matched filtering will be reviewed. Then, its application to range and azimuth compression will be developed. The overall SAR impulse response will be deduced by assuming a point scatterer in the two dimensional space (τ, η) as a Dirac's delta at the position (τ_0, η_0) , characterized by a complex scattering amplitude

$$\sigma_s(\tau_0, \eta_0) = \sqrt{\sigma} e^{j\theta} \delta(\tau - \tau_0, \eta - \eta_0) \quad (2.3)$$

where $\delta(\tau, \eta)$ is the two-dimensional Dirac's function. The function σ denotes the complex radar cross section and θ is the scattering phase.

2.1.2.1. Pulse compression

In order to obtain a sufficient Signal to Noise Ratio, SNR in the following, high energy pulses would be necessary. Besides, short pulses provide better resolutions. However, due to power limitations in transmission devices, pulses can not be arbitrarily short. Since large pulses induce low resolution performances, pulse compression techniques have to be employed. The effectiveness of the compression is measured by means of the compression ratio which is the relation between the resolution after processing and the original pulse length. It can be expressed as

$$\text{compression ratio} = \frac{\tau_p}{r_t} \quad (2.4)$$

where r_t is the time resolution. The compression ratio depends on the design of the transmitted waveform. Imaging radars are designed so that the time bandwidth product $B\tau_p$ is large, so that $r_t \approx 1/B$. Thus, the compression ratio is approximately equal to the time bandwidth product. Several options exist for design of the transmitted waveform $p(t)$ [25] [26], but the most extended one is a linear frequency modulation or chirp signal with a FM rate of β/π Hz/s⁻¹

$$p(t) = \exp\left\{j(\omega_0 t - \beta t^2)\right\} \text{ for } |t| \leq \tau_p / 2 \quad (2.5)$$

where ω_0 is the carrier frequency of the radar expressed as radians / s⁻¹, β is a phase quadratic term often designed as the chirp rate and the bandwidth B is expressed in Hz as

$$B = \beta\tau_p / \pi. \quad (2.6)$$

The instantaneous phase of the signal in radians is

$$\phi(t) = \omega_0 t - \beta t^2 \quad (2.7)$$

and the instantaneous frequency in Hz, given by the time derivative of the phase, is

$$f(t) = (\omega_0 - 2\beta t) / 2\pi. \quad (2.8)$$

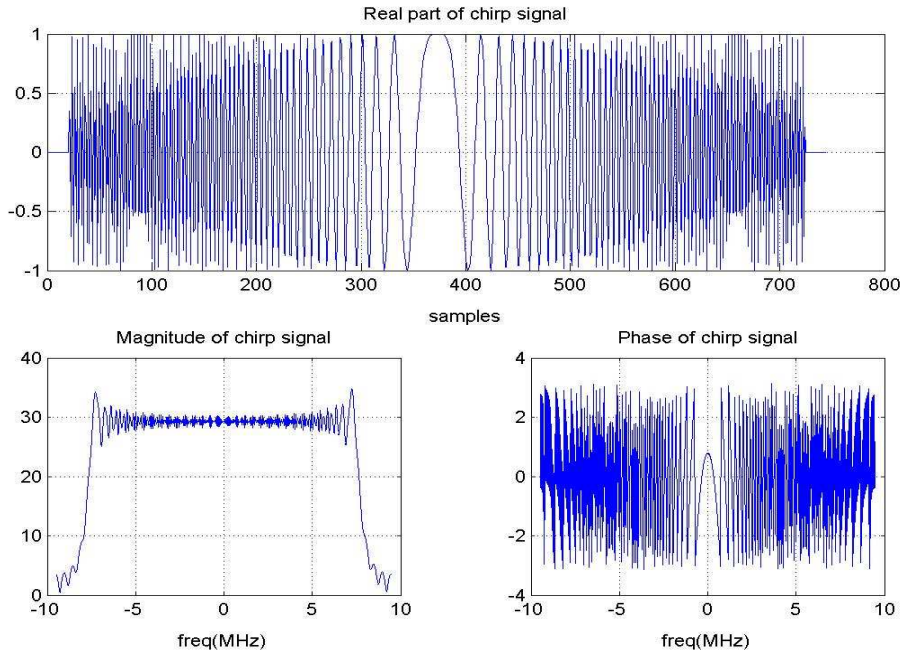


Figure 5. Down chirp signal representation.

The retrieval of the properties of the illuminated scene is achieved by analyzing the variations introduced in the echo reflected back to the receiver. This operation is referred to as focusing and it is usually carried out in radar applications through a matched filtering process. Specifically, matched filtering consists of convoluting the received signal with a suitable reference function consisting on a time reverted, complex conjugate copy of the transmitted pulse. Since the return from a point scatterer is a delayed, scaled version of the transmitted pulse, the response after matched filtering is given by

$$h_r(t) = \int_{-\tau_p/2}^{\tau_p/2} \exp(i\beta s^2) \exp(-i\beta[s+t]^2) \text{rect}\left(\frac{s+t}{\tau_p}\right) ds \\ = (\tau_p - |t|) \text{sinc}\left(\frac{\beta}{\pi} t [\tau_p - |t|]\right) \text{rect}\left(t/\tau_p\right) \quad (2.9)$$

where

$$\text{rect}(t) = \begin{cases} 1 & |t| \leq \frac{1}{2} \\ 0 & |t| > \frac{1}{2} \end{cases} \quad (2.10)$$

and $\text{sinc}(t) = \frac{\sin \pi t}{\pi t}$.

The first positive zero of this signal is often taken as a measure of the time resolution r_t . This is controlled by the *sinc* function and occurs when $\beta t(\tau_p - t) = \pi$, with solution

$$t = r_t = \frac{\tau_p}{2} \left(1 - \sqrt{1 - \frac{4}{B\tau_p}} \right). \quad (2.11)$$

Matched filtering maximizes the SNR if additive white noise is assumed and it is, therefore, the optimum solution in terms of SNR. However, matched filtering typically results in relatively high sidelobes, which are usually mitigated by windowing the reference signal, thus partially mismatching the filter, at the cost of reducing the resolution. From an implementation point of view, matched filtering assumes that the sampling frequency and the PRF satisfy the Nyquist-Shannon criterion. In range, this can become a technological challenge if very high resolution is required. In azimuth, however, it introduces fundamental trade-offs between swath width, range ambiguities and azimuth resolution. Therefore, alternative focusing options have been explored such as the ones based on the MUSIC algorithm [27], on CAPON and APES techniques for spectral estimation [28] or on Compressive Sensing [29].

2.1.2.2. Compression in range

Once the RAW data has been recorded, the first operation performed is range compression. The pulse compression in the range direction is performed on a pulse-by-pulse basis, which is the standard form of processing in most types of radar systems.

A point target whose distance from the radar is R_0 returns a signal of duration τ_p after a delay τ_d with respect to transmission

$$\tau_d = 2R_0 / c \quad (2.12)$$

The minimum and maximum measurable ranges are determined by the time interval between two emitted pulses which corresponds to the inverse of the *PRF*. They are usually referred to as near and far ranges. The distance between these ranges is the swathwidth:

$$\text{swathwidth} < \frac{c}{2\text{PRF}}. \quad (2.13)$$

An important concern regards resolution, which is defined as the minimum distance between two resolvable point targets. In radar theory, it is well known that the best attainable time resolution r_t is inversely proportional to the bandwidth B of the transmitted signal. Time resolution is directly related to space slant range resolution r_s

$$r_s = c / 2B . \quad (2.14)$$

The range compression is performed by correlating the received pulse with the complex response h_r , the corresponding matched filter to the transmitted pulse. Signal s_{rc} resulting from the compression in range can be expressed as

$$s_{rc}(\tau, \eta; \tau_0) = \sigma_s(\tau_0, \eta_0) \omega(\tau - \tau_0, \eta_0) \tau_p \text{sinc}\left(\frac{4\pi\beta\tau_p}{c}(\tau - R(\tau - \tau_0, \eta_0))\right) \quad (2.15)$$

where $R(\tau - \tau_0, \eta_0)$ represents the sensor to scatterer distance and $\omega(\tau - \tau_0, \eta_0)$ is the illumination given by the antenna pattern which takes into account range attenuation, system losses, etc.

2.1.2.3. Compression in azimuth

After range processing on a single pulse, the measurement in each range gate contains a contribution from each scatterer in a space interval in azimuth which is controlled by the azimuth beamwidth. The main particularity of SAR principle consists of the exploitation of the nearly quadratic range variation of a point scatterer as the beam illuminates it, see Figure 6.

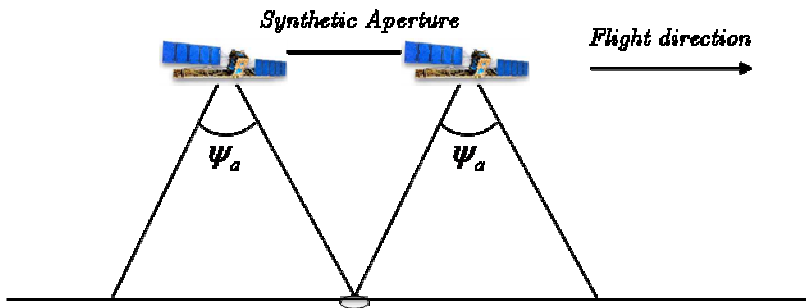


Figure 6. Aperture Synthesis concept.

A reference coordinate system can be defined for a scatterer X located on the line on the ground corresponding to a slant range R_0 with the x -axis corresponding to the azimuth direction and with the origin fixed at X . With this, the distance R between the moving platform of the sensor and the scatterer satisfies $R^2 = R_0^2 + x^2$. If the beam is narrow, the scatterer is just illuminated when $x \ll R_0$, in which case

$$R \approx R_0 + \frac{x^2}{2R_0} . \quad (2.16)$$

The corresponding two way phase delay at the carrier frequency is

$$\phi(x) = -\frac{4\pi R_0}{\lambda} - \frac{2\pi x^2}{\lambda R_0}. \quad (2.17)$$

This is equivalent to linear frequency modulation in space. In spatial coordinates, the equivalent of the pulse length is the synthetic aperture length D_s , which is the azimuth distance illuminated at range R_0 . If denoting ψ_a the azimuth beamwidth which follows $\psi_a = \lambda / d_a$:

$$D_s = R_0 \psi_a. \quad (2.18)$$

Therefore, the spatial bandwidth in cycles·m⁻¹ is given by

$$\frac{1}{2\pi} \times \frac{4\pi}{\lambda R_0} \times D_s = \frac{2}{d_a}. \quad (2.19)$$

And the associated spatial resolution is expressed as

$$r_a = \frac{d_a}{2}. \quad (2.20)$$

Hence, the azimuth focusing is equivalent to synthesizing a large antenna, of length D_s . Since ψ_a is proportional to λ , D_s is linearly proportional to both the slant range and the wavelength.

From the point of view of the deduction of the impulse response, the azimuth compression is performed by correlating the received RAW signal after range compression s_{rc} with the impulse response in azimuth h_a expressed as

$$h_a(\tau, \eta; \tau_0) = \omega(\tau_0, \eta) \exp\left(-j \frac{4\pi}{\lambda} R(\tau_0, \eta)\right) \delta(\tau - R(\tau_0, \eta)). \quad (2.21)$$

With this, we have for the retrieved reflectivity S for a particular point (τ_1, η_1) :

$$\begin{aligned}
S(\tau_1, \eta_1) &= \int_{-\infty}^{\infty} \int_{-\infty}^{\infty} s_{rc}(\tau, \eta; \tau_0) h_a(\tau, \eta - \eta_1; \tau_1) d\tau d\eta \\
&= \int_{-\infty}^{\infty} \int_{-\infty}^{\infty} \sigma_s(\tau_0, \eta_0) \omega(\tau_0, \eta - \eta_0) \tau_p \text{sinc}\left(\frac{\pi\beta\tau_p}{c}(\tau - R(\tau - \tau_0, \eta_0))\right) \exp\left(-j\frac{4\pi}{\lambda}R(\eta - \eta_0; \tau_1)\right) \\
&\quad \cdot \omega_{ref}(\eta - \eta_1; \tau_1) \delta(\tau - R(\eta - \eta_1; \tau_1)) \exp\left(j\frac{4\pi}{\lambda}R(\eta - \eta_1; \tau_1)\right) d\tau d\eta \\
&= \sigma_s(\tau_0, \eta_0) \int_{-\infty}^{\infty} \omega_{ref}(\eta - \eta_1; \tau_1) \omega(\tau_0, \eta - \eta_0) \tau_p \text{sinc}\left(\frac{4\pi\beta\tau_p}{c}(R(\eta - \eta_1; \tau_1) - R(\eta - \eta_0; \tau_0))\right) \\
&\quad \cdot \exp\left(j\frac{4\pi}{\lambda}(R(\eta - \eta_1; \tau_1) - R(\eta - \eta_0; \tau_0))\right) d\eta
\end{aligned} \tag{2.22}$$

where ω_{ref} is defined as the reference azimuth weighting function. Assuming $\tau_1 \approx \tau_0$,

$$R(\eta - \eta_1; \tau_1) - R(\eta - \eta_0; \tau_0) \approx \Delta\tau - \frac{\eta\Delta\eta}{\tau_0} + \frac{1}{2\tau_0}(\eta_1^2 - \eta_0^2) \tag{2.23}$$

where $\Delta\eta = \eta_1 - \eta_0$ and $\Delta\tau = \tau_1 - \tau_0$.

Hence,

$$S(\tau_1, \eta_1) = \sigma_s(\tau_0, \eta_0) \tau_p \sin c\left(\frac{4\pi\beta\tau_p}{c} \Delta_\tau\right) \exp\left(j\frac{4\pi}{\lambda} \Delta_r\right) \int_{-\infty}^{\infty} \omega_{eff}(\eta - \eta_0, \tau_0) \exp(-j2\pi f\tau) d\tau \tag{2.24}$$

with $\omega_{eff}(\eta - \eta_0, \tau_0) \approx \omega(\eta - \eta_0, \tau_0) \omega_{ref}(\eta - \eta_1, \tau_1)$

As a consequence,

$$S(\tau, \eta) = \sigma_s(\tau_0, \eta_0) \exp\left(j\frac{4\pi}{\lambda}(\tau - \tau_0)\right) \text{sinc}\left(\frac{\pi(\tau - \tau_0)}{r_s}\right) \text{sinc}\left(\frac{\pi(\eta - \eta_0)}{r_a}\right). \tag{2.25}$$

Therefore, the SAR system response can be considered as a rectangular filter with a range and azimuth bandwidths equal to $2B/c$ and $2/d_a$ respectively.

2.1.3 Applications of SAR systems and needs of unsupervised techniques

Due to their all weather observation capability, independently from the day – night cycle, SAR systems have already proven to be well suited for a number of civilian applications, regarding Earth monitoring at different scales. This section will go through a brief overview of several examples of applications, both in land and in the oceans. Special attention will be given to maritime applications, since they constitute the main concern of this dissertation. The review of applications confirms the potential of SAR systems. And the requirements of near-real time treatment of great amounts of data justify the need of automatic methods of segmentation for the effective operability of SAR systems.

- **Agriculture**

Spaceborne SAR sensors constitute an efficient method for mapping crop characteristics over large areas and tracking temporal changes in soil conditions [30] [31]. This is focused to manage the optimization of the exploitation process in what is called *precision farming* [32]. In particular, multipolarization configurations are able to distinguish between different types of crops, see Figure 7 [33].



Figure 7. RADARSAT-2 image from the Ribeirão Preto in Brazil, acquired in Fine Quad-Pol mode on February the 19th, 2008.

- ***Forestry***

Forests constitute a fragile natural resource. Their monitoring from space is useful for management purposes. For example, tracking by means of SAR sensors can be employed to estimate biomass [34] [35] [36], to reveal clear cut areas and prosecute eventual illegal deforestation [37] or to evaluate the damages caused by a fire [38].

- ***Geology***

SAR data is used to monitor and detect oil seeps [39] - reducing the risk and cost of drilling. It is also used to derive geophysical terrain information, such as surface roughness, which is useful for understanding processes such as bedrock weathering and the sorting of unconsolidated solid materials. One of the most important applications of SAR technology nowadays is the possibility to obtain 3D topographic maps by means of SAR interferometry [40].

- ***Coastal and marine surveillance***

The intensification in the past years of offshore resource based operations has prompted governments and industry agents to look for monitoring solutions. Satellite borne tools constitute a powerful option, providing large coverage and observation capability at night. The main operational applications concerning marine surveillance are ship detection, oil spill monitoring, see Figure 8, wind field estimation, shallow-water bathymetry mapping, monitoring of glaciers which are one of the most sensitive elements to the global warming, see Figure 9, current fields [41], etc.

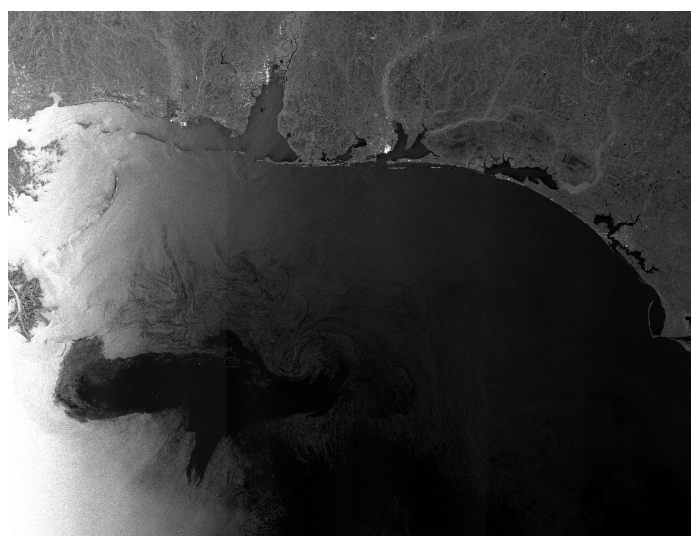


Figure 8. ENVISAT image from the Gulf of Mexico, acquired on April the 29th, 2010 on the occasion of the explosion of the BP offshore drilling rig.



Figure 9. ERS image of the Wilkins Ice Shelf along the West Antarctic Peninsula, acquired on January the 13th, 1992.

2.2 Associated difficulties for automatic SAR image interpretation

An operational and intensive exploitation of SAR images is not viable with completely supervised means. Automatic techniques able to produce rapid, reproducible and reliable results are to be provided instead. These techniques should be designed to work with minimal operator intervention and they should avoid specific tuning to a particular image. As it will be shown in this section, these requirements are especially difficult to satisfy with SAR imagery. This section proposes a review of the main drawbacks associated to the automatic understanding of SAR data, independently of the application.

2.2.1 Speckle

A SAR image can be modeled as the convolution of the local complex reflectivity of the observed area $\sigma(\tau, \eta)$ with the impulse response of the SAR system $h(\tau, \eta)$

$$S(\tau, \eta) = \sigma(\tau, \eta) \otimes h(\tau, \eta) \quad (2.26)$$

where \otimes stands for convolution. It has been seen that the SAR system impulse response $h(\tau, \eta)$ may be interpreted as a bidimensional low pass filter, in such a way that the finite local support of this filter determines the spatial resolution of the SAR system. The spatial area embraced by this impulse response is known as resolution cell. In the SAR imaging process, linearity is assumed; the imaged scene is modeled as a set of N individual scatterers whose scattered fields superpose linearly as

$$S(\tau, \eta) = \sum_{k=1}^N \sigma_k(\tau, \eta) \otimes h(\tau, \eta) \quad (2.27)$$

where $\sigma_k(\tau, \eta)$ is the complex reflectivity of the k th individual scatterer in the resolution cell. The Born model [42] is assumed and no interaction between individual scatterers is considered.

Equivalently,

$$S(\tau, \eta) = \sum_k^N |a_k| e^{j\phi_k} \quad (2.28)$$

where $|a_k|$ and ϕ_k are respectively the amplitude and the phase of the contribution of the k th scatterer. When the resolution cell contains a single scatterer or when the contribution of an individual scatterer is largely dominant, the pixel is said to represent a point or deterministic target. In this situation, the complex value of the pixel must be interpreted in terms of the physical properties and geometry of the individual scatterer. On the contrary, when the number of scatterers increases, the reflectivity of the pixel results from a random walk process, see Figure 10. If N is large enough, it is usually assumed that the amplitudes and the phases of the scatterers are independent [43] [44]. Then, by means of the central limit theorem, it can be proven that the real and the imaginary parts of $S(\tau, \eta)$ may be modeled as independent, zero mean, equally distributed Gaussian random variables.

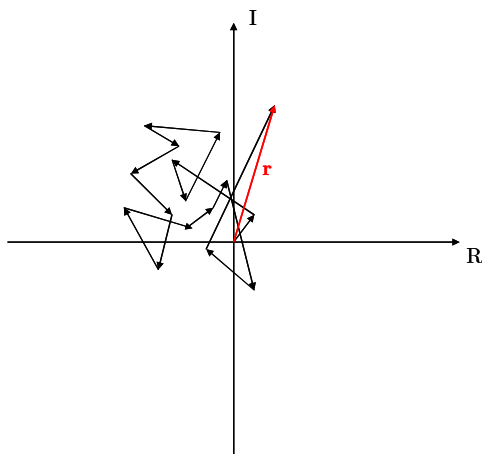


Figure 10. Two dimensional random walk modeling.

With this, the intensity I of a SAR image, $I = |S(\tau, \eta)|^2$ follows a negative exponential distribution:

$$p_I(I) = \begin{cases} \frac{1}{\sigma} e^{-I/\sigma} & I \geq 0 \\ 0 & \text{otherwise} \end{cases} \quad (2.29)$$

with mean value and standard deviation, both equal to σ . The observed phase of $S(\tau, \eta)$ is uniformly distributed over $[-\pi, \pi]$. The effect of the random walk imposes to consider that the value of the pixel has to be understood in statistical terms, characterized by σ . Consequently, $I(\tau, \eta)$ may be expressed as [45]

$$I = \sigma n. \quad (2.30)$$

The parameter σ represents the radar cross section of the scene, whereas n is a multiplicative noise component, referred to as speckle and described by a negative exponential distribution with unitary mean and variance

$$p_n(n) = e^{-n}. \quad (2.31)$$

Speckle filters are often used to reduce the noise-like effect of speckle, but even if they are able to effectively smooth speckle, they inevitably affect information content. Among the speckle filters proposed in literature, the most relevant ones are the Lee filter [46], the Kuan filter [47], the Gamma filter [48] and the Frost filter [49]. Figure 11 shows the effect of Lee filtering through an example of application over a SAR image of a coastal area.

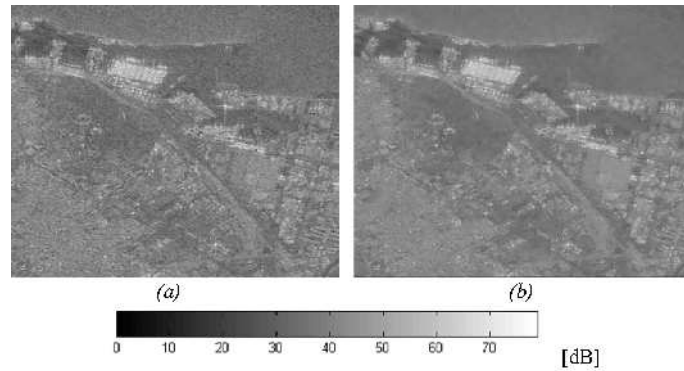


Figure 11. Example of application of Lee filter with a window size of 11 x 11 px. in a RADARSAT image of the area of Barcelona (Spain). (a) SAR imagette (b) Result of Lee filter.

Strictly speaking, even if treated as multiplicative noise in the equations, speckle is a measure of the interference between the scatterers within the resolution cell. As seen previously, if the number of scatterer contributions is large, speckle is considered as fully developed and treated statistically. In fact, this is the approximation assumed in most of the applications. Nonetheless, new systems with improved resolution capabilities impose a revision of this assumption. Consider for example the TerraSAR-X sensor with a maximum achievable spatial resolution in range of 0.65 – 1 m. If the spatial resolution is improved, the number of scatterers within a resolution cell decreases and, as a consequence, the hypothesis of fully developed speckle may not be accurate enough in some cases. Furthermore, if a limited number of contributions is assumed, it should be interesting to explore if some kind of information can be inferred from the intensity of a single pixel about the type of distribution of the individual scatterers within a resolution cell.

2.2.2 Spatial correlation due to processing

In the scope of the applications treated in this dissertation, one of the most critical imaging effects to be taken into account is the spatial correlation induced by the focusing. Let's analyze it, starting from the linear imaging equation

$$\begin{aligned} S(x) &= (C(R)\sigma(x)*k(x) + n(x))*h(x) \\ &= C(R)\sigma(x)*k(x)*h(x) + n(x)*h(x) \end{aligned} \quad (2.32)$$

where

$k(x)$ can be regarded as a prefilter containing two effects, the beam weighting and the Doppler shift

$C(R)$ is a coefficient dependent of range R whose magnitude is given by

$$|C(R)|^2 = \frac{P_T G_R^2 \lambda^2 G_p}{(4\pi)^3 R^4 L} \quad (2.33)$$

with P_T is the peak transmitted power, G_R is the one-way power gain of the antenna pattern at the specified range, L allows for system losses and G_p is the processing gain due to the range compression.

It can be deduced [50] that the auto correlation function $R_s(x)$ for the observed voltage $\varepsilon(x)$

$$R_s(x) = |C|^2 \sigma^0 R_{h_a}(x) + N R_l(x). \quad (2.34)$$

Since the data are sampled, we have for the complex correlation coefficient at lag k in the azimuth direction $\rho_a[k]$ for an ideal case with sample spacing following exactly the Nyquist sampling criteria

$$\rho_a[k] = \text{sinc}(k) = \frac{\sin \pi k}{\pi k} = \begin{cases} 1, & k = 0 \\ 0, & k \neq 0 \end{cases}. \quad (2.35)$$

In this ideal case, no correlation will be observed between pixels. Nevertheless, in practice, the data are oversampled and consequently pixels are correlated in realistic cases. This spatial correlation together with speckle produces in the intensity SAR images a characteristic granular pattern, awkward for segmentation purposes in general and especially when spot detection is considered.

2.2.3 Large dynamic range

It has been seen previously that a SAR data set contains information of the combined reflectivity, including both amplitude and phase, of the individual resolution cells. The reflectivity strongly depends on the radar cross section of the backscattering target. The radar cross section is subject to a great span of variation, depending on the point of view and the nature of the backscatterer. This results in a large dynamic range, which can not be handled by typical image processing algorithms and which constitutes a serious inconvenience for further post-processing techniques.

Usually, the dynamic range is reduced prior to the representation of the image or to the application of enhancement techniques by means of a logarithm operation [50] [51].

2.3 SAR imaging of the ocean surface

The applications tackled in this thesis involve essentially oceanic scenarios, see Figure 12. Therefore, this section is devoted to analyze the particularities of SAR images when maritime scenarios are considered.

Oceans are nonlinear dynamic systems producing waves at different scales: long waves with a length of several hundred meters, intermediate waves with a length of tens of meters and short waves less than one meter long. This is usually described by means of sea surface energy spectrum [52]. Nowadays, it is widely assumed in the literature that the SAR transform applied to sea mapping can be assimilated to a process in two steps. The first one consists of a modulation of the backscattering energy around its mean σ_0 by the sea surface motivated by the tilt modulation, which is a geometric effect due to the variation of the angle between the

sea surface and the radar beam [53] and an hydrodynamic effect due to the non uniformity of the gravity capillary wave spectrum. The energy backscattered back to the radar due to Bragg scattering is related to this spectrum [54]. The second step is the modulation produced by the motion of the sea surface. With this, SAR Fourier coefficients of the sea surface can be modeled as [55]

$$\tilde{X}_{SAR}(k) = |A|^{-1} \int_A X_{RAR}(x) \cdot e^{jkd(x)} \cdot e^{jkdx} dx \quad (2.36)$$

where A is a given surface and x is a two-dimensional array with range and azimuth components. $d(x)$ are the Doppler shifts produced by orbital wave velocities and k is the wavenumber vector.

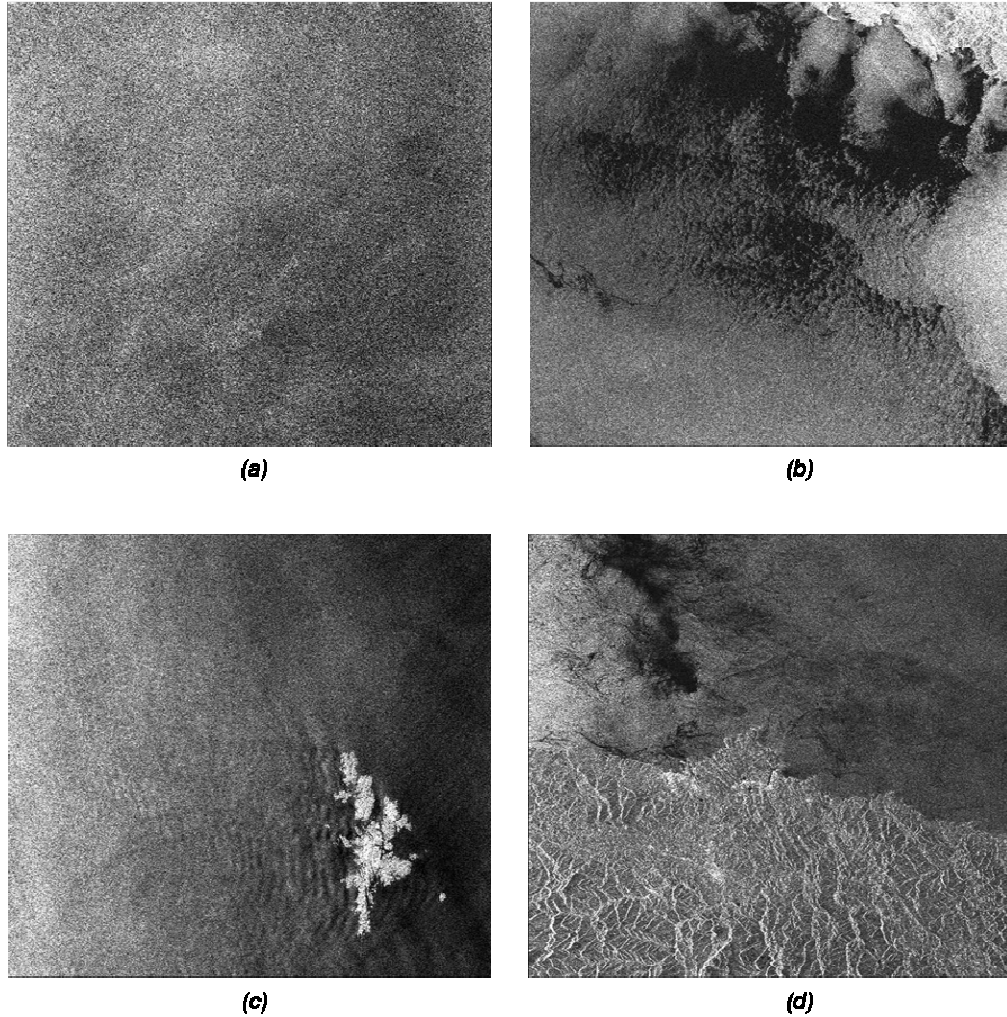


Figure 12. Examples of oceanic scenarios in SAR images. (a) RADARSAT image of the Cantabrian Sea. (b) RADARSAT image of the Adriatic Sea. (c) RADARSAT image of the North Sea. (d) RADARSAT image of the coast of Gijón (Spain).

2.4 Summary

After reviewing the mechanisms involved in the acquisition of SAR data, the potential of SAR systems for a number of civilian applications has been highlighted in this chapter. Nevertheless, an operational use of SAR data requires further development of rapid, dedicated, unsupervised techniques for data mining. Since SAR images are 2D representations of local scattering properties of an illuminated scene, conventional image post processing tools, conceived to deal with optical imagery, provide limited efficiency when applied to radar signals.

This observation constitutes the main motivation of this dissertation which is to design automatic data mining methods, specifically conceived to deal with SAR data for a number of applications. Hence, the particularities of the nature of SAR information, associated to the processes of data acquisition and processing, have been identified in this section in order to manage them.

Chapter 3. A multiscale framework for the exploitation of SAR data

An observation that arises from different experiments carried out to check the feasibility of automatic segmentation of SAR data is that existing signal processing techniques are not as good as a human operator, who is better at managing complex clutter situations [1]. More specifically, the eye is an extremely sophisticated system sensitive to local regularity, identifying a texture over two fundamental properties: the orientation of its elements and its frequency content [57] [58] [59]. From a signal processing point of view, this translates into performing a time-frequency analysis. Moreover, the human vision can also manage contextual information thanks to its capability of focusing and relating elements at different scales. In signal processing terms, this means performing a multiscale or multiresolution analysis. Figure 13 gives an intuitive illustration of the multiscale concept. The image displayed consists in a mosaic of small images involving different objects and scenes, as it can be appreciated in the zoom in the right. Nevertheless, at first sight, these elements are not appreciable and the most noticeable feature in the overall image is a monumental building with four easily distinguishable towers. As a consequence, if looking for edges for example, this image can be viewed at least at three scales. The coarser one will deal with the contour of the building, the second one, finer, will enhance edges due to the limits of the different rectangular images constituting the mosaic, and the third one, will have to do with the contour of the different objects constituting the smaller pictures.

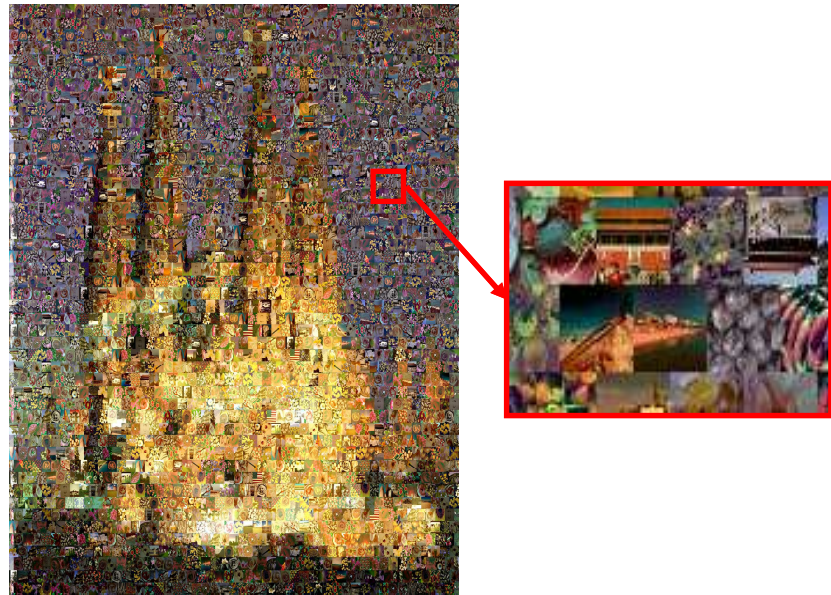


Figure 13. Mosaic picture of the Sagrada Familia Temple in Barcelona (Spain) illustrating the multiscale concept.

This chapter aims at presenting tools for multiscale time-frequency analysis and then justifying the interest of stating a multiresolution framework for the automatic exploitation of SAR imagery. More specifically, this chapter is structured as follows. First, the multiscale time-frequency concept is presented and different mathematical tools are considered in Section 3.1 with special emphasis on the WT. After overviewing the properties of multiresolution analysis in parallel to the characteristics of SAR imagery, the suitability of stating a multiscale time-frequency framework for the automatic exploitation of SAR data is justified in Section 3.2. A brief summary concludes this chapter in Section 3.3.

3.1 Multiscale time – frequency concept

A time (similarly space) – frequency (similarly scale) decomposition of a signal can be obtained through a projection over atoms well localized in time and frequency. More specifically, these atoms are waveforms that have a minimal spread both in time and frequency. Hence, a projection of a complex phenomenon in such a basis results in a mapping of its energy content into tiles in the time-frequency plane. The most important concept underlying the tiling of the time-frequency plane is the Heisenberg uncertainty principle. It was first demonstrated in 1927, starting from an intuitive statement with large implications in a number of diverse fields ranging from physics to philosophy: “The more precisely the position is determined, the less precisely the momentum is known” [60]. In the scope of time – frequency decomposition, this principle states that the atomic waveforms can not be arbitrarily small both in time and frequency. If the support of the tiles is represented by means of rectangles, this implies that

their minimum area is fixed. If the window is wide in time, the accuracy in the measure in frequency will be high at the expense of low localization capabilities. The frequency can not be provided instantly. The notion of instantaneous frequency remains to be defined.

- **Theorem 3.1. Heisenberg Uncertainty Theorem**

The temporal variance σ_t^2 and the frequency variance σ_ω^2 of $f \in L^2(\mathbb{R})$ satisfy

$$\sigma_t^2 \sigma_\omega^2 \geq \frac{1}{4} \quad (3.1)$$

with

$$\sigma_t^2 = \frac{1}{\|f\|^2} \int_{-\infty}^{\infty} (t-u)^2 |f(t)|^2 dt \quad (3.2)$$

and

$$\sigma_\omega^2 = \frac{1}{2\pi \|f\|^2} \int_{-\infty}^{\infty} (\omega - \xi)^2 |\hat{f}(\omega)|^2 d\omega \quad (3.3)$$

where u and ξ are given by

$$u = \frac{1}{\|f\|^2} \int_{-\infty}^{\infty} t |f(t)|^2 dt \quad (3.4)$$

and

$$\xi = \frac{1}{2\pi \|f\|^2} \int_{-\infty}^{\infty} \omega |\hat{f}(\omega)|^2 d\omega \quad (3.5)$$

where \hat{f} is the Fourier Transform, FT in the following, of f .

Then, a complete multiscale time-frequency representation is obtained by covering the time frequency plane with several groups of atoms with varying dimensions.

There are multiple methods that provide a time – frequency decomposition of a given signal (Short Time Fourier Transform – STFT in the following - , Wigner Ville distribution among others [61] [62]). This section overviews the properties of the STFT and of the WT in order to justify the advantages of the latter for SAR data exploitation purposes.

3.1.1 Short Time Fourier Transform (STFT)

The Fourier analysis theory is based on decomposing any periodical function in the set of complex exponentials $\{e^{int}\}_{n \in \mathbb{Z}}$. Given an integrable function $f(t)$, its FT $\hat{f}(\omega)$ is obtained as

$$\hat{f}(\omega) = \int_{-\infty}^{\infty} f(t) e^{-j\omega t} dt \quad (3.6)$$

and gives a measure of how much oscillations the function f presents at frequency ω . When the FT is applied to a function, the result is independent of the time variable t . The spectral analysis is performed globally over the length of the signal and, as a consequence, this tool can not be employed to analyze the frequency behavior of a phenomenon locally.

The most natural way to overcome this handicap is to divide the whole integration interval into smaller subintervals. The duration of these intervals is fixed by the finite length of a window function $w(t)$ that is translated by a varying time parameter τ .

$$\hat{f}(\omega, \tau) = \int_{-\infty}^{\infty} f(t) w(t - \tau) e^{-j\omega t} dt. \quad (3.7)$$

As a result, the STFT gives a two-dimensional decomposition of a one-dimensional signal, in comparison with the classical FT which is a one-dimensional transform. The additional dependence on a time variable of the STFT with respect to the classical FT provides sensitivity to the spatial exceptional features of the function analyzed. The frequency behavior of spatial irregularities is otherwise fuzzed in the spectral distribution of the overall function when estimated through the FT.

Figure 14 presents a comparison of the time-frequency analysis performed by the FT and the STFT. As observed, the tiling performed by the FT eliminates any time sensitivity in the transformed frequency domain. This drawback is not present in the tiling performed by the STFT.

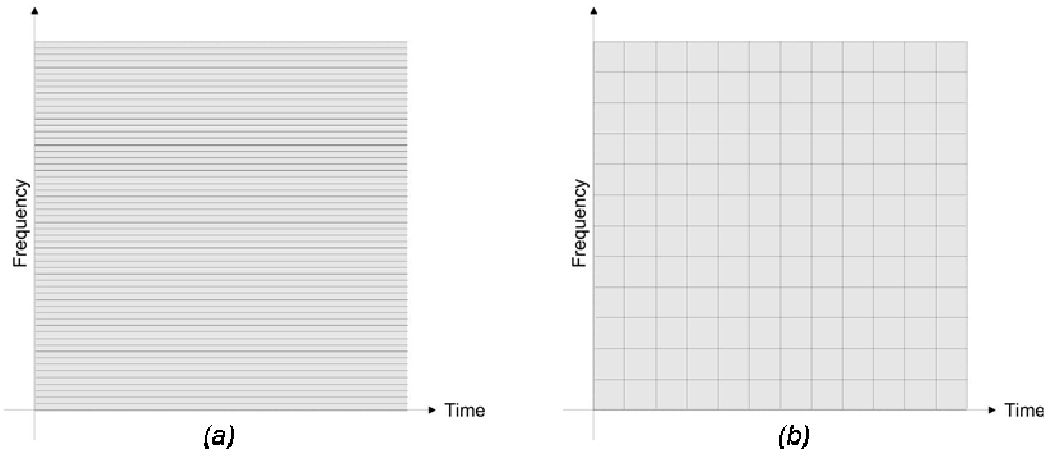


Figure 14. Tiling of the time-frequency plane carried out by the FT (a) and the STFT (b).

Nevertheless, it is worth noting that the sensitivity to temporal changes with the STFT is obtained at the expense of a degradation of the frequency with respect to the FT: in the STFT time frequency decomposition, the tiles are wider in the frequency dimension. Moreover, the division of the time frequency plane with the STFT is performed by means of a regular framing. All the tiles have the same area, this implying that the achievable resolution both in time and in frequency is fixed a priori through the length of the window $w(t)$. The resolution requirements in time as well as in frequency depend on the application focused and on the type of function analyzed. For example, slow variations in time (similarly in frequency) do not require high temporal (similarly frequency) resolution. For stationary processes, the resolution parameter (through the dimensions of $w(t)$) can be adjusted optimally, but for non stationary ones, a deeper analysis is performed with a framing of the time frequency plane through tiles of varying dimensions. The most extended tool for providing such a multiscale time frequency analysis is the WT.

3.1.2 The Wavelet Transform

In the last decade, wavelet techniques have emerged with their remarkable properties as a powerful signal processing tool. They have already proven their usefulness in a number of applications related to diverse domains: signal estimation [63] [64] [65], target detection and classification [66], compression [67], prediction and filtering [68], synthesis [69].

Among all the multiscale time-frequency methods, the WT presents advantages with respect to other techniques, since it offers high flexibility and it holds the key for the successes of detection and estimation in non-stationary environments [70]. In fact, the STFT and the Wigner-Ville transform are not always suitable for transient phenomena. Nevertheless, an efficient use of the WT requires adjusting conveniently several parameters, noticeably the type of WT and the type of mother wavelet, according to the application focused. This section presents the basic aspects and properties of the WT.

3.1.2.1. Basics of the Wavelet Transform

This section presents the mathematical formulation of the different types of WT, while introducing the notation employed in the rest of the dissertation.

- ***Continuous Wavelet Transform (CWT)***

Given a function $\psi(x)$ which satisfies the condition

$$\int_{-\infty}^{\infty} \psi(x) = 0 \quad (3.8)$$

with unity power and centered in $x=0$, the function $\psi_{a,b}(x)$ is defined as

$$\psi_{a,b}(x) = \frac{1}{\sqrt{a}} \psi\left(\frac{x-b}{a}\right) \quad (3.9)$$

where $a, b \in \mathbb{Z}, a \neq 0$. The function $\psi(x)$ is called the mother wavelet. The functions $\{\psi_{a,b}(x)\}_{a,b \in \mathbb{Z}}$ constitute the family of wavelets resulting from translations and dilations of the mother wavelet. The Continuous Wavelet Transform (CWT) of a function, $f(x)$, is defined as

$$Wf(a,b) = \int_{-\infty}^{\infty} f(x) \frac{1}{\sqrt{a}} \psi^*\left(\frac{x-b}{a}\right) dx \quad (3.10)$$

where $*$ indicates conjugation. The CWT can be also written as

$$Wf(a,b) = f(x)^* \bar{\psi}_a(b) \quad (3.11)$$

where $\bar{\psi}_a(b) = 1/\sqrt{a} \psi^*(-x/a)$. The parameter b is called the translation parameter, whereas a is called the dilation parameter. This parameter can be also interpreted as the inverse of the frequency ω . Thus, the CWT can be seen as a filtering of $f(x)$ by dilated band-pass filters, whose impulse response is given by the wavelet functions.

The issue arising at this point is whether or not it is possible to recover the function $f(x)$ from the transformed values $Wf(a,b)$, i.e., whether it is possible or not to define an inversion formula. If the wavelet function $\psi(x)$ satisfies the admissibility condition [71],

$$C_\psi = \int_{-\infty}^{\infty} \frac{|\hat{\psi}(\omega)|^2}{|\omega|} d\omega < \infty \quad (3.12)$$

then $f(x)$ can be reconstructed as

$$f(x) = \frac{1}{C_\psi} \int_0^{\infty} \int_{-\infty}^{\infty} Wf(a,b) \frac{1}{\sqrt{a}} \psi\left(\frac{x-b}{a}\right) db \frac{da}{a^2} \quad (3.13)$$

which is called the inverse continuous wavelet transform of $f(x)$, denoted by ICWT. The wavelet function $\psi(x)$ is defined in such a way that both, $\psi(x)$ and $\hat{\psi}(\omega)$ are window functions, allowing to define its centers and variances. The wavelets $\{\psi_{a,b}(x)\}_{a,b \in \mathbb{Z}}$ are centered at the positions $xa+b$, with a time width equal to $\Delta x a$. The corresponding FTs have their centers at the positions ω/a , whereas they have a frequency width of $\Delta\omega/a$. This means

that the CWT obtains the information relative to $f(x)$ in the time dimension in a window of width $\Delta x a$ centered at $xa + b$, and in the frequency dimension with a window of width $\Delta \omega / a$ centered at ω/a . Consequently, the frequency support of $\psi(x)$ is larger for high frequencies than for low frequencies, whereas its time support is low for high frequencies and larger for low frequencies. As it can be deduced, the region of influence of the functions $\{\psi_{a,b}(x)\}_{a,b \in \mathbb{Z}}$, i.e., the dimensions and position of the time-frequency atoms in the time-frequency plane, is adapted to the nature of this plane. Figure 15 depicts the behavior of the functions $\{\psi_{a,b}(x)\}_{a,b \in \mathbb{Z}}$, schematically represented by rectangles.

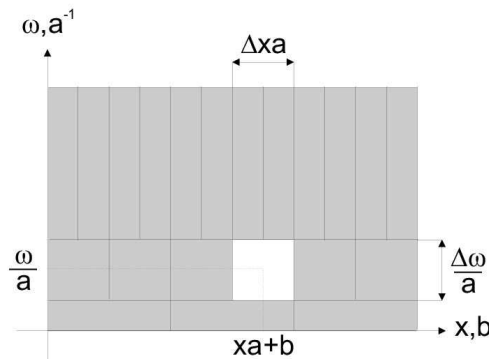


Figure 15. Time-frequency plane tiling performed by the continuous WT at discrete positions of the translation parameter b and the dilation parameter a .

The CWT is not suitable to analyze the properties of discrete series, as for instance, SAR imagery. For this reason, it is necessary to explore the possibility to obtain a discrete set of the support given by the parameters a and b , from which it was possible to completely characterize a given function.

- **Discrete Wavelet Transform (DWT)**

Keeping in mind the concept of the time-frequency plane, any sampling of the continuous parameters a and b should be done in such a way that the discrete wavelet family resulting from this sampling is able to decompose $f(x)$. In the frequency dimension, these functions are centered at the positions ω/a with a spread equal to $\Delta\omega/a$. In order to obtain a full coverage, it is therefore necessary to sample it at the positions $\{a_0^i\}_{j \in \mathbb{Z}}$ with $a_0 > 1$. The time domain is uniformly sampled at intervals proportional to the scale a_0^i . As a consequence, the components of the discrete set $\{\psi_{i,m}(x)\}_{i,m \in \mathbb{Z}}$ have the expressions

$$\psi_{i,m}(x) = \frac{1}{a_0^{i/2}} \psi\left(\frac{x - a_0^i b_0 m}{a_0^i}\right) \quad i, m \in \mathbb{Z} \quad (3.14)$$

with $b_0 > 0$. Given the previous set $\{\psi_{i,m}(x)\}_{i,m \in \mathbb{Z}}$, any function $f(x)$ can be decomposed as a series

$$f(x) = \sum_{j,m \in \mathbb{Z}} \langle f(x), \psi_{i,m}(x) \rangle \psi_{i,m}(x) \quad (3.15)$$

where $\langle f(x), \psi_{i,m}(x) \rangle$ is obtained as

$$Wf(i,m) = \langle f(x), \psi_{i,m}(x) \rangle = \int_{-\infty}^{\infty} f(x) \frac{1}{a_0^{i/2}} \psi^* \left(\frac{x - a_0^i b_0 m}{a_0^i} \right) dx. \quad (3.16)$$

This equation receives the name of Discrete Wavelet Transform, DWT in the following, which is very similar to the expression of the CWT. It is important to notice that the above expression represents a mapping from the original one-dimensional space denoted by x onto a two dimensional space denoted by i and m . The DWT is obtained through a continuous integration process. Moreover, the dimensionality of the space supporting the discrete wavelet values, referred to in the following as transformed or wavelet domain, has increased with respect to the time or space domain (also referred to as original domain of the function $f(x)$). The underlying concept is that, in the original domain only time or space information is available, whereas the transformed domain is able to give time or space information, within the parameter m , as well as frequency or scale information, within the parameter i .

Special attention will be given to the particular case in which the parameter $a_0 = 2$ and $b_0 = 1$. This particular case is referred to as dyadic discrete WT or simply DWT, in which the wavelets have the following expressions

$$\psi_{i,m}(x) = \frac{1}{\sqrt{2^i}} \psi \left(\frac{x - 2^i m}{2^i} \right) \quad i, m \in \mathbb{Z}. \quad (3.17)$$

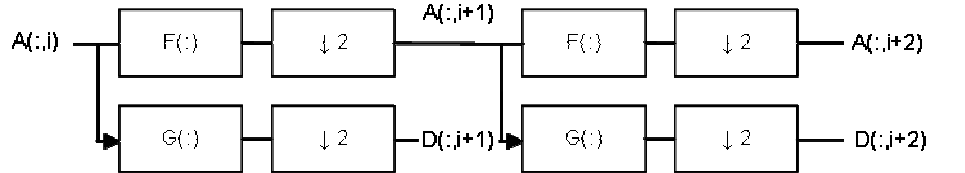
The advantage of this particular case relies in the fact that fast computations of the DWT are possible, but also a link between the DWT and certain filtering schemes is possible.

At this point, it is worth summarizing the ideas behind sampling the CWT. Under proper conditions, a sampling based on translations and dilations of the wavelet $\psi(x)$ makes possible to obtain a discrete basis for the space in which $\psi(x)$ is defined, i.e., x . Therefore, it is possible to express any function $f(x)$ as a linear combination of the components of this basis. The properties of this linear expansion depend on the characteristics of the wavelet function $\psi(x)$ (properties as individual function), but also on how the continuous set of wavelet

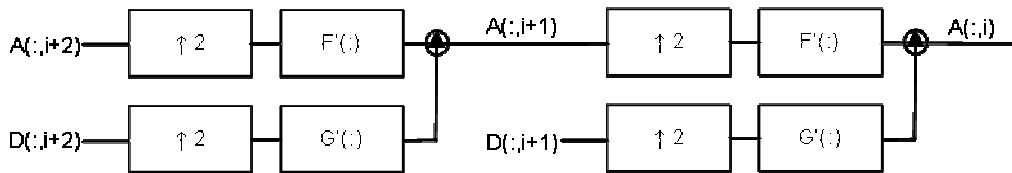
functions $\{\psi_{a,b}(x)\}_{a,b \in \mathbb{Z}}$, obtained from translations and dilations of the function $\psi(x)$, is sampled to derive the discrete set $\{\psi_{i,m}(x)\}_{i,m \in \mathbb{Z}}$.

- ***Fast Discrete Wavelet Transform***

Equation (3.17) establishes the decomposition of a given function $f(x)$ in a discrete set of elementary functions or wavelets $\{\psi_{i,m}(x)\}_{i,m \in \mathbb{Z}}$. Said in a different way, the set of elementary functions $\{\psi_{i,m}(x)\}_{i,m \in \mathbb{Z}}$ forms a basis of the space of functions $f(x)$, where the term $\langle f(x), \psi_{i,m}(x) \rangle$ represents the weight of the particular function $\psi_{j,m}(x)$ in the reconstruction of $f(x)$. The term $\langle f(x), \psi_{i,m}(x) \rangle$ represents the DWT and it can be also interpreted as the projection of the function $f(x)$ in the space created by the elementary function $\psi_{i,m}(x)$. The fact that the mean value of any wavelet function $\{\psi_{i,m}(x)\}_{i,m \in \mathbb{Z}}$ is equal to zero allows to interpret the projection $\langle f(x), \psi_{i,m}(x) \rangle$ as a high pass filtering of the original function $f(x)$ at a particular spatial location, detailed by the parameter m , and a particular frequency scale, given by the parameter j . Consequently, for a particular frequency scale j , the function $f(x)$ can be decomposed into two parts: one containing the high frequency content and the second one containing the low-frequency content. The high frequency information is obtained through the projection $\langle f(x), \psi_{i,m}(x) \rangle$, that is, the DWT, whereas the low-frequency content is obtained through a different projection $\langle f(x), \phi_{i,m}(x) \rangle$, where the support functions $\{\phi_{i,m}(x)\}_{i,m \in \mathbb{Z}}$, called *scaling functions*, are interpreted as a low pass filter of the original function $f(x)$.



(a)



(b)

Figure 16. Iterated two branch filter bank to calculate the DWT. (a) Fast DWT. (b) Fast IDWT. This scheme calculates the WT with two scales: $A(:,i)$ represent the coarse approximation coefficients whereas $D(:,i)$ are the detail or wavelet coefficients.

From a practical point of view, the DWT is obtained as a recursive filtering or multiband filtering of the original function $f(x)$ by a series of high and low frequency filters [71]. Figure 16 gives an example of the transformation and the inverse transformation process. The continuous function $f(x)$ is originally represented by the discrete samples $A(:,i)$, that is the samples at the original frequency scale i . These samples are first low-pass filtered by the filter $F(:)$, and sub-sampled by a factor of 2 to satisfy the Nyquist criteria, giving as a result the coefficients $A(:,i+1)$. In addition, the function is also filtered by the high-pass filter $G(:)$, and sub-sampled by a factor of 2 to satisfy the Nyquist criteria, giving as a result the coefficients $D(:,i+1)$. That is, the coefficients a_j are separated into the low frequency coefficients $A(:,i+1)$ and the high frequency coefficients $D(:,i+1)$. This process can be iterated on the low frequency coefficients. The reconstruction of the original coefficients a_j from the transformed coefficients through the filters $F'(:)$ and $G'(:)$. The filters $F(:)$ and $G(:)$ are called wavelet decomposition filters whereas $F'(:)$ and $G'(:)$ are known as wavelet reconstruction filters. This wavelet decomposition scheme is known as the Mallat decomposition algorithm [71].

- ***Two-dimensional Wavelet Transform***

SAR data are two-dimensional data. Accordingly, it is necessary to define a two-dimensional WT algorithm. Despite non-separable wavelets exist for two-dimensional signals, separable schemes are preferable as computationally efficient algorithms can be defined to calculate the two-dimensional WT. A two-dimensional signal $f(x_1, x_2)$ is said to be separable if $f(x_1, x_2) = f(x_1)f(x_2)$, where x_1 and x_2 represent the two signal dimensions, assumed to be independent. Consequently, the two-dimension DWT can be obtained as an extension of the one-dimensional algorithm applied independently to each one of the signal dimensions. The two-dimensional fast discrete WT is obtained by applying the Mallat algorithm independently to the image's rows and columns. Figure 17 details this decomposition scheme. The one-dimensional Mallat algorithm states that the transformed coefficients can be obtained by recursively iterating a basic cell, containing a low- and a high-pass filter followed by downsampling of a factor of 2, to the approximation coefficients. In the two-dimensional case, as the basic cell is iterated two times to derive the wavelet coefficients for each wavelet scale i , four sets of coefficients are derived. One corresponding to the coarse approximation coefficients or low-frequency coefficients, denoted by $A(:,:,i)$, and three sets of detail or wavelet coefficients denoted by $H(:,:,i)$, $V(:,:,i)$ and $D(:,:,i)$, also known as high-frequency coefficients. Since the input signals are two-dimensional signals, the coefficients $H(:,:,i)$, $V(:,:,i)$ and $D(:,:,i)$ contain directional information. The coefficients $H(:,:,i)$ contain the information about the horizontal details, $V(:,:,i)$ contain details about the vertical details and finally $D(:,:,i)$ contain the diagonal details.

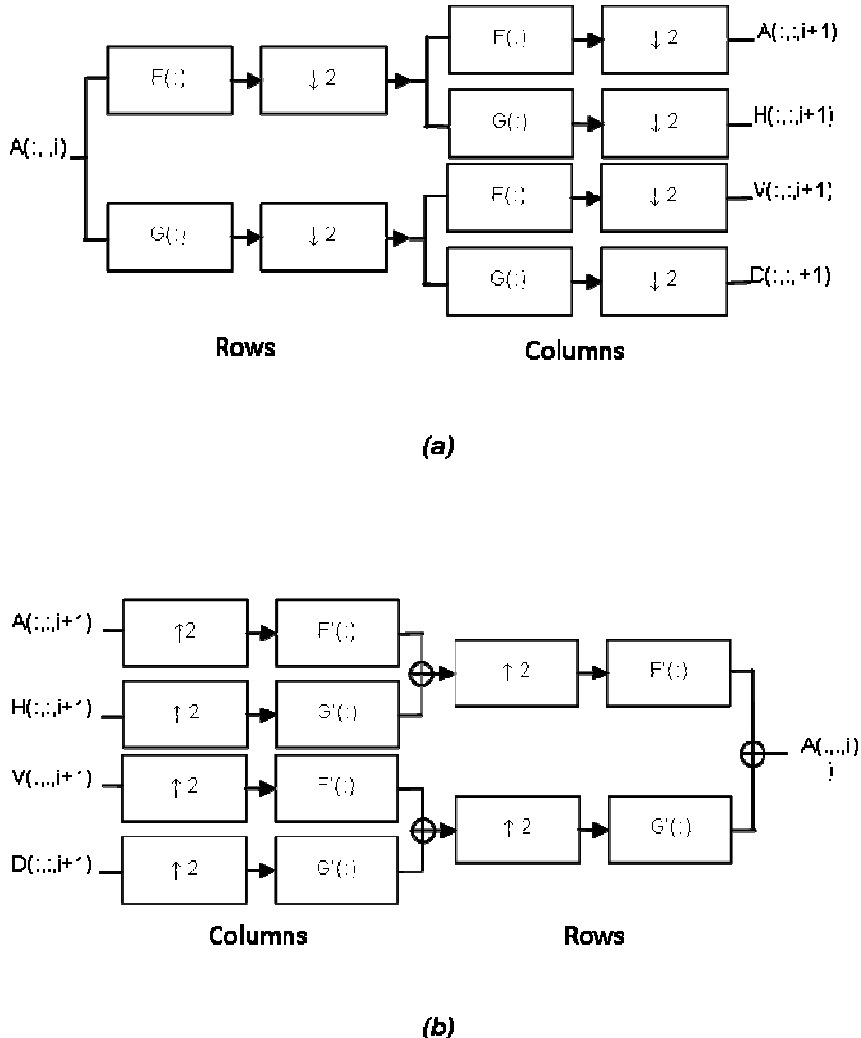


Figure 17. Separable two-dimensional filter bank which calculates the two-dimensional DWT for separable dimensions. (a) Fast two-dimensional DWT. (b) Fast two-dimensional IDWT. The coefficients $A(:, :, i)$ represent a low frequency coefficients of the original signal whereas $D(:, :, i)$, $V(:, :, i)$ and $H(:, :, i)$ are the wavelet of high frequency coefficients.

- **Stationary Wavelet Transform (SWT)**

In the scope of this dissertation, special attention is given to the Stationary Wavelet Transform, SWT in the following, which is an extension of the standard DWT. The basic idea of the SWT is to fill in the gaps caused by the dyadic decimation step in the DWT [72]. More specifically, at each level, the filters are modified, by padding them out with zeroes. Due to the absence of subsampling, the components in the transformed domain have the same dimensions than the data in the original domain, at the expense of an introduction of redundancy in the representation. Figure 18 shows a flowchart of the operation of the two dimensional SWT.

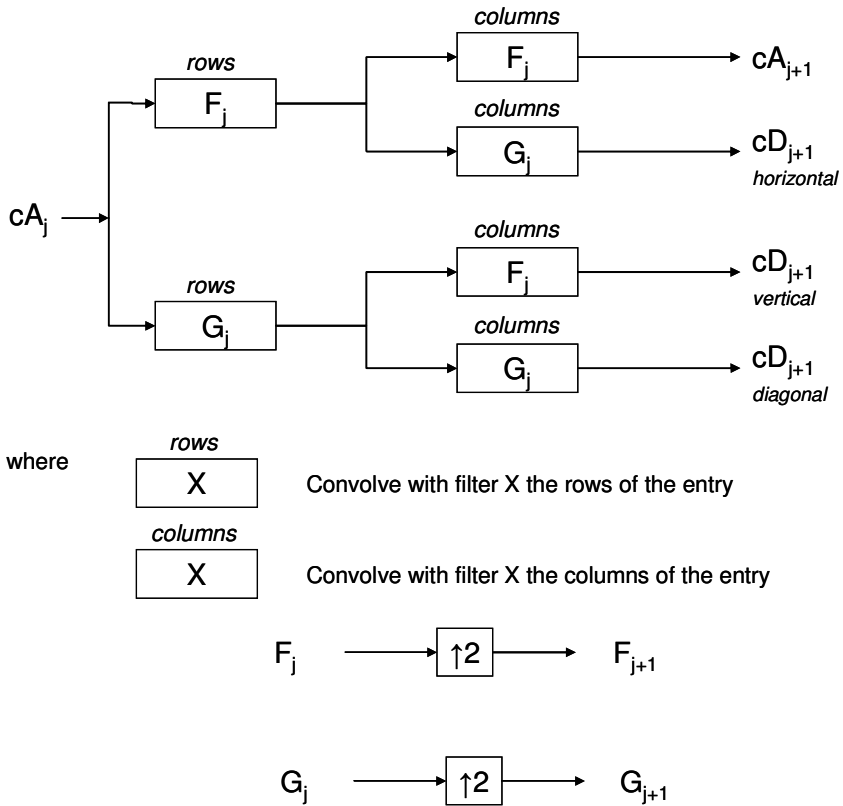


Figure 18. Flowchart of the two dimensional SWT.

3.1.2.2. Properties of the WT

Historically, the WT has been mostly used for compression purposes. For example, the popular jpeg algorithm [73] is a direct application of the WT. Nevertheless, in the scope of this dissertation, the WT is employed as an analysis tool for complex non stationary processes, rather than a method for reducing redundancy. Moreover, an original aspect of the algorithms exposed in following chapters underlies on working and providing results directly in the transformed wavelet domain, avoiding inversion. This section exposes succinctly the properties of the WT that make it particularly useful for the analysis purposes focused in this dissertation: the use of the WT as a multiscale differential operator and the WT as an estimator of local regularity. More specific details will be given in depth in the chapters exposing the techniques that make use of these properties.

One of the main concerns of this dissertation is to identify (Chapter 4 and Chapter 5) and measure (Chapter 6) the regularity of a SAR signal as much locally as possible. Wavelet theory is especially appropriate for this purpose due to their sensitivity to discontinuities, added to their multiscale capability. This sensitivity is closely related to the concept of vanishing

moment which is a crucial parameter to be taken into account for the correct use of the WT as an analysis tool. A wavelet ψ has p vanishing moments if

$$\int_{-\infty}^{\infty} t^k \psi(t) dt = 0 \quad \text{for } 0 \leq k < p. \quad (3.18)$$

This means that ψ is orthogonal to any polynomial of degree $p-1$. The following theorem relates the number of vanishing moments of ψ to the vanishing derivatives of $\hat{\psi}(\omega)$ at $\omega=0$ and to the number of zeros of $\hat{h}(\omega)$ at $\omega=\pi$.

- **Theorem 3.2. Vanishing Moments.**

Let ψ and ϕ be a wavelet and a scaling function that generate an orthogonal basis. Suppose that $|\psi(t)| = O((1+t^2)^{-p/2-1})$ and $|\phi(t)| = O((1+t^2)^{-p/2-1})$. The four following statements are equivalent:

- (i) The wavelet ψ has p vanishing moments.
- (ii) $\hat{\psi}(\omega)$ and its first $p-1$ derivatives are zero at $\omega=0$.
- (iii) $\hat{h}(\omega)$ and its first $p-1$ derivatives are zero at $\omega=\pi$.
- (iv) For any $0 \leq k < p$, $q_k(t) = \sum_{n=-\infty}^{\infty} n^k \phi(t-n)$ is a polynomial of degree k .

3.1.2.3. The Wavelet Transform as a multiscale differential operator

In the following, it will be shown that a wavelet with n vanishing moments can be written as the n^{th} order derivative of a function θ . Suppose that ψ has a fast decay, i.e. that for any decay exponent $m \in \mathbb{Z}$, there exists C_m such that

$$\forall t \in \mathbb{R}, |\psi(t)| \leq \frac{C_m}{1+|t|^m}. \quad (3.19)$$

- **Theorem 3.3.**

A wavelet ψ with a fast decay has n vanishing moments if and only if there exists θ with a fast decay such that

$$\psi(t) = (-1)^n \frac{d^n \theta(t)}{dt^n}. \quad (3.20)$$

As a consequence,

$$Wf(u, s) = s^n \frac{d^n}{du^n} (f * \bar{\theta}_s)(u) \quad (3.21)$$

with $\bar{\theta}_s = s^{-1/2} \theta(-t/s)$. Moreover, ψ has no more than n vanishing moments if and only if $\int_{-\infty}^{\infty} \theta(t) dt \neq 0$.

Hence, since the WT can be understood as a multiscale differential operator, it can be employed for detecting singularities. Singularities are non differentiable points in a function. They can be detected by finding the abscissa where the wavelet modulus maxima converge at fine scales. The wavelet modulus maxima are, at each scale, the local maxima of the absolute value of the wavelet coefficients. It will be seen that these local extremes are related across scales and that a local maxima in the finest scales produced by the presence of a discontinuity is transmitted over larger scales. Therefore, these multiscale modulus maxima are used to locate discontinuities and edges in images. For example, if the wavelet has only one vanishing moment, the modulus maxima correspond to local maxima in the function; if the wavelet has two vanishing moments, the modulus maxima correspond to high curvatures. As a consequence, the selection of the mother wavelet employed has to be done accordingly to the type of discontinuity focused. On the other hand, the following theorem proves that if $Wf(u, s)$ has no modulus maxima at fine scales, then f is locally regular.

- ***Theorem 3.4. Theorem of Hwang and Mallat***

Suppose that ψ is C^n with a compact support, and $\psi = (-1)^n \theta^{(n)}$ with $\int_{-\infty}^{\infty} \theta(t) dt \neq 0$. Let $f \in L^1[a, b]$. If there exists $s_0 > 0$ such that $|Wf(u, s)|$ has no local maximum for $u \in [a, b]$ and $s < s_0$, then f is uniformly Lipschitz (or Hölder) n on $[a + \varepsilon, b - \varepsilon]$ for any $\varepsilon > 0$.

3.1.2.4. The Wavelet Transform as an estimator of local regularity of a signal

When looking for singularities or when measuring the regularity of a signal, the main drawback is to deal with non stationary signals, rapidly varying. According to the Heisenberg principle, already introduced, a high resolution in frequency – equivalently a high sensitivity to the regularity of a signal - implies a low resolution in space – equivalently reduced capabilities of locating the positions of the changes of regularity. As seen before, the WT divides the time – frequency domain with atoms of varying dimensions, i.e. some atoms have higher sensitivity in time, whereas some others have higher sensitivity in space. By doing so, it has the capability of treating a given signal at different time and frequency resolutions. The WT can progressively focus on localized signal structures with a zooming procedure, by reducing the scale parameter. Moreover, it can manage the results of this multiresolution capability, in order to provide a local measure of the regularity of a signal. This measure is called the Lipschitz exponent. Lipschitz exponents provide uniform regularity measurements over time intervals, but also at any point v . If f has a singularity at v , which means that it is not differentiable at v , then the Lipschitz exponent at v characterizes this singular behavior.

- **Definition. LIPSCHITZ regularity**

A function f is pointwise Lipschitz $\alpha \geq 0$ at v , if there exists $K > 0$ and a polynomial p_v of degree $m = \lfloor \alpha \rfloor$ such that

$$\forall t \in \mathbb{R},$$

$$|f(t) - p_v(t)| \leq K |t - v|^\alpha \quad (3.22)$$

A function f is uniformly Lipschitz α over $[a,b]$ if it satisfies (3.22) for all $v \in [a,b]$, with a constant K that is independent of v .

The Lipschitz regularity of f at v or over $[a,b]$ is the sup of the α such that f is Lipschitz α .

The decay of the WT amplitude across scales is related to the uniform and pointwise Lipschitz regularity of the signal. If its Lipschitz exponent is 1, then the function is assumed regular [71]. Figure 19 displays a 3D representation of the power distribution of a signal in the time-frequency plane. Different decays across scales are noticeable.

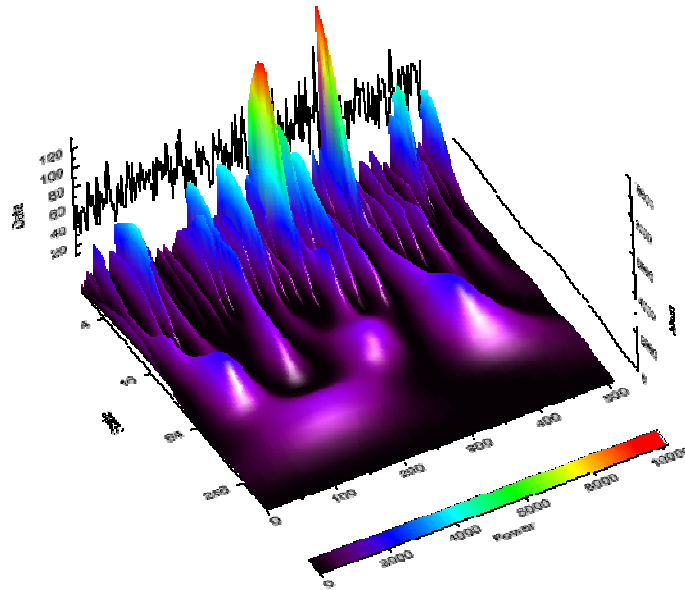


Figure 19. Three dimensional representation of the power distribution of a signal in the time-frequency plane.

Measuring the asymptotic decay is equivalent to zooming into signal structures with a scale that goes to zero. Suppose that the wavelet ψ has n vanishing moments and is C^n with derivatives that have a fast decay. This means that for any $0 \leq k < n$ and $m \in \mathbb{Z}$ there exists C_m such that $\forall t \in \mathbb{R}$,

$$|\psi^{(k)}(t)| \leq \frac{C_m}{1 + |t|^m}. \quad (3.23)$$

The following theorem relates the uniform Lipschitz regularity of f on an interval to the amplitude of its WT at fine scales.

- **Theorem 3.5.**

If $f \in L^2(\mathbb{R})$ is uniformly Lipschitz $\alpha \leq n$ over $[a, b]$, then there exists $A > 0$ such that $\forall (u, s) \in [a, b] \times \mathbb{R}^+$,

$$|Wf(u, s)| \leq As^{\alpha+1/2}. \quad (3.24)$$

Conversely, suppose that f is bounded and that $Wf(u,s)$ satisfies (3.24) for an $\alpha \leq n$ that is not an integer. Then f is uniformly Lipschitz α on $[a+\varepsilon, b-\varepsilon]$, for any $\varepsilon > 0$.

According to the pointwise Lipschitz regularity, the following theorem gives a necessary and a sufficient condition.

- **Theorem 3.6. Theorem of Jaffard**

If $f \in L^2(\mathbb{R})$ is Lipschitz $\alpha \leq n$ at v , then there exists A such that $\forall (u,s) \in \mathbb{R} \times \mathbb{R}^+$,

$$|Wf(u,s)| \leq As^{\alpha+1/2} \left(1 + \left| \frac{u-v}{s} \right|^{\alpha} \right). \quad (3.25)$$

Conversely, if $\alpha < n$ is not an integer and there exist A and $\alpha' < \alpha$ such that $\forall (u,s) \in \mathbb{R} \times \mathbb{R}^+$,

$$|Wf(u,s)| \leq As^{\alpha+1/2} \left(1 + \left| \frac{u-v}{s} \right|^{\alpha'} \right) \quad (3.26)$$

then f is Lipschitz α at v .

3.1.2.5. Cone of influence

When evaluating the pointwise regularity by means of a space – scale decomposition of a signal with a mother wavelet ψ , it is necessary to be aware of the amplitude of the cone of influence for this specific mother wavelet to carry out a correct interpretation. If the wavelet ψ has a compact support equal to $[-C, C]$, the cone of influence of a spatial point v in the space - scale plane is the set of points (u,s) such that v is included in the support of $\psi_{u,s}(t)$, which is equal to $[u - Cs, u + Cs]$ (see Figure 20).

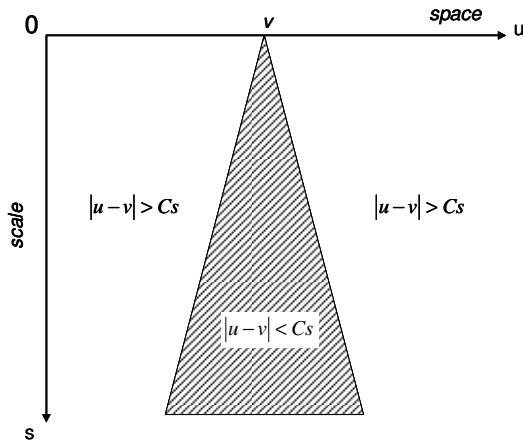


Figure 20. General cone of influence in the space – scale plane.

The cone of influence for a given mother wavelet can be empirically determined by computing the space – scale decomposition with this wavelet for a Dirac function as input signal. As an example, the wavelet decomposition of a Dirac function, evaluated with a Mexican Hat mother wavelet is represented in Figure 21.

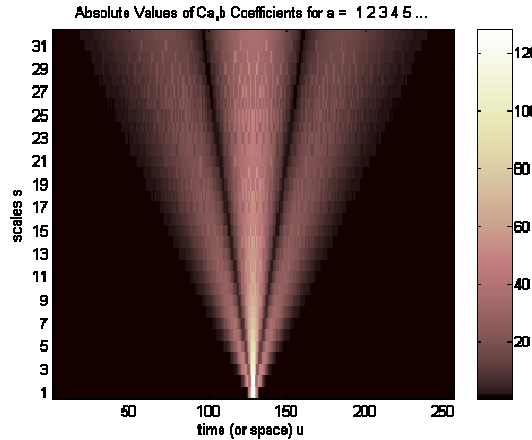


Figure 21. Cone of influence for a Mexican Hat mother wavelet.

Intuitively, the cone of influence formalizes the fact that the presence of a discontinuity in a point has an effect spread out over neighboring spatial positions. Since the amplitude of the area of influence increases with the scale, at low frequencies the space – scale decomposition represents a combination of pointwise regularity measures over a large area, i.e. its uniform regularity. When several singularities are present, only the non-overlapping parts of the cones satisfy (3.26).

3.1.2.6. Intrascale and interscale correlations

In the literature, the WT is often assumed to be a whitening process. This assumption is particularly useful for compression purposes [74]. The wavelet coefficients are then modeled as independent jointly Gaussian [66] [68] [75] [76] or non-Gaussian [64] [65] [74] [77]. However, it has been shown that correlated processes induce correlations between wavelet coefficients, both within subbands at the same scale and across scales. This correlation is mainly due to structural features such as lines, edges, corners. Clustering and persistence have to be taken into account as secondary properties. On the one hand, clustering states that adjacent coefficients are likely to have similar intensity values [78]. On the other hand, due to persistence, the intensity of a coefficient tends to propagate across scales [79] [80].

More specifically, wavelet-domain hidden Markov models have proven to effectively capture the statistical dependencies found between wavelet coefficients [81] [69] [82] [83]. Moreover, they suggest that the following step would be to design methods for taking advantage of these correlations. This is the main originality of the techniques developed in the scope of this dissertation, presented in the following chapters.

3.1.2.7. Practical considerations when using wavelet tools

When using wavelet techniques, it is essential to select the appropriate parameters of the transform, according to the application focused, since results may critically depend on this selection. More specifically, both the type of WT as well as the nature of the wavelet family involved, have to be considered carefully.

3.1.2.8. Selection of the type of WT

It has already been seen in previous sections that the WT provides essentially a decomposition of a given signal into different frequency components in a localized manner, contrarily to the FT. An overview of the different types of transform has also been provided. The WT has to be chosen properly attending to the purposes of the analysis and to the characteristics of the input signal. For example, the selection of a one or two dimensional transform is straightforwardly conditioned by the one or two dimensional nature of the function to be analyzed. The selection of a discrete or continuous transform is not so direct, even if certainly a discrete transform suits better to a discrete input, thus avoiding interpolation related drawbacks. Nevertheless, a continuous transform is more appropriate than the discrete one for analysis purposes at the expense of a higher redundancy load. Another aspect is the orthogonality or non orthogonality of the transform. This property is particularly relevant for applications searching a reduction of the redundancy of the input signal such as for compression purposes. However, since redundancy is not a critical issue in the applications

focused in the scope of this dissertation, this factor will not be conclusive. Another selectable feature of the WT is the subsampling after the application of the filters: a decimated or an undecimated scheme can be used. Several algorithms presented in this dissertation rely on combinations of wavelet coefficients within the same scale or at different scales. Moreover, results are provided directly in the transformed domain. Hence, by avoiding the subsampling with a SWT, intermediate products are produced having all of them the same dimensions that the input signal. As a consequence, this scheme is preferred for it favors direct combinations of wavelet subbands.

3.1.2.9. Selection of the wavelet family

In order to select the appropriate mother wavelet, the size of its support both in time and in frequency, as well as its number of vanishing moments, have to be taken into account. For instance, there is a trade-off between these two parameters. In essence, it must be affirmed that the number of vanishing moments is related with the length or support of the filter itself, in such a way that the larger the support, the larger the number of vanishing moment. Specifically, the vanishing moments refer to the number of zeros of the frequency filter response at the discrete frequency π . In the applications focused in the scope of this dissertation, it is important to preserve as precisely as possible the location of the edge. Hence, a short spatial support is preferred. Furthermore, it has been previously seen that SAR images tend to be irregular, presenting a lot of discontinuities due to speckle. As a consequence, a high number of vanishing moments is not necessary for their analysis. Moreover, the algorithms proposed in the following chapters take profit of the spatial coincidence of local maxima at different scales due to the presence of discontinuities. In order to effectively have this spatial co-occurrence, the mother wavelet used must exhibit a linear phase and an even number of coefficients.

3.2 A multiscale framework for the interpretation of multiscale information

The most exceptional events in a signal, whatever its nature, are also the ones that contain most of the information. In an image, these high entropy content elements are spots and edges. Managing them permits an efficient structure extraction which offers then potential for high level image interpretation. The complex mammal vision system operates similarly. When confronted to a scene, it handles the exposed data, first focusing on conspicuous boundaries which capture its attention and deducing then structure of the overall ensemble through them. Furthermore, the eye can focus on elements at different scales, handling the information content of a scenario at different levels. The main objective of this dissertation is to establish a multiscale framework based on the WT for the automatic interpretation of SAR

data. With the background inspiration of the operation of the vision system, the multiscale differential capability of the WT will be employed to enhance conspicuous edges in a SAR image. Then, multilevel techniques will be studied to reveal and then analyze texture and useful information, by avoiding speckle. This section justifies the suitability of wavelet tools for the interpretation of SAR data.

3.2.1 Multiplicative model for speckle

First, it will be shown that a multiscale framework presents advantages when dealing with edge detection in signals presenting multiplicative noise, such as SAR data, as seen in previous Chapter.

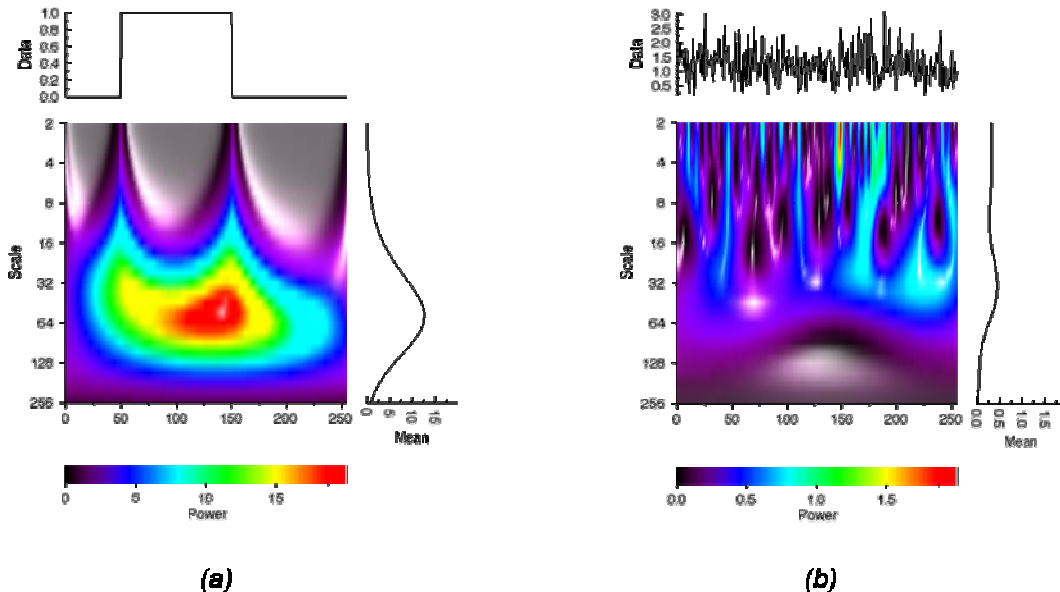


Figure 22. Time frequency (or space – scale) representations of two simulated 1D signals corresponding to a noiseless step signal (a) and to a speckle-like pattern (b).

Figure 22 represents two 1D signals and their corresponding multiscale time – frequency (similarly, space - scale) representation (by means of a Gaussian wavelet). The horizontal axis corresponds to time or space, whereas the vertical one represents frequency or scale: low scales (high frequencies) are at the top of the representation. Such a representation is useful to provide an idea of the distribution of energy of the signal analyzed according to scales. The left column shows a step and from its multiscale representation, it can be deduced that the energy is concentrated at higher scales – equivalently, low frequencies - (more precisely, at those corresponding to the length of the step). The right column exhibits a 1D simulation of

speckle. It can be noticed that the energy is less concentrated at a particular frequency, even if low scales (i.e. high frequencies) are privileged.

As already stated in previous chapter, the main difference between optical and radar data is the presence of additive Gaussian noise in front of multiplicative speckle respectively. Figure 23 highlights the difference of energy distribution in the space – scale plane. On the one hand, the left column results from the pointwise product of the step signal in the left column of Figure 22 with the speckle signal in the right column of Figure 22. This signal simulates a typical SAR signal.

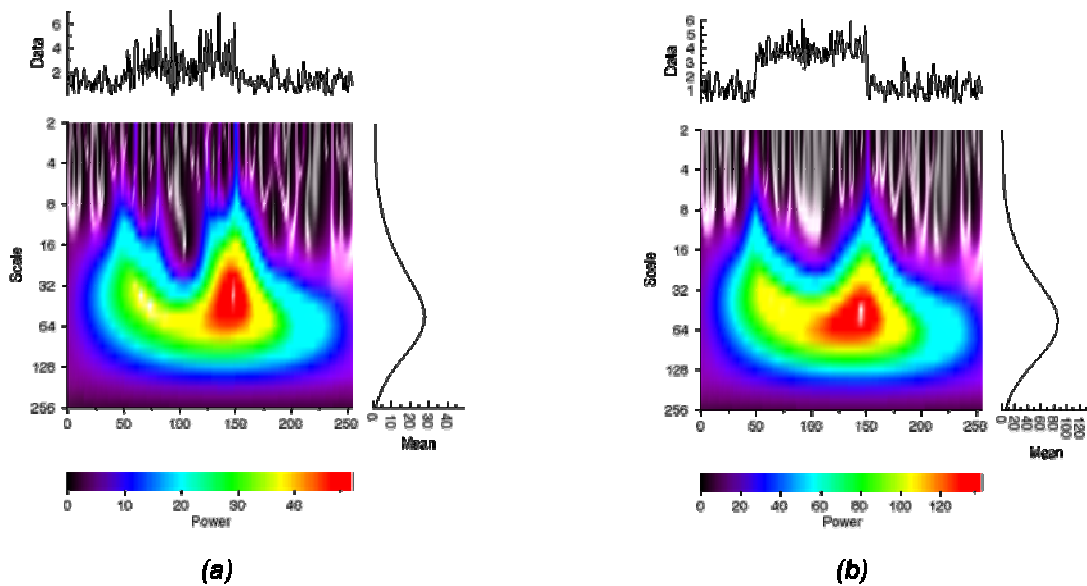


Figure 23. Time frequency (or space – scale) representations of two simulated 1D signals corresponding to the product of a step and a speckle signals (a) and to the sum of a step and a Gaussian noise-like signals (b).

Due to the multiplicative nature of speckle, even if concentrated at lower scales, its effect is transmitted to lower frequencies. As a consequence, up to the eighth scale (if using a dyadic transform, this corresponds to the third iteration), local maxima due to the presence of edges are not noticeable. On the other hand, the right column corresponds to the space – scale energy distribution of the pointwise sum of the step signal with a Gaussian noise like pattern, simulating a realistic optical situation. It can be observed, that contrarily to the SAR signal, noise remains concentrated at higher frequencies and local maxima due to the presence of the borders of the step are appreciable even at the very first scales.

3.2.2 Product model for SAR data

The nature of SAR data presents itself a multiscale behavior. In fact, speckle is produced by the combination of scatterers within a resolution cell and thus it can be considered as a pixel to pixel spatial variability characteristic. Besides, variations corresponding to intrinsic texture in a non homogeneous area tend to be appreciable at larger scales. As a consequence, the observation of a small area of pixels of a SAR image exhibits a noise-like pattern, meaningless in appearance, as it can be seen on the left column of Figure 24. Nevertheless, even if due to its multiplicative nature, speckle affects to all scales, when confronted to a larger scene, an observer is able to manage it and distinguish the most relevant features, focusing its multiscale observation capability to higher scales (i.e. lower frequencies or larger areas). In the right column of Figure 24, a coastal scene with different characteristic elements (the sea, the land, the harbor, an urban area...) can thus be easily discriminated.

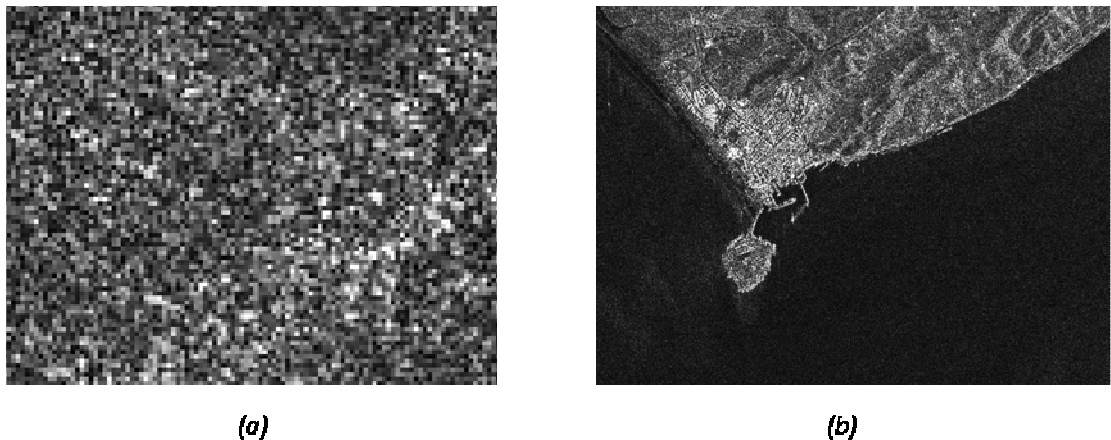


Figure 24. RADARSAT SAR image (F4 mode) of the area of Gibraltar (right column) and zoom of a homogeneous portion of the entire image.

The product model [84] formalizes this multiresolution notion stating for the intensity $I(j)$ of pixel (x, y) :

$$I(x, y) = \mu_I T(x, y) F(x, y) \quad (3.27)$$

where μ_I is the mean intensity, $T(x, y)$ is the texture random variable and represents the natural within-field spatial variability and $F(x, y)$ corresponds to speckle which is also a random process. T and F are considered statistically independent. This decomposition enables the identification of different ranges of scales. As a consequence, in order to analyze properly SAR data, the consideration of a multiscale approach is the most suitable.

3.3 Summary

This chapter has presented the multiresolution time-frequency notion and has justified its application to the automatic exploitation of SAR data. Among the different mathematical tools available to perform multiscale decompositions, the preference on the WT has been confirmed. Its properties have been exposed in detail and the interest of its application to the exploitation of SAR data has been highlighted.

Hence, once the multiscale framework established for the exploitation of SAR data, the most efficient strategy to manage the information of a scene is to identify first the elements with a higher entropy content such as spots (Chapter 4) and edges (Chapter 5). This will allow to extract the overall structure of a scene. Then, attention will be driven on the analysis of textural patterns (Chapter 6).

Chapter 4. Automatic spot detection in SAR imagery

In order to develop a novel framework based on multiscale time-frequency methods for the analysis and automatic exploitation of SAR data, the first canonical problem to treat is spot detection. A spot may be defined as a small, compact, isolated area that is different in color, material or texture from its surroundings. In order to handle this intuitive and common sense definition automatically within a computerized scheme, the notions of size, localness, compactness and difference have to be translated into quantitative parameters, understandable by a machine system with no high level interpretation means.

A large number of applications are based on spot detection. In the scope of this dissertation, spot detection will be treated mainly in the context of ship detection in spaceborne SAR images. But spot detection is also present in a large number of very diverse domains, such as in medical applications (e.g. the detection of micro calcifications in mammograms [85]), in astronomy (stars tracking [86]), in technology (segmentation of microarrays images [87]) and of course in different remote sensing applications others than ship detection (detection of permanent scatterers [88], cars tracking, etc.). Figure 25 displays several examples of applications related to spot detection.

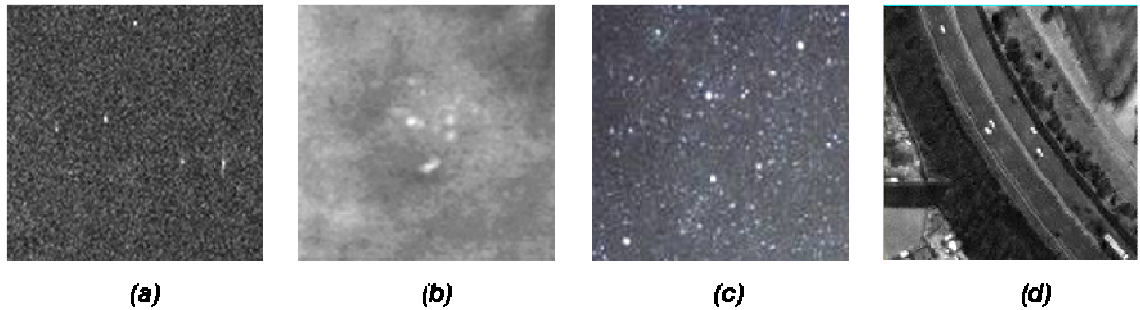


Figure 25. Different scenarios involving spot detection. (a) Ships on a SAR image, (b) Micro calcifications in a mammogram, (c) Stars tracking, (d) Cars in an optical image from IKONOS.

Any general scheme for automatic spot detection essentially comprises three steps: tiling of the input image in smaller subimages. Then, for each subimage, application of a spot enhancement algorithm and finally labeling or decision to determine the presence or absence of a targeted spot. Figure 26 presents the flowchart of the overall automatic spot detection chain.

In the literature dealing with segmentation in SAR imagery, the most extended type of object detection algorithm proposes the evaluation and further application of a threshold over a sliding window of fixed dimensions [89]. This type of method assumes a given statistical distribution of the input image and, therefore, it provides good performance in homogeneous scenarios, but fails otherwise. This dissertation is focused on the analysis of enhancement techniques to be applied before labeling in order to improve the overall segmentation results. In fact, unlike in optical imagery, in SAR data, which is highly heterogeneous, a robust enhancement phase is critical to provide acceptable detection rates.

After a detailed review of main drawbacks regarding automatic spot detection in speckled SAR images in Section 4.1 and in Section 4.2, a multiscale algorithm for spot enhancement is proposed in Section 4.3. Its performance is tested on simulated images and compared to the one of a conventional speckle filter. Then, it is shown in Section 4.4 that ship detection in SAR images can be considered as a particular case of spot detection. Hence, the technique presented is directly applied to SAR images for ship monitoring purposes and its operability is assessed through comparison with available groundtruth, with results provided by other operational methods and with visual inspection. Section 4.5 extends the algorithm to multiscale data and results on multichannel data are evaluated. Conclusions of the chapter are presented in Section 4.6.

Along this chapter, some figures are given with no scale. This is done when scales are meaningless, since qualitative results are intended instead of quantitative ones. Moreover, the stress usually relies on the difference of values between samples, more than in their absolute values.

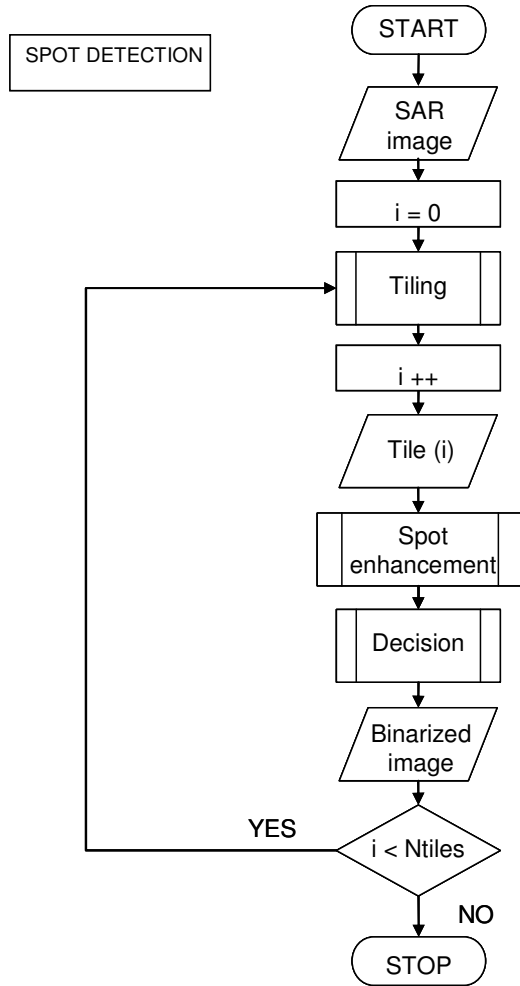


Figure 26. Flowchart of the overall automatic spot detection chain.

4.1 Main drawbacks of spot enhancement

Aiming to achieve a consistent scheme for unsupervised spot detection in SAR images, several difficulties have to be considered. These drawbacks are associated both:

- (i) to the characteristics of SAR images
- (ii) to the translation of the intuitive concept of spotness into a machine interpretable framework

(i) Drawbacks associated to the nature of data

On the one hand, it has been seen in Chapter 2 that SAR images present speckle, which is a noise like phenomena, affecting in a multiplicative way, the useful information content of data. Besides, a granular pattern appear in the images, due to an artifact of the imaging system that produces correlation between pixels. This coarseness of the spatial structure is fundamental in quantifying the ability to detect small targets against a distributed background. Actually, it must be observed here that the grains produced by the spatial correlation of speckle satisfy the conditions stated by the definition to be spots, even if they do not constitute useful elements of information. As a consequence, in the scope of spot detection, complementary criteria have to be added in order to perform an effective detection, distinguishing between targeted spots and intrinsic speckle grains. Hence, it will be established in the framework of SAR images that targeted spots tend to be slightly bigger and / or present a higher intensity than those produced by the intrinsic coarseness of the images due to speckle. Moreover, the density of grains is higher and more homogeneous than that of spots. Nevertheless, in some cases, the frontier can be fused. As an example, Figure 27 is a fragment of an oceanic scene, as perceived by a SAR sensor. In the centre of the image, a spot can be noticed. It corresponds to the presence of a small fishing ship in the sea surface. However, it can be observed that its aspect is very similar to surrounding speckle grains. In that case, a reliable discrimination through automatic means is awkward, in the absence of additional auxiliary information.

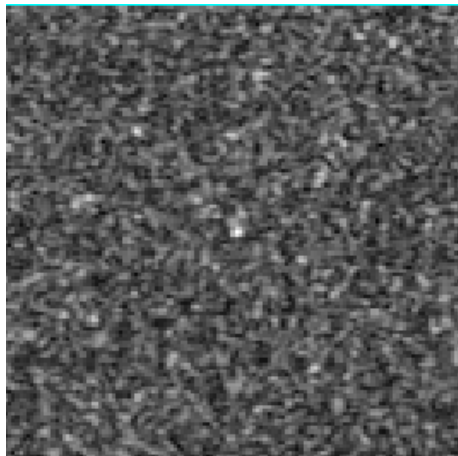


Figure 27. Fragment of SAR image of the ocean with a spot in the centre due to the presence of a small ship.

(ii) Drawbacks associated to the quantization of the definition of spot

On the other hand, according to the difficulties related to the statement of a valid translation of the notion of spot into quantitative terms, it is helpful to consider that a spot can be seen as a group of a reduced number of neighboring pixels, isotropically distributed, with similar intensity values. Furthermore, a spot is a high entropy element in the sense that its presence is exceptional in the overall scene. As a consequence, the distribution of targeted spots is sparse contrarily to the homogeneous dense distribution of grains due to speckle. As a consequence,

in machine understandable terms, a spot is a maximum of the local spatial correlation. Since the evaluation of the local correlation involves a given number of elements, it is inherently related to a scale concept. Moreover, it has been seen in previous chapter that a multiscale time-frequency decomposition of a signal reflects its local regularity.

As a consequence, a multiscale time-frequency framework presents features well suited for the automatic extraction of spots in a complicated scenario. Next section explores in detail how the presence of spots appears in a multiscale time / frequency decomposition.

4.2 Spots in the multiscale time / frequency plane

It is interesting to analyze how the notion of spotness is reflected in a multiscale time – frequency representation of the considered signal. Figure 28 is the representation of a simulated SAR image. It consists on a speckle matrix of 256 x 256 pixel. The speckle amplitude matrix has been generated as the modulus of a matrix whose both real and imaginary parts are random elements, normally distributed with zero mean and unitary variance. A spot of dimensions 4 x 4 pixel with a constant intensity value equal to twice the mean of the image has been included in the centre of the image.

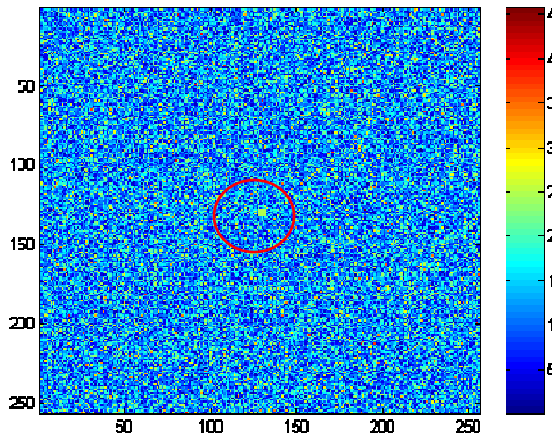


Figure 28. Simulated SAR image with a spot in the center (red circle).

Figure 29 is a horizontal cut intercepting the spot of the simulated SAR image in Figure 28. The rapid variations due to speckle producing localized intensity peaks can be observed. Moreover, it is worth noting that the intensity value of the targeted spot is below the maximum intensity value of the matrix.

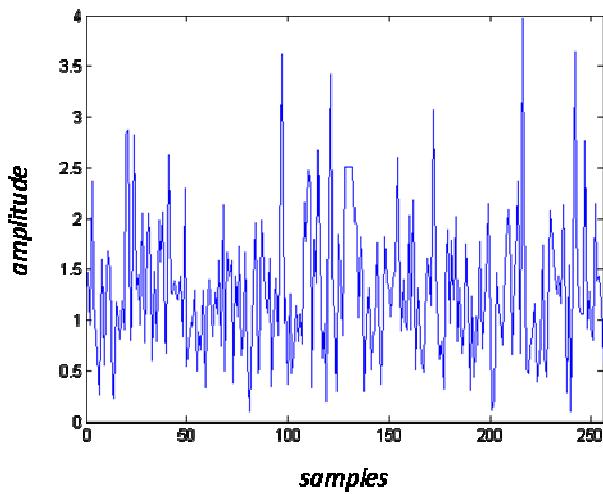


Figure 29. Horizontal cut of image in Figure 28.

The power of the multiscale time (similarly space) / frequency (similarly scale) representation of this 1D signal is obtained with a continuous Morlet wavelet and result is shown in Figure 30. The representation has been restricted to the central part of the signal in order to avoid border effects. Blue corresponds to low intensity values, while red corresponds to higher ones. The horizontal axis represents time (or space) and the vertical one is the frequency (or scale). The finer scales (higher frequencies) are the ones at the top of the representation.

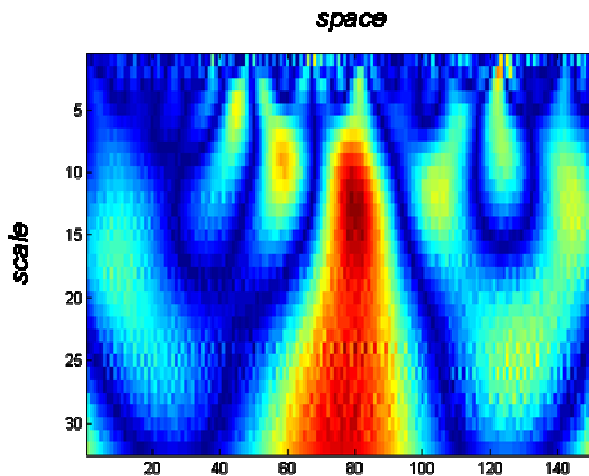


Figure 30. Time (horizontal axis) / frequency (vertical axis) representation of signal in Figure 28.

If considering the first scale at the top of the time – frequency representation, a high number of local maxima can be observed. Nevertheless, none of them stands out from the rest. Moreover, the consideration of the smallest scale is in that case totally inefficient for spot

detection since it can be seen that the first scale is, for the parameters of this example, blind to the presence of a spot, which does not produce any local maxima. When progressing across scales going down in the representation, the number of local maxima at each scale diminishes. In particular, it can be noted that the maxima at highest frequencies, due to the presence of speckle, rapidly vanish. On the contrary, several local maxima appear progressively at different places. Specially, a local maximum appears at about scale 10 and is transmitted over scales, producing a global maximum in the space / scale plane. It corresponds to the presence of the spot in the centre of the 1D signal analyzed. As a consequence, a simultaneous consideration of several scales can reveal the presence of certain targets, otherwise undetectable.

4.3 Algorithm designed for spot enhancement

Attending to the difficulties identified in previous sections, it is proposed to inscribe unsupervised spot detection in a multiscale time / frequency framework. This section is devoted to present a novel technique for spot enhancement on SAR imagery. It will be called Unsupervised Spot Enhancement Algorithm, USEA in the following.

4.3.1 Theoretical principles

This section aims at presenting the fundamentals of the algorithm proposed for spot enhancement in SAR imagery.

4.3.1.1. Preliminary considerations

The great variety of multiscale time / frequency methods has already been mentioned. Among the span of possibilities, the techniques designed in this dissertation – specifically, spot detection – are based on the wavelet theory. The importance of selecting properly, according to the application focused, the type of WT as well as the type of mother wavelet has been already highlighted in Chapter 3. In the scope of this chapter, we will use:

- SWT for the type of WT. The use of the SWT, which is redundant, provides intermediate products with the same dimensions than the input image. This property is particularly adequate for the application concerned, since the result is intended to be provided directly in the transformed domain. Therefore, no inversion is required for the algorithms we are dealing with.
- Haar wavelet for the type of mother wavelet (Figure 31). The selection of the mother wavelet has to rely on the consideration of the number of vanishing moments, as well as on the size of its support. According to these criteria for the selection of the wavelet as well as to the type of application focused, the Haar basis is considered in the following. First, the Haar wavelet has the shortest support among all orthogonal wavelets, which is

related to high resolution capabilities in time / space at the expense of coarse localization properties in frequency. It has only two non-zero coefficients at $n=0$ and $n=1$. Second, it has only one vanishing moment, i.e., it can be considered as a multiscale differential operator of order 1. In that sense, it can be treated as the Canny edge detector, not well localized in frequency and therefore not well suited to approximate smooth functions, but appropriate to spot detection.

-

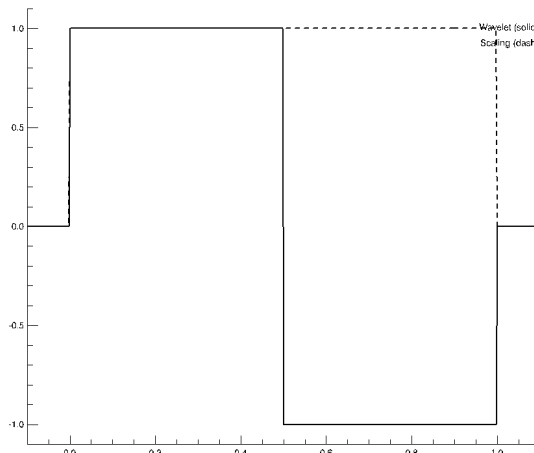


Figure 31. Representation of the Haar wavelet (solid line) and its corresponding scaling function (dashed line).

4.3.1.2. Detailed example of operation

USEA in SAR imagery will be presented and justified through a detailed example of operation in a simulated SAR image. The input simulated signal consists on a 256×256 pixel speckle matrix in which three targets have been embedded, distributed along the diagonal of the image, crossing it from the upper left corner to the bottom right one (see Figure 32 and Figure 33). The speckle amplitude matrix has been generated as in previous examples as the modulus of a matrix whose both real and imaginary parts are random elements, normally distributed with zero mean and unitary variance. All three targets share the same intensity, but exhibit different dimensions: the target in the upper left corner is 2×2 pixel wide, the central target is 4×4 pixel wide and the target in the lower right corner is 8×8 pixel wide. Figure 33 shows cuts of the simulated image intercepting the targets.

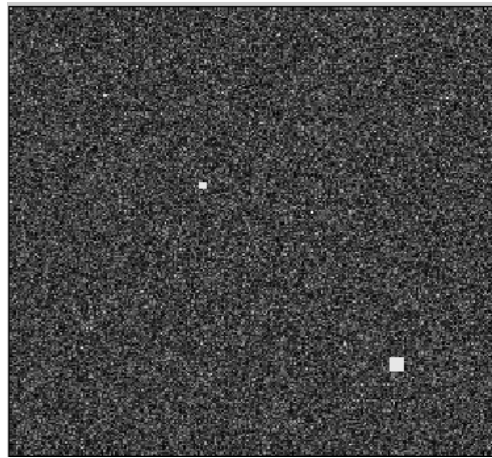


Figure 32. Simulated image with three targets of different dimensions.

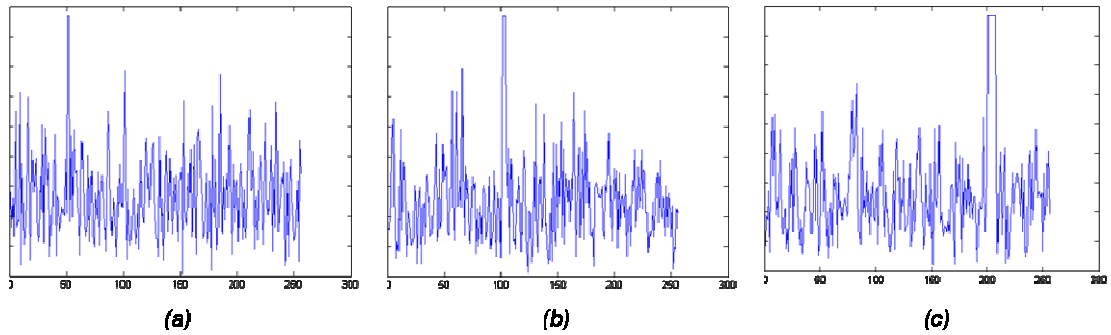


Figure 33. Horizontal cuts of the simulated image intercepting the targets. Target in the upper left corner (a), central target (b), target in the lower right corner (c).

At each iteration of the SWT, four components are produced, each one with the same dimensions than the input. One consists on a lowpass filtered version of the input image and the other ones reflect the bandpass content of the signal, at three different directions: horizontal, vertical and diagonal. Figure 34 shows the three bandpass components obtained for the first four consecutive scales.

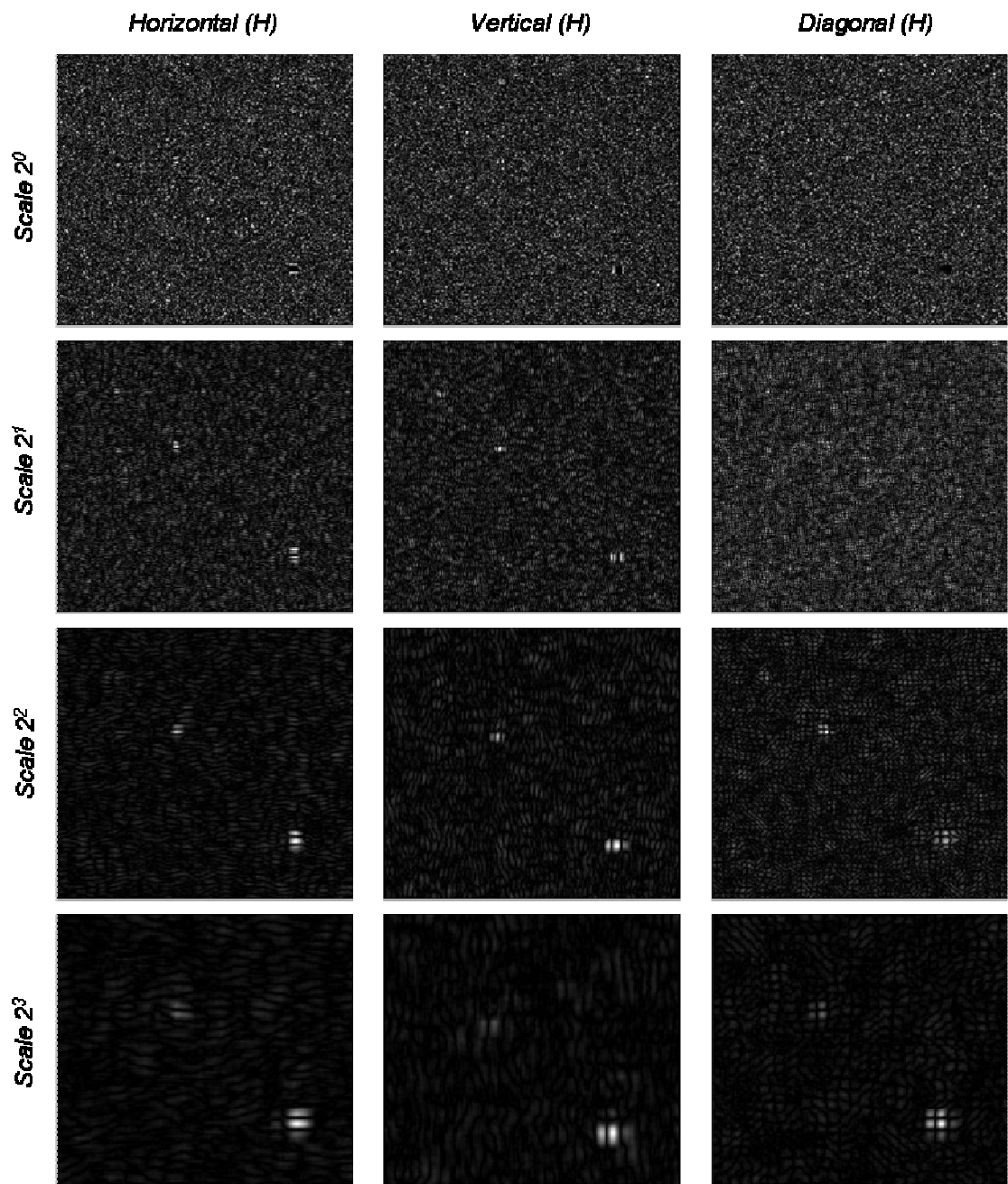


Figure 34. Absolute value of bandpass components obtained after the application of 4 scales of the SWT on the simulated image in Figure 32.

The consideration of the components obtained after a single iteration of the SWT is not meaningful by its own for spot enhancement purposes in speckled SAR images (see first row of the table in Figure 34). After two iterations, even if the presence of speckle is still appreciable, the SWT highlights the spots, especially in the horizontal and the vertical components. If going through scales, it can be observed that the effects of speckle are progressively reduced at the

expense of a loss of resolution: the boundaries of targets appear blurred. Moreover, it should be noticed that due to the isotropic distribution of pixels within a spot, local maxima produced by the presence of a target spatially coincide between subbands corresponding to different orientations. It is worth noting that the spatial co-occurrence of local maxima does not happen for background speckle. USEA is based on this difference of behavior of the targeted spots in front of speckle. In order to take advantage of this feature to enhance the presence of spots, a pointwise product is applied. This operation results in a worthy enlargement of contrast between the spot and its surrounding area.

Figure 35 shows the result of the pointwise product applied to the absolute value of the bandpass components for the first three consecutive scales. Both the effect of the pointwise product as well as the multiscale capabilities of the algorithm can be appreciated.

On the one hand, the outcome of the product can be analyzed by considering separately each scale. If focusing for example on the first one, one can notice that even if the presence of the smallest target (the one in the upper left corner) is not perceivable in any of the wavelet subbands obtained after a first iteration of the SWT, it comes to light with the product. In the resulting image, the spot contains the brightest pixels in the image and the horizontal cut intercepting it, shown in Figure 36, illustrates the contrast achieved with respect to the background. In such circumstances, since the margin of possible threshold values leading to a successful result is large, the automatic evaluation of a threshold is easy (trivial in most of the cases) and this final decision step will lead with high probability to a correct detection with no false alarms. Similar observations are valid for the other scales and the rest of the targets.

On the other hand, the multiscale capabilities of the algorithm can be analyzed by considering the evolution of the aspect of each target for the result of the pointwise product through the different scales. For instance, the first scale enhances the two smaller spots (the one in the upper left corner and the one in the centre), the second scale privileges the two larger ones (the one in the centre and the one in the down right corner) and, in the third scale, just the biggest spot is appreciable.

Figure 37 shows the flowchart of USEA in SAR imagery, summing up the different steps detailed before.

Regarding computational cost, the most expensive operation is the SWT. For a one dimensional vector of length 2^N , computing all the elements of the decomposition takes $O(N2^N)$ operations (in front of the $O(2^N \log(2^N))$ of the FFT, for example). In 2D, this one dimensional process has to be repeated thrice for each row of the input matrix. Hence, computing the SWT takes $O(3N2^{2N})$ operations in two dimensions. Additionally, the pointwise product computed at each scale requires $2^N \times 2^N$ basic operations.

Once the basics of USEA introduced, its main properties are reviewed.

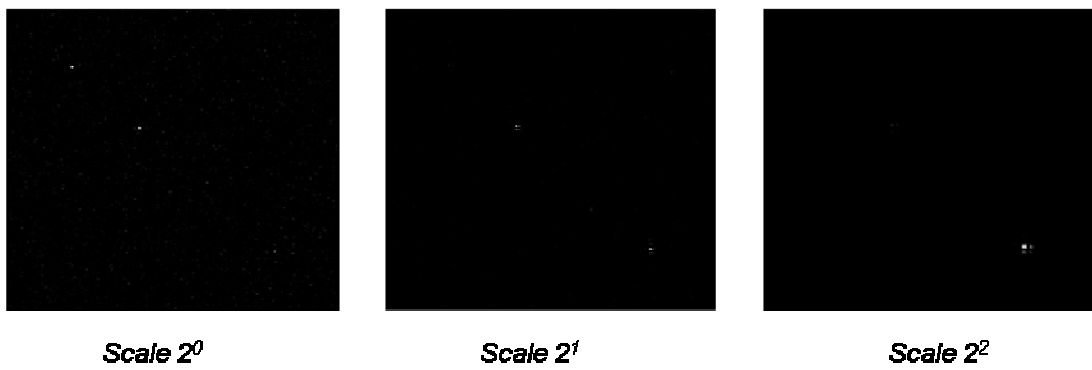


Figure 35. Results of pointwise product of the absolute value of bandpass components at 3 different scales.

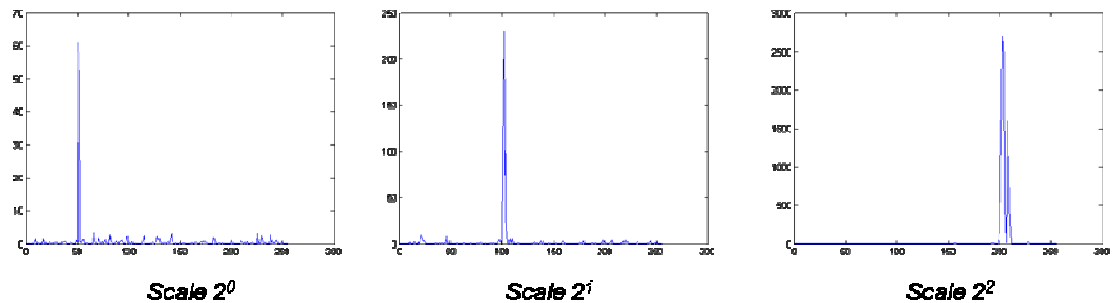


Figure 36. Horizontal cuts of the 3 targets embedded in the simulated image, as appreciable after the application of the spot enhancement technique presented. Target in the upper left corner (left), central target (centre), target in the lower right corner (right).

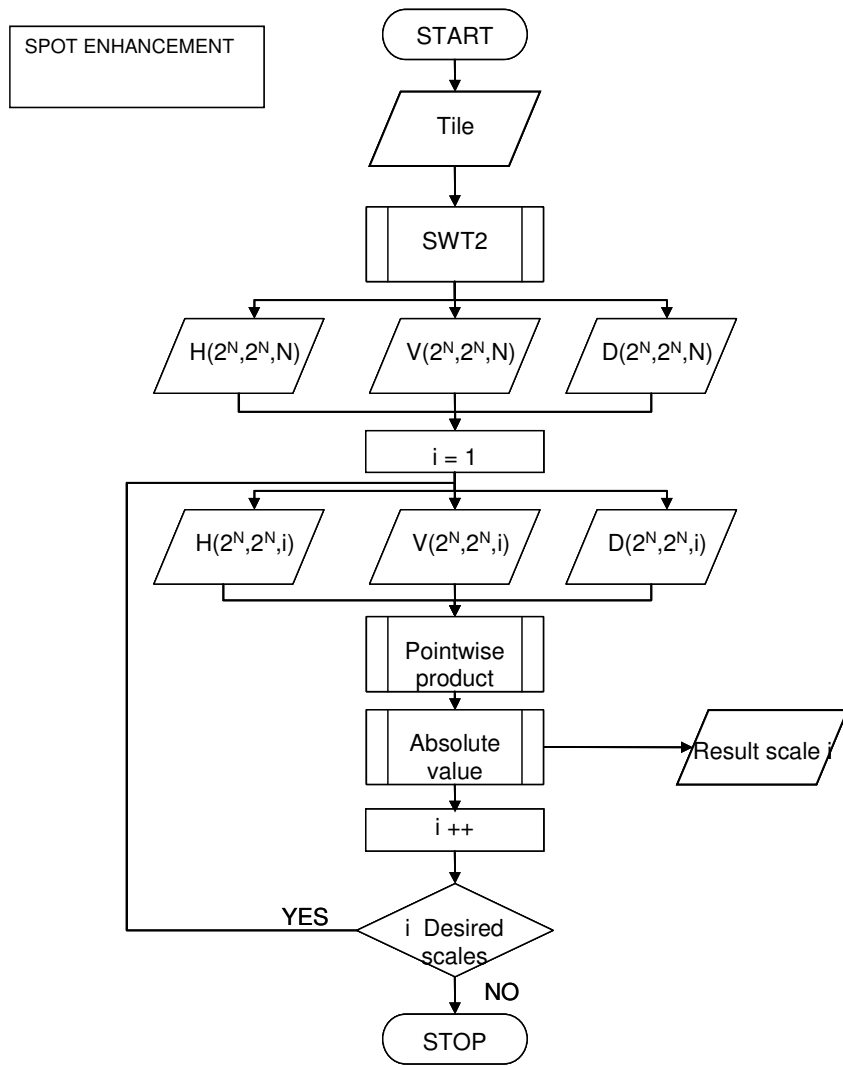


Figure 37. Flowchart of USEA.

4.3.2 Properties of USEA

4.3.2.1. Preservation of the spatial resolution

Contrarily to other approaches, the method proposed does not include any preprocessing step. In particular, in order to avoid the effects of speckle, a smoothing filter is often applied before prescreening. For spot detection purposes, smoothing is a cumbersome operation. For instance, filtering is linked to a sliding window of fixed dimensions. Hence, a small window will result in a poor performance of the filtering process, while a large one will usually dramatically soften the presence of a punctual spot. As a consequence, an efficient alternative to handle

the effects of speckle in spot detection applications is to include the smoothing in the detection process. In the method proposed in this dissertation, the detection is proposed to be carried out in the wavelet transformed domain, through combination of the bandpass components. Thus, an indirect smoothing operation is integrated at each iteration of the WT, but since the filter comes from a Haar mother wavelet with just two coefficients, the original resolution is preserved as much as possible. Therefore, even smaller spots can be detected. Figure 37 shows two examples of application of the proposed algorithm on two oceanic SAR scenes, exhibiting small spots (corresponding to vessels) embedded in a homogeneous speckled background. It can be observed that the method does not degrade original resolution, while highlighting the presence of the targets.

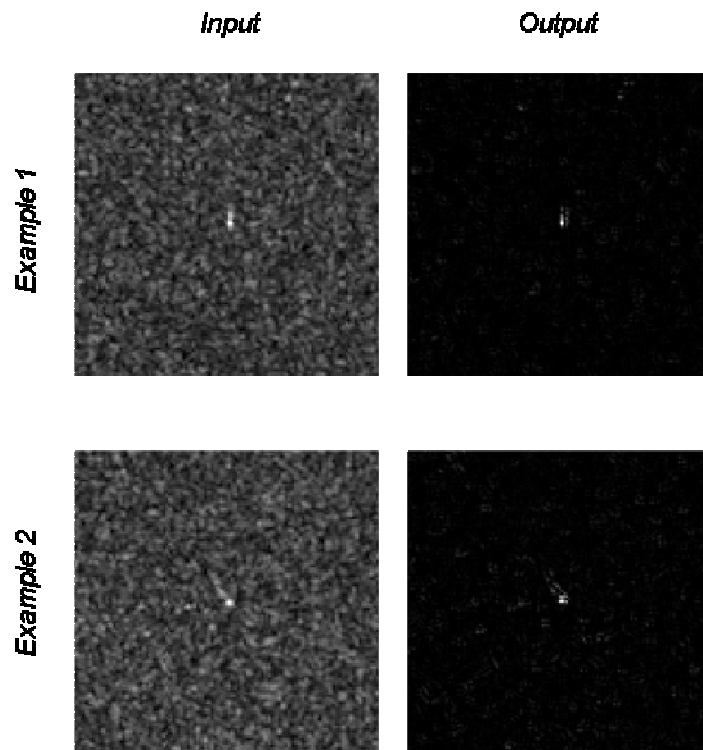


Figure 38. Two examples of application of USEA to the detection of small targets (direct result, no threshold applied) in a RADARSAT image, SGF mode, HH pol., acquired in June 2005.

4.3.2.2. Spot to background contrast enhancement

The most noticeable effect of the algorithm is the enhancement of contrast reached between the targeted spot and its surroundings. Since this separation of distributions is directly related to the success of the final decision step, the significance s is defined in order to quantitatively estimate the impact of the proposed technique:

$$s = \frac{x_{target} - \hat{x}_{background}}{\sigma_{background}} \quad (4.1)$$

where x_{target} stands for the peak intensity of the target, $\hat{x}_{background}$ stands for the value of the background mean and $\sigma_{background}$ is the background standard deviation. The larger the significance, the larger the region in which a threshold will provide a correct detection and, as a consequence, the higher the probability to perform an efficient segmentation in an unsupervised way.

Considering that we are dealing with heavy tailed distributions, it can be assumed that the peak of the histogram completely vanishes after thrice the standard deviation of the background going from the background mean. It is worth noting that the standard deviation of the background is different from the standard deviation of the overall population which is much larger and meaningless in practice, due to the heavy tailed nature of the distribution. As a consequence, it is reasonable to consider that a correct detection will be presumably reached with very high probability if the intensity of the target is higher than the mean plus thrice the standard deviation of the background, i.e.:

$$x_{target} > \hat{x}_{background} + 3\sigma_{background} \quad (4.2)$$

$$x_{target} - \hat{x}_{background} > 3\sigma_{background} \quad (4.3)$$

$$\frac{x_{target} - \hat{x}_{background}}{\sigma_{background}} > 3 \quad (4.4)$$

$$\Rightarrow s > 3 \quad (4.5)$$

Hence, a significance higher than 3 will permit a vast rank of possible values for thresholds and will therefore lead very likely to a correct detection.

Some illustrative examples are shown in Figure 39 and in Figure 40 with their corresponding histograms. They correspond to difficult situations for detection of vessels in oceanic SAR images: heterogeneous background and small targets. In order to image the difficulty of deciding the way of setting the threshold, directly related to the capabilities of detection, a gray square has been superimposed to the histogram representing the region in which the application of a threshold will provide a correct result: detection of the targeted spot with no false alarms. Hence, a wider colored zone signifies a higher flexibility in the evaluation of the threshold and thus larger possibilities of success in the automatic detection. The enlargement of this region of successful thresholding produced by the application of USEA illustrates its goodness.

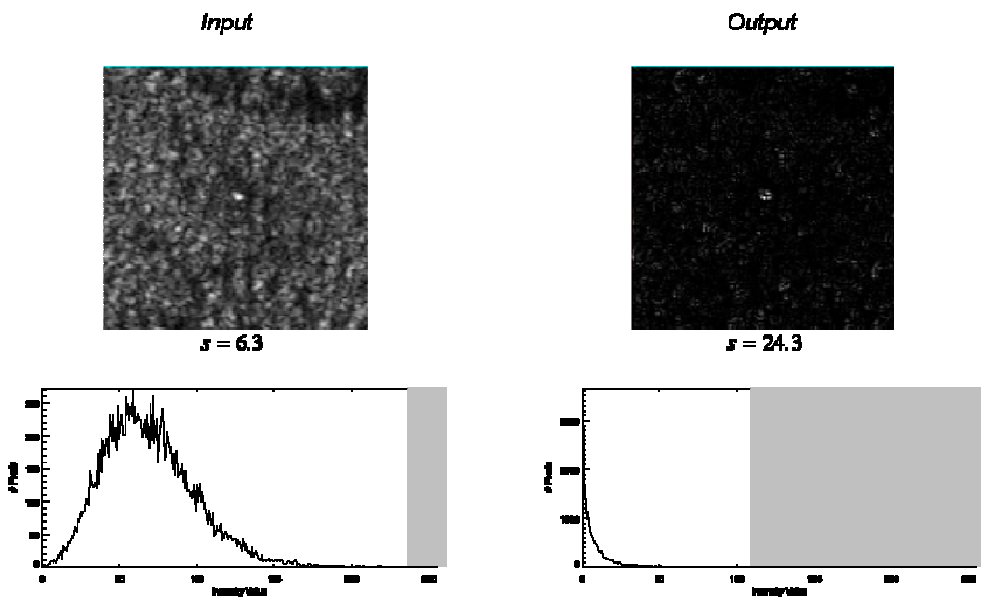


Figure 39. Enhancement of contrast performed by USEA. First row: original image (ENVISAT ASAR image, IM mode, VV pol., acquired in May 2004) and result (direct result, no threshold applied). Second row: corresponding histograms with the region of applicability of a successful threshold.

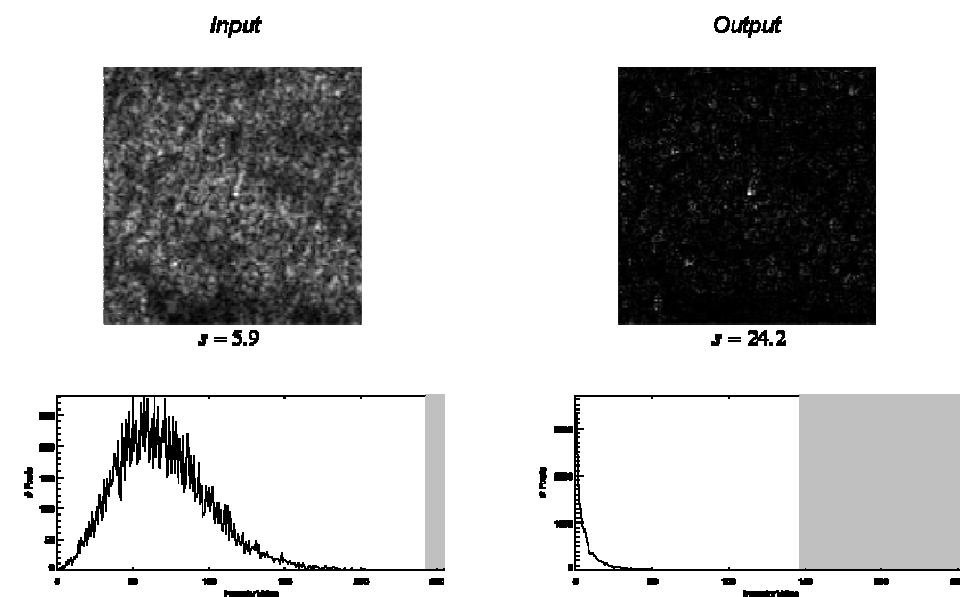


Figure 40. Enhancement of contrast performed by USEA. First row: original image (ENVISAT ASAR image, IM mode, VV pol., acquired in May 2004) and result (direct result, no threshold applied). Second row: corresponding histograms with the region of applicability of a successful threshold.

4.3.2.3. Nature of the statistical distribution invariant in the wavelet domain

It has been stated previously that, due to speckle, the most reasonable way of facing the interpretation of SAR data is by assuming that SAR images of non stationary and non ergodic scenarios are realizations of some underlying random variable. Therefore, the research of the most adequate analysis tools requires the determination of the statistical characteristics of these underlying random processes. The knowledge of the probability density function (which is usually inferred through the histogram of the image) makes the intrinsic randomness of the problem more manageable. Nevertheless, the great diversity of natural scenarios observed by the SAR sensors translates into images with different statistical characteristics. Therefore, it is difficult to establish a statistical that fits real data in any situation. Thus, an interesting property of USEA is that it brings any statistical distribution of the input data to one which is always of the same type at the output. Hence, decision rules, associated to the evaluation of a threshold, are easier.

It is demonstrated through extensive modeling of real data that the subband decompositions have significantly non-Gaussian statistics that are best described by families of heavy-tailed distributions such as the alpha-stable family [90]. More specifically, it is usually assumed for the wavelet coefficients that they follow an exponential probability density function $f_x(x)$ of the form:

$$f_x(x) = K \exp \left[- \left(\frac{|\sqrt{x}|}{\alpha} \right)^\beta \right] \quad (4.6)$$

with

$$K = \frac{\beta}{2\alpha\Gamma(1/\beta)} \quad (4.7)$$

and

$$\beta = F^{-1} \left(\frac{\text{mean}^2}{\text{variance}} \right) \quad (4.8)$$

where

$$F(x) = \frac{\Gamma(2/x)}{\Gamma(3/x)\Gamma(1/x)} \quad (4.9)$$

In the algorithm proposed in this dissertation, after the wavelet decomposition, a spatial product is applied. Let us consider $z = xy$ and let us assume x and y independent random

variables with the same distribution, then the probability density function of the resulting coefficients follows

$$f_z(z) = \int_{-\infty}^{+\infty} \frac{1}{|x|} f_{xy}\left(x, \frac{z}{x}\right) dx. \quad (4.10)$$

As x and y are independent

$$f_{xy}(x, y) = f_x(x) f_y(y) \quad (4.11)$$

Moreover, x and y have the same statistical distribution. Then

$$f_z(z) = \int_{-\infty}^{+\infty} \frac{1}{|x|} f_x(x) f_x\left(\frac{z}{x}\right) dx \quad (4.12)$$

Finally

$$f_z(z) = \int_{-\infty}^{+\infty} \frac{1}{|x|} K \exp\left[-\left(\frac{|x|}{\alpha}\right)^\beta\right] K \exp\left[-\left(\frac{|z/x|}{\alpha}\right)^\beta\right] dx \quad (4.13)$$

$$f_z(z) = K^2 \int_{-\infty}^{+\infty} \frac{1}{|x|} \exp\left[-\left(\frac{|x|}{\alpha}\right)^\beta - \left(\frac{|z/x|}{\alpha}\right)^\beta\right] dx \quad (4.14)$$

So, even if the resulting formula is not very suggestive, it turns out that the final image has always the same nature of statistical distribution, independently from the type of statistical distribution of the input image. This feature makes the algorithm more robust to heterogeneities than conventional approaches which assume beforehand a particular statistical distribution of the input. This feature can be observed in the example given in Figure 41. It consists on a SAR oceanic scene with a spot in the centre surrounded by a heterogeneous background. The heterogeneities in the sea surface deviate the obtained histogram from the expected one according to SAR theory (see Chapter 2) and observable in the examples given in Figure 15 and Figure 16. Nevertheless, after the application of USEA, it can be observed that the resulting distribution follows the expected trend, even despite the different statistic distribution of the input. If the output coefficients are always ordered according to the same nature of probability density function, the subsequent automatic evaluation of the threshold is easier to set and thus detection success is increased.

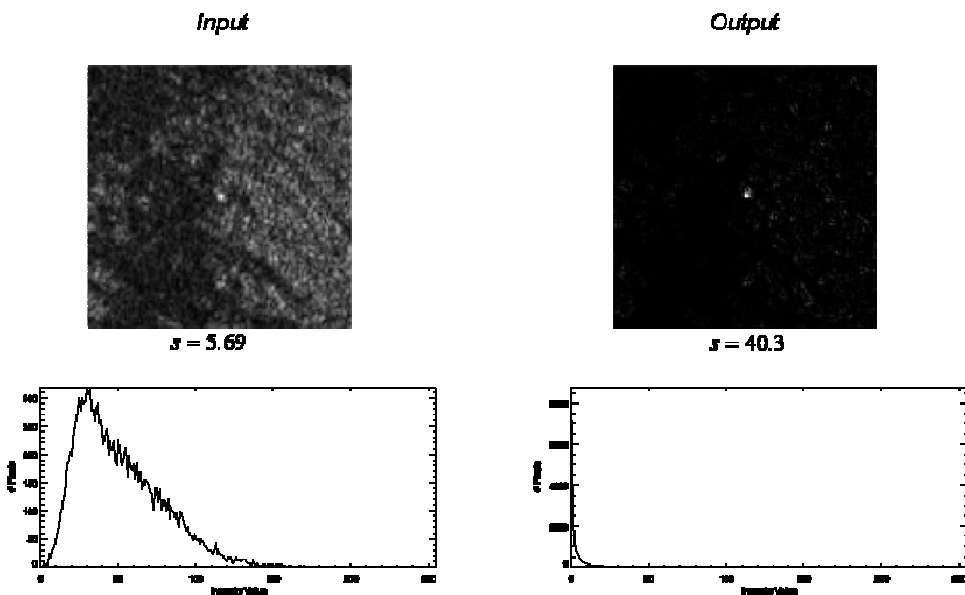


Figure 41. Application of USEA to a heterogeneous scene (RADARSAT image, SGF mode, HH pol., acquired in September 2001). First row: original image and result (direct result, no threshold applied). Second row: corresponding histograms.

4.3.2.4. Capability of managing discontinuities at different scales

The technique proposed has a multiscale capability, i.e. it can focus on different elements at different scales. This means, for example, that if there exists some a priori information about the range of dimensions of the spots to be detected, the method can be adjusted to a given span of scales. As a consequence, the algorithm proposed can intelligently manage discontinuities, which usually constitute a source of false alarms. As an example, Figure 42 (left) shows a SAR image with a vessel in its centre surrounded by ice sheets. The backscattered intensity in the ice sheets is similar to that of the vessel. As a consequence, the automatic discrimination by means of CFAR approaches is particularly non efficient in that case. Figure 42 (right) displays the space / scale decomposition of a horizontal cut of the original image intercepting the vessel. It can be observed that, due to the difference of dimensions, the maximum produced by the presence of the ship occurs at a different scale than that due to the presence of the ice sheet. Hence, the consideration of the multiscale behavior of a signal permits the discrimination of features with similar intensity characteristics. The ambiguity in the intensity image between the ship and the ice sheet – from the point of view of algorithms exclusively based on the application of a threshold to the intensity image – has been solved in the time – frequency plane that is sensitive not only to the intensity values but also to their spatial distribution. It is worth noting that, even if this particular example involves ice sheets, most of the sources of heterogeneities in the sea surface occur at different scales than ships which tend to occupy the smallest scales.

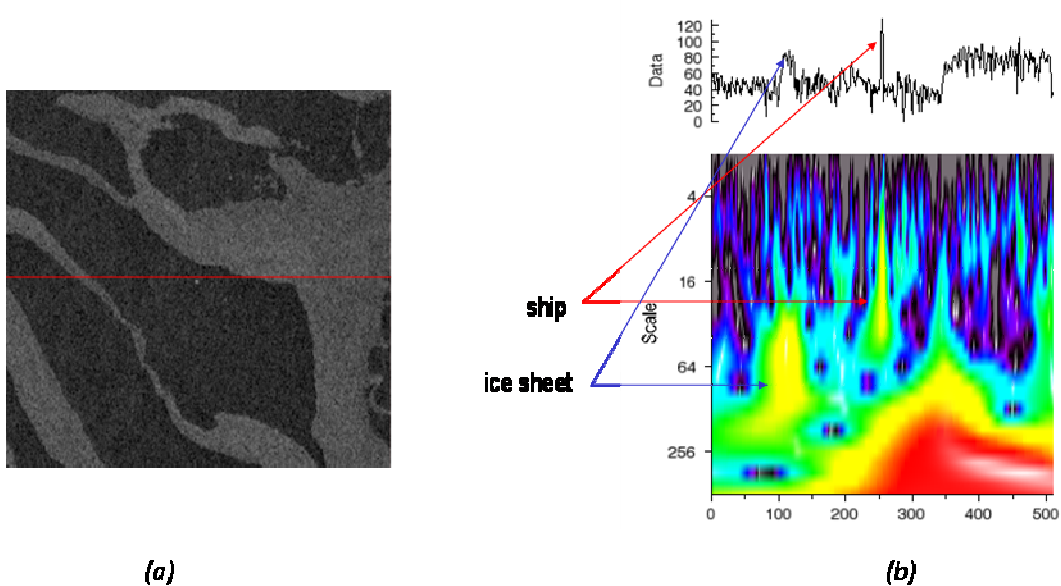


Figure 42. (a) SAR scene of a vessel surrounded by ice sheets and **(b)** corresponding space / scale decomposition of cut of the image.

The technique proposed takes advantage of the spatial constructive coincidence of local maxima in the wavelet domain which occurs only if the structure is localized and approximately isotropic. Therefore, other types of structures, for example elongated ones, are not enhanced as well, even if their response to the radar pulse is very intense. A second example in which a ship appears very close to an ice shelve is shown in Figure 43. The maximum value of reflectivity of the image occurs on the ice surface. As a consequence, this particular situation of detection can not be solved directly by the application of a threshold on the image. To illustrate this point, a threshold whose value is the maximum intensity of the target has been applied. The resulting binarized image exhibits a lot of false alarms which can not be removed since an augmentation of the value of the threshold is accompanied by a loss of the target. On the contrary, after the application of USEA (see Figure 44), in this example, the target becomes the maximum value in the image and it is then possible to choose the value of the threshold among a large span of values leading to a correct detection: consisting in a positive detection for the central target with no false alarms.

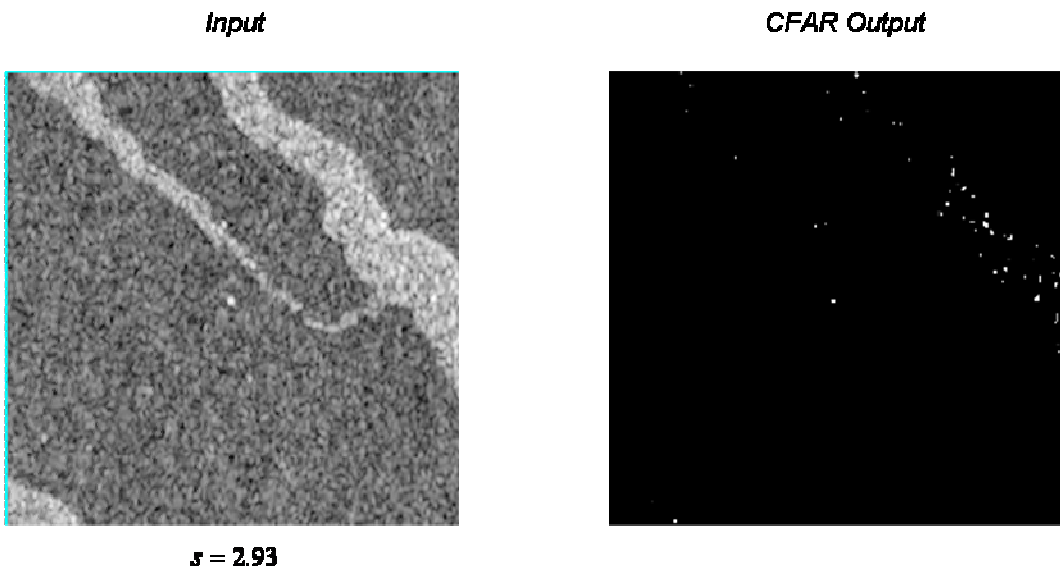


Figure 43. Application of USEA to a heterogeneous scene. (a) Original image (RADARSAT image, SCN mode, HH pol., acquired in January 2003). (b) Result of the direct application of a threshold.

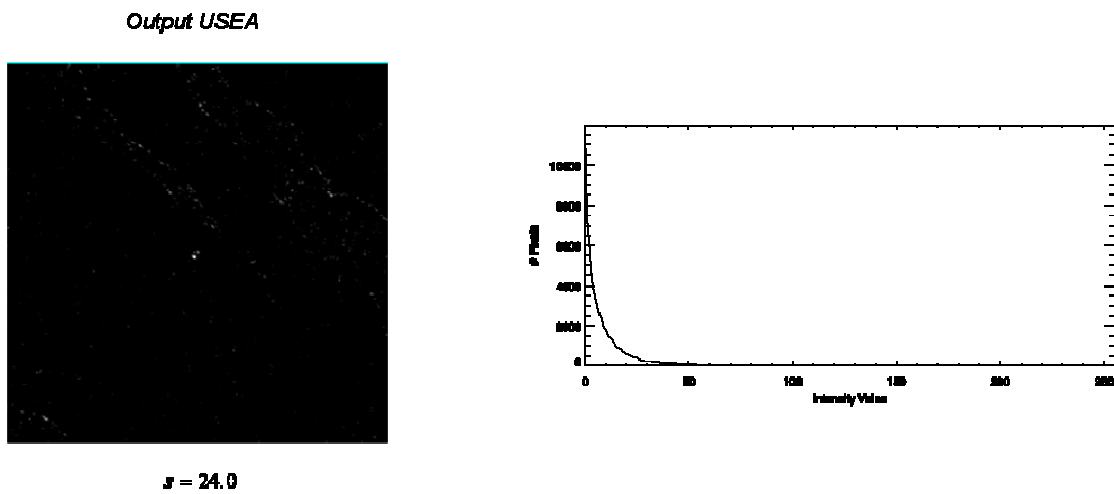


Figure 44. Result of the application of the proposed algorithm to the image in Figure 43 (direct result, no threshold applied) and corresponding histogram.

Figure 45 shows as well examples of detection of vessels in coastal areas, by means of USEA. Since the land usually appears largely brighter than the sea, automatic detection is difficult near to the coast with conventional techniques based on the application of adaptive thresholds [92]. For instance, two situations are possible and both of them lead to an erroneous detection. If the proportion of land in the moving window used to compute the threshold is too large, it can increase the value of the threshold resulting in a misdetection of

the vessel (if it does not sufficiently bright). Otherwise, the most common situation is that the ship is detected but most of the inland pixels produce false positives.

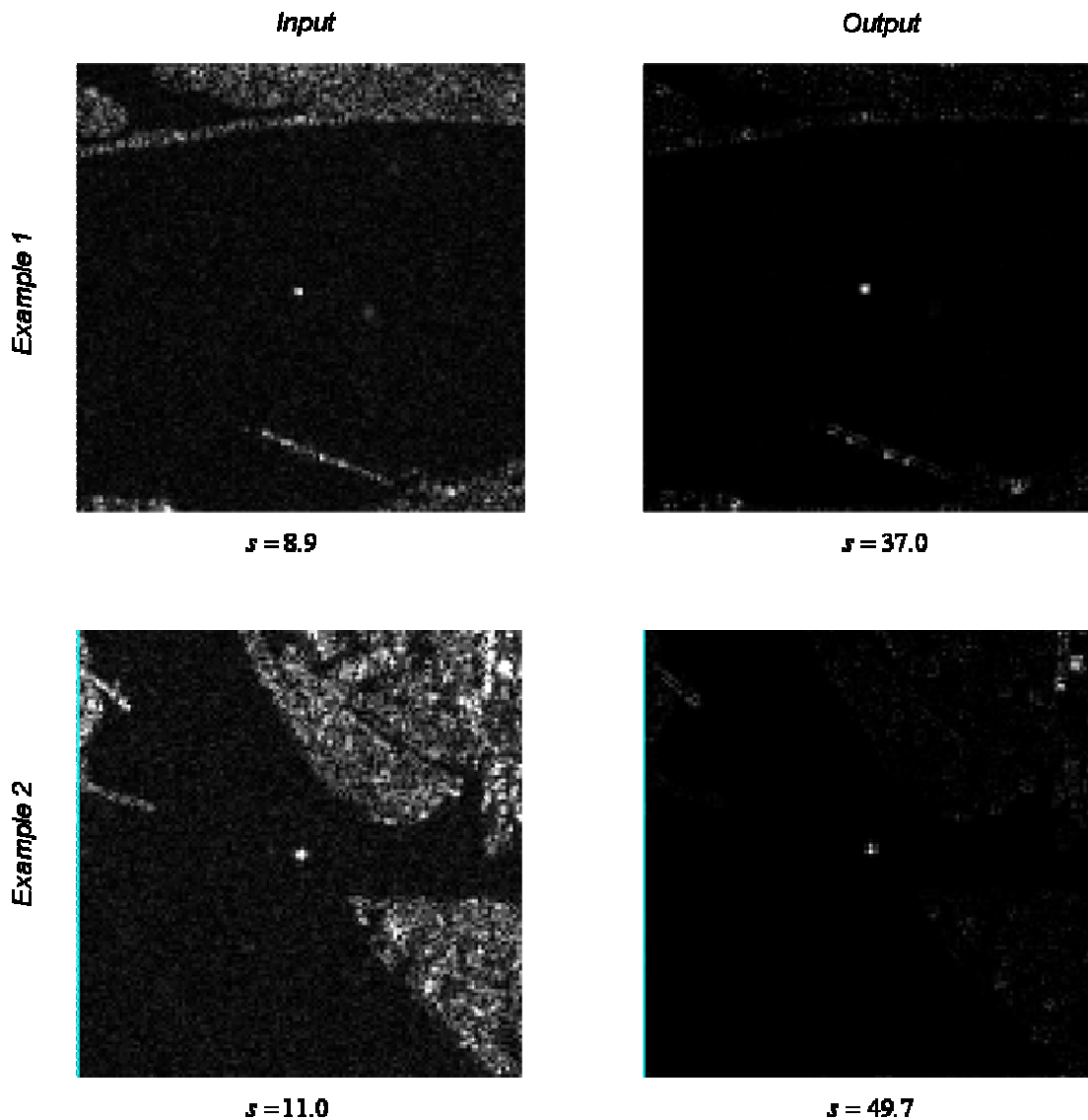


Figure 45. Two examples of application of USEA in a harbor (direct result, no threshold applied).
RADARSAT image, SGF mode, HH pol., acquired in October 2004.

4.3.2.5. Detection not exclusively dependent on the intensity

As seen, USEA does not exclusively depend on the intensity of the targets' signature with respect to that of its surroundings. It also depends on the local spatial correlation, which produces the spatial coincidence of local maxima in the wavelet subbands. As a consequence,

USEA is better suited than conventional techniques based on the direct application of a threshold to detect weak targets with low reflectivities. As a matter of fact, this high sensitivity may be regarded as a possible disadvantage. Nevertheless, this technique has been conceived in the belief that the critical issue in the kind of application focused is detection, rather than false alarms. In fact, it is easier to discard a false positive for a final user than to identify false negatives and a missed target can have very serious consequences.

4.3.3 Validation through simulated data

The algorithm proposed for spot enhancement is first tested on a simulated image. The simulated image consists on a 1024×1024 px. speckle matrix in which an ensemble of 100 targets has been embedded. The targets are themselves ordered following a 10×10 matrix (see Figure 47). They present different sizes and intensity values. Specifically, the different parameters used are compiled in Figure 46.

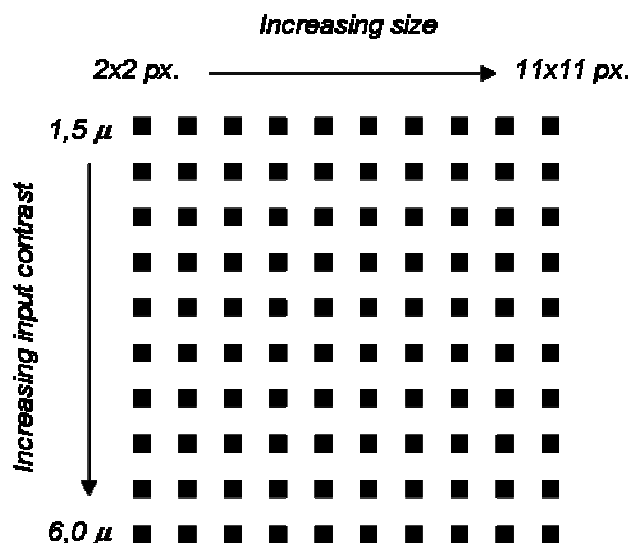


Figure 46. Parameters employed for the targets in the simulated image.

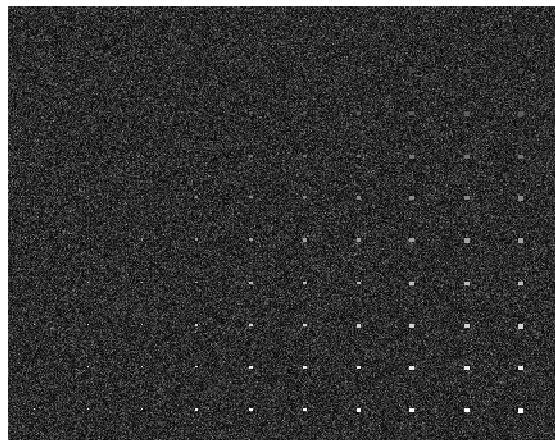


Figure 47. Simulated SAR image with a matrix of targets.

Five iterations of USEA are applied to the simulated image. Figure 48 displays the results obtained for scale 2^2 and 2^3 .

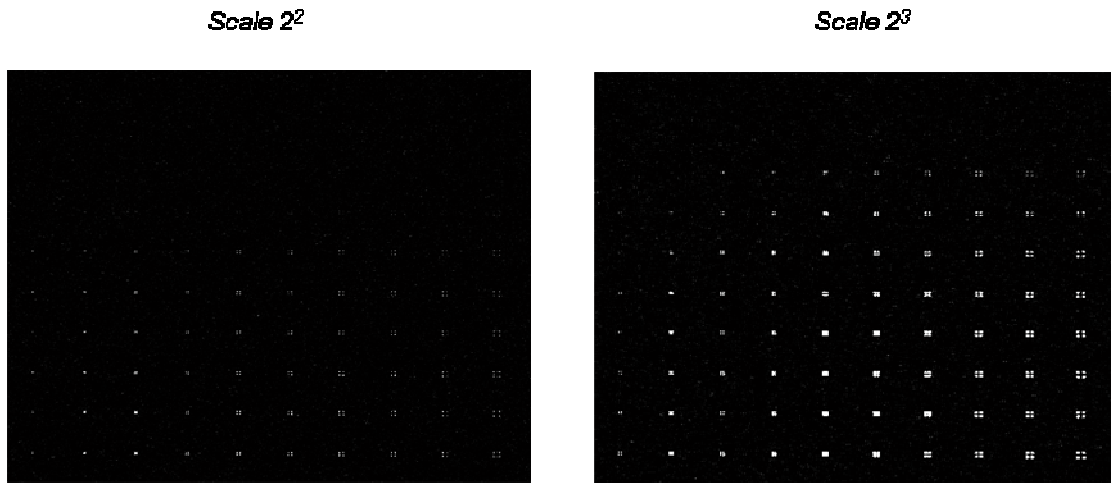


Figure 48. Result of the application of USEA to the simulated image in Figure 47.

The most noticeable effect of the algorithm, appreciable at first sight by comparing input and output images is the increase in target to background contrast, simultaneous to a reduction of speckle. For instance, it can be observed that a number of targets not visible in the original image appear in the result. On the other hand, the performance of the method presented depends on the initial target to background contrast: targets in the top row are barely distinct after the application of the spot enhancement.

The difference of behavior between the two scales presented can easily be observed. As expected, the scale 2^2 highlights the smaller targets (the brightest spots in the result are the ones placed in the left columns), whereas the scale 2^3 privileges bigger ones (the brightest spots are in this case the ones of the central columns). For the sake of clarity, the rest of the scales are omitted, but in higher scales the most extended targets are highlighted. Nevertheless, it is worth noting that even if highest scales favor biggest targets, smallest ones do not disappear due to the property of persistence of local maxima across scales.

In order to provide a more accurate evaluation of the performance of USEA as a function of the input target to background contrast and as a function of target size, several graphs are plotted in Figure 49. On the one hand, the left column illustrates the increase in contrast after the application of the multiscale technique presented for three consecutive scales: 2^2 , 2^3 , 2^4 . More specifically, for each scale, several curves are plotted in the graph. Each curve corresponds to targets sharing the same size but presenting different target to background contrast in the input image (columns in the simulated matrix). It can be observed, that the increment in contrast can be adjusted by a quadratic law. For the smallest scale considered (2^2), all the curves exhibit approximately an identical trend, independently from the input target size. On the contrary, for higher scales, the aperture of the parabola depends on the target size: if the dimensions of the target are small with respect to the scale, the increase in the output contrast is slower. On the other hand, the right column, exhibits graphs showing the performance of the algorithm as a function of the target size. Each one corresponds to a different scale (2^2 , 2^3 , 2^4). For each graph, several curves are plotted, corresponding to the output contrast for targets sharing the same input target to background contrast, but having different sizes (lines in the simulated target matrix). At the smallest scale considered, there is not a clear dependence of the performance of the algorithm designed on the size of the input target. Nonetheless, it is worth noting that for higher scales, the performance rapidly increases with the size for targets whose dimensions are similar to the corresponding scale and remains almost unchanged for larger ones.

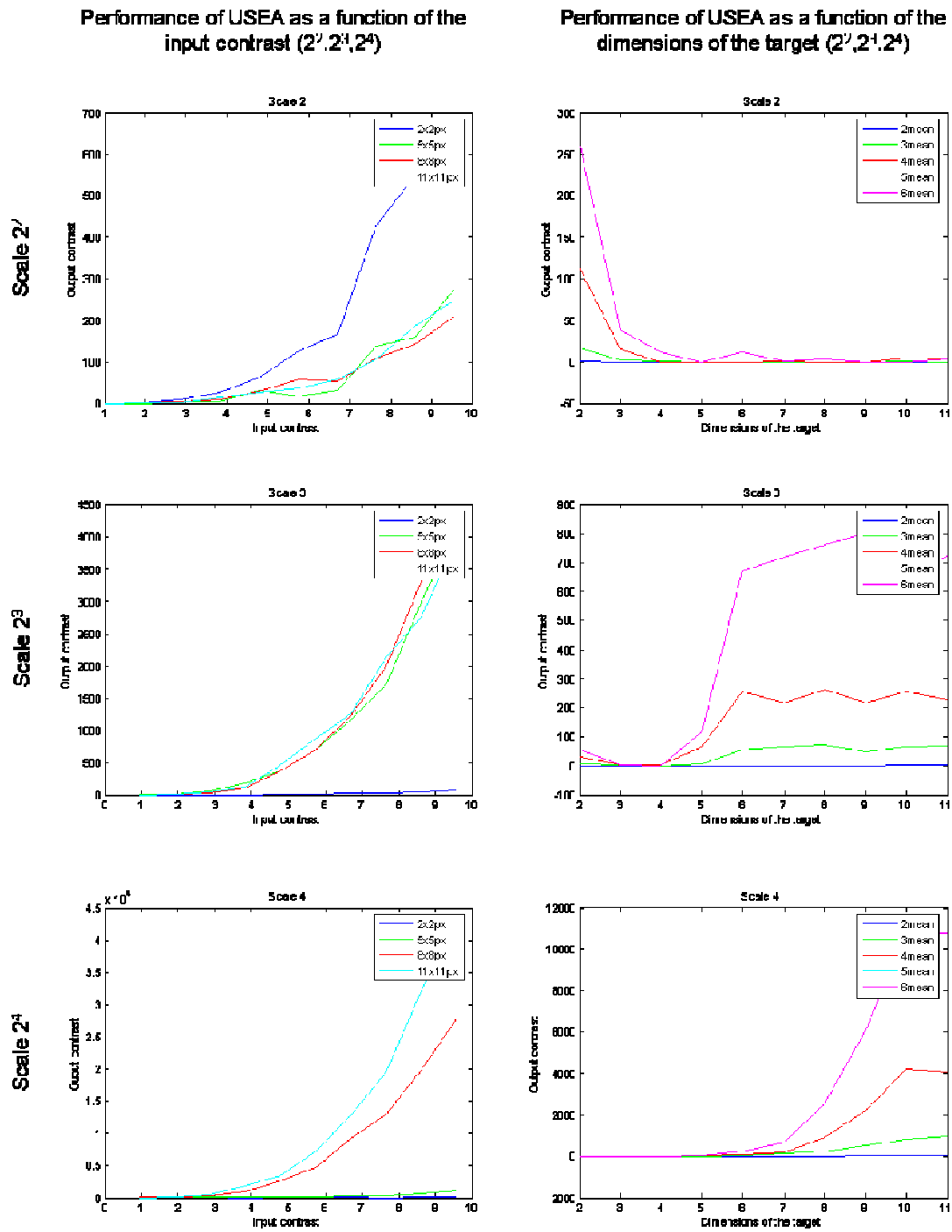


Figure 49. Performance of USEA as a function of the input target to background contrast (left column) and of the target size (right column) for different scales.

In order to compare the performance of USEA with conventional methods, the Lee filter [91], which is the most relevant among speckle filters in the literature, has been applied to the

simulated image. The Lee filter relies on the multiplicative model of speckle and, after a first Taylor expansion, it deduces an estimation $\hat{\sigma}$ of the useful information content through minimization of the mean square error:

$$\hat{\sigma} = \bar{I} + k(I - \bar{I}) \quad (4.15)$$

where I is the observed intensity, \bar{I} its mean and parameter k is evaluated as:

$$k = \frac{\text{var}(I) - \bar{I}^2}{\sigma_n^2 + 1} - \bar{I}^2 \quad (4.16)$$

with σ_n the standard deviation of speckle and var stands for variance. The filter process is performed by applying a sliding window of given dimensions, in which the mean and the variance are estimated. The mean and the variance are approximated respectively by the arithmetic mean and the sample variance of the pixels within the window. Hence, the dimensions of the window constitute an important parameter determining the efficiency of the filtering process. This parameter handles the trade-off between speckle reduction and sensitivity to small targets: a large window favors noise suppression resulting in a higher target to background contrast, but can produce an excessive blurring of small spots with low contrast. Figure 26 displays the result of filtering the simulated image with the matrix of targets with a Lee filter with two different window sizes: one of 5x5 pixel (left column) and one of 11x11 pixel (right column).

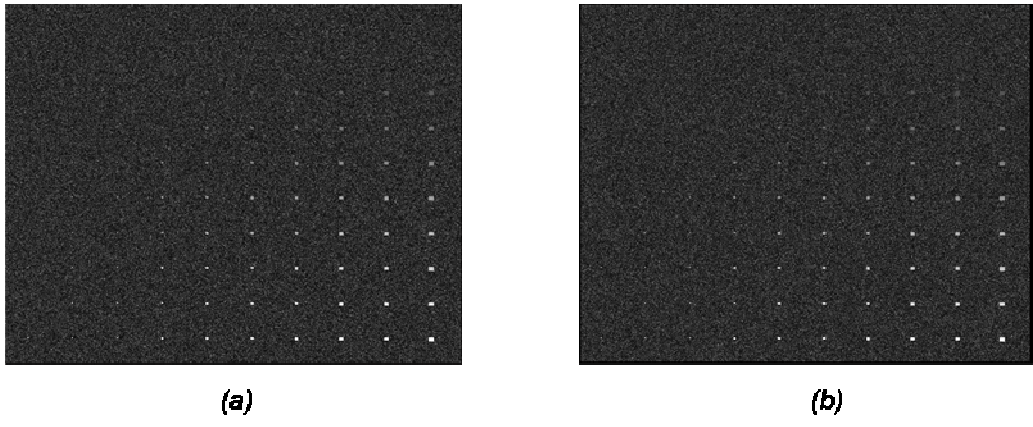


Figure 50. Effect of the Lee filter on the simulated image with two different window sizes: one of 5x5 px. (a) and one of 11x11 px. (b).

The performance of the Lee filter is analyzed as a function of the input target to background contrast and as a function of the target size. Figure 51 shows results obtained for the application of the Lee filter with a window size of 11x11 pixel. It can be observed that, in the case of the Lee filter, the output contrast increases linearly with the input contrast, whereas it is independent on the target size.

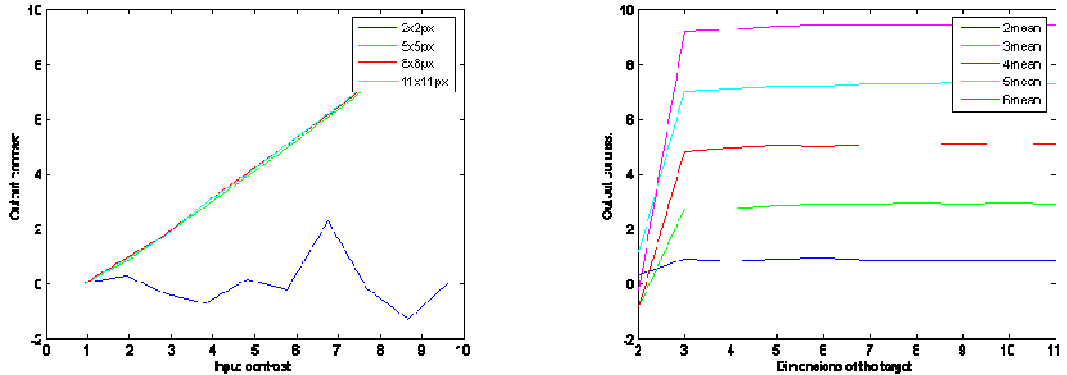


Figure 51. Performance of Lee filter (with a window size of 11x11 px.) as a function of the input target to background contrast (left column) and of the target size (right column) for different scales.

In order to illustrate simultaneously the performance of both USEA and of the Lee filter, the output contrast as a function of the input contrast on the one hand as well as the output contrast as a function of the target size in the other are plotted together for both techniques (see Figure 52). A logarithmic representation has been chosen for the results obtained with USEA at scale 2^3 and for the Lee filter with a window size of 11x11 pixel. The difference of behavior of the performance of both algorithms as a function of the input contrast and of the window size can be noticed again. Moreover, it can be observed that the contrast reached with USEA is considerably higher than the one provided by conventional filtering.

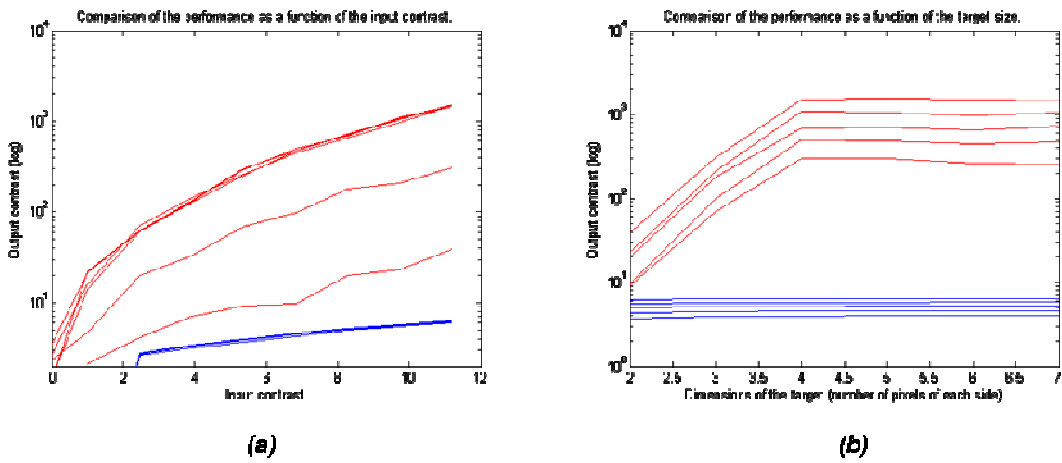


Figure 52. Comparison of the performances of the multiscale algorithm proposed (red curves) and of the Lee filter (blue curves) as a function of the input target to background contrast (a) and of the target size (b) for different scales.

4.4 Application to ship monitoring with SAR sensors

In the scope of SAR, an eminent application of spot detection is ship monitoring. This section aims at analyzing the operability of USEA for vessel detection purposes. After a discussion about the state of the art regarding advances in maritime experiments with SAR data, a procedure based on USEA is described and tested in an unsupervised way over SAR images. Results are compared to groundtruth, when available, to results obtained by other operational methods and to visual inspection.

4.4.1 State of the art

Maritime monitoring from space is one important field of application of SAR imagery. It includes among others traffic surveillance, maritime security, fisheries and border control [92]. Carrying out an effective control of fishing activities is essential to guarantee a sustainable exploitation of sea resources: illegal fishing can lead to over-exploitation, catches over safe biological limits and disturbances to the fisheries habitat. It is also crucial to detect smuggling and illegal immigration movements. As the regulated areas are extended, they are difficult to monitor by means of traditional reconnaissance methods such as planes or patrol vessels. Spaceborne SAR sensors are able to provide a powerful surveillance capability allowing the observation of broad expanses, independent from weather effects, so much during the day as during the night and they do not require any kind of active cooperation of the vessel. For instance, since January 1st of 2005, all European Community fishing vessels exceeding 15 meters overall length are subject to have installed on-board a VMS for controlling purposes. The Vessel Monitoring System (VMS) [93], is basically an on-board transponder that provides vessel identification and position via satellite communications. Although this transponder-based monitoring system provides accurate results it is not perfectly suitable for monitoring illegal activities as the hardware can be intentionally disconnected or damaged. A complementary or even alternative solution is provided by SAR imagery. Aware of this problem, the European Community has promoted several concerted actions that brought together different parties active in space-based ship detection. The IMPAST and the DECLIMS projects have been the most important initiatives in this direction. IMPAST is an acronym for Improving Fisheries Monitoring Through Integrating Passive and Active Satellite Based Technologies [94]. The main specific objective of IMPAST was to develop a near-real time pre-operational automatic system for correlating the VMS reports from a fishery and SAR detections in order to identify and pursue vessels in breach of fishing regulations. DECLIMS stands for Detection and Classification of Marine Traffic from Space and it provided a focus for research into the use of satellite imagery for maritime vessel detection, classification and identification, evaluate and compare the performances of the different algorithms, strengthen

the infrastructure capable of meeting demands of users and set the requirements of new sensors and platforms towards the operational needs of vessel monitoring [95].

Ship detection in SAR images can be regarded as a particular problem of spot detection. Due to the great diversity of types of vessels, the wide range of image modes and resolutions and the distortions affecting the signatures of the ships, no a priori information about nor size neither shape can be employed to assist efficiently the detection process. In fact, low resolution of the sensors and motion distortion render the ship's signature rather featureless, since the same ship can present very different signatures depending on a number of unpredictable random variables, mainly related to sea state. An extensive review of the factors affecting to the signature characteristics can be found in [96].

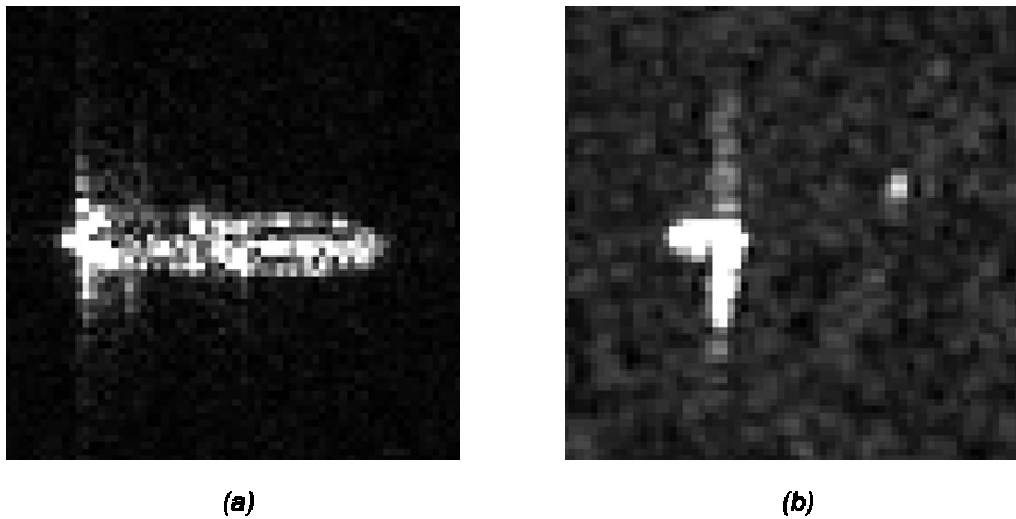


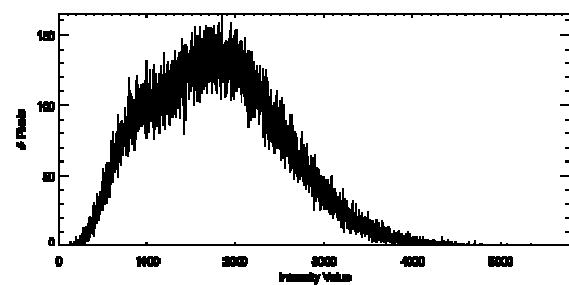
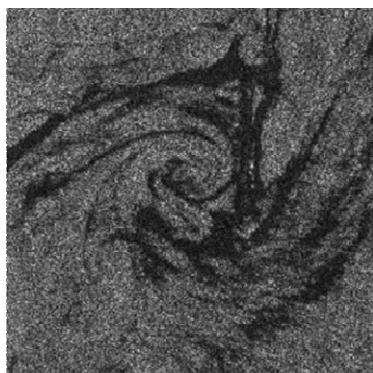
Figure 53. (a) Ship in a high resolution SAR image. (b) Two ships in a low resolution SAR image.

Nowadays, several systems present operational status for automatic ship detection purposes on SAR imagery. The prime examples are the Ocean Monitoring Workstation (OMW) [97] [98], the Alaska SAR Demonstration (AKDEMO) system [99] [100], the SUMO system from the European Community Joint Research Centre [101] [102] [103] and the Qinetiq's MAST system (Qinetiq). All of them rely on an initial preprocessing step to enhance SAR image and make subsequent stages easier. Speckle filters are usually applied but, even if they effectively enhance the visual quality of the images, there are no guarantees they will contribute to improve the performance of later detection algorithms. Then, a prescreening step follows the preprocessing in order to look for potential ship pixels. All the operational systems are nowadays based on a Constant False Alarm Rate (CFAR) approach which interprets the difference between the spot and its surrounding area as a difference of intensity levels [104]. Then a threshold is evaluated and pixels are classified according to this set value. Even if some attempts have been made with global thresholds [105], [106], adaptive threshold methods are

the most common prescreening algorithms for target detection in radar imagery [100] [99]. However, it must be noted that the evaluation of the threshold is still a critical and awkward process and the value of the threshold is often adjusted empirically, by trial and error [96]. Furthermore, in [100], the authors suggest that better results may be obtained by using a dynamic target window, i.e. allowing the target window to change size by using for example a series of target windows of varying size and choose the one with largest mean. This observation justifies the statement of the multiscale framework for ship detection purposes. An interesting prescreening algorithm has been proposed by researchers at Lockheed Martin Canada [107]. It is based on a multiresolution analysis and hence it is especially applicable to high resolution imagery. Specifically, the prescreener is a practical multiresolution algorithm for target detection in uniform clutter, relying on the assumption that man-made objects are easily detectable at low resolution because their scattering is more persistent than that of natural or natural objects. The steps involved are: the application of a discrete WT; the extraction of the relevant subbands; the formation of low resolution amplitude images; the application of a Rayleigh CFAR detector to the amplitude image; the extraction and delimitation of the corresponding regions of interest in the original imagery; the application of a Weibull or K distribution CFAR to the final regions of interest.

The underlying reasoning associated to CFAR techniques is valid and efficient if the observed scene is sufficiently homogeneous but it fails elsewhere. Essentially, these algorithms assume the homogeneity of the image to be analyzed within a region of fixed dimensions. Through the values of the signal in this cluster of samples, some statistical parameters are estimated and they are used to adjust the histogram to the probability density function of a particular statistical distribution previously assumed to characterize clutter, where the most popular hypothesis is the K-distribution. Then, a threshold is calculated and its application leads directly to a binarized image. Hence, summing up, the validity of CFAR approaches strictly depends on two conjectures: the assumption of a particular nature of statistical distribution and the hypothesis that a considerable contrast exists between the vessel to be detected and the surrounding sea. Nevertheless, these requirements are not always met [108] [109], as it can be observed in two different examples shown in Figure 54 and Figure 55.

Example 1



Example 2

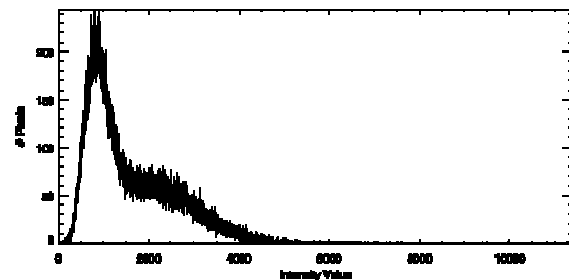
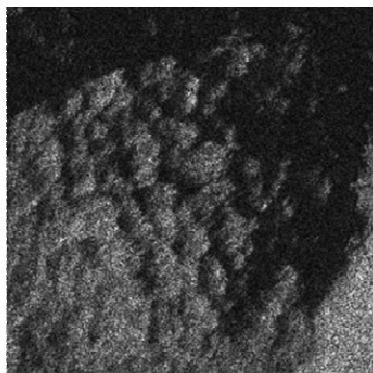


Figure 54. Two examples of heterogeneous oceanic scenes with their respective histograms.

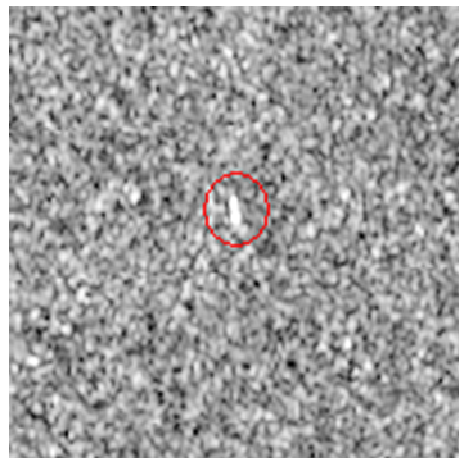
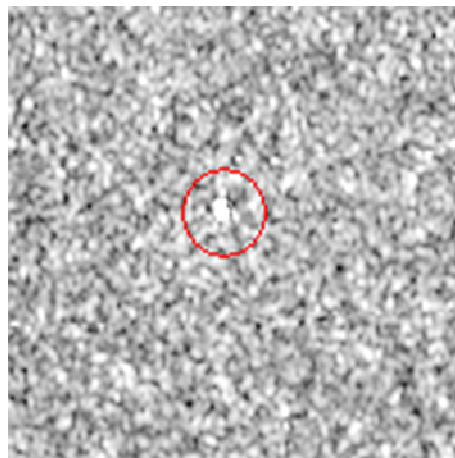


Figure 55. Two examples of ships signatures (enclosed in a circle) exhibiting a low contrast respect to the background sea surface.

Recently, several alternative methods to conventional CFAR techniques have been explored. In [110], the use of the fourth moment, the normalized kurtosis, is proposed and the method was found suitable for ship detection in open ocean conditions. [111], [112] have developed a system based on fuzzy decisions, used to assign confidence values to the detections. In [113], a ship detector referred to as the Neural Network Dempster Shafer technique is explored. In [114], a technique is proposed that uses an image segmentation approach based on a neural clustering scheme designed as “probabilistic winner take all”. In [115], a simple ship detection technique on SAR images is presented based on the cross correlation between two images extracted by moving windows of a small size from the multilook SAR images.

4.4.2 Application of the spot detection algorithm designed to automatic ship detection in SAR imagery

USEA has been implemented to be able to efficiently process complete SAR images of different types. A final threshold step has been added after the application of the algorithm based on the WT. A text file is then obtained with the list of positions of eventual targets. This procedure is completely unsupervised and it takes few minutes, depending on the dimensions of the image. In order to test the performance of the algorithm proposed, the positions obtained have been compared to ground truth data (when available), to the detections of other automatic algorithms (tested on the same images within the scope of the DECLIMS project) and to visual inspection. Two examples of complete processing are presented hereafter.

4.4.2.1. Example of operation in a RADARSAT image

The first example of analysis corresponds to a RADARSAT image, SGF mode of 8892 x 8711 pixel acquired in July 2002 in the Cantábrico area, Northern Spain (see Figure 56). The resolution is about 22 m in range x 27 m in azimuth. This image has been selected because the region usually presents a high traffic of fisheries and because most of the vessels are difficult to detect (they are small and some of them are wooden vessels).

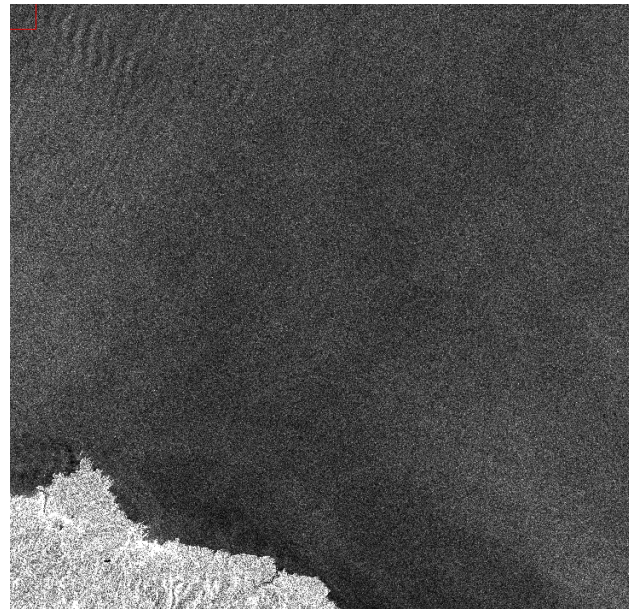


Figure 56. RADARSAT image of the Cantabrian area, Northern Spain.

103 targets were detected by USEA. The specific distribution of these positives is as follows:

- 22 targets detected by other automatic algorithms and corresponding quite probably to vessels, 5 of them reported their VMS position.
- 2 targets not detected by other automatic algorithms but with a reported VMS position, as shown in Figure 57 .

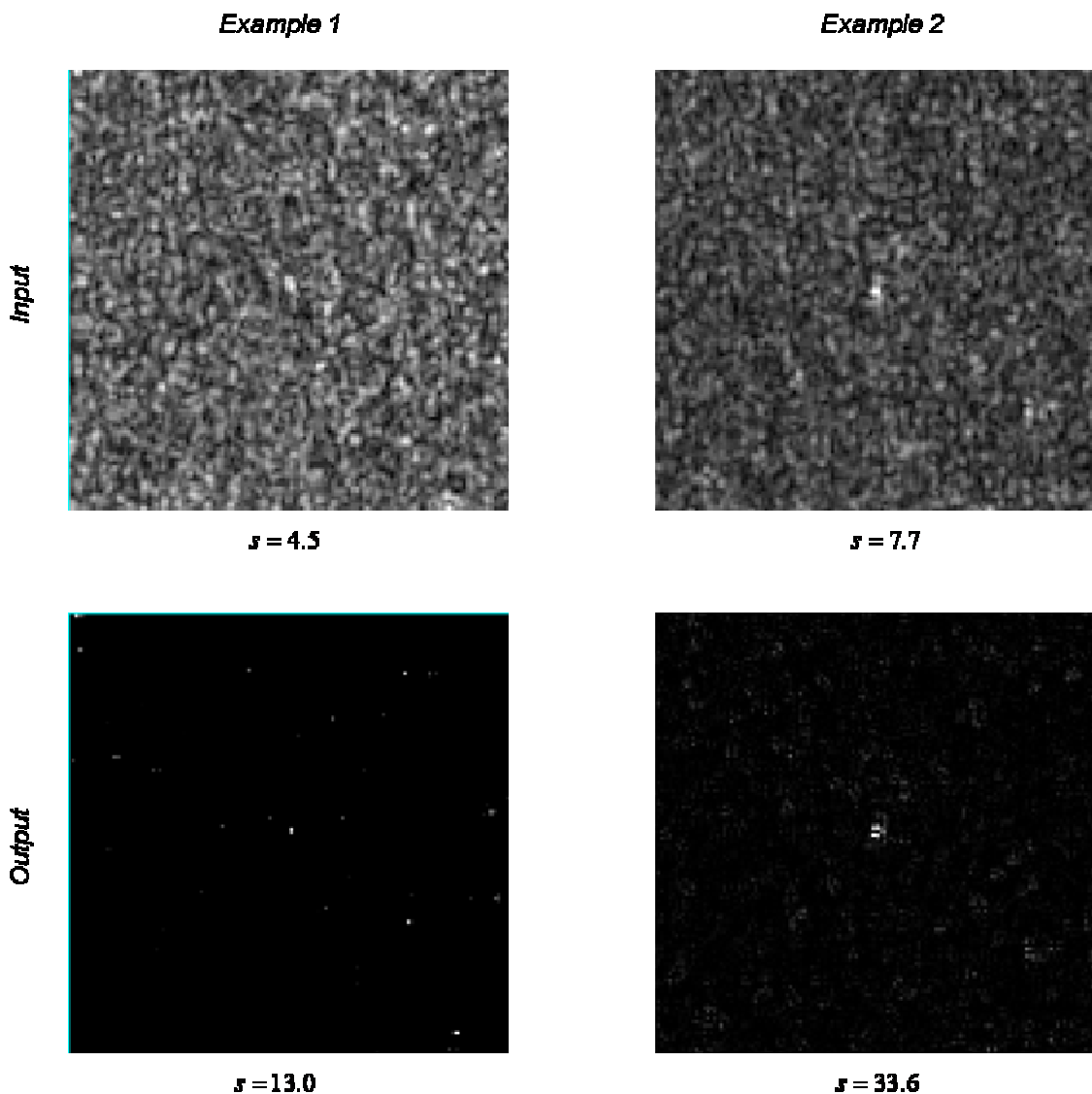


Figure 57. Positives (direct result, no threshold applied) validated through VMS positions.

- 56 targets not detected by other automatic algorithms and corresponding quite probably to ships signatures (visual inspection). Some representative examples are shown in Figure 58.

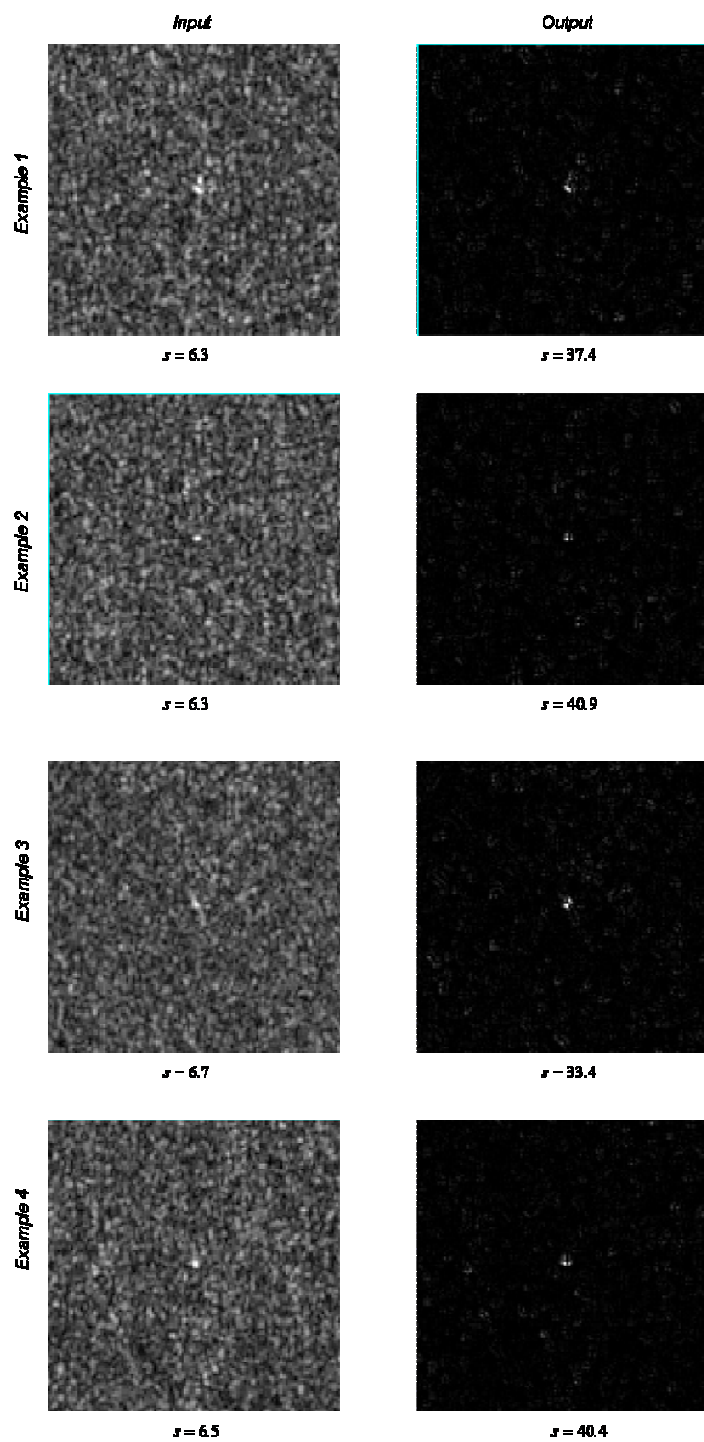


Figure 58. Four representative examples (direct result, no threshold applied) of positives corresponding probably to ships.

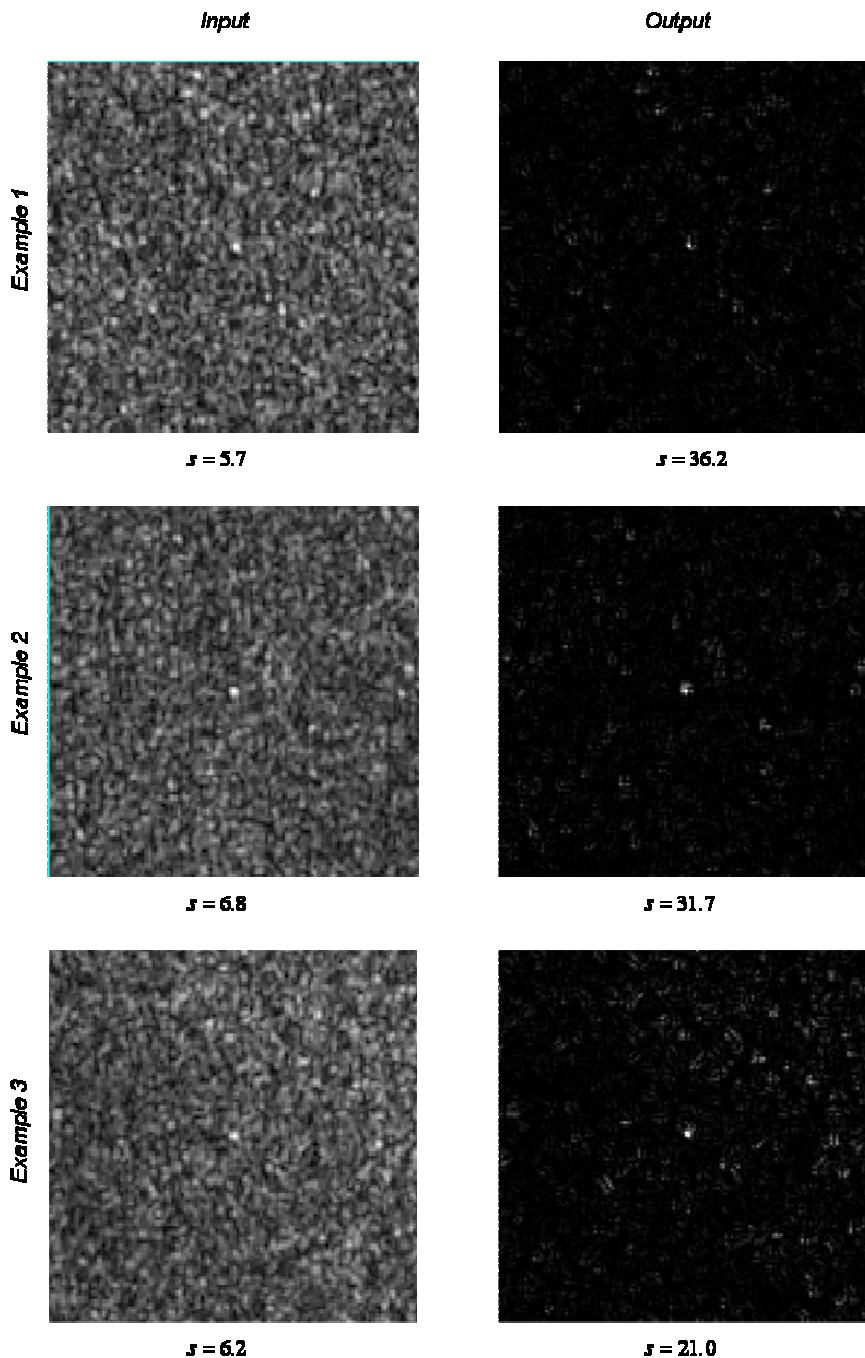


Figure 59. Three representative examples (direct result, no threshold applied) of positives in which visual inspection could not decide whether they correspond to a possible target or not.

- 23 targets not detected by other automatic algorithms and visual inspection can not decide whether they may correspond to ships signatures or not. Some representative examples of this category are shown in Figure 36. It may be interesting to notice that, even if a decision is not possible, the automatic algorithm is performing correctly since

each positive is due to the presence of a spot in the original image. Moreover, these spots could reasonably constitute signatures of ships. In fact, two examples of signatures certainly belonging to ships (as VMS ground truth was available) can be seen in Figure 59 and they are similar to the examples shown in this one.

Additionally, visual inspection did not find any other possible target not detected by USEA.

4.4.2.2. Example of operation in an ENVISAT image

The second example of analysis corresponds to an ENVISAT ASAR IMP image of 4641 x 8513 px. acquired in July 2004 (Figure 60). The resolution is about 30 x 30 m.

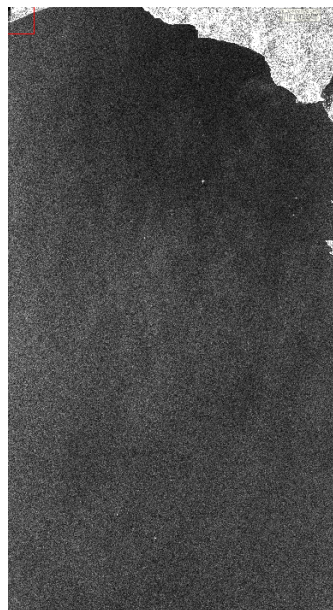


Figure 60. ENVISAT image corresponding to the second example of application of the algorithm to an ENVISAT image.

In this image, 100 targets were detected by USEA. The specific distribution of these positives is as follows:

- 66 targets detected by other automatic algorithms and corresponding quite probably to ships signatures.

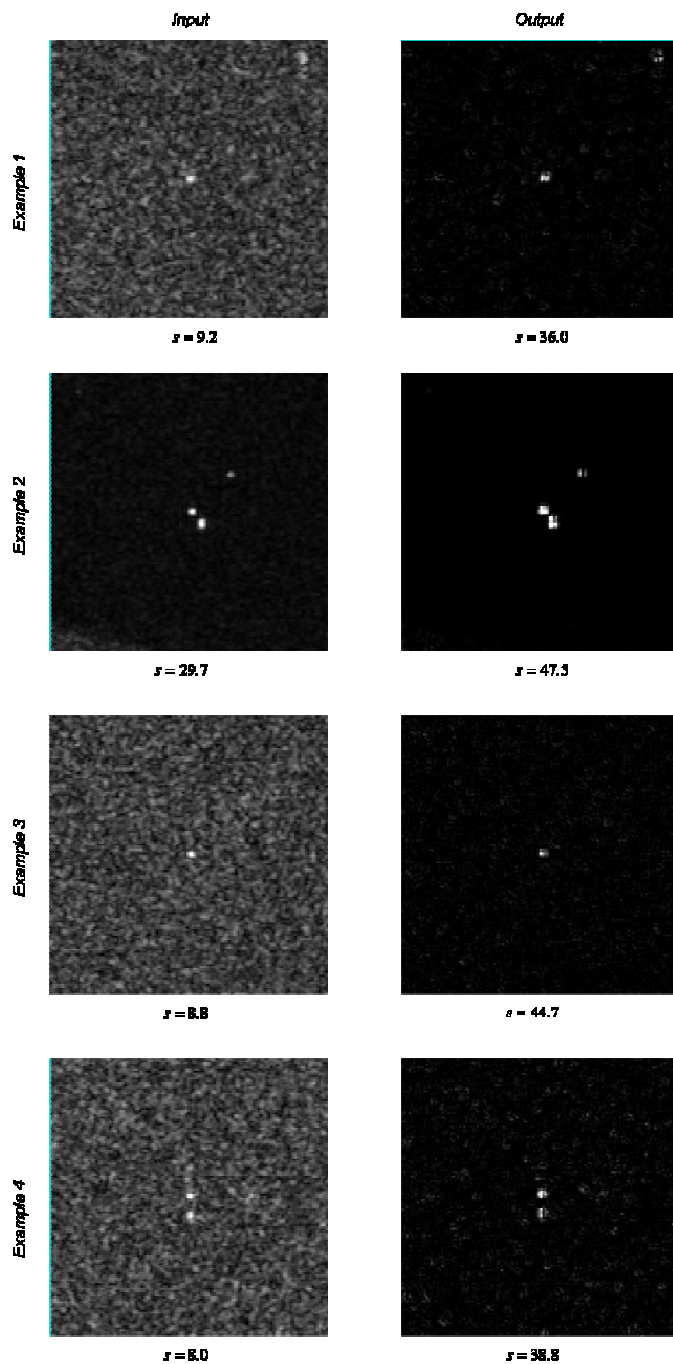


Figure 61. Four representative examples (direct result, no threshold applied) of positives corresponding probably to ships.

- 26 targets not detected by other automatic algorithms and corresponding quite probably to ships signatures. Some illustrative examples are shown in Figure 61.

- 8 targets not detected by other automatic algorithms and visual inspection can not decide whether they may correspond to ships signatures or not. Some illustrative examples are shown in Figure 62.

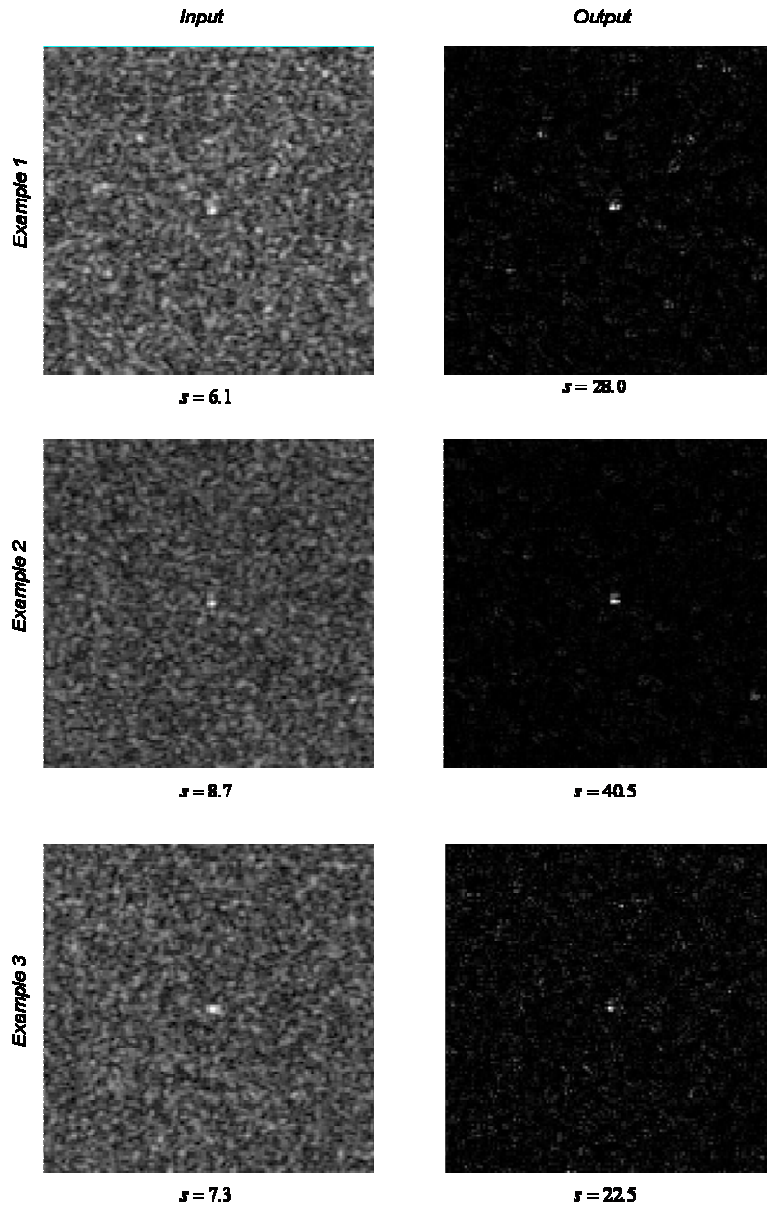


Figure 62. Three representative examples (direct result, no threshold applied) of positives in which visual inspection could not decide whether they correspond to a possible target or not.

Additionally, visual inspection did not find any other possible target not detected by the proposed algorithm.

4.5 Extension to multichannel data

Most of the development of ship detection algorithms to date has concentrated on single channel SAR imagery, certainly due to the fact that most of the available SAR sensors up to now (RADARSAT-1, ERS-1, ERS-2) collected single channel data. However, ENVISAT already presents dual polarized capabilities and, very recently, several operative fully polarimetric spaceborne SAR systems have been launched, such as the Canadian RADARSAT 2, the German TerraSAR X and the Japanese ALOS. It is anticipated [116] [110] that the additional information contained in polarimetric data will improve ship detection (as well as classification and even identification) capabilities. In fact, [117] states that the use of multichannel data will overcome drawbacks of current single channel ship detection algorithms, which have high false alarm rates and require human supervision.

Despite the absence of operative multichannel sensors, research efforts have already been carried out to compare different transmitter and receiver polarization combinations for ship detection purposes. These studies take advantage of the fact that ERS data is VV polarized while RADARSAT-1 follows an HH polarization. Up to now, it is widely accepted that the RADARSAT-1 data is better for ship detection (as opposed to ship wake detection) [118] [98]. It must be noted however that the difference between these sensors is not just limited to the polarization but other factors come into play such as resolution, incidence angle and radar frequency. However, it is assumed that HH polarization has a lower ocean clutter signature than VV. Hence, ship-sea contrast is higher for HH polarization and detectability improves with increasing incidence angle. This also explains why VV is best suited for imaging ship wakes and other ocean surface features, which are barely visible in HH. In [117], a comparison of the ship detection potential of the four linear polarization channels (HH, HV, VH and VV) is carried out. The data for the study was collected by the Convair-580 C-band SAR system developed by CCRS. The study concludes that the use of multichannel data can overcome drawbacks of single channel ship detection algorithms, which have false alarms and require human supervision.

Moreover, several papers [119] [120], have investigated the use of polarization entropy for ship detection. The polarization entropy they consider is the one proposed by the Cloude and Pottier's target decomposition method [121], which extracts entropy and an alpha angle from the polarimetric data. Their results show that using polarization entropy is an effective way of enhancing the contrast between ships and the ocean.

4.5.1 Experiments with dual polarized data

In the scope of this dissertation, a preliminary experiment with dual polarized images from the European ENVISAT ASAR system in its alternative polarization (AP) operation mode. In this mode, ASAR is not able to provide fully polarimetric information, but partial polarimetric. In this case, the system records two instead of three SAR images. Despite the complete polarimetric information about the scatterer of interest can not be retrieved, the channel

diversity can be used to improve ship detection. This section is, then, devoted to present two approaches to exploit the availability of multiple SAR images with the aim of improving ship detection on the basis of the algorithm presented previously.

The first point to consider when multiple SAR images are available is how to combine them in such a way that ship detection is improved. A related reasoning can be found in [109]. USEA consists on the spatial product of the different components of the WT of the input SAR image, based on the idea that ship locations are not altered by the transform itself. Since PolSAR systems, ENVISAT in what it follows, acquires the PolSAR images at the same instant of time, one can extend the previous idea in order to consider the spatial product of the different SAR images provided by the ENVISAT system. Consequently, it is possible to define two approaches to perform ship detection when multiple SAR images are available. They are both depicted in Figure 63.

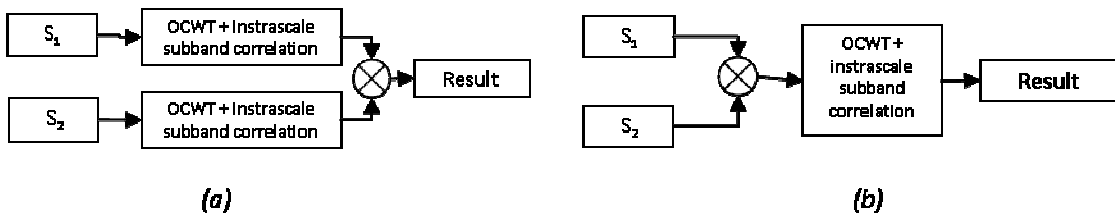


Figure 63. Ship detection algorithms with PolSAR data. (a) Algorithm based on the spatial product of the single SAR imagery detection results. (b) Algorithm based on performing ship detection on the spatial product of SAR images. S_1 and S_2 denote every one of the SAR images considered by the detection algorithms.

As observed in Figure 63, both algorithms work under the same principle. The unique difference lies on considering whether to apply the algorithm for ship detection on single SAR images before or after the spatial product of the different polarimetric SAR images. Both algorithms have been applied to several ENVISAT datasets acquired in AP mode. Based on the parameter of significance, in order to quantify ship detection performance, it has been determined that both approaches presented in Figure 63 perform similarly. Therefore, considering a criterion of minimum computational cost, the second option is considered to perform ship detection with PolSAR images. As observed, the second approach applies just once the single SAR imagery ship detection algorithm to the spatial product of the different images provided by the SAR system.

Detailed results considering the second approach presented in Figure 63 are analyzed in Figure 64 and Figure 65. The first conclusion which can be extracted from both figures is the expected result that to consider multiple SAR images improves ship detection. If one considers Figure 64f, compared with Figure 64d and Figure 64e, it is possible to observe that the proposed algorithm is able to double the significance parameter, which implies a better detection capacity and a decrease of the false alarm rate.

Since PolSAR data is sensitive to the geometric properties of the target under study, depending on the particular position of a given ship with respect to the imaging system, some ships may not appear in one of the SAR images. This situation is clearly visible in Figure 65. As a result, the ship under study would be only detected on the first SAR image. Nevertheless, this situation can be still exploited with USEA for PolSAR data, as observed in Figure 65. Despite the ship is not visible in the second SAR image, the information of this image can be exploited in order to reduce the effect of the clutter on the first SAR image. Again, one may observe that USEA is able to double the detection capability, even in awkward situations.

The results provided by the algorithms presented and analyzed in this section, make possible to conclude that, even taking into account the limitations of the ENVISAT AP imaging mode in order to provide complete polarimetric information, this imaging mode can be successfully exploited to improve ship detection. The presented algorithms have considered only two polarimetric SAR images, i.e. two data channels, to perform ship detection. Nevertheless, these algorithms can be easily extended to fully polarimetric SAR data by considering three instead of two polarimetric SAR images, or even to other multidimensional SAR system configurations.

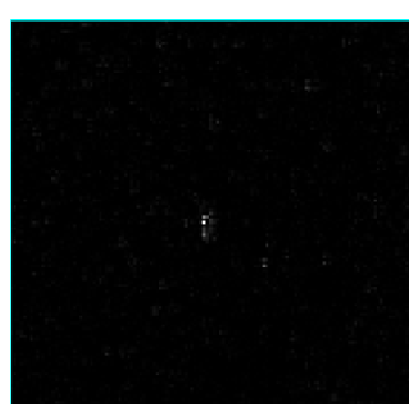
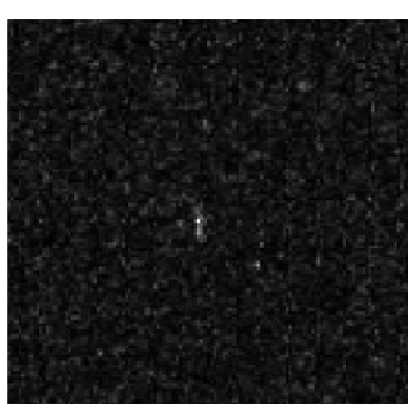
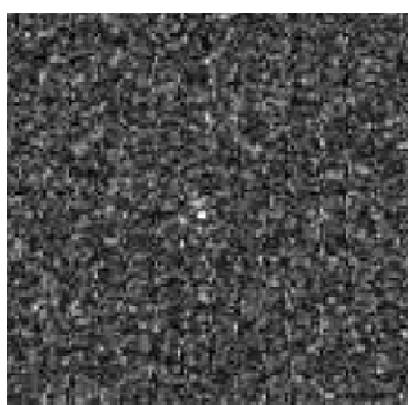
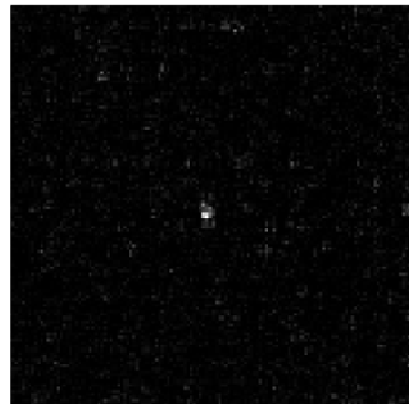
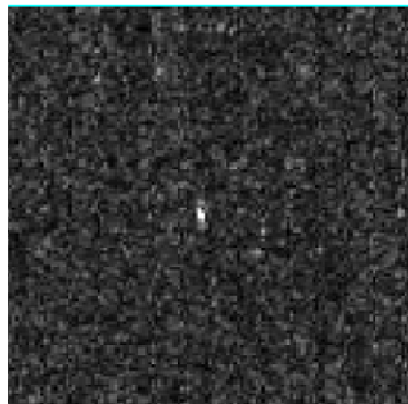
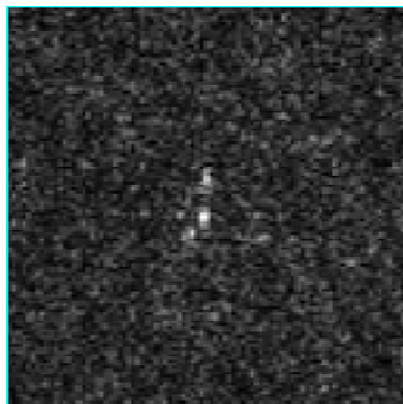
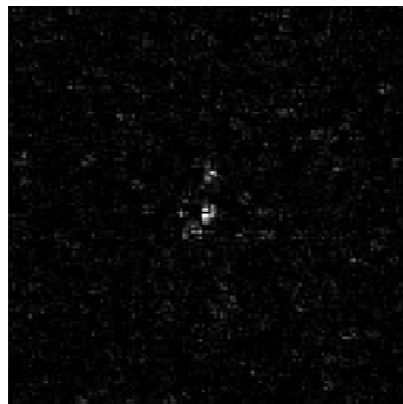


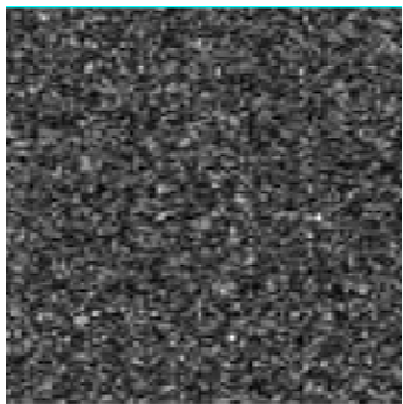
Figure 64. (a) First SAR image HH pol., (b) Second SAR image HV pol., (c) Spatial product of SAR images, (d) Ship detection applied of the image a), (e) Ship detection applied of the image b), (f) Ship detection applied to the spatial product of SAR images.



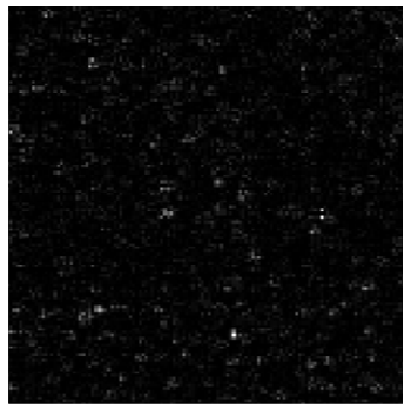
(a) $s=10.6$



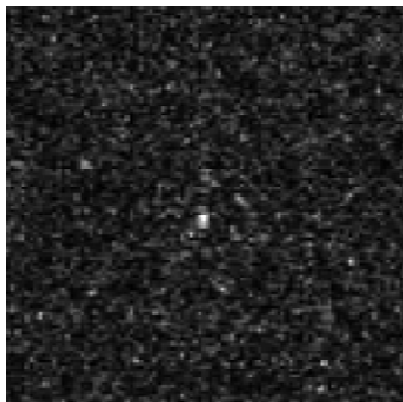
(d) $s=25.7$



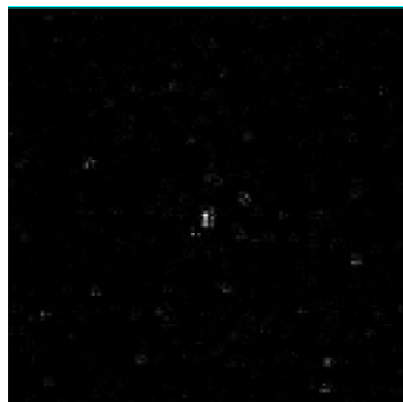
(b) $s=1.07$



(e) $s=0$



(c) $s=11.9$



(f) $s=55.3$

Figure 65. (a) First SAR image HH pol., (b) Second SAR image HV pol., (c) Spatial product of SAR images, (d) Ship detection applied of the image a), (e) Ship detection applied of the image b), (f) Ship detection applied to the spatial product of SAR images.

4.5.2 Experiments with full-Pol data

The aim of this section is to analyze the enhancement of the detection performance of USEA by adapting it to images acquired by RADARSAT-2, with multipolarization and improved resolution capabilities. An example of RADARSAT-2 polSAR data of the area of Barcelona is shown in Figure 66. It has already been discussed in previous chapters that polarimetry offers polarization diversity which is useful to discriminate geometrical aspects of the scatterers in the illuminated scene. The counterpart is that this is obtained at the expenses of a reduction of swath width.

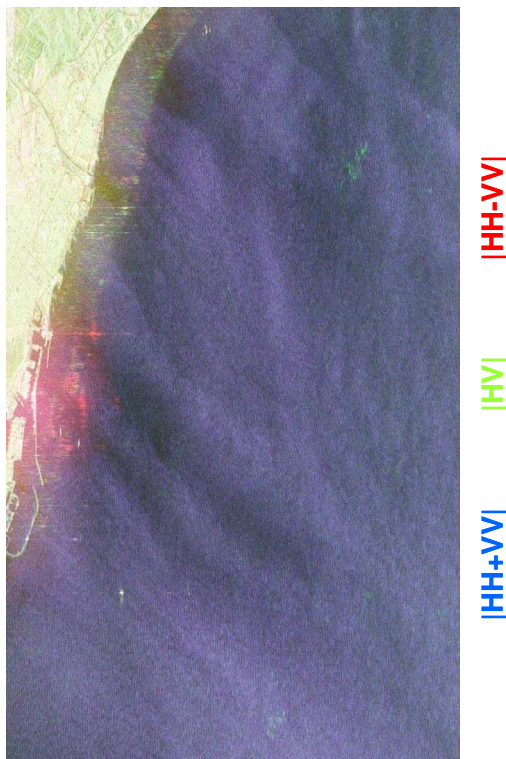


Figure 66. Polarimetric RADARSAT-2 image of the area of Barcelona (Spain). Pauli RGB decomposition.

In the context of ship detection, several hypotheses were made before the availability of fullPol spaceborne data. Some of them have been overviewed in the introduction of this section. A set of RADARSAT-2 data of the area of Barcelona (Spain) acquired in December 2008 will be employed to experimentally verify them.

The first hypothesis analyzed is that for incidence angles relevant to RADARSAT-2, cross-polar channels provide better target to clutter ratio. This has been verified for the set of data considered. As an example, Figure 67 shows the four polarization channels of a scene containing three targets in a calm sea state. It can be observed at first sight that the cross-polar channels (bottom row) offer a higher contrast between the targets and their background than the co-polar ones.

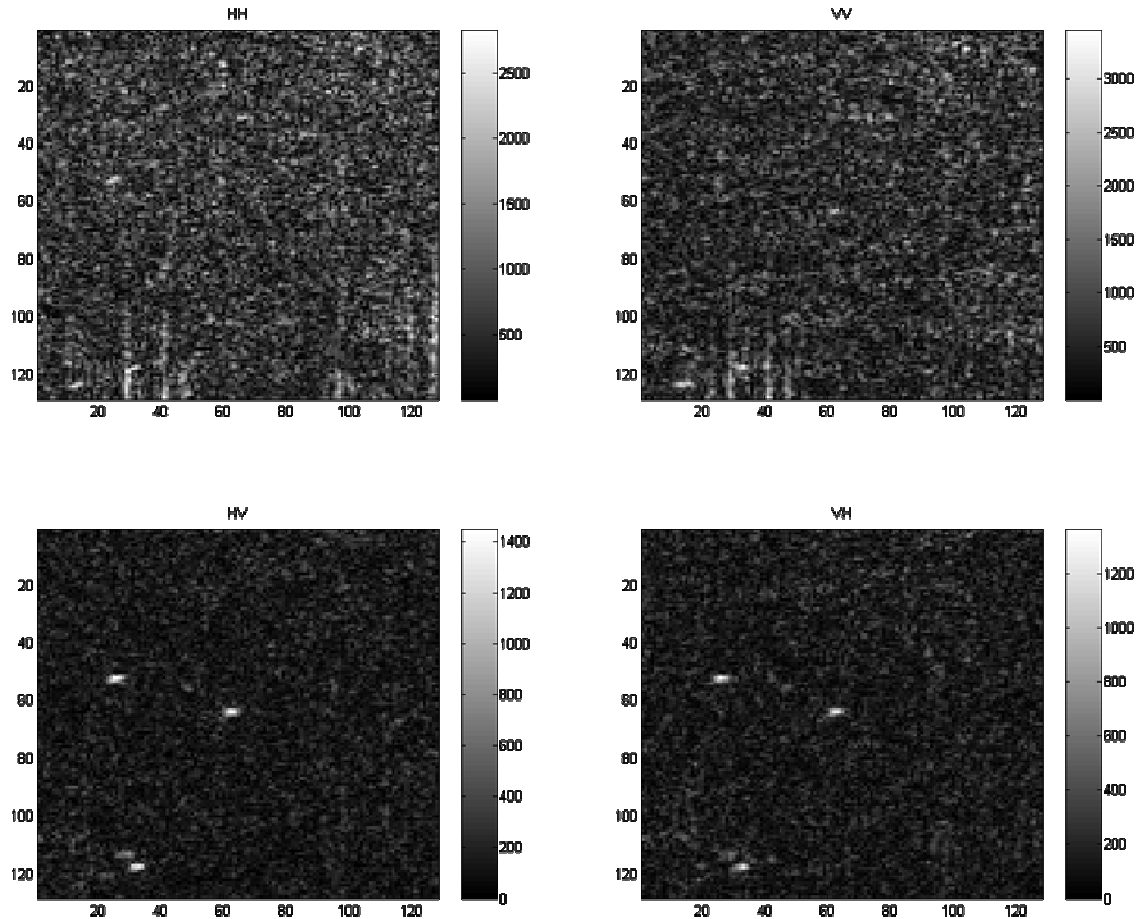


Figure 67. Intensity of the four polarization channels of an oceanic scene with three targets. The cross-polarized channels exhibit a higher target to clutter ratio.

Furthermore, simulated signatures following scattering models [123] anticipated that ships' signature is dominated by strongly polarized dihedral like mechanisms. Dihedrals are enhanced through the absolute value of the difference between both co-polar channels. For the set of data available, this hypothesis has been verified. As an example, the absolute value of the difference between the values of both co-polar channels for the same image considered before is represented in Figure 68.

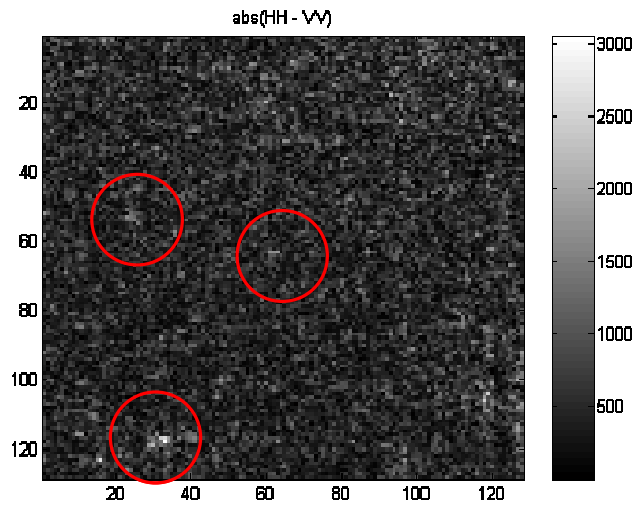


Figure 68. Enhancement of dihedral-like mechanisms by means of the difference between co-polar channels.

The second hypothesis considered involves the notion of polarization entropy. Theoretically, it is expected [119] [120] that polarization entropy constitutes an effective way of enhancing contrast between the ships and the ocean. This has been verified for the set of data considered, but it has been found that the contrast achieved is not sufficient in most of the cases. An example is shown in Figure 69 .The polarization entropy with a 5×5 pixel window is evaluated for the same image of previous Figure 67. It can be observed that targets are not enhanced in the resulting entropy image.

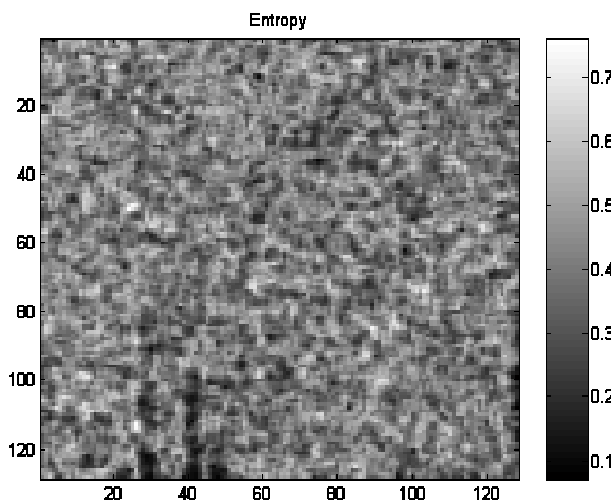


Figure 69. Polarization entropy with a 5×5 px. window for the image considered in previous Figure 67.

Once the theoretical hypotheses analyzed, a multiscale method will be proposed for the enhancement of the contrast between ships and background sea clutter in order to increase ship detectability. In previous section, the multiscale technique proposed for automatic ship detection has been adapted to be applied on dual polarized ENVISAT AP images. It has been shown that the availability of polarization diversity could be successfully exploited to improve ship detection rates. Following the same reasoning, two options are proposed for the extension of USEA to multichannel data (see Figure 70 and Figure 71).

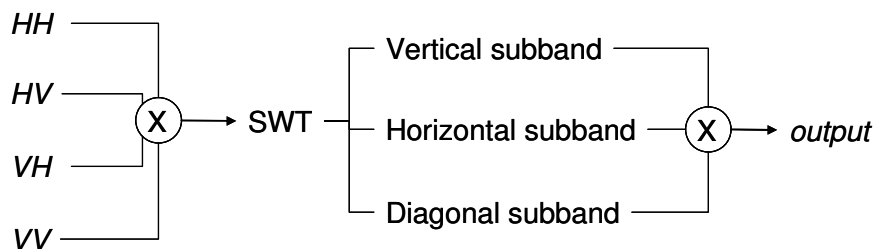


Figure 70. First option of extension of USEA to multichannel data.

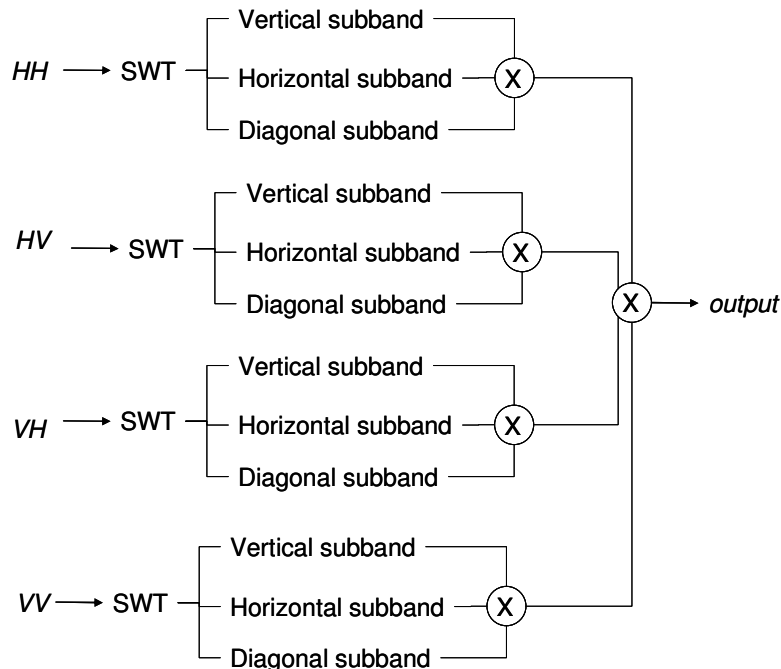


Figure 71. Second option of extension of USEA to multichannel data.

The first option (see Figure 70) consists on applying first the pointwise product to the four polar channels and then applying the algorithm proposed for spot enhancement in single channel to the result. The second option (see Figure 71) separately runs the method designed

on each polar component and then combines the results by means of a pointwise product. It is worth noting that the aim of this method, whatever the option selected, is to automatically increase, as much as possible, the contrast between the targeted ships and the surrounding sea in order to assure detection by means of further thresholding. For doing so, it takes advantage of the polarization diversity but it ignores the phase information.

The proposed approach for ship detection on full-Pol data will be tested on a set of RADARSAT-2 images of the area of Barcelona's harbor, in the Mediterranean Spanish coast, acquired on December 2008. In the scope of this chapter, the results obtained on two representative examples of target detection will be shown (see Figure 72 and Figure 74). Available groundtruth confirms the presence of the ships in the center of each scene selected. For each example, the increase of contrast will be evaluated for each option exposed previously and results will be compared with the polarization entropy with a 5×5 pixel window. The significance value, defined in section 4.3.2.2, is evaluated for each case. The examples considered have been chosen for they represent difficult situations of detection. In both examples, the target appears with a very low contrast mainly in the co-polar channels. Moreover, there are a lot of sea spikes in the background sea and this remains a major drawback for multipolarization ship detection, since sea spikes present dihedral like mechanisms, as vessels.

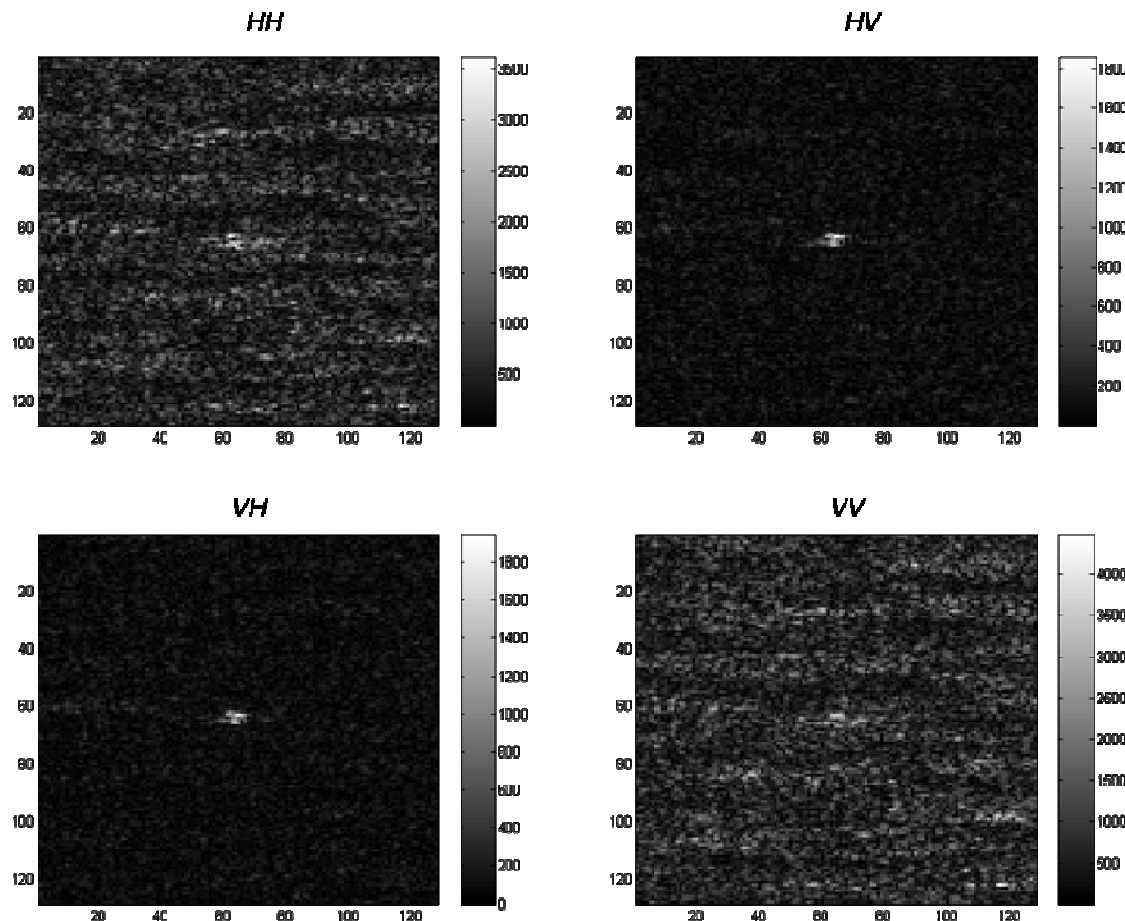


Figure 72. First example of ship detection situation.

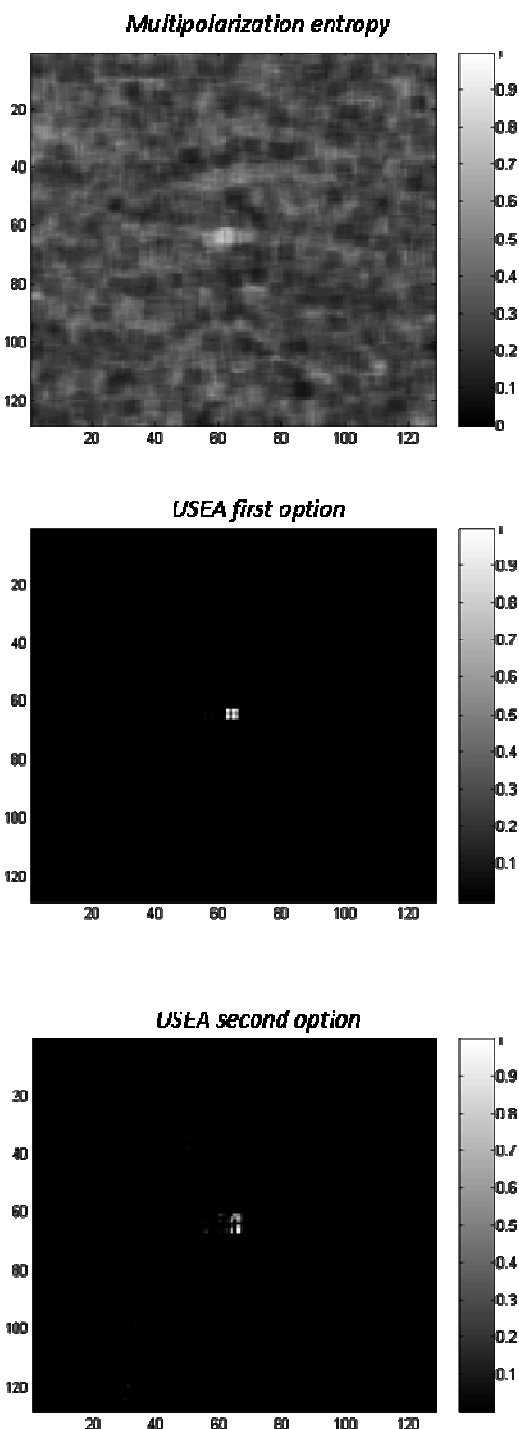


Figure 73. First example of ship detection situation. (top) Result of the multipolarization entropy, $s=5.9$. (second row) USEA, first option, $s=3.8 \cdot 10^7$. (third row) USEA, second option, $s=9.2 \cdot 10^9$.

It can be observed in Figure 73 that, even if the presence of the target is revealed in the resulting multipolarization entropy, the vessel to sea contrast achieved is not sufficient for an automatic detection. On the contrary, USEA enhances noticeably the target, whatever the option selected. Due to the high significances achieved, it can be considered that an automatic decision through thresholding is straightforward. Moreover, it is worth noting that sea spikes do not appear in the results. Similar observations are valid for the second example considered. A second example is presented in Figure 74 and in Figure 75.

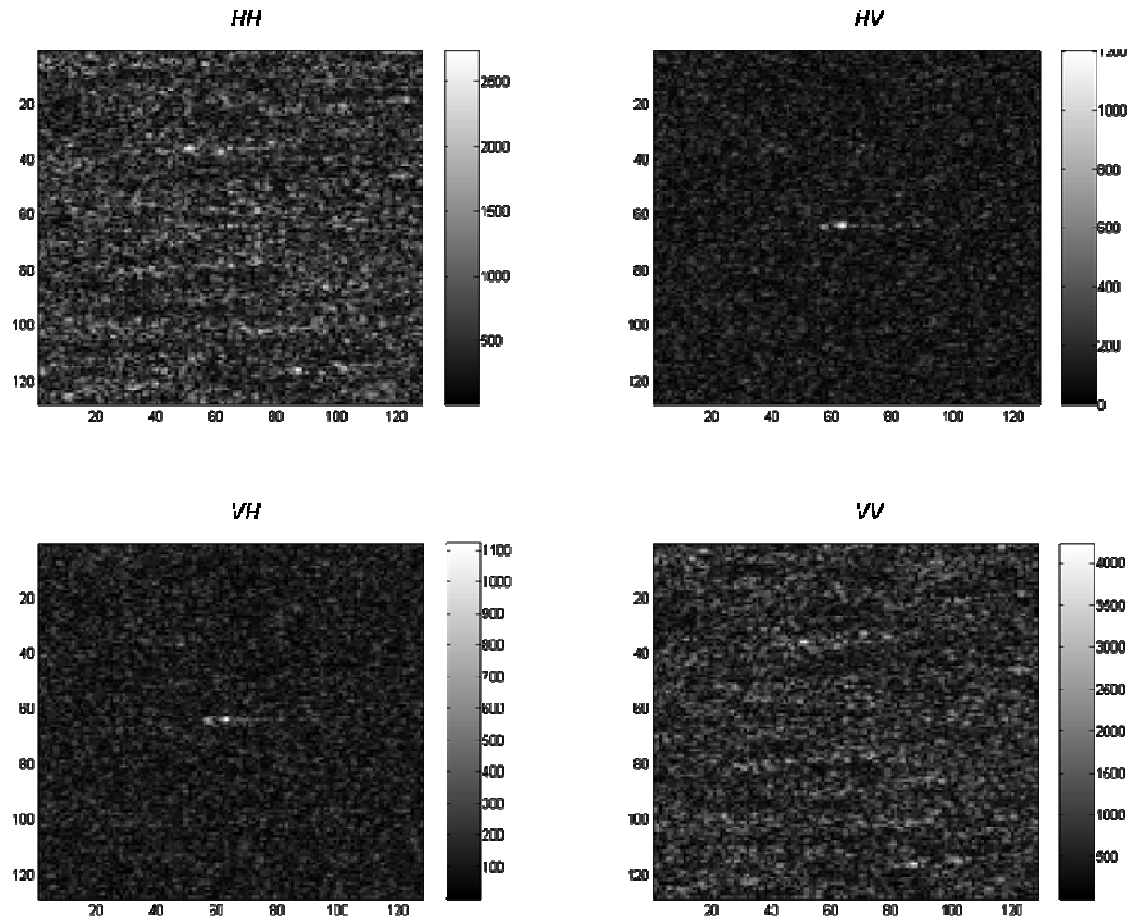


Figure 74. Second example of ship detection situation.

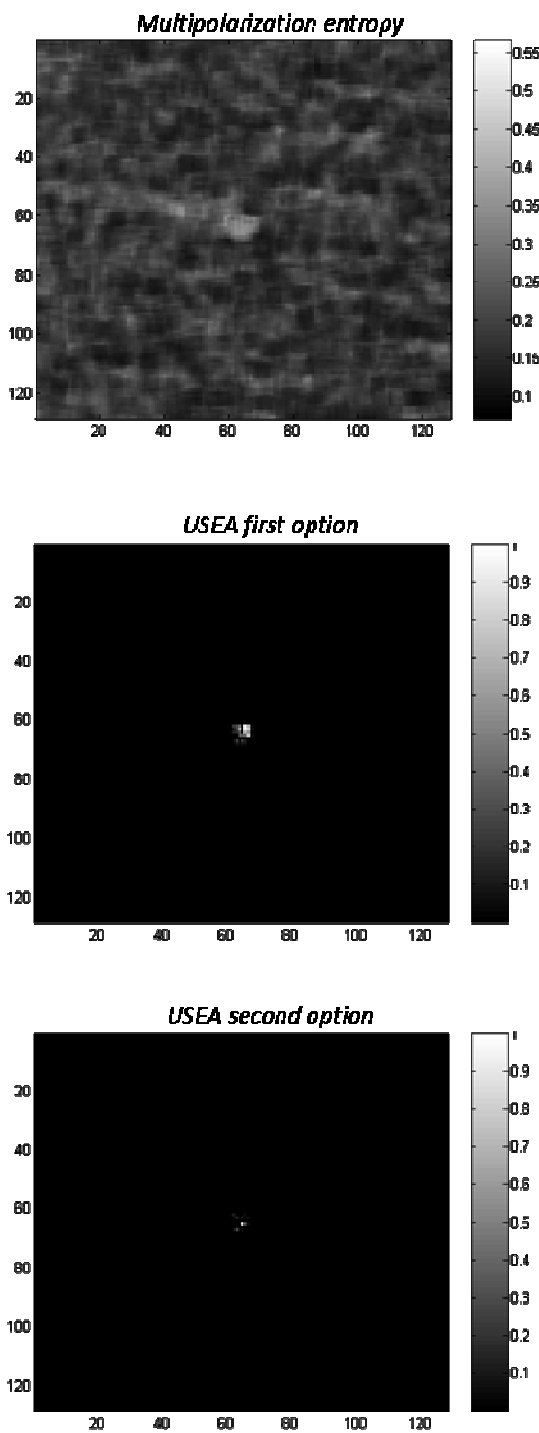
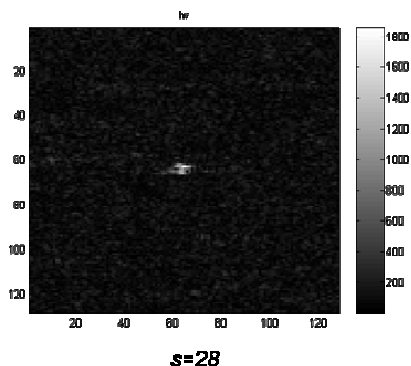


Figure 75. Second example of ship detection situation. (top) Result of the multipolarization entropy, $s=5.8$. (second row) USEA, first option, $s=6.8 \cdot 10^3$. (third row) USEA, second option, $s=5.0 \cdot 10^4$.

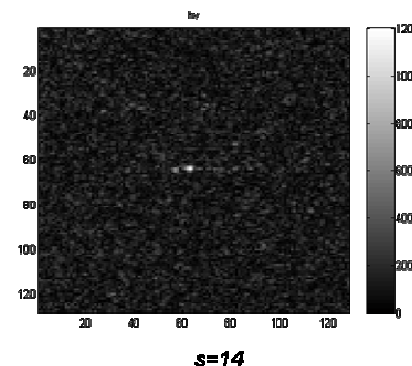
The usefulness of PolSAR data for ship detection purposes is still today a matter of discussion. Since different information appears in the different channels, an intelligent management of

the polarization channels can help in discarding false alarms in some particular cases. Moreover, the availability of polarization diversity permits enhancing the target to clutter ratio. Figure 76 compares for the two examples considered previously, the enhancement of contrast reached for the consideration of a single cross-polar channel with the one obtained by taking into account all the polarization channels. It can be observed that an enhancement of contrast of about 30 – 50 dBs is obtained when employing the polarimetric diversity with respect to the single channel case. Nonetheless, the contrast achieved in the single channel case is largely enough for a further automatic decision step. As a consequence, it should be carefully analyzed if polarimetric data obtained at the expenses of a reduction of the swath width is necessary for ship detection purposes.

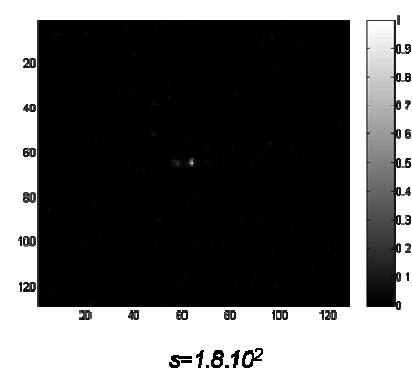
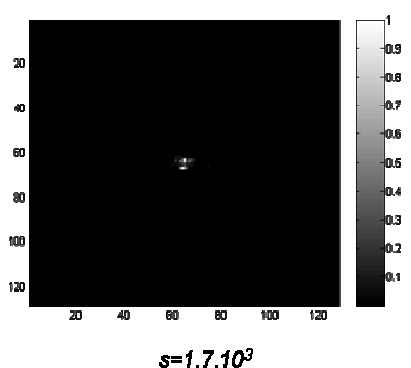
Example 1



Example 2



Output USEA for single channel data



Output USEA for PolSAR data

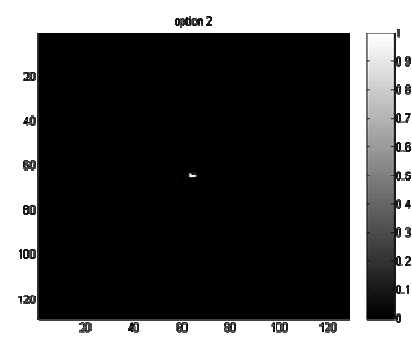
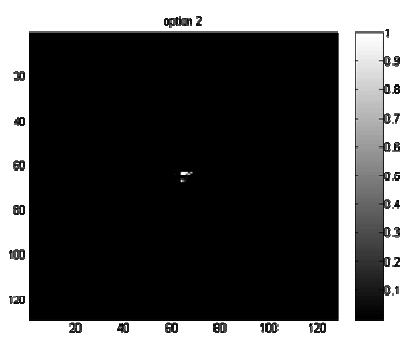


Figure 76. Comparison of contrast enhancement for single and multichannel data for two particular examples.

4.6 Conclusions

As seen in previous chapters, in order to handle efficiently the information content in an image, the elements with highest entropy are to be identified first. Due to their exceptionality, spots can reveal important hints about the structure of the data considered.

This chapter has identified the difficulties associated to automatic spot detection in SAR images. Then, based on this, a multiscale algorithm called USEA has been presented, based on an intrascale combination of wavelet coefficients. The algorithm is simple and not computationally costly. From the point of view of signal processing, the main originality of USEA is that, contrarily to conventional filters, it provides a qualitative result directly in the wavelet transformed domain. With this, thresholding of wavelet coefficients and further inversion, which are often problematic processes, are avoided. Furthermore, working directly in the wavelet transformed domain has several advantages. For instance, coefficients in the wavelet domain are sparse, following heavy-tailed distributions. Since the objective of spot detection is to enhance contrast between targets and background, this is particularly suitable. Moreover, almost independently of the kind of statistical distribution of the signal in the original domain, wavelet coefficients always follow the same type of statistical distribution. As a consequence, the unsupervised application of a threshold in the final decision step is easier and more effective after the application of USEA, since the statistical distribution of coefficients is well known in advance. Besides, it has been shown that the common assumption that considers the WT as a whitening process is simplistic in some situations. A residual correlation remains both between subbands in the same scale and at different scales. In the scope of this chapter, intrascale correlation has been exploited. It has been shown that it is very efficient to enhance the presence of localized isotropic patterns.

The performance of USEA has been first tested on simulated images. The algorithm has proven to be robust and effective at enhancing the presence of spots, even when they exhibit a low contrast with respect to the speckled background in the original image. The most noticeable effect of USEA is the high contrast achieved in most of the cases. This enlargement of contrast renders the final decision step trivial.

Then, it has been shown that ship monitoring in SAR images can be treated as a particular application of spot detection. Therefore, the algorithm has been tested on SAR maritime images and its operability for automatic ship detection purposes has been evaluated, comparing it to ground truth data when available, to the performance of other operational algorithms and to visual inspection. High rates of successful detection have been reached, with no false alarms. USEA has been then adapted to be applied to half and fully polarimetric data. It has been shown that polarimetric diversity improves ship detection capability. It has also been empirically proven that USEA overcomes for ship detection purposes the polarization entropy parameter. Nevertheless, the usefulness of fully polarimetric data for vessel monitoring still deserves further discussion.

The algorithm presented in this chapter is nowadays being exploited by the Spanish firm GMV [122] for border's security and control purposes. It has also been successfully used with optical imagery [124].

In the scope of ship monitoring, next step to be addressed is ship classification. Then, in a different direction, in the future, it would be worth testing the capabilities of the USEA in applications, other than ship detection in SAR images. In inland SAR data, USEA may be applied to the detection of permanent scatters. Due to its sensitivity, it is expected to be efficient for this purpose. Besides, USEA can be applied to biomedical data for example in the interpretation of mammograms.

After spots, edges and frontiers are the elements with highest entropy content in an image. They constitute the object of the following chapter.

Chapter 5. Automatic detection of linear features in SAR imagery

As mentioned previously, in order to handle the information contained in an image, the priority is to extract its overall structure. For doing so in an effective way, attention has to be drawn from the elements with a high to low entropy content. As a consequence, after spot detection treated in previous chapter, edge detection is to be addressed next.

Edges of structures in images are very often the most important features for pattern recognition. For instance, we can identify an object from a rough outline of its contours. Nevertheless, the definition of edge is cumbersome. According to the common sense definition, an edge is understood as the separation between two adjacent solid surfaces. Therefore, edges do not exist as real entities; the concept is a mere entelechy. In an image processing context, in an attempt to translate the common sense definition to machine interpretable terms, an edge could be defined as points where the image intensity has sharp transitions. Nevertheless, image textures can contain themselves sharp intensity variations which are not considered as edges. As a matter of fact, once again, the discrimination of edges versus textures depends on the scale of analysis and hence a useful definition has to be considered as application dependant. Moreover, in images constituted by pixels, the definition of edge is not unambiguous, since ideally the edge is an infinitely narrow area between two regions and this concept has no correspondence in the discrete domain. Therefore, ideally an edge would be exactly the region between two pixels. Since this notion lacks of sense in

practice, the pixel classified as edge should be the nearest one to the edge, but there are always at least two pixels equally distant to the frontier between regions.

Automatic schemes for edge extraction rely on two steps: first one is edge enhancement and the second one is edge labeling. Due to speckle, edge enhancement is particularly crucial in SAR images. The main original contribution of this chapter is a multiscale edge enhancement technique. After reviewing the state of the art in section 5.1, the algorithm designed for automatic edge enhancement in SAR imagery will be presented in Section 5.2. Section 5.3 introduces the final edge labeling step and presents results of the overall chain detection chain on simulated and real data.

5.1 Preliminary considerations

5.1.1 Main drawbacks and state of the art

In a computerized scheme, in essence, edge detection is to be reached in two steps: edge enhancement and edge labeling (see Figure 77). Unlike optical imagery, in SAR data, which is highly heterogeneous, a robust edge enhancement phase is critical in order to provide acceptable detectability rates.

The edge enhancement stage consists of highlighting as much as possible the presence of edges with respect to background. As a result, after edge enhancement, pixels corresponding to the position of an edge should have high values, in contrast to “non edge pixels” that should present an intensity as low as possible. Moreover, in order to assure a correct performance of the subsequent edge labeling step, “edge pixels” should be aligned as much as possible along the edge line and they should not be sparse and isolated from each other. Edge enhancement is usually performed through techniques applying derivation (simple differences, Canny and Sobel filter [1], Prewitt filter [126] [127], morphological gradients...), eventually combined with smoothing. A special attention should be given to traditional Canny filter.

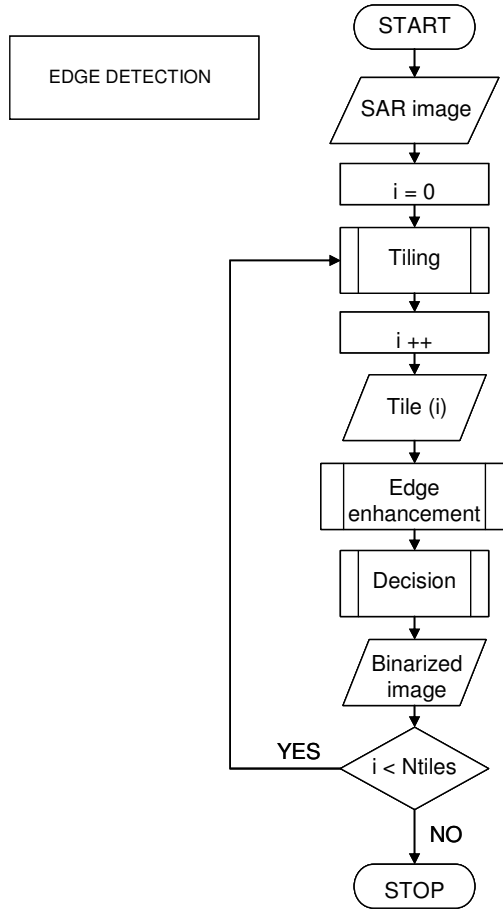


Figure 77. Flowchart of the overall edge detection chain.

- **Canny Edge Detection**

The Canny algorithm [128] enhances sharp variations in the analyzed image $f(x_1, x_2)$ by calculating the modulus of its gradient vector

$$\vec{\nabla}f = \left(\frac{\partial f}{\partial x_1}, \frac{\partial f}{\partial x_2} \right). \quad (5.1)$$

The partial derivative of f in the direction of a unit vector $\vec{n} = (\cos \alpha, \sin \alpha)$ in the $x = (x_1, x_2)$ plane is calculated as an inner product with the gradient vector

$$\frac{\partial f}{\partial \vec{n}} = \vec{\nabla}f \cdot \vec{n} = \frac{\partial f}{\partial x_1} \cos \alpha + \frac{\partial f}{\partial x_2} \sin \alpha. \quad (5.2)$$

The absolute value of this partial derivative is maximum if \vec{n} is colinear to $\vec{\nabla}f$. This implies that $\vec{\nabla}f(x)$ is parallel to the direction of maximum change of the surface $f(x)$. With this, a point $y \in \mathbb{R}^2$ is defined as an edge if $|\vec{\nabla}f(x)|$ is locally maximum at $x=y$ when $x = y + \lambda \vec{\nabla}f(y)$ for $|\lambda|$ small enough.

- **Multiscale Canny Edge Detection**

A multiscale version of the Canny edge detector was proposed by [71]. Let's suppose a convolution kernel $\theta(x)$ and two wavelets ψ^1 and ψ^2 which are the partial derivatives of θ :

$$\psi^1 = -\frac{\partial \theta}{\partial x_1} \text{ and } \psi^2 = -\frac{\partial \theta}{\partial x_2}. \quad (5.3)$$

We consider a dyadic transform and we denote $x = (x_1, x_2)$. With this:

$$\psi_{2^j}^k(x_1, x_2) = \frac{1}{2^j} \psi^k\left(\frac{x_1}{2^j}, \frac{x_2}{2^j}\right) \text{ and } \bar{\psi}_{2^j}^k(x) = \psi_{2^j}^k(-x). \quad (5.4)$$

These edge enhancement methods, specifically conceived to deal with signals with additive noise, provide limited efficiency in SAR applications, due to the presence of speckle which is a multiplicative noise-like pattern: a significant increase in intensity in the useful signal is intrinsically accompanied by a local increase in speckle power. As a consequence, the derivation produces an enhancement of speckle eventually hiding the difference of intensity in the meaningful part of the signal (see Figure 78).

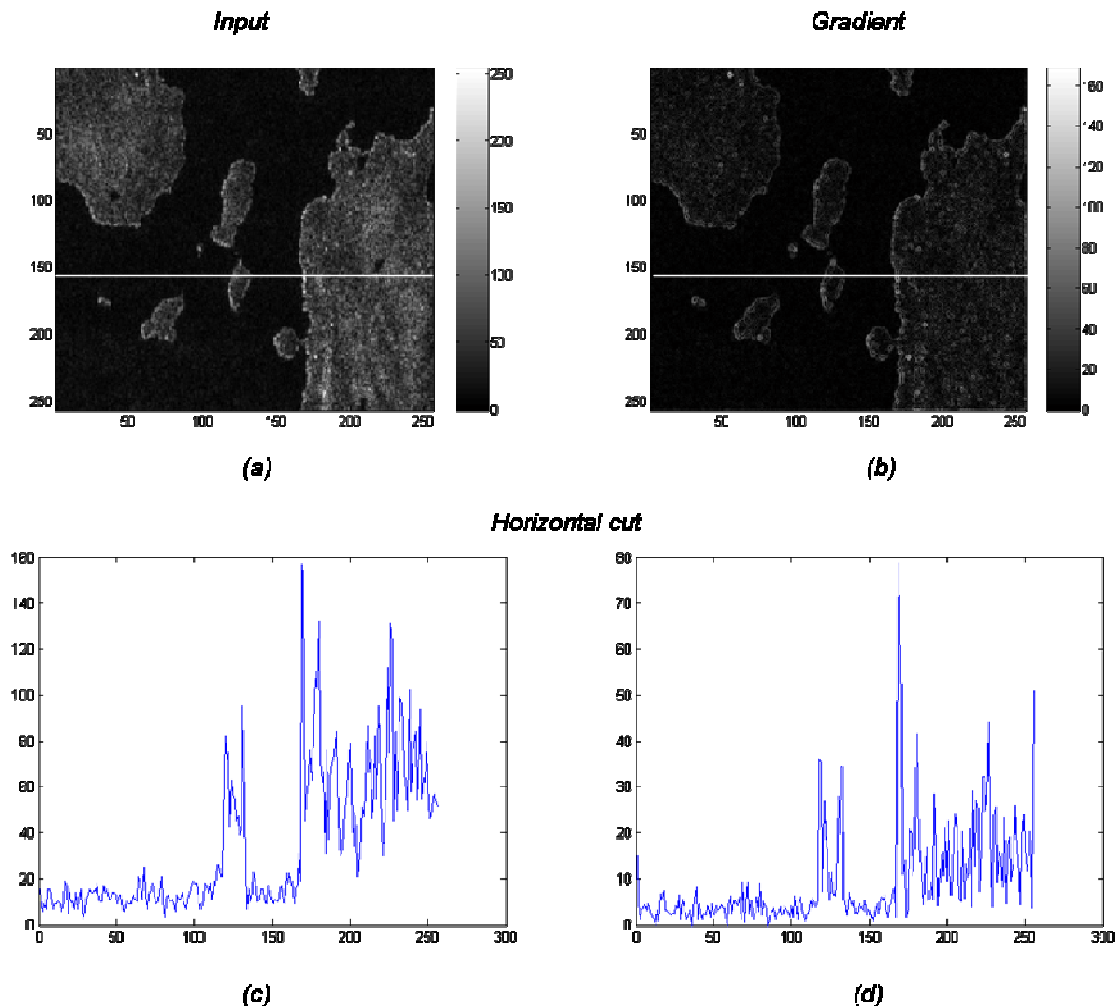


Figure 78. (a) SAR scene of a coastal area and (c) plot of a horizontal cut. (b) Image resulting from applying the gradient to the original scene and (d) plot of a horizontal cut.

The main original contribution of this chapter is the presentation of a specific algorithm for edge enhancement in SAR imagery, based on a combination of wavelet coefficients. It will be called Unsupervised Edge Enhancement Algorithm, UEEA in the following. In the general signal processing literature, several multiscale approaches, relying on the analysis of the information contained in the wavelet domain, have been proposed [130] [131] [132] [133]. UEEA is different as it does not assume any a priori information of the input data, e.g. any nature of statistical distribution, nor a particular type of edge. The non assumption of particular features of the input signal makes avoids the need of preliminary settings and makes it more flexible and suitable to SAR scenarios, subject to a great variability. Moreover, similarly to USEA, the technique for spot detection presented in the previous chapter, it envisages the segmentation directly in the transformed domain, thus saving computational cost and eventual artifacts due to inversion. Further differences with existing algorithms will be highlighted throughout the Chapter. In the specific scope of SAR, in [133], an interesting review of existing edge detection algorithms is provided. A group of techniques is based on the evaluation of a ratio of averages

over a sliding window or region growing techniques ([134] [135] [136] [137]). Such type of methods present a low computational load, but they are highly dependent on the dimensions of the window and they are not robust in noisy scenes. Another group of algorithms is based on the wavelet theory. For instance, in [138] [139], an edge detector is proposed based on a threshold operation of wavelet coefficients. Despite a low computational cost and a good contrast, edge thickness is too high which gives poor precision in its location.

5.1.2 Application of the logarithm transform

It has been seen in Chapter 2 that when dealing with the analysis of SAR images, one of the most problematic issues is the multiplicative aspect of speckle. For instance, in signal estimation, it is more difficult to handle multiplicative noise factors than additive ones, since in the first case, useful and useless information are intimately mixed together. As a consequence, we propose converting the multiplicative scheme into an additive one by means of the application of the logarithm (homomorphic transform) [140]:

$$\log(I) = \log(\sigma n) = \log(\sigma) + \log(n). \quad (5.5)$$

If no spatial correlation is considered, speckle transformed this way is additive and signal independent and its probability density distribution is approximately Gaussian. Figure 79 represents a simulated speckle matrix and the result of applying the logarithm transform to it, as well as the corresponding histograms of both of them.

It is worth mentioning that, in the following, in order to avoid the logarithm of zero, a constant value is added to the whole image before the application of the logarithm. This amplitude shifting has no effect in the observations made in the scope of this chapter.

The application of the logarithm transform permits disentangling speckle effects and useful information content of the data. Moreover, the logarithm is helpful in reducing the large dynamic range of SAR data. In the SAR community, there exist opinions reluctant to the use of the logarithm previous to the analysis of SAR data. Actually, the logarithm is a non-linear transformation not integrable and the inversion of logarithmically transformed images can produce artifacts. For inversion purposes, such as precise retrieval of the scattering properties of the illuminated scene, this fact can be difficult to manage. Nevertheless, it is worth noting that this Chapter is concerned with automatic segmentation issues, searching qualitative results rather than quantitative measures. Therefore, the application of the logarithm is not problematic in that case and it is particularly useful when dealing with edge enhancement.

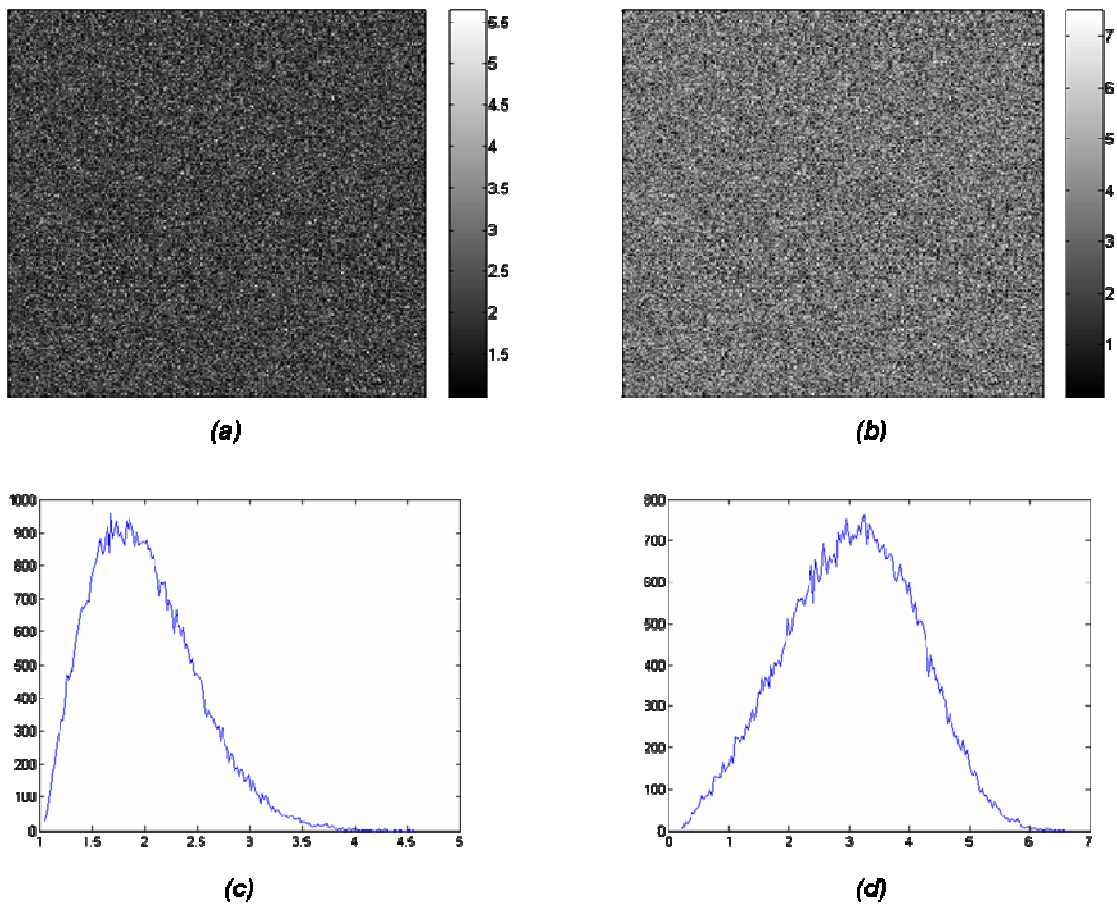


Figure 79. (a) Simulated speckle intensity matrix and (c) corresponding histogram. (b) Logarithm transform of the simulated speckle intensity matrix and (d) corresponding histogram.

The effect of the application of the logarithm on SAR imagery is illustrated hereafter through a simulated 1D signal. This signal is generated as follows. First, an array of 256 samples is created as simulating amplitude of speckle such as the modulus of a vector whose both real and imaginary parts are random elements, normally distributed with zero mean and variance equal to 0.5. Then, the value of a central portion of the array is doubled. Figure 80 displays the simulated 1D signal generated, as well as its logarithm transform. The effect of the logarithm can be appreciated on the signal. Even if the standard deviation of the noise like component is increased, speckle turns from a multiplicative into an additive noise like pattern, in such a way that its standard deviation is less dependent on the amplitude of the useful component of the signal: low amplitude parts of the signal exhibit a noise-like component with an energy level comparable to high amplitude ones. As a consequence, useful and useless components of the signal are separated. In the specific example shown in Figure 80, the standard deviation of the low intensity pixels is approximately 0.64 in front of 3.06 for the high intensity pixels (almost five times that of the low intensity region). After the application of the logarithm transform, the standard deviation of the low intensity pixels is of 5.8 in front of 6.8 for the high intensity pixels: the standard deviation can be considered almost the same in both regions.

Nevertheless, it can be noticed that the logarithm transform is not sufficient to enhance the presence of edges by means for example of a direct gradient operation: at first sight, edges do not appear more distinguishable in the logarithm transformed signal than in the original one.

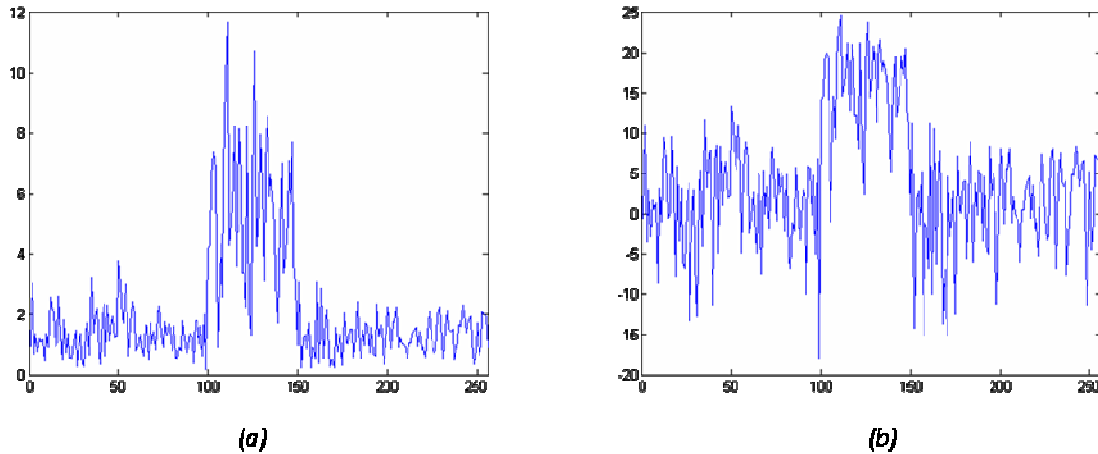


Figure 80. (a) Intensity of a simulated 1D signal of a step embedded in multiplicative speckle and (b) its logarithm transform.

In parallel, a space / scale representation of the signal is estimated through the SWT with a Haar mother wavelet (see Figure 81). It can be observed how the edges of the region whose values have been doubled are enhanced at highest scales corresponding to low frequencies. The effect of the logarithm transform is also observable on the space / scale representation of the signal. Figure 81 presents the space / scale decomposition of the 1D simulated signal in Figure 80 together with the space / scale decomposition of its logarithm transform. The enhancement of the frontiers of the step signal in high scales can be appreciated in both cases through peaks in the bottom of the time / frequency plane corresponding to low frequencies. Hence, the multiscale decomposition permits the localization of meaningful edges, difficult to discriminate in the input signal. Moreover, the time / frequency representation reveals the main advantage of using the logarithm transform. Figure 81 (bottom) represents a cut of the wavelet decomposition at a particular scale (scale 4). In the multiscale decomposition, added to the dominant peaks due to the presence of meaningful discontinuities in the signal, a number of local maxima produced by the noise component appear. Nonetheless, the standard deviation of these useless local maxima in the decomposition of the simulated signal, with no application of the logarithm transform, is not homogeneous: there are higher peaks in the location of the step than outside. On the contrary, in the decomposition of the logarithm transformed signal, peaks have the same maximum amplitude everywhere. As a consequence, edge detection can be performed independently of the local amplitude of the input signal. This feature is extremely important for edge detection purposes.

Previous observations suggest the interest of using the logarithm operation combined to a multiscale approach for automatic edge enhancement purposes.

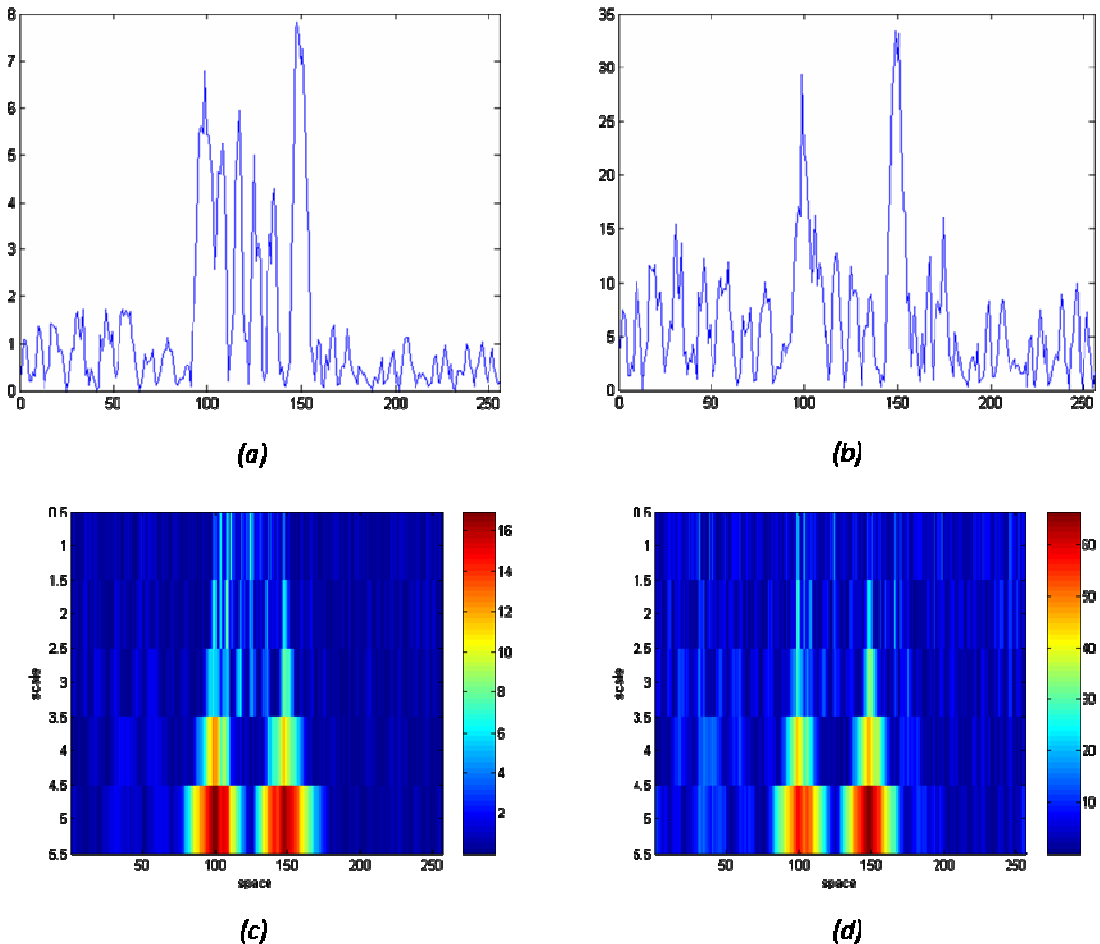


Figure 81. (a) Simulated 1D simulated signal and (b) its logarithm transform (right). (c) and (d) Corresponding space/scale representations.

5.2 Algorithm designed for automatic edge enhancement on SAR imagery

5.2.1 Theoretical principles

The algorithm for edge enhancement in SAR imagery proposed in this chapter, UEEA, relies on the difference of behavior along wavelet scales of speckle in front of edges. This effect is introduced by means of a simulated example in Figure 82. Both for a simulated 1D speckle signal (see Figure 82, (b)) and for a simulated 1D step (see Figure 82 (a)), the time-frequency representation is represented (computed by means of the SWT with a Haar wavelet) (see

Figure 82 (c), (d)). Then, the mean of the correlation across scales is evaluated at each point (see Figure 82 (e), (f)). The differences between useful signal and speckle are observed.

On the one hand, the meaningful discontinuities are highlighted by the WT and they tend to persist over scales as it has been discussed in Chapter 3. This effect can be observed in the time – frequency representation of the 1D step signal: the flanks of the step appear in the time – frequency representation as local maxima at every scale (see Figure 82, (c)). Moreover, the correlation between scales is high at these points as it can be observed from Figure 82, (e): the peaks of correlation appear exactly at the location of the edges.

On the other hand, speckle is progressively smoothed through scales: values at the bottom of the time – frequency representation corresponding to high scales (low frequencies) are lower than the ones at the top corresponding to low scales (high frequencies) (see Figure 82, (d)). Moreover, speckle is almost spatially uncorrelated between scales, as noticed in Figure 82, (f).

Let us analyze and justify in detail this difference of behavior. As seen previously, the WT can be expressed as

$$Wf(a,b) = \int_{-\infty}^{\infty} f(x) \frac{1}{\sqrt{a}} \psi^* \left(\frac{x-b}{a} \right) dx. \quad (5.6)$$

In the framework of this chapter, we will use the Haar wavelet, which can be expressed as

$$\psi(t) = \begin{cases} 1, & 0 \leq t < \frac{1}{2} \\ -1, & \frac{1}{2} \leq t < 1 \\ 0, & \text{otherwise} \end{cases} \quad (5.7)$$

With this:

$$Wf(a,b) = \frac{1}{\sqrt{a}} \int_b^{a/2+b} f(x) dx - \frac{1}{\sqrt{a}} \int_{a/2+b}^{a+b} f(x) dx. \quad (5.8)$$

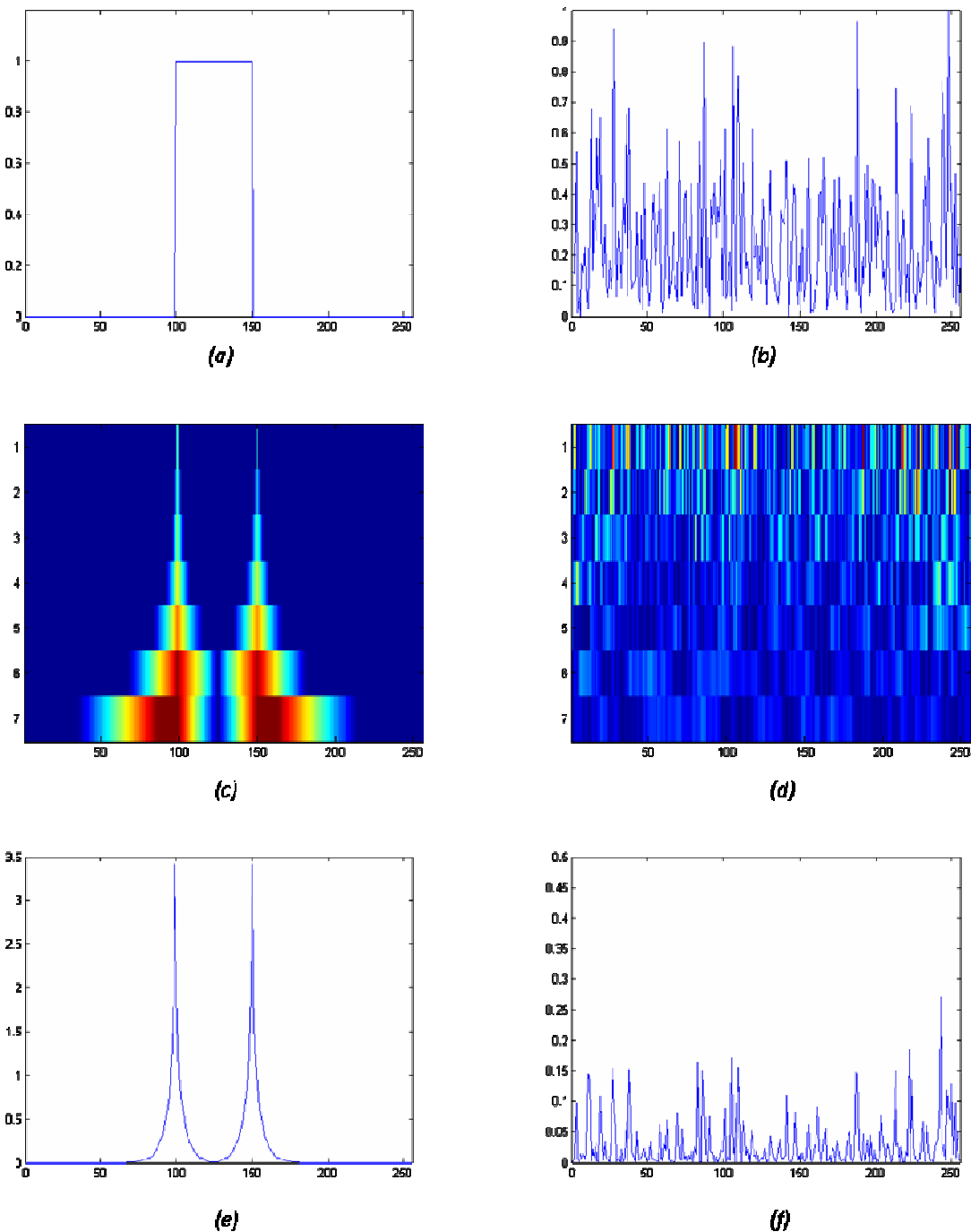


Figure 82. Multiscale time – frequency behavior of a simulated step signal (a) and of a simulated 1D speckle signal (b). (c) and (d) are the respective scale / space representations (obtained through the SWT with a Haar mother wavelet). (e) and (f) represent the mean of the correlation across scales for each point.

If, as seen in Section 5.1.2, the logarithm of the signal is taken in order to manage multiplicative speckle, it can be supposed:

$$f(\tau) = \log(\sigma(\tau)n(\tau)) = \log(\sigma(\tau)) + \log(n(\tau)) \quad (5.9)$$

where n stands for speckle and σ represents the useful information content of the radar signal.

Hence:

$$Wf(a,b) = \frac{1}{\sqrt{a}} \int_b^{a/2+b} [\log(\sigma(x)) + \log(n(x))] dx - \frac{1}{\sqrt{a}} \int_{a/2+b}^{a+b} [\log(\sigma(x)) + \log(n(x))] dx \quad (5.10)$$

$$Wf(a,b) = \frac{1}{\sqrt{a}} \left[\int_b^{a/2+b} \log(\sigma(x)) dx - \int_{a/2+b}^{a+b} \log(\sigma(x)) dx \right] + \frac{1}{\sqrt{a}} \left[\int_b^{a/2+b} \log(n(x)) dx - \int_{a/2+b}^{a+b} \log(n(x)) dx \right]$$

As a consequence, the WT can be seen as the addition of the difference between the averaging of the curves corresponding to the useful part of the signal and to speckle over two adjacent intervals of same duration. The length of these intervals is determined by the difference between the limits of the integral. Therefore, in both cases, this length is directly the half of the scale, $a/2$. In general terms, if the function is homogeneous along both intervals, the absolute value of the difference will be low. On the contrary, if there is a discontinuity in the trend of the curve, it will increase. Moreover, the maximum of this difference occurs when the discontinuity happens just in the frontier between the intervals. Hence, in the WT of the logarithm of the SAR signal, the influence of speckle is low, since its contribution in each of the semi-intervals counteracts with the other:

$$\begin{aligned} & \int_u^{s/2+u} \log(n(\tau)) d\tau - \int_{s/2+u}^{s+u} \log(n(\tau)) d\tau \approx 0 \\ \Rightarrow Wf(a,b) & \approx \frac{1}{\sqrt{a}} \left[\int_b^{a/2+b} \log(\sigma(x)) dx - \int_{a/2+b}^{a+b} \log(\sigma(x)) dx \right]. \end{aligned} \quad (5.11)$$

It is worth noting that this value is especially low when the interval is large (i.e. high scales at the bottom of the time / frequency representation in Figure 82) since a large interval permits to have a sufficiently representative number of samples of the stochastic speckle process. In that case, if simplifying, the absolute value of the transform accounts for the difference of homogeneity of the useful part of the signal (speckle free) between both subintervals.

The previous mathematical development can easily be extended to any other type of mother wavelet. Nevertheless, it can be noticed that the effects observed, particularly the approximation in **¡Error! No se encuentra el origen de la referencia.** are conditioned to the anti-symmetry of the mother wavelet.

When considering a single scale of the WT, it can be observed in **¡Error! No se encuentra el origen de la referencia.** that the size of the interval influences the capability of the WT both to localize the precise position of the edge and to be unaffected by speckle. In a large interval size (equivalently, in a large scale) the effect of the averaging is more important and the presence of speckle is thus better nullified through the counteraction of both integrals. Nevertheless, in that case, the higher sensitivity in the detection of the discontinuity is obtained at the expense of a lower precision in the estimation of its location. Since this trade-off is inherent to a time-frequency decomposition, it is unavoidable by taking into account just a single scale. We propose instead a combination of several scales in order to take profit of the good performance in resolution of the lower ones and sensitivity to the presence of discontinuities of the higher ones.

In order to take advantage of the difference of local correlation across scales between the edge and speckle, the combination is performed through interscale pointwise product which permits taking advantage simultaneously of the benefits of the span of scales considered. Low values of speckle achieved with intervals with large lengths reduce through multiplication the higher values present in higher scales. Moreover, due to their spatial co-occurrence, local maxima due to a discontinuity contribute constructively, when multiplying the scales. Since the energy due to the irregularity of the signal is mainly located at low scales, the resolution of fine scales is preserved. Furthermore, while discontinuities due to speckle do not persist, the ones produced by the presence of a meaningful edge appear tend propagate over scales. As a consequence, interscale pointwise product neglects small isolated discontinuities. In [130], statistical characteristics of the multiscale product are analyzed. It is shown that additive Gaussian noise is uncorrelated between scales and that the resulting distribution of probabilities is generally non-Gaussian heavy tailed.

Based on these observations, the algorithm exposed in Figure 83 is proposed. At each iteration of the SWT in 2D, added to a low pass filtered version of the input signal, three bandpass components are obtained, each one enhancing discontinuities in a different direction. After normalizing each of these subbands to their maximum and taking their absolute value, the pointwise maximum is evaluated. Since the components in the same scale are uncorrelated, taking the maximum value permits avoiding as much as possible speckle (contrarily to an intrascale combination with the sum such as in [132]). The same operation is carried out with different scales. Then, the different intermediate maxima calculated previously are combined through pointwise multiplication. The effect of the pointwise product is to reflect the spatial correlation between components. If the spatial correlation is high, the result of the pointwise product will be so. Moreover, it has been already observed that the presence of a significant edge contrarily to local maxima due to background clutter is transmitted over scales. As a consequence, the spatial correlation between scales is high for edges and low elsewhere.

If necessary and if some kind of a priori information is available, the number of iterations can be adjusted accordingly. Otherwise, in the current situations of the applications focused in the scope of this dissertation, five iterations suffice to provide satisfactory results.

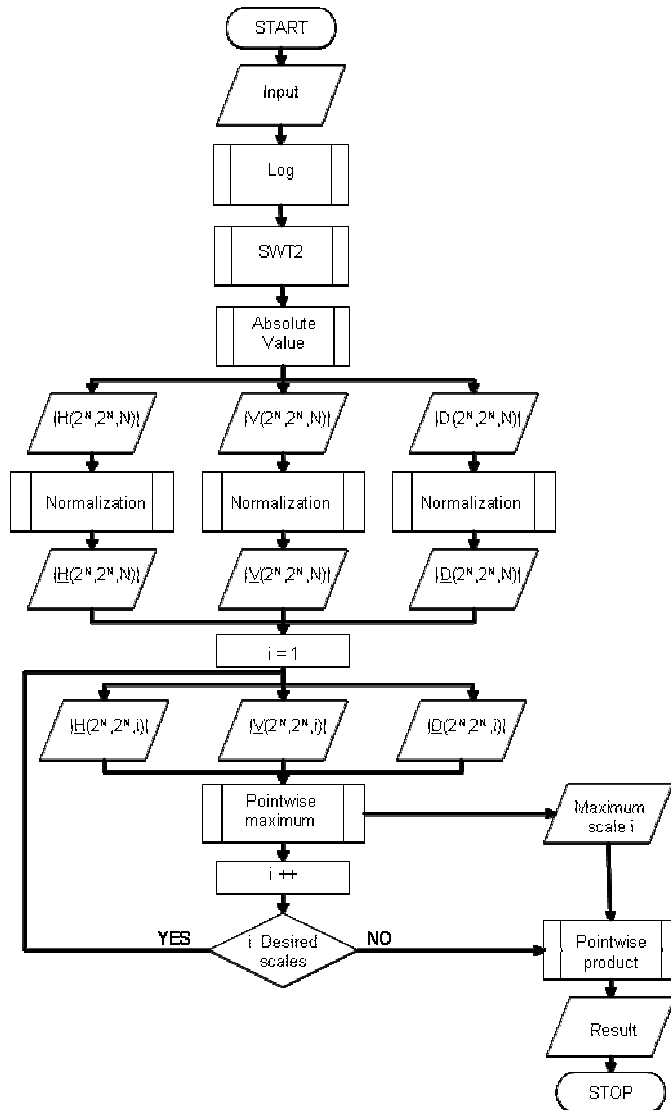


Figure 83. Flowchart of UEEA.

5.2.2 Detailed example of operation in a simulated image

A detailed example of application of UEEA in a simple simulated image is shown hereafter. The image is a speckle matrix $S(x, y)$ in which a square with an increased intensity has been embedded (see Figure 84). The intensity in the square has been augmented through multiplication with a constant value m :

$$I(x, y) = m \cdot S(x, y) \text{ with } m \in \mathbb{R}. \quad (5.12)$$

In the example treated in this section $m=5$. The speckle amplitude matrix has been generated as the modulus of a matrix whose both real and imaginary parts are random

elements, normally distributed with zero mean and variance equal to 0.5. A horizontal cut of the image has been included. Once again, from its observation, the inefficiency of performing edge enhancement by means of gradient evaluation can be deduced. Furthermore, multiplicative nature of speckle is appreciable: the intensity of noise-like pattern increases with the intensity of the information. After the application of the logarithm transform, the multiplicative behavior turns into an additive one and therefore the intensity of speckle is less dependent on the intensity of the useful part of the signal (see Figure 85).

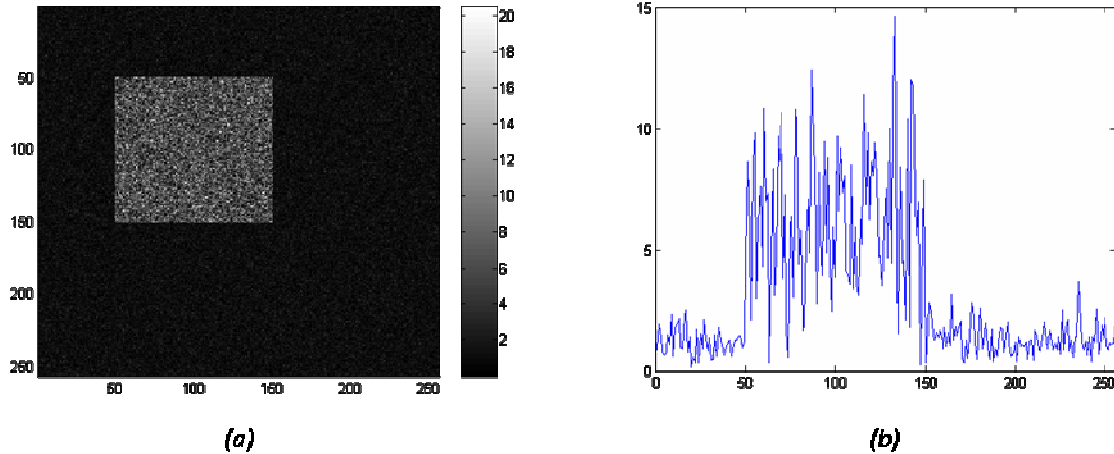


Figure 84. (a) Simulated image constituted by a square embedded in a speckle matrix and (b) horizontal cut.

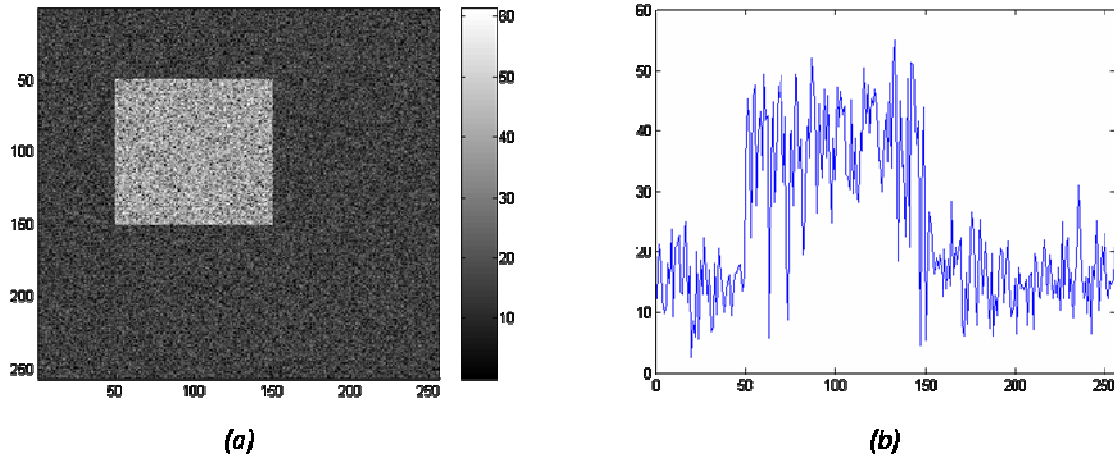


Figure 85. (a) Logarithm transform of the simulated image in Figure 84 and (b) horizontal cut.

The application of the SWT results in a lowpass and three bandpass components for each scale. Each of the bandpass subbands enhances details at a different orientation: horizontal,

vertical and diagonal. Figure 86 shows the absolute value of the bandpass wavelet components at three different scales.

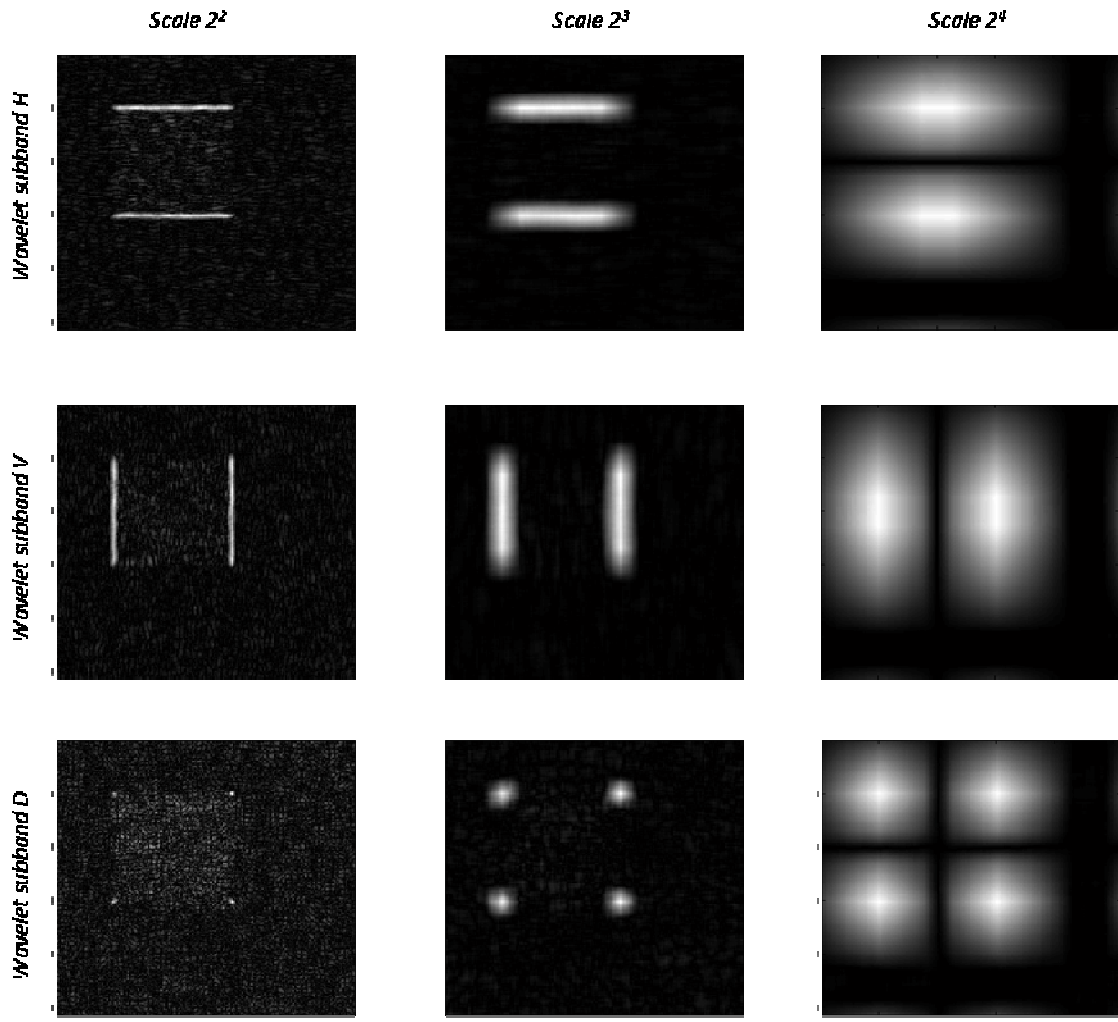


Figure 86. Absolute value of the bandpass wavelet components at three different scales.

Then, at each iteration, the pointwise maxima of the absolute value of the normalized subbands is evaluated. The corresponding pointwise maxima calculated from the subbands displayed in Figure 87. The effect of the trade-off between resolution and signal to noise ratio, discussed previously can be observed. In the three images, the presence of the borders of the square has been effectively enhanced. Nevertheless, at the fifth scale, the contrast between the edge and the background is noticeably more important than in the lower scale: signal to noise ratio increases with scale. On the other way, frontiers are progressively blurred: resolution decreases with the scale.

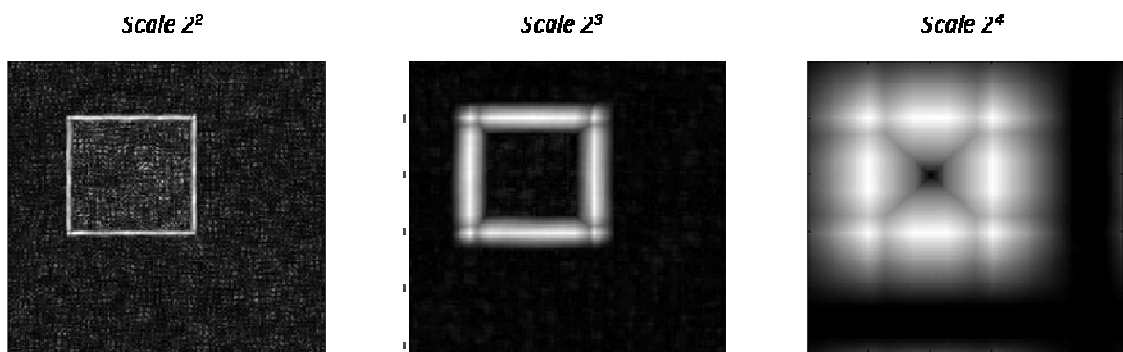


Figure 87. Pointwise maxima of the absolute value of the bandpass wavelet components at three different scales.

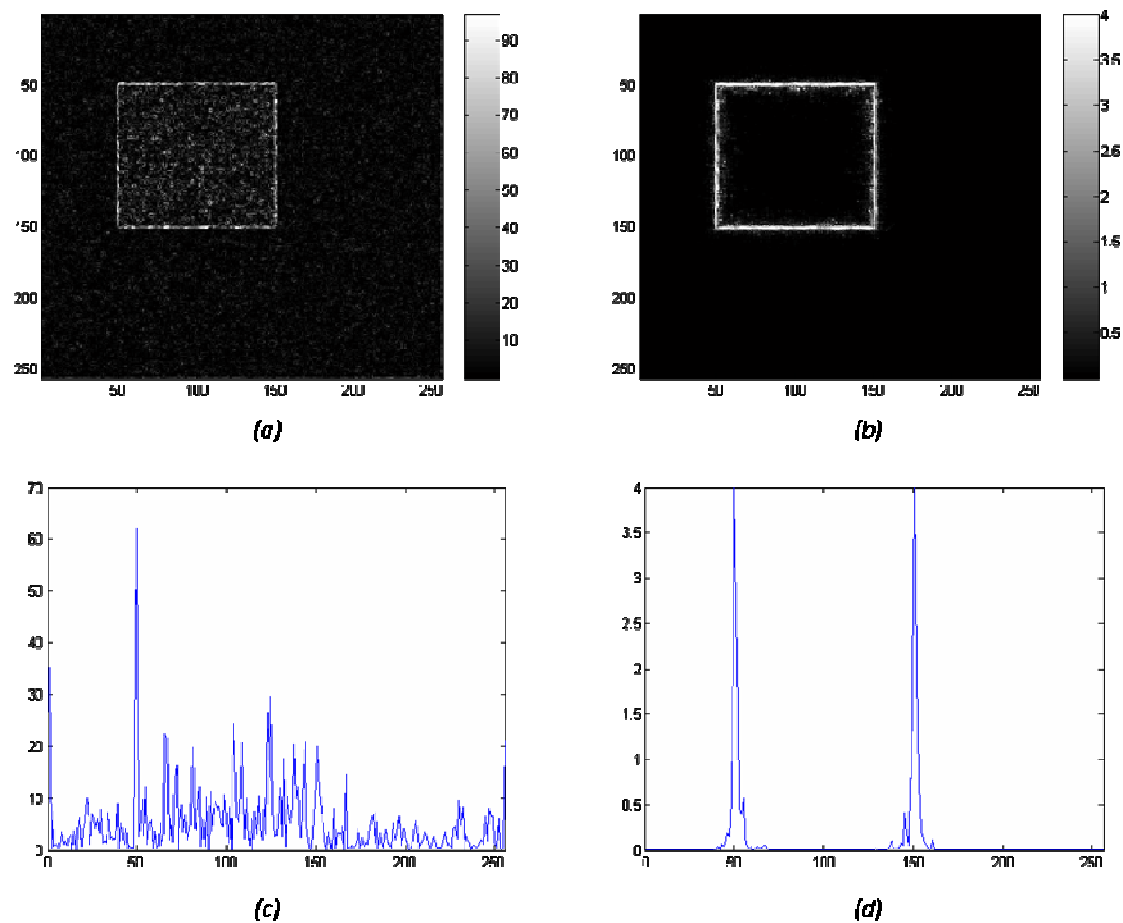


Figure 88. Edge enhancement of the simulated image. (a) Output of the Sobel filter and (c) horizontal cut. (b) Output of UEEA and (d) horizontal cut.

The multiscale pointwise product conciliates these two benefits, aiming to overcome the time frequency trade-off inherent to the wavelet decomposition. Figure 88 shows the result of the application of UEEA on the simulated image in Figure 84, compared to the result obtained by means of the Sobel filter. The contour of the square appears neatly in the output of the proposed algorithm. The horizontal cut superimposed to the output image reflects the enhancement of contrast achieved between the edge and the surrounding background.

The square shape presented in the previous examples is useful for illustrative purposes but it may be thought too simple. Hence a more complicated shape has been simulated by drawing a coast by means of random +1/-1 displacements along the vertical direction. Results are shown in Figure 89.

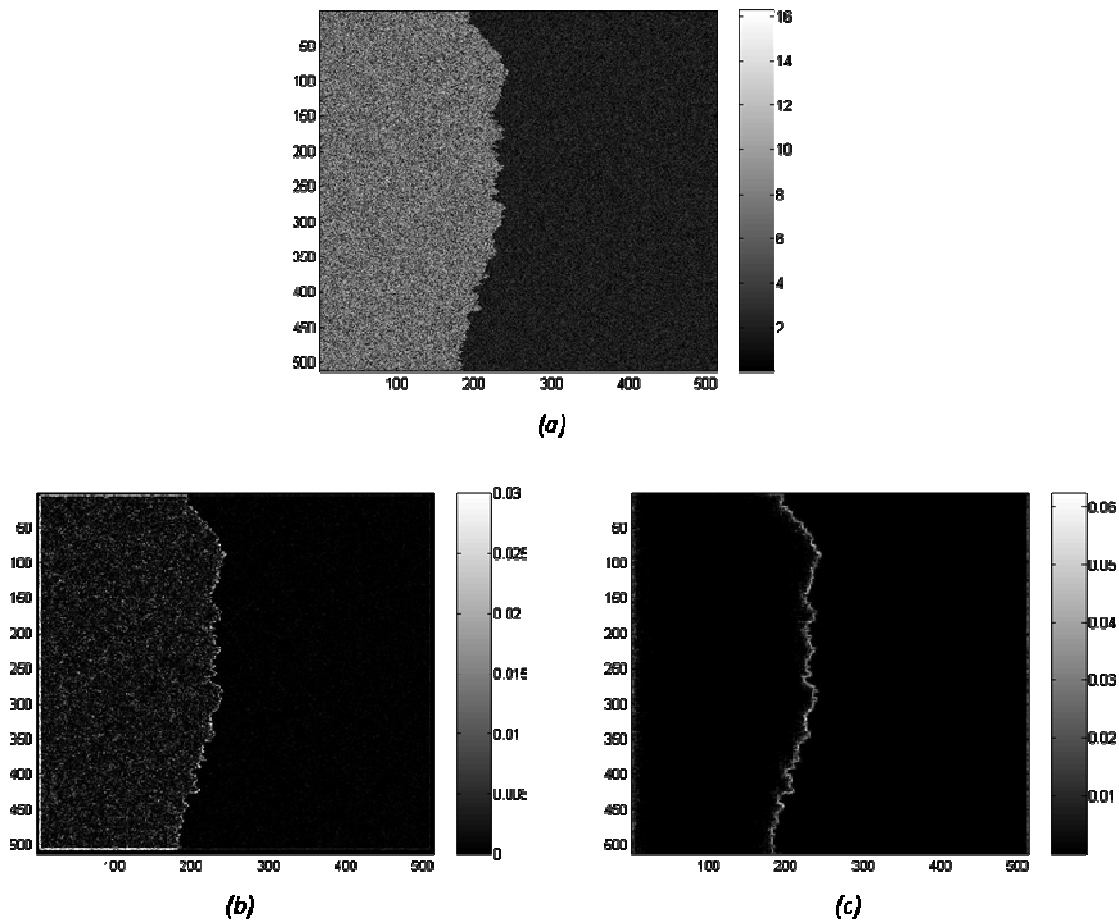


Figure 89. Edge enhancement of the simulated image in (a) as obtained with the Sobel filter (b) and with UEEA (c).

5.2.3 Properties

This section is devoted to review the main properties of UEEA in SAR imagery.

First consideration concerns simplicity. UEEA is simple and its computational cost is low. It is an iterative process just requiring two operations per iteration: the application of a single iteration of the SWT and the evaluation of the pointwise maxima. No previous calibration is required [141] since this application is not concerned with a precise retrieval of radar cross section values, but just with contrast in intensity. Moreover, any prefiltering step is added and the method is no dependent on the statistics of the input image. Hence, the capability of adaptation of the method to very diverse scenarios, with no need of a priori knowledge or settings is a useful feature in views of its integration in an unsupervised chain.

One of the main interests of UEEA is that it provides a result directly in the wavelet domain. As a consequence, contrarily to conventional wavelet filters, it does not require any inversion step, such as in [133], which is usually an awkward process, often introducing artifacts. On the other hand, working on the transformed domain implies considering differential values, rather than absolute ones. Hence, the dependence on the overall power of the input image is not so tight and problematic, which is an advantage for automatic procedures.

Nevertheless, at first sight, the most noticeable effect of UEEA is the contrast achieved between edges and background, which is in fact the main objective of any edge enhancement algorithm. In order to evaluate the performance of UEEA, a contrast parameter CP will be considered. It accounts for the contrast obtained in the result between the intensity of the edge and that of the surrounding area as a function of the contrast between the two regions delimiting the edge in the input image. More specifically, the contrast in the result is defined as the difference between the mean value of the intensity of pixels corresponding to the edge I_e and that of pixels corresponding to the background I_b , divided by the standard deviation of the background σ_b . Similarly, the contrast between regions in the input image is defined as the difference between the mean intensity of the brightest region at one side of the edge I_{r1} and that of the other one I_{r2} , divided by the standard deviation of the latter σ_{r2} :

$$CP = \left| \frac{I_e - I_b}{\sigma_b} / \frac{I_{r1} - I_{r2}}{\sigma_{r2}} \right|. \quad (5.13)$$

The graph in Figure 90 illustrates the evolution of the CP parameter for simulated images as a function of the constant multiplicative value m . It can be deduced that the gain in contrast reached by UEEA can be considered as having a linear behavior. This is coherent with expectations. For instance, the constant slope of the curve proves that edge enhancement capabilities of the technique proposed are not dependent on the contrast in the input image.

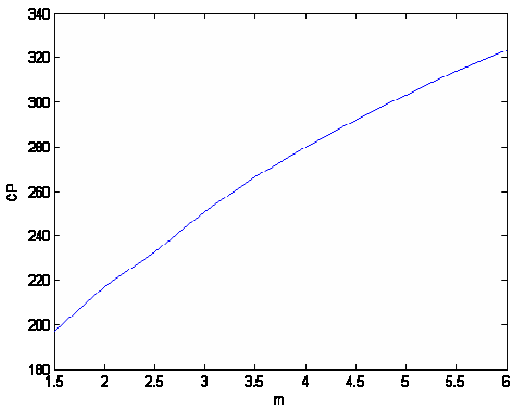


Figure 90. Contrast enhancement as a function of input contrast achieved by UEEA.

5.2.4 Application to coastline enhancement in SAR imagery

In the framework of this dissertation, UEEA has been essentially used for automatic coastline detection in SAR imagery. A set of SAR images has been taken into consideration for validation purposes. RADARSAT and ENVISAT data with different characteristics (acquisition mode and resolution) have been tested. They correspond to maritime scenarios in which the main objective is to enhance the shoreline. The interest of performing an automatic extraction of the coastline from remote sensing data is meaningful. It is sometimes challenging to obtain a precise map of the coastline (similarly, of ice sheets) in some regions and circumstances with other tools. Moreover, the coastline is subject to a temporal evolution (slow and natural due to erosion, abrupt and natural due to an environmental disaster such as a tsunami and abrupt and artificial due to a man-made alteration of the coastline) which provides useful information about the behavior of the ocean currents or a wide variety of patterns related to the climate change. From an economical point of view, for coastal management and planning, it is crucial to monitor the zones subject to long term erosion or to evaluate the affected zones in case of natural disaster, through the evaluation of the deformations in the coastline. Furthermore, the automatic extraction of the coastline in remote sensing images is extremely useful as a segmentation tool in other applications. For example, when performing automatic ship detection, a previous land mask step has to be included in any algorithm. As seen in previous chapter, it consists of eliminating the land areas that have to be neglected when looking for vessels. Up to now, it is usually performed by using auxiliary external data such as maps available from other sources. Nevertheless, on the one hand, geo-positioning of the satellite image has limited accuracy in some cases and this can lead to image shifts in the azimuth direction together with a consequent displacement with respect to the land mask. On the other hand, available land masks are of limited accuracy and there are problems with small islands and coastal man-made constructions. Figure 91 shows an example of application of an available land mask in a coastal SAR image. The blue line superimposed to the image corresponds to the contour of the land mask. It can be observed that the misplacement of the land mask covers a part of the sea and thus induces a blind area in which vessels would not be detected. On the contrary, a land area is misinterpreted as water and hence produces a number of false alarms, marked by yellow circles.

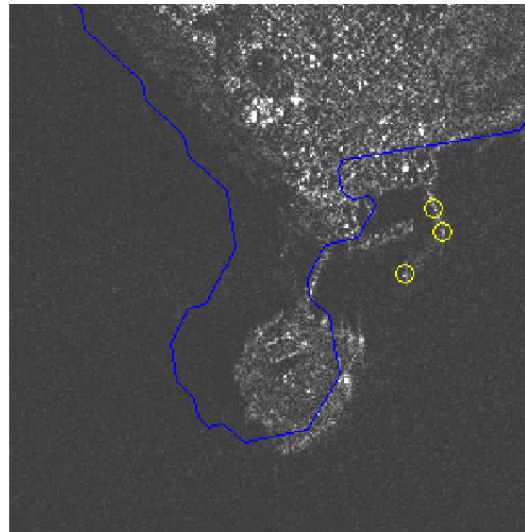


Figure 91. Example of application of an external land mask in a SAR image.

Hence, to overcome this issue, it would be extremely beneficial to perform land mask directly on the remote sensing image, through an efficient technique of segmentation.

General difficulties associated to image processing in SAR data have already been overviewed. In the particular framework of automatic extraction of the coastline, several specific drawbacks have to be considered. The most remarkable one is the diversity of scenarios. In some images, the energy backscattered by the land is higher than that returned by the sea surface and, thus, land areas tend to appear brighter – in mean value – than the ocean ones, see Figure 92a. Nevertheless, this situation is reverted in other cases (even between two acquisitions belonging to the same area of observation), see Figure 92b. Moreover, non stationarity – both in time and space – of the multiple processes involved results often in images exhibiting at different areas opposite situations (a sea surface brighter than the inland zone and vice versa). Even, in some situations, there is absolutely no contrast between regions to be segmented, see Figure 92c. As a consequence, a detection exclusively based on the intensity value is not viable. Furthermore, SAR images tend to present a great diversity of heterogeneities, see Figure 92d. Since they are unpredictable and they lack of efficient models, they are unavoidable and they constitute a source of false alarms.

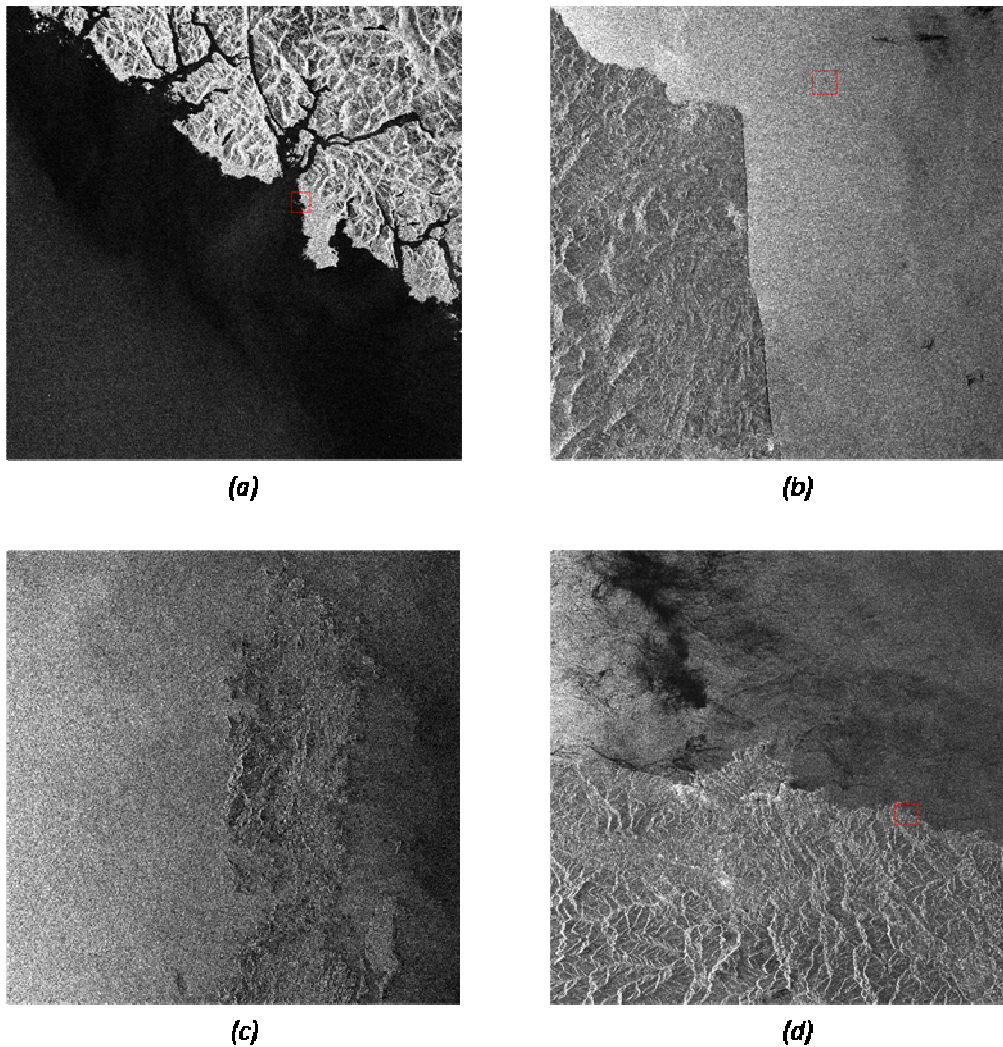


Figure 92. Examples of the diversity of maritime scenarios in SAR images.

The test set is constituted by neat situations, homogeneous and with a considerable contrast between the land and the sea, together with awkward ones, heterogeneous and in which the land and the sea areas are almost undistinguishable. For comparison purposes, the same examples have been processed with the Sobel filter, after applications of the logarithm transform and smoothing through a Lee filter of window size of 11×11 pixel. Some illustrative results are reported hereafter.

First example, see first row of Figure 93, consists of an ENVISAT image. The reflectivity of the oceanic surface is homogeneous and there exist a high contrast between the land and the sea areas. The land zone presents only a few heterogeneities. The most noticeable is a coastal urban area. The second example, see second row of Figure 93, exhibits as well a homogeneous sea surface. Nevertheless, this scenario presents several difficulties. First one is a very small contrast between sea – land areas. Another drawback is the existence of discontinuities in the land due to topography. Third example, see third row in Figure 93, shows an irregular coastline

profile with small islands in the ocean and a lake in the land. The contrast between the land and the sea is rapidly varying, mainly due to fluctuations in the oceanic reflectivity. Moreover, the existence of topography is another aspect that makes segmentation difficult. The last example, see fourth row in Figure 93, is a highly speckled RADARSAT image. The contrast between the land and the sea is irregular throughout the coastline. Moreover, due to the presence of beaches, the shoreline appears fuzzed in some areas.

Even after filtering with the Lee method, the operation of Sobel, which is very sensitive to heterogeneities, is affected by speckle. Hence, edges appear even in homogeneous sea areas, as it can be observed in the second example in Figure 93. Moreover, edge enhancement by means of the Sobel filter is highly dependent on the intensity of the input image: the density of peaks detected by the Sobel filter is higher in areas with a high reflectivity, see last example in Figure 93. As a consequence, the coastline is not enhanced from the rest of discontinuities.

In contrast, if the regions to be segmented are sufficiently homogeneous, UEEA enhances efficiently the frontier between them, with a large contrast between the coastline and the background: it should be reminded that background is considered to be constituted by both water and inland areas. The enhancement of contrast achieved is not dependent on the contrast of the input image. Furthermore, the shoreline appears sufficiently thin, for UEEA degrades resolution just slightly when compared to other methods of smoothing. In fact, as seen in Section 5.2, the combination of scales preserves good localization capabilities of finest scales and, since the mother wavelet selected for this application is the Haar function, with two coefficients, the technique is affected by a loss of resolution due to an averaging of only two pixels. Additionally, in similarly homogeneous scenarios (see first example in Figure 93), the operation of UEEA is benefited if the contrast between the regions is high, since therefore the edge is more pronounced and easily detectable.

In non homogeneous scenes, UEEA is sensitive to edges produced by structures others than the coastline such as for example patterns due to topography, rivers or urban areas. Nevertheless, even if they do not belong to the coastline, it is worth noting that these enhanced edges are to be understood as effective ones and not as artifacts introduced by the algorithm.

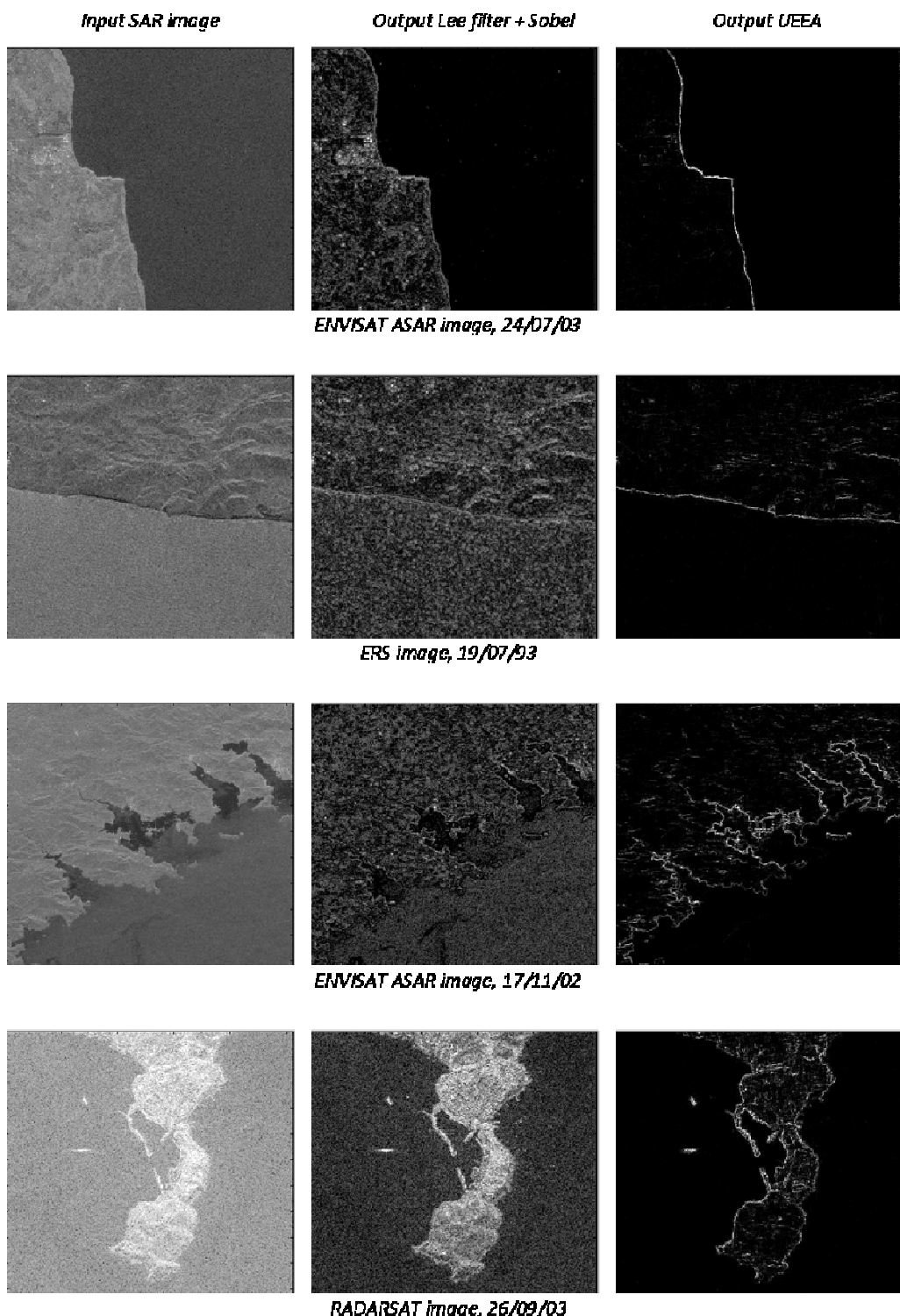


Figure 93. Examples of operation of the UEEA on SAR imagery, compared to Lee + Sobel edge enhancement.

5.3 Edge labeling with Geodesic Active Contour

5.3.1 Theoretical principles

Once the transition estimation completed, if willing to build an unsupervised scheme, a final decision step is required. It consists of the segmentation of the input image in two classes: edges and no edges. Two options are to be considered: binarization through thresholding and use of an active contour. The straightforward strategy for segmentation is gradient binarization through thresholding. This option is usually not robust for several reasons. Mainly, the threshold is difficult to define automatically. Furthermore, noise and artifacts may appear and pixels belonging to contours may not be connected. Alternatively to the application of a threshold, the use of active contours, even if more computationally costly, is preferred.

Essentially, a geodesic active contour or snake consists of forcing the evolution of a close curve towards the points of high gradients. More specifically, let the Geodesic Length (GL), be defined as $GL = \oint g(\nabla x) ds$, where g is a function of ∇x , which is the gradient estimated through the edge enhancement algorithm:

$$g(\nabla x) = \frac{1}{1 + \|\nabla x\|^p}, \text{ with } p \in \mathbb{R}. \quad (5.14)$$

In the scope of this dissertation, p is set to 1. Hence, the objective of the snake is to find the curve $C(s)$, such that GL is minimum. This objective function can be minimized by steepest descent. If we consider C to be a function of time t , the Euler – Lagrange equations yield the curve evolution equation [142]:

$$\frac{\partial C}{\partial t} = g \kappa \vec{N} - \langle \nabla g, \vec{N} \rangle \vec{N} \quad (5.15)$$

where κ is the Euclidean curvature, \vec{N} is the unit inward normal, $\langle ., . \rangle$ stands for the scalar product and ∇ for the gradient operator. Nevertheless, from the point of view of practical implementation, it is worth using level sets methods. In that case, instead of evolving the one dimensional curve C , we evolve a two dimensional surface u . C is then the zero level set of u and u is said to be an implicit representation of C . It is shown in [143] that the evolution of u can be expressed as

$$\frac{\partial u}{\partial t} = g(\kappa + c) \|\nabla u\| + \left\langle \nabla g, \frac{\nabla u}{\|\nabla u\|} \right\rangle \|\nabla u\| \quad (5.16)$$

where c is a constant erosion parameter and κ is defined as:

$$\kappa = \operatorname{div} \left(\frac{\nabla u}{\|\nabla u\|} \right) \quad (5.17)$$

div is the divergence operation. Hence, the minimization is done by initially setting a default surface u_0 (u at $t=0$), and then actualizing it, iteration after iteration (each iteration represents a differential of time dt), according to:

$$u_t(x, y) = u_{t-1}(x, y) + dt \cdot \beta \quad (5.18)$$

where

$$\beta = g(x, y) \cdot (\kappa + c) \|\nabla u\| + \left\langle \nabla g, \frac{\nabla u}{\|\nabla u\|} \right\rangle \|\nabla u\|. \quad (5.19)$$

Figure 94 summarizes the different steps for the implementation of the Geodesic Active Contour.

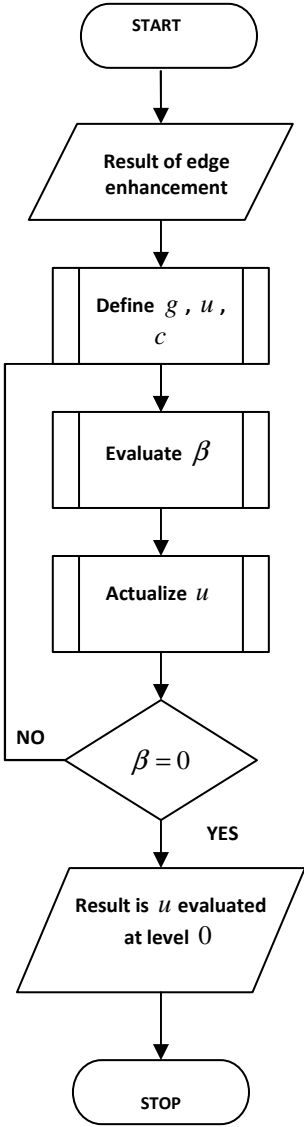


Figure 94. Flowchart of the Geodesic Active Contour.

Special attention should be paid to the selection of the default surface u_0 . u_0 is the initial surface defining a starting contour from which the algorithm is going to evolve until adjusting to the desired frontier. As a consequence, a condition for the initial contour is to be outside the region enclosed by the targeted contour. Hence, if it is assumed that no a priori information is available about the location of the coastline, the straightforward option is to fix as the default contour the external frame of the input image. In that case, the default surface u_0 is calculated as the distance of every point of the surface to the frame of the image. Nevertheless, it must be noted that this default initial contour often requires a large number of iterations before convergence to the result. Therefore, in order to save computational cost, the initial contour should be ideally as close as possible to the final result. An efficient alternative to handle this issue is to consider high scales of the wavelet decomposition, taking

profit of the multiscale framework in which the algorithm proposed for edge enhancement relies. More specifically, it has been already seen in previous sections, that high scales of the WT – equivalently, low frequencies – provide a coarse filtered version of the input image. Hence, a coarse landmask may be obtained from low frequency components. In particular, the technique proposed will employ the intrascale maximum of the fifth iteration of the WT. A rough threshold of this intermediate component results in a binarized image which constitutes an approximate estimation of the targeted contour and which can be efficiently employed as the default surface to the snake algorithm. Since, the edge enhancement step proposed previous to edge detection already computes the wavelet decomposition of the input signal, no computational load is added. Moreover, since this contour is closer to the result than the outside frame of the image, the fact of taking it as the initial contour of the Geodesic Active Contour considerably enhances the computational performance of the algorithm. An example of default initial surface calculated through high scales of the wavelet representation is shown hereafter in Figure 95.

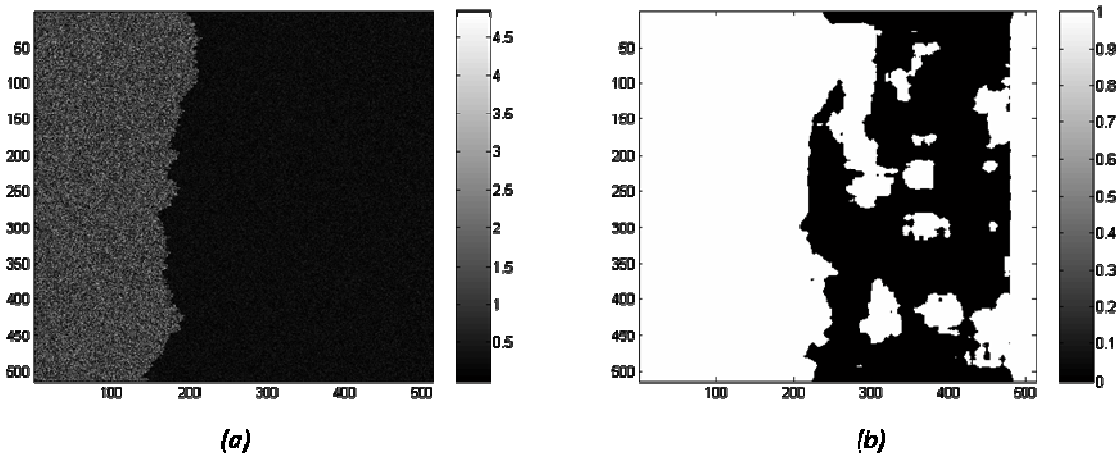


Figure 95. (a) Simulated SAR image and (b) default initial surface employed.

The appropriate selection of the initial surface is also critical when dealing with topography. The ridges of mountains and hills appear in SAR images as bright elongated edges, which are enhanced by the UEEA. Even if this is not an incorrect behavior of UEEA, it constitutes a drawback for the unsupervised extraction of the coastline. The use of the initial surface previously introduced can manage this situation. This is straightforwardly justified by the fact that edges induced by topography appear as maxima in the intensity of the input image and the presence of large scale edges is widely more unlikely in the sea than in inland areas. Several examples of scenes with topography patterns are shown in Figure 96. They represent difficult situations for coastline extraction, not only due to the presence of topography, but also because of the low contrast between the sea and inland areas, of the shadows induced by topography and of the spatial heterogeneity. The examples have been extracted from an ENVISAT PRI image of the island of Tenerife (Spain) in the Eastern Atlantic Ocean. The logarithm of the intensity of the input images is represented in the left column. The column in

the center corresponds to the application of the UEEA for each example. It can be observed that the coastline has been correctly enhanced with a large contrast with respect to the homogeneous background. Nonetheless, topography patterns have also induced a high number of edges. For coastline detection purposes, the presence of these secondary edges has to be blurred in order to obtain a proper land mask. This will be achieved by adjusting the initial surface of the GAC to a rough mask obtained from the thresholding of a low frequency intermediate product of the UEEA. This component is shown in the right column of Figure 96.

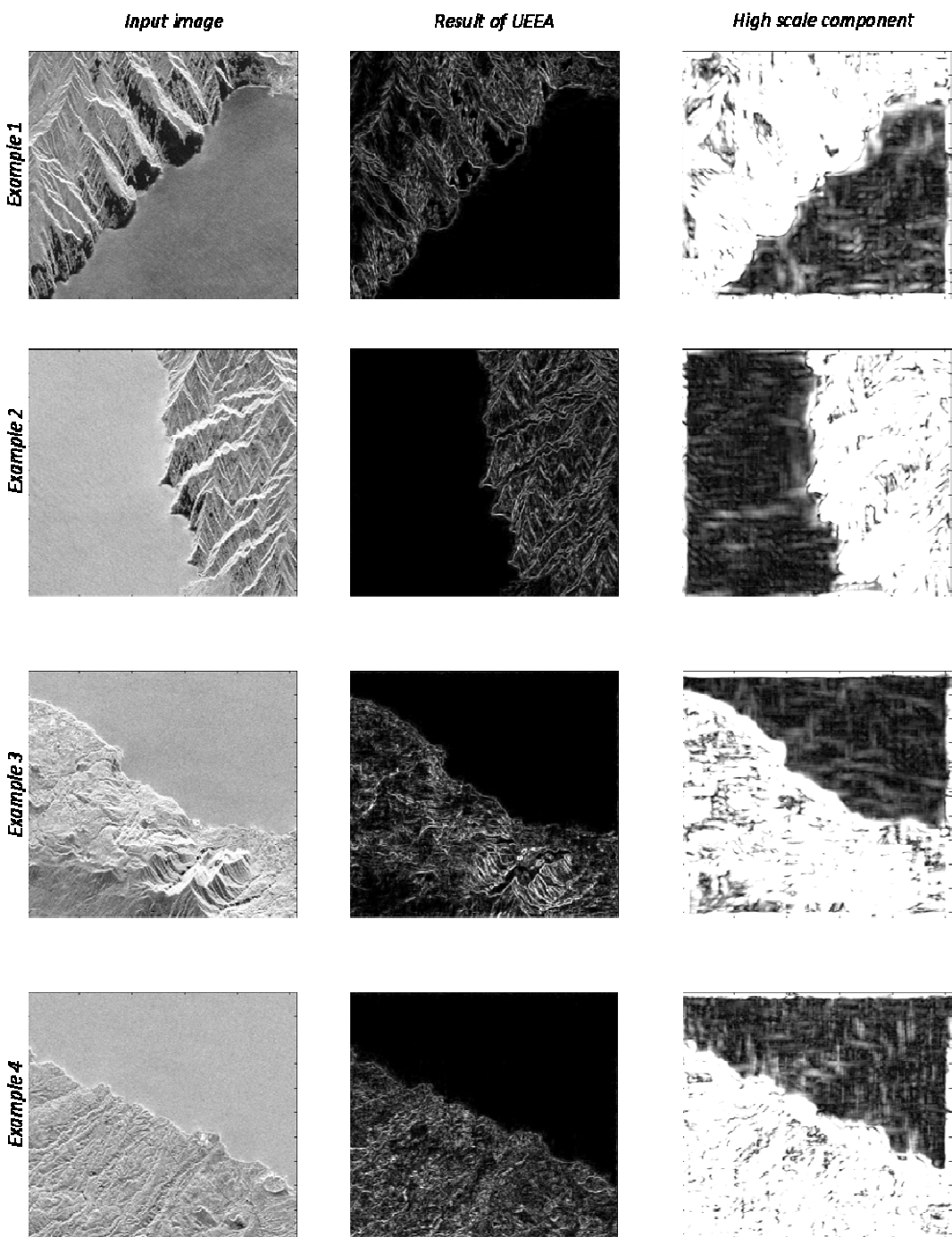


Figure 96. Examples of coastline enhancement in the presence of topography. (left column) Input image (centre column) Result of the application of UEEA. (right column) Low frequency component employed for the evaluation of the initial surface of the GAC.

5.3.2 Validation through simulated images

5.3.2.1. Definition of quality parameters

The estimation of the goodness of the segmentation is difficult and application dependant. Probably due to this fact, it is worth noting here the lack in the literature of a consensus of quality parameters concerning edge detection. As a consequence, the comparison between different techniques usually relies exclusively on mere visual appreciation factors. Nonetheless, in order to provide a tentative quantitative estimation of the goodness of the approach, three parameters are proposed and defined in this section.

The first parameter concerns the capability of localization of the algorithm that is the closeness of the detected edge to the location of the real edge in the input image. Mathematically, there are different parameters measuring the distance between curves. The most extended is the Hausdorff distance. The Hausdorff distance $H(A, B)$ between two sets of points on two curves A and B is the maximum over each element a of A of the minimum over each element b of B of the distance d (according to the underlying metric in the plane) from a to b . More concisely:

$$H(A, B) = \max_{a \in A} \left(\min_{b \in B} (d(a, b)) \right). \quad (5.20)$$

Taking into account the characteristics of the application, the objective is here to provide a measure of the error which is the distance between the real and the retrieved edges. Hence, an appropriate measure of the error in a discrete context can be defined as:

$$\text{error} = \frac{1}{\text{card}(A)} \sum_{a \in A} \min_{b \in B} (d(a, b)). \quad (5.21)$$

From a practical point of view, the evaluation of this parameter has been implemented as follows. For every single point of the longest curve, its distance to the closest point in the other curve is computed. Then, the mean value of this set of distances constitutes the error. This error rate makes sense only if the edge is effectively detected, but misplaced. Two additional rates are estimated in order to account for misdetections. These parameters are: the probability of false positives, p_{FP} , and the probability of false negatives p_{FN} . The probability of false negatives measures the quantity of elements belonging to the class “edge” and misclassified as “no edge” and, similarly, the probability of false positives reflects the quantity of individuals classified as “edge” and contrarily being part of “no edge”. Let us define four classes: E_{input} “confirmed edges in the input image”, E_{output} “detected edges” (i.e. “edges in the output image”), NE_{input} “confirmed no edges in the input image”, NE_{output} “detected no edges” (i.e. “no edges in the output image”). With this:

$$p_{FP} = \frac{\text{card}\{E_{output} \cap NE_{input}\}}{\text{card}\{E_{output}\}} \text{ and } p_{FN} = \frac{\text{card}\{E_{input} \cap NE_{output}\}}{\text{card}\{E_{input}\}}. \quad (5.22)$$

It is worth noting that these values make sense only if an existing edge is not detected or if the algorithm finds non existing edges. Therefore, the rates p_{FP} and p_{FN} are to be understood as complementary to the error parameter, defined previously: if an existing edge is detected but misplaced, p_{FP} is considered null.

Another aspect to be observed is edge thickness. Since, by definition, an edge is infinitely thin in an ideal case, a high thickness of the result signifies the incapability of the technique to locate the edge. This fact usually constitutes a drawback when directly applying a threshold [138] [139]. On the contrary, when using a Geodesic Active Contour, the edge line is only one pixel wide by construction.

These quality parameters can be estimated precisely in simple simulated images, but their evaluation is usually unfeasible in real images with no available groundtruth.

5.3.2.2. Results

This section presents examples of results of the whole chain of edge detection constituted by UEEA previous to the application of a geodesic active contour on simulated data. The set of simulations tested is constituted by images synthesized as speckle matrices with squares embedded, as specified in section 5.2.2. Several examples are shown in Figure 97. The corresponding parameters of the simulation as well as the evaluated errors are included in the figure.

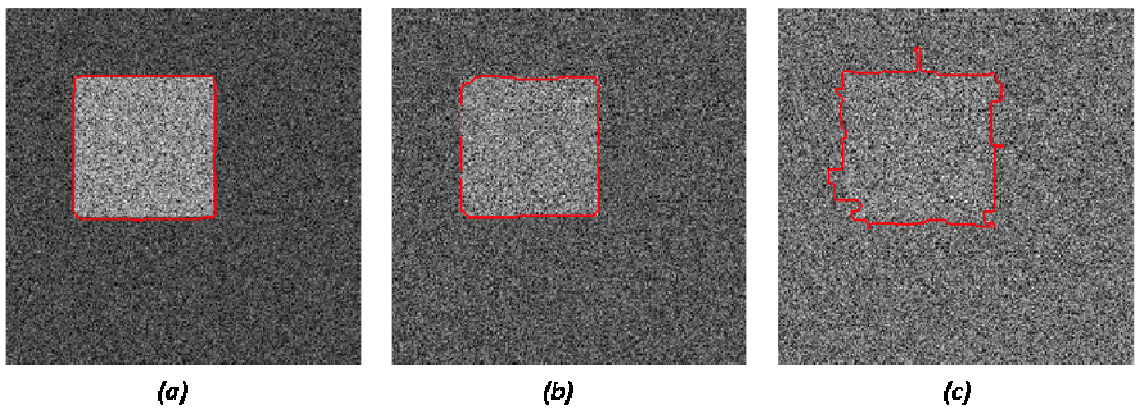


Figure 97. Examples of detection of the overall chain of coastline extraction on simulated images. (a) $m=2.5$, error=0.1125, $p_{FP}=0$. (b) $m=1.5$, error=0.25, $p_{FP}=0$, $p_{FN}=0$. (c) $m=1.2$, error=1.1625, $p_{FP}=0.06$, $p_{FN}=0.1$.

It can be observed that if there exist a sufficient contrast in the input image, $m \geq 1.5$, the external contour of the square is detected precisely, in spite of a slight smoothing of angles. No

artifacts appear. For lower values of contrast in the input image, see Figure 97c, the presence of the square is detected, but its shape can not be accurately retrieved.

5.3.3 Validation through real data

This section is devoted to present results of the performance of the technique proposed in this chapter in SAR images. Since the quality parameters introduced in the section 5.3.2.1. are not possible to evaluate in real scenarios, the shoreline extracted is superimposed to the input SAR image, in order to provide a visual evaluation of the goodness of UEEA.

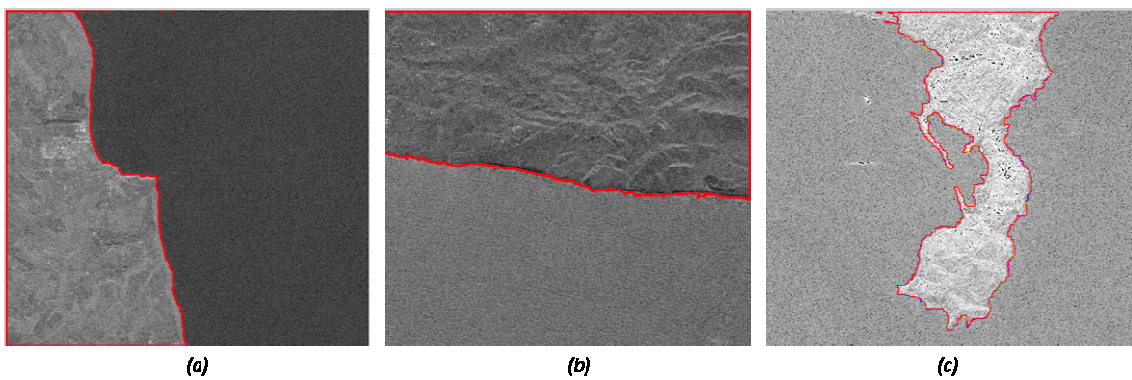


Figure 98. Examples of detection of the overall chain of coastline extraction on SAR images. (a) ENVISAT ASAR image, 24/07/03. (b) ERS-1 image, 19/07/93. (c) RADARSAT image, 26/09/03.

The observation of the results obtained in SAR images confirms a good match of the detected coastline to the shoreline visually inferred. It is worth noting that the red line has been highlighted for representation purposes but the result is one pixel wide. Moreover, it should be observed the correct performance of the method, despite the diversity of scenarios. First example is the simplest one (see Figure 98a), since the sea surface is homogeneous and there exist a high contrast between both land and sea areas. The coastline is retrieved precisely. The second example (see Figure 98b) is more difficult for edge detection purposes due to the low contrast between the land and the sea and to the presence of topography patterns. Visually, two slight deviations can be appreciated in the result. Nonetheless, globally, the detected coastline matches closely the real one. The difficulty of the third example (see Figure 98c) relies essentially on the heterogeneities in the land and on the difference of contrast throughout the shoreline. Moreover, the coastline presents thin man made structures. High resolution capabilities are necessary to detect them properly.

As seen previously, the presence of topography in the input image makes automatic coastline detection particularly difficult. Hence, special attention will be given to this type of scenarios. Several examples are shown in Figure 99. Intermediate products for these examples, in

particular the output of UEEA and the initial surface to GAC, have already been presented in Figure 96. It can be observed that the detected coastline matches the shoreline visually determined. The topography drawback has been overcome.

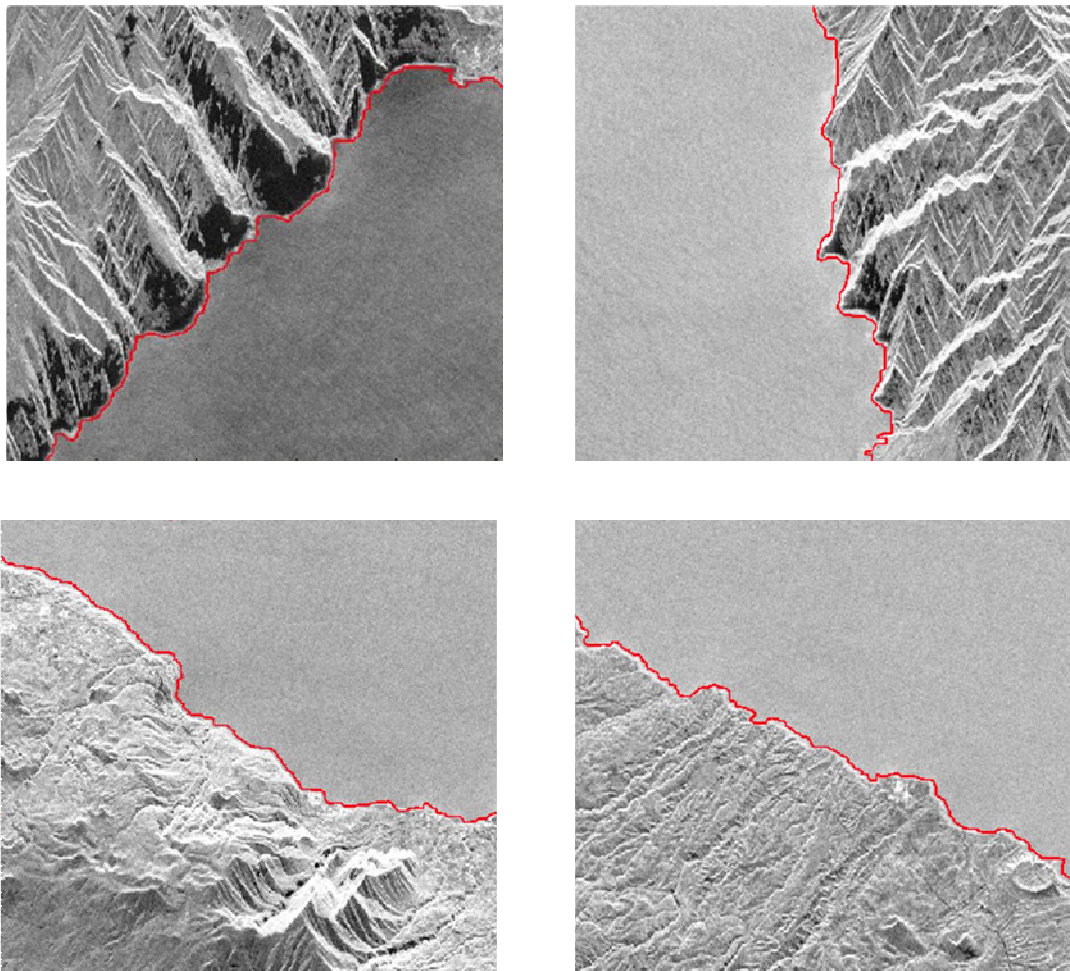


Figure 99. Examples of detection of the overall chain of coastline extraction on SAR images with topography patterns.

It has already been mentioned that from the point of view of applications, automatic coastline extraction can be used for ship detection purposes with respect to the land mask step. It has also been suggested that instead of using maps from external sources, it is more efficient to detect the land areas directly in the image by means of post-processing techniques. Figure 100 shows the result of applying the technique designed for coastline extraction to the same input image of Figure 91. Three layers have been superimposed. The first one corresponds to the optical image (source: Google Earth), the second one is the SAR image and the last one corresponds to the output of the edge extraction algorithm designed. It can be observed that

this land-mask matches more accurately the land area. This fact results in a higher performance of ship detection algorithms.

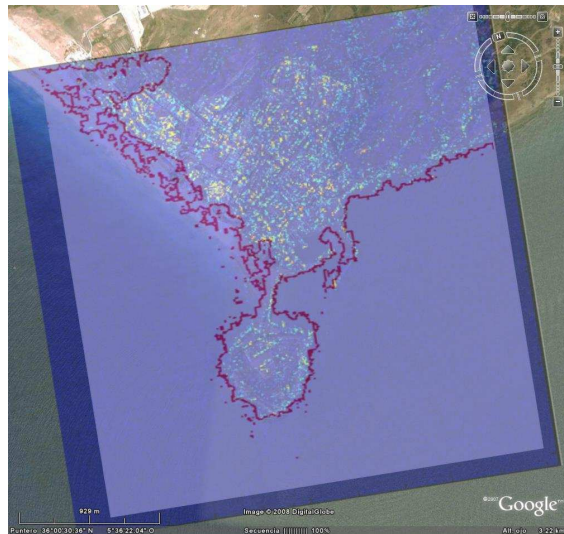


Figure 100. Example of application of unsupervised coastline extraction to a coastal SAR image.

5.4 Conclusions

In this chapter, edge enhancement in SAR images has been addressed. It has been shown that due to speckle, it constitutes a difficult issue. Moreover, it has been justified that the concept of edge is inscribed in a multiscale framework. Especially, it has been observed that the presence of an edge tends to persist over scales in a WT representation.

Hence, taking into account these considerations, a multiscale algorithm for the unsupervised extraction of most significant edges, called UEEA has been presented. It has been designed specifically to deal with speckled SAR images. UEEA proposes a simple and robust edge enhancement operation directly in the wavelet transformed domain. Contrarily to conventional filters, working in the wavelet transformed domain permits avoiding inversion steps which are usually awkward. Besides, wavelet coefficients can be combined in non linear ways. In particular, UEEA essentially relies on an interscale combination of wavelet subbands, taking advantage of the property of persistence of edges across scales. With this, a high contrast is reached between the edge and background with a minimum degradation of the spatial resolution since a Haar wavelet with a short spatial support (only two coefficients) has been employed. The edge enhancement phase has proven to be critical in heterogeneous SAR images and UEEA constitutes a good solution to deal with this type of data. It does not require any type of pre-filtering of the data and it is independent on the statistics of the input image.

The capability of adaptation of the method to very diverse scenarios, with no need of a priori knowledge or settings is a useful feature in views of its integration in an unsupervised chain for processing SAR images. UEEA has been tested on simulated and SAR data in the scope of coastline extraction. It has proven to be robust and effective for this application. Its performance has been compared to that of a Sobel filter applied after a Lee filter, even if it is difficult to provide a rigorous quantitative comparison between methods applied to edge detection.

Then, after edge enhancement, the application of a Geodesic Active Contour technique has been chosen for the final decision step. The coastline extracted which is an entirely connected line of one pixel wide, matches accurately the targeted frontier. The issue of topography has been widely discussed since it constitutes a key difficulty for unsupervised coastline extraction purposes. It has been shown that a suitable management of the default surface introduced to the Geodesic Active Contour, based on intermediate products generated by UEEA, can successfully deal with topography.

Chapter 6. Automatic analysis of textures in maritime SAR imagery

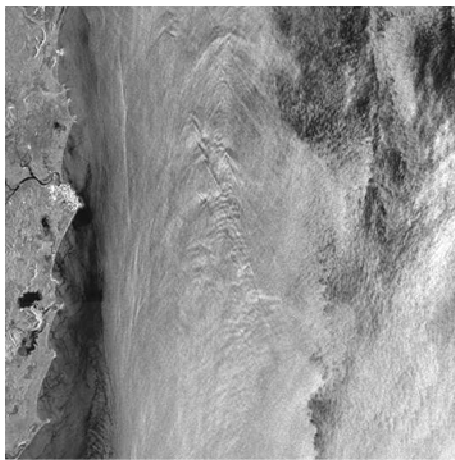
In signal processing terms, spots and edges contain most of the information, i.e. the higher entropy, about the structure of an image [144]. As already seen in previous chapters, their discrimination permits tackling the most relevant elements in the image. Nevertheless, in some cases, once the structure of the image revealed, it is necessary to analyze the distribution of subtle relations between pixel amplitudes to reach a deeper comprehension of the image content. In the mammal visual system, this implies that the eye focuses on texture, which is commonly defined as the “visual quality of a pattern”. Such an intuitive concept is imperfectly approximated in image processing terms by estimating the “local statistics of a pattern” [144]. This requires defining the shape and dimensions of a window and then estimating the statistical moments of the samples observed. In order to capture the finest relations between pixels, a determination of high order moments is necessary. However, this requires involving a large number of samples to perform a correct estimation, i.e. a large window, which in turn degrades spatial resolution capabilities of the analysis. If the distribution of samples is not homogeneous, large windows are not able to capture discontinuities. In that case, the estimation of local moments is not well adapted to the spatial changes of the scene. Moreover, an optimum evaluation of statistical moments of a given population needs a previous knowledge of the model behind the distribution of the samples, which can not be always established in an accurate form.

This chapter is devoted to propose, justify and test an alternative method of study of singularities distribution, based on the multiscale estimation of the Lipschitz (equivalently Hölder) exponent [162]. This technique does not require an a priori determination of a stochastic model for the data under study. Furthermore, the multiscale determination of the measure of the local irregularity, understood as the amount of diversity between the intensity of the samples considered, is less subject to the restrictions of spatial resolution, encountered by the statistical moment estimation in local windows.

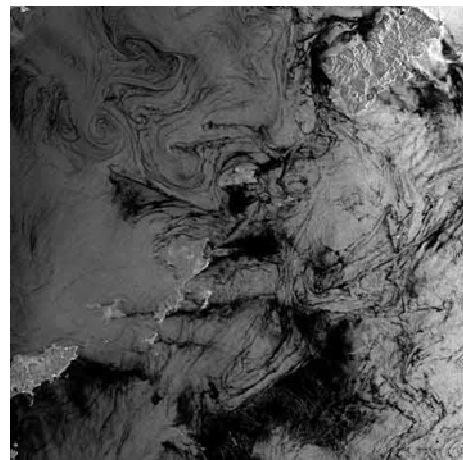
In SAR maritime images, the characterization of the local irregularity of the sea surface should permit an effective segmentation, useful in several applications. For instance, surface currents and other natural and man-made features modulate the sea surface roughness and thus the radar cross section.

Examples of such features are current fronts (see Figure 101a), maritime eddies (see Figure 101b), internal waves (see Figure 101c), oil pollution (see Figure 101d), underwater bottom topography and upwelling, among others. Hence, they are reflected in the distribution of pixel intensities in the resulting SAR image. In particular, oil pollution in the ocean will be addressed in this Chapter.

The structure of this Chapter is as follows. Section 6.1 is devoted to review the main drawbacks related to the analysis of textures in SAR maritime images. Section 6.2. presents a multiscale algorithm for the local estimation of the regularity of a signal. It is applied to automatic oil spill detection in SAR images. The rationale of the application, as well as results obtained, are shown in Section 6.3. Conclusions are presented in Section 6.4.



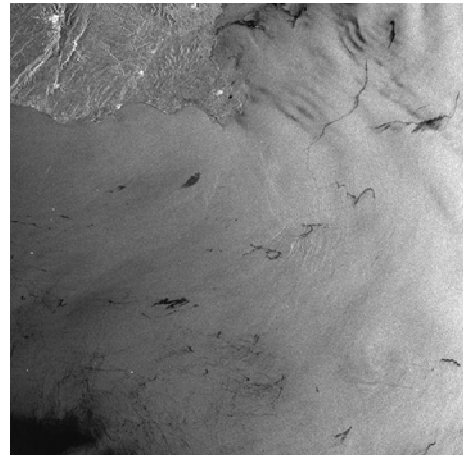
(a)



(b)



(c)



(d)

Figure 101. Natural and artificial phenomena in SAR maritime images. (a) Current fronts. (b) Maritime eddies. (c) Internal waves. (d) Oil pollution.

6.1 Main drawbacks

In image processing terms, the consideration of the process of generation of the data, as well as the nature of the observed features, will define the appropriate tools to be employed in further analysis. As a consequence, this section is devoted to explore the characteristics of the sea surface, to analyze how they are translated by the SAR imaging process and then, to define a multiscale framework, suitable for the analysis.

6.1.1 Turbulent nature of the sea surface

Fractal geometry is widely considered the most suitable tool to describe natural patterns [144]. Fractals are geometric entities that present self-similarity. Roughly speaking, this implies that the fractal patterns present the same aspect when observed at different scales. They are often the result of iterative processes such as turbulences. As a consequence, fractality is present in most of natural elements. In particular, it has been verified that the sea surface is fractal under certain assumptions [146] [147]. According to [148], a sea surface can be modeled by a finite sum of sinusoidal waves with a mean propagating direction corresponding to the wind direction. With this, a 2D dynamic sea fractal surface can be defined as [146].

6.1.2 Sea surface in SAR images

This section analyzes the effect of the SAR imaging system on the properties of the sea surface. It has already been exposed in Chapter 2, Section 2.3, that SAR systems essentially retrieve roughness patterns. Radar electromagnetic waves are backscattered by the sea surface. According to the Bragg resonance effect, backscattering is directed by gravity capillary waves which are of the order of the wavelength. Nevertheless, due to the resolution of orbital sensors, longer waves are to be taken into account since, at pixel level, the energy backscattered to the sensor corresponds to the combination of the reflections of the electromagnetic wave of the sea surface in the area of a resolution cell. Due to electromagnetic reflection laws, the wave backscattered back to the sensor corresponds mostly to the contributions of the elements of the surface perpendicular to the incident wave. In order to illustrate this effect, two examples of sea states are presented in Figure 102 and in Figure 103.

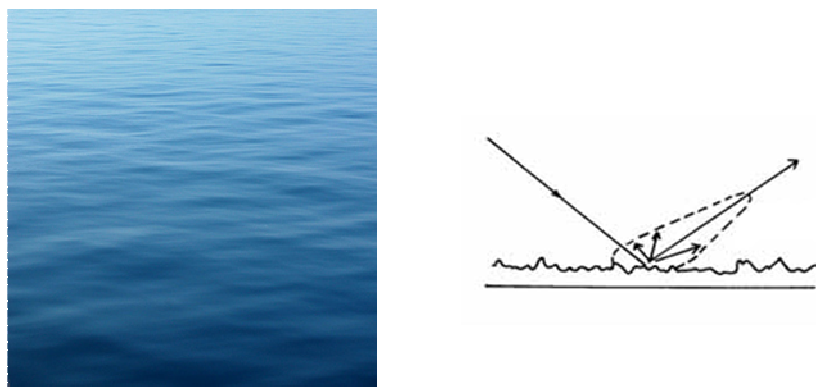


Figure 102. Backscattering as a function of sea surface roughness, in calm sea conditions.

On the one hand, Figure 102 presents a calm sea so that its surface is smooth. In this situation, a small amount of energy is backscattered back to the sensor since due to reflection laws. The

electromagnetic wave strikes a flat surface and is reflected in the opposite direction with an angle with respect to the sea surface equal to the angle of incidence [151].

On the other hand, Figure 103 presents an agitated sea, with a high roughness. In these conditions, the amount of energy backscattered to the sensor is higher than in previous example.



Figure 103. Backscattering as a function of sea surface roughness, in turbulent sea conditions.

Let us now justify the suitability of the assumption of a fractal model for the sea surface. Several experiments have been devoted to analyze the effect of SAR imaging of a maritime scene. In [149], the sea surface is divided into facets, smaller than the SAR resolution but larger than the electromagnetic wavelength. In order to account for the short waves, a microscopic random roughness is superimposed to the facets. The intermediate wave effect is included by adding a random tilting to the facet mean plane [150]. Then, the electromagnetic return from each planar facet is evaluated, based on the Bragg resonance effect, which is the most dominant scattering mechanism for marine scenes at intermediate incidence angles. The Kirchhoff approximation is employed [151]. This study emphasizes the importance of the short waves in SAR imaging formation process.

Moreover, it has been shown that the signal scattered retains the fractal properties of the imaged surface. This assumption has been first theoretically suggested and proven in [148] [152] [153]. In particular, it has been shown that, by using the small perturbation method, backscattering coefficient of a fractional Brownian motion isotropic random rough surface for a pixel pq can be expressed in terms of fractal parameters as

$$\sigma_{pq}^0 = \left(8k^4 \cos^4 \vartheta\right) |\alpha_{pq}|^2 \frac{S_0}{(2k \sin \vartheta)^{(2+2H)}} \quad (6.1)$$

where

$$S_0 = H \cdot T^{2(1-H)} 2^{2H} \frac{\Gamma(1+H)}{\Gamma(1-H)} \quad (6.2)$$

ϑ is the incidence angle, α_{pq} is a coefficient depending on dielectric constant, polarization and incidence angle, k is the spatial frequency, H is the Hurst exponent, T is a characteristic length of a fractional Brownian motion surface, called topography and Γ is the Gamma function.

Besides to the theoretical justification, the fractal model assumption has also been experimentally confirmed [154].

6.1.3 Multiscale framework for the analysis of textures in maritime SAR

images

The chaotic nature of turbulent flows requires using statistical means for their understanding. However, the main difficulty in the analysis of turbulence is that it has to be able to preserve local singularities of the signal [155]. The distribution of the singularities may be studied statistically by means of calculation of local energy spectra, the evaluation of structure functions and the singularity spectra, as detailed in Sections 6.1.3.1, 6.1.3.2 and 6.1.3.3 respectively. Even if the previous parameters are not explicitly employed in this dissertation, it is useful to mention them since it can be observed through their definition that wavelet theory is more suitable for this purpose than classical techniques, such as the FT [156] [157].

6.1.3.1. Energy spectrum

The evaluation of the energy spectrum $E(k)$ by means of the FT has been one of the most widely used techniques for turbulence analysis. The Fourier energy spectrum $E(k)$ of a one dimensional function $f(x)$ which is the modulus of the FT of its two-point correlation

$$E(k) = \frac{1}{2\pi} |\hat{f}(k)|^2 \quad (6.3)$$

where $\hat{f}(k)$ is the Fourier transform of $f(x)$.

The WT permits an estimation of the energy spectrum locally, $\tilde{E}(x,k)$ through the L^2 norm of the WT:

$$\tilde{E}(x,k) = \frac{1}{2c_y k_0} \left| \tilde{f}\left(x, \frac{k_0}{k}\right) \right|^2 \quad \text{for } k \geq 0 \quad (6.4)$$

where k_0 is the peak wave number of the analyzing wavelet ψ and

$$c_\psi = \int_0^{+\infty} \frac{|\hat{\psi}(k)|^2}{k} dk . \quad (6.5)$$

The mean wavelet spectrum $\tilde{E}(k)$ is obtained by integrating the space – scale decomposition in the spatial dimension. It can be expressed as

$$\tilde{E}(k) = \int_0^{+\infty} \tilde{E}(x, k) dx . \quad (6.6)$$

It is worth noting that the mean wavelet spectrum $\tilde{E}(k)$ is a smoothed version of the Fourier energy spectrum $E(k)$. Moreover, it gives the correct Fourier exponent for a power-law Fourier energy spectrum $E(K) \propto k^{-\beta}$ provided that the analyzing wavelet has at least $n > (\beta - 1)/2$ vanishing moments [158].

6.1.3.2. Structure functions

In the study of turbulence, a fundamental parameter is the p^{th} order structure function $S_p(r)$ defined as

$$S_p(r) = \frac{1}{L} \int_0^L |f(x) - f(x+r)|^p dx \quad (6.7)$$

where $L \gg r$ is the length of the signal. If $f(x)$ is self-similar then the structure functions will have a power law dependence on the scale r

$$S_p(r) = r^{\zeta(p)} . \quad (6.8)$$

The first order structure function $\zeta(1)$ provides a measure of the smoothness of $f(x)$. The velocity increment $\Delta f(x, r) = |f(x) - f(x+r)|$ is equivalent to a WT with a Haar wavelet. Moreover, it has been shown [159] that the exponent $\eta(p)$ defined as

$$\tilde{S}_p(r) = \frac{1}{L} \int_0^L |\tilde{f}(x, r)|^p dx \propto r^{\eta(p)} \quad (6.9)$$

is the same as $\zeta(p)$ provided $p > 1$ and $\zeta(p) < p$. Furthermore, this development is independent of the mother wavelet employed.

6.1.3.3. Singularity spectrum

In order to characterize a multifractal function, it is necessary to calculate its singularity spectrum $D(\alpha)$. It is defined as the Hausdorff dimension of the set of points with Hölder exponent α

$$D(\alpha) = D_F \{x, \alpha(x) = \alpha\}. \quad (6.10)$$

The singularity spectrum of a monofractal function consists of a single point, whereas the singularity spectrum of a multifractal is a curve.

6.2 Algorithm for the estimation of the Lipschitz exponent based on the Wavelet Transform

The characteristics of SAR images of the ocean surface have been considered in previous Sections. Furthermore, the interest of inscribing the analysis of this type of data in a multiscale framework has been introduced. This section proposes measuring the local roughness of the sea surface through the Lipschitz regularity. In particular, an algorithm to estimate the local Lipschitz exponent based on the WT is presented. For the sake of clarity, it is worth mentioning that the Lipschitz exponent is also called the Hölder exponent. In this dissertation, both terms will be used.

For practical considerations, it is worth specifying that the mother wavelet employed for texture analysis will be the “Mexican hat” one, unless otherwise stated. The normalized expression of Mexican hat wavelets which correspond to the second derivative of a Gaussian is

$$\psi(t) = \frac{2}{\pi^{1/4} \sqrt{3}\sigma} \left(\frac{t^2}{\sigma^2} - 1 \right) \exp\left(\frac{-t^2}{2\sigma^2} \right) \quad (6.11)$$

which is equivalent in frequency to:

$$\hat{\psi}(\omega) = \frac{-\sqrt{8}\sigma^{5/2}\pi^{1/4}}{\sqrt{3}} \omega^2 \exp\left(\frac{-\sigma^2\omega^2}{2} \right) \quad (6.12)$$

An example of Mexican hat wavelet function is represented in Figure 103.

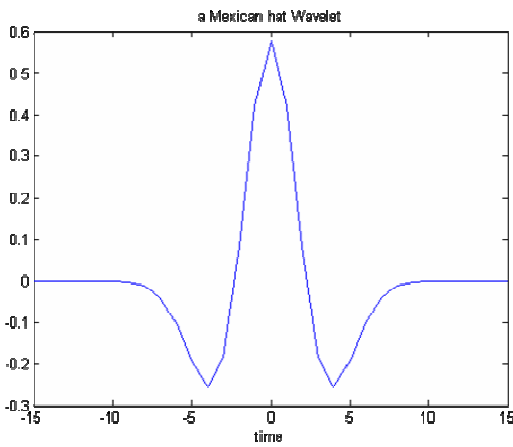


Figure 104. Mexican hat wavelet function in time domain.

These wavelet functions are well localized both in space and in frequency and they are orthogonal to low order polynomials which is a feature of special interest for singularity analysis. Since the Mexican hat mother wavelet has two vanishing moments, we can generally estimate Hölder exponents lower up to two which constitutes a good trade-off for the applications focused in the scope of this chapter. Furthermore, several types of wavelets have been tested, but the Mexican hat family of functions has empirically proven to be the best suited for the purposes of this section. In [160], the Mexican hat or the Lorentzian mother wavelet is also employed, whereas in [161] cubic splines are employed.

6.2.1 Wavelet Transform Modulus Maxima

Section 3.1.2.2.2 in this dissertation was devoted to review the theoretical principles of the use of the WT as an estimator of the local regularity of a signal. In particular, the Lipschitz exponent was defined. Moreover, a necessary condition was stated:

If $f \in L^2(\mathbb{R})$ is uniformly Lipschitz $\alpha \leq n$ over $[a, b]$, then there exists $A > 0$ such that:

$$\forall (u, s) \in [a, b] \times \mathbb{R}^+, \quad |Wf(u, s)| \leq As^{\alpha+1/2}. \quad (6.13)$$

As a consequence, the inequality states that in order to estimate the Lipschitz exponent α , it is not necessary to have the value of the WT decomposition at every point of the space – scale plane, but it is enough with the local maxima of the modulus in the space direction. For instance, a modulus maximum is a point (u_0, s_0) in the space – scale plane such that $|Wf(u, s_0)|$ is locally maximum at $u = u_0$. Therefore:

$$\frac{\partial Wf(u_0, s_0)}{\partial u} = 0. \quad (6.14)$$

The set of WT modulus maxima constitutes a skeleton of the transformed signal, providing a complete and stable description. As a consequence, the signal can be reconstructed from this set of coefficients which contain the information about sharp transitions and singularities [162].

An example is shown in Figure 105 and in Figure 106. Figure 105 shows a 1D signal representing a fractional Brownian motion process. Figure 106a displays its time frequency decomposition by means of the continuous WT with Mexican hat wavelet functions. Figure 106b is the representation of the local maxima connected along the scale direction in maxima lines or ridges. Longest maxima lines converge at small scales to the position of spatial points in which the most meaningful discontinuities of the signal occur. As a consequence, for signal analysis or reconstruction purposes, shortest maxima lines are sometimes discarded. Singularities of a signal are detected by finding the abscissa where the wavelet modulus maxima converge at fine scales.

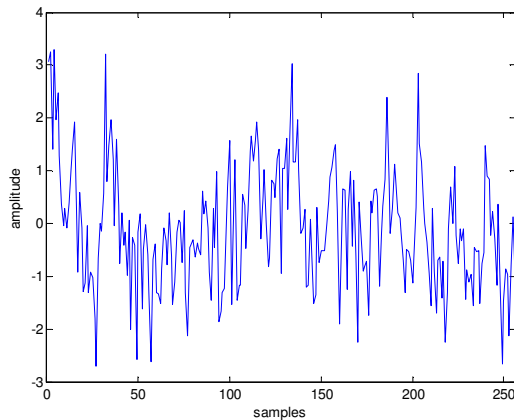


Figure 105. 1D Fractional Brownian motion process.

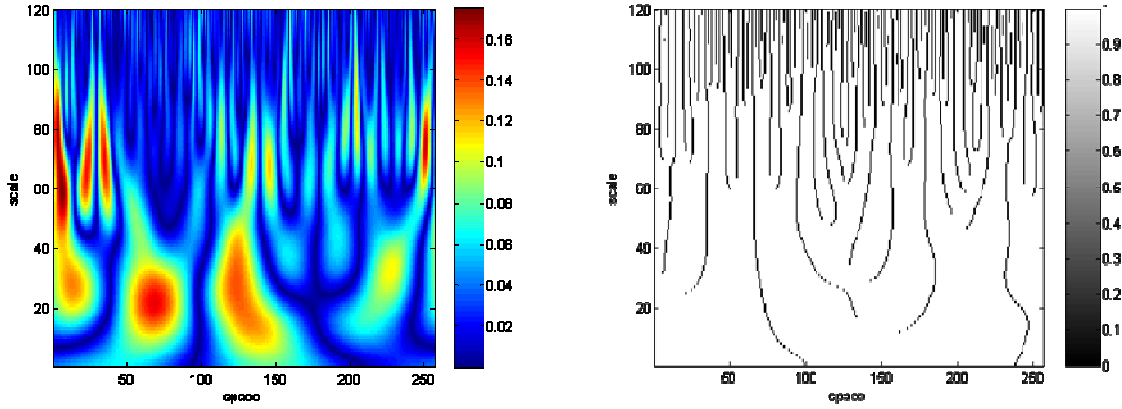


Figure 106. (a) Modulus of the space – scale decomposition with a continuous WT and a Mexican Hat mother wavelet. (b) Scale – space map of the local maxima.

It has been shown in section 3.1.2.2.1. that the WT could be considered as a multiscale differential operator. Let's consider a wavelet ψ with exactly n vanishing moments and a compact support. There exists θ of compact support such that $\psi=(-1)^n\theta^{(n)}$ with $\int_{-\infty}^{+\infty}\theta(t)dt\neq 0$. With this, it can be deduced from equation (6.14) that local maxima occur at points $u=u_0$ such that

$$\begin{aligned} \frac{\partial}{\partial u}\left[s^n\frac{d^n}{du^n}(f*\bar{\theta}_s)(u_0)\right] &= 0 \\ \Leftrightarrow \frac{d^{n+1}}{du^{n+1}}(f*\bar{\theta}_s)(u_0) &= 0 \end{aligned} \tag{6.15}$$

For example, if the wavelet ψ has exactly one vanishing moment, wavelet modulus maxima are the maxima of the first derivative of the result of smoothing f with $\bar{\theta}_s$. As a consequence, local maxima account for different types of irregularities (discontinuities, edges, high curvatures) of the signal. Moreover, it can be proved inversely [163] that if $Wf(u,s)$ has no modulus maxima at fine scales, then f is locally regular.

Once the irregularities have been located, their Lipschitz exponents have to be evaluated in order to identify the nature of the discontinuity. As introduced in section 3.1.2.2.2., the Lipschitz exponent can be measured by looking at the decay of the amplitude of the wavelet decomposition along the maxima lines, which implies projecting the maxima lines on the scale – amplitude plane (see Figure 107).

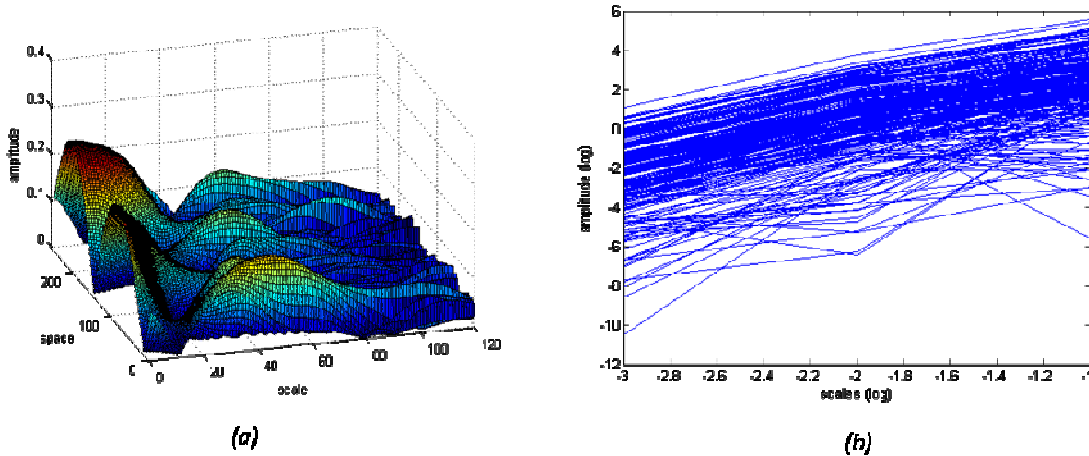


Figure 107. (a) 3D representation of the modulus of the WT of a 1D signal in the space – scale plane.
(b) Example of projection of ridges on the scale – amplitude plane.

When measuring the Lipschitz regularity, it is important for a correct interpretation to take into account the cone of influence of the wavelet, introduced in section 3.1.2.2.3. In particular, the aperture of the cone of influence determines the maximum scale that can be considered in order not to have influence of other close singularities. Let's suppose an isolated singularity at v . Then, the regularity of v is reflected in the decay of the modulus maxima included in the cone $|u-v| \leq Cs$. Hence, f is uniformly Lipschitz α in the neighborhood of v if and only if there exists $A > 0$ such that

$$|Wf(u,s)| \leq As^{\alpha+1/2}. \quad (6.16)$$

By applying the \log_2 to both sides of the inequality:

$$\log_2 |Wf(u,s)| \leq \log_2 A + \left(\alpha + \frac{1}{2} \right) \log_2 s \quad (6.17)$$

$$\Leftrightarrow \frac{\log_2 |Wf(u,s)| - \log_2 A}{\log_2 s} - \frac{1}{2} \leq \alpha \quad (6.18)$$

As a consequence, the Lipschitz exponent α at v can be interpreted as the maximum slope of $\log_2 |Wf(u,s)|$ as a function of $\log_2 s$ minus $1/2$ along the maxima lines converging to v (see Figure 107 right). In practice, graphs of $\log_2 |Wf(u,s)|$ versus $\log_2 s$ contain oscillations imposed to the power-law behavior, which make it difficult to estimate the slope at high scales.

From the point of view of practical implementation, the extension to 2D is not straightforward even if the theory exposed previously holds independently of the number of dimensions. Once the continuous 2D WT computed, local maxima are connected through scales and, as a result, ridges evolve in 3D (see Figure 108).

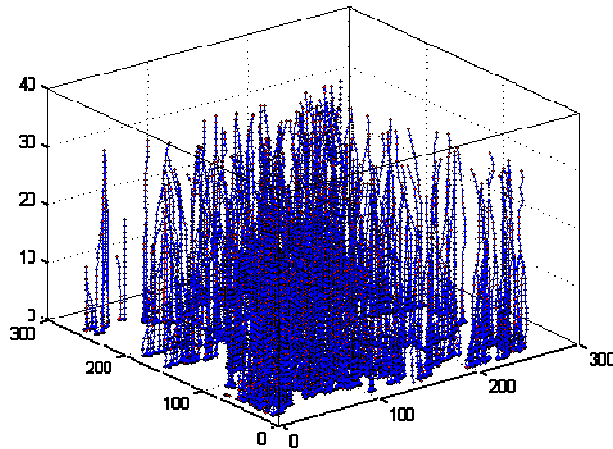


Figure 108. 3D evolution of ridges of a 2D signal.

One limitation of the estimation of the Lipschitz exponent based on the WT modulus maxima is that it is stated assuming isolated singularities. This assumption is not always valid in complex scenarios. Moreover, the set of regularity exponents retrieved is sparse and this fact makes interpretation difficult. The gradient modulus projection method is proposed as a natural extension of the modulus maxima technique to obtain a complete representation of the regularity of a signal [160].

6.2.2 Gradient modulus projection

The gradient modulus projection technique is based on the definition of local energy dissipation. It consists of computing the wavelet decomposition of the modulus of the gradient of the signal to be analyzed. Let's denote $\nabla f(u,s)$ the gradient of function f and $W|\nabla f(u,s)|$ its WT. It can be shown [160] that the regularity of a signal can be pointwise estimated through the slope of the wavelet coefficients across scales, s :

$$W|\nabla f(u,s)| \propto s^\alpha \quad (6.19)$$

where α is the Lipschitz exponent at point u . As a consequence, a measure of α can be obtained by performing linear regression to the evolution of logarithmic transform of wavelet coefficients at point u across scales (see Figure 109).

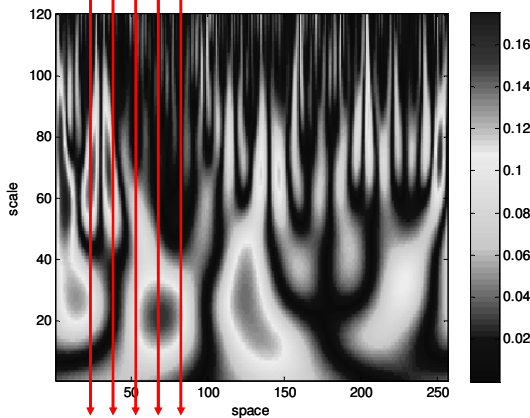


Figure 109. Estimation of the Hölder exponent by gradient modulus projection.

The main advantage of the alternative technique presented in this section is that it produces a dense representation. For instance, a Lipschitz exponent is associated to every single point and not only to those ones in which a ridge ends up.

6.2.3 Estimation of the fractal dimension based on the Wavelet Transform

As seen in section 6.1.1, fractality or eventually multifractality is a fundamental property of turbulent flows. As a consequence, a measure of the fractality constitutes a useful parameter to characterize a natural feature, involving turbulent processes.

There exist several methods to retrieve fractality. Traditionally, the most popular has been box counting [164] which results from a direct application of the topological definition of the concept of fractality. Specifically, the fractal dimension D_s can be expressed as

$$D_s = \frac{\ln N(\lambda)}{\ln(\lambda_0 / \lambda)} \quad (6.20)$$

where $N(\lambda)$ is the number of objects of scale λ , measured from the initial overall size λ_0 , needed to cover the set presenting self-similarity. Nonetheless, more sophisticated techniques have been explored. A comparison of some of them is carried out in [160].

The fractal dimension of a pattern can be directly extracted from the Hölder exponent [162] [165] [166] such as

$$D_s = N + 1 - H \quad (6.21)$$

where N corresponds to the Euclidean dimension of the space considered. For example, that section is concerned with measuring roughness and therefore, $N=2$. H is the Hurst exponent, which is related to the Hölder or Lipschitz exponent as:

$$H = \frac{\alpha - 1/2}{2}. \quad (6.22)$$

6.3 Application to oil spill detection in maritime SAR images

The techniques of analysis of local regularity presented in previous sections will be applied to the detection of oil spills in the sea surface in SAR images.

Monitoring of pollution in the seas is one of the main concerns of the GMES Marine Core Service. Oil spills in the ocean have long term consequences in the coastal and marine habitat, posing a serious threat to ecology. In the public conscience, the most striking oil discharges in the ocean are accidental ones, such as the Prestige casualty in November 2002 in the Galician coast (see Figure 110 or the explosion of the BP drilling rig in the Gulf of Mexico in April 2010 (see Figure 8). Nonetheless, accidents on tankers and platforms make up only 7% of the pollution in the seas [167] and the main source of marine pollution is due to deliberate and illegal oil spills in the open sea for tanker cleaning. As a consequence, the prosecution of responsibilities can contribute to the prevention and reduction of oil pollution in the ocean, whereas an early warning can reduce environmental damage.



Figure 110. Prestige accident in November 2002 in Spain and manual clean up of the coasts.

Traditional means of surveillance such as planes or patrol vessels are expensive and have limited efficiency, since they are not able to cover large areas and they can not operate by night and under adverse weather conditions. On the contrary, thanks to their capability to

cover large areas, in all weather conditions, during the day as well as during the night, spaceborne SAR systems constitute an extremely promising alternative to traditional surveillance methods [161] [168]. SAR sensors can identify pollutants from crude-oil emulsions, run-off water from acidic pitch deposits on land, drilling fluids from offshore oil rigs, waste from fish production plants and fish fat remaining on the sea surface. Due to their resolution, the insufficient revisit time and the actual low performance of automatic techniques due to the high number of false alarms, nowadays, disaster management strategies can not be exclusively based on SAR systems [169]. Nevertheless, due to their unique properties, they potentially constitute a useful support of spill response decision making agents. They provide regular and large coverage over areas which are not easily surveyed with aircrafts. Besides, in front of aircrafts, satellite operations are more cost effective and they furnish a better overview of oil spreading. In Europe, the European Maritime Safety Agency (EMSA) supports an operational service on oil spill detection in European waters and new SAR sensors are planned to be launched in the near future [170].

Once the images acquired, they have to be efficiently interpreted. This post processing step presents several difficulties, discussed in detail later on and the interpretation is usually performed manually, by an experienced analyst. Apart from its low time efficiency, manual detection of oil spills in SAR images is subject to a high variance, according to [171]. As a consequence, segmentation has to be performed automatically.

6.3.1 Oil spills in SAR images

Oil spills and films of natural surfactant materials, provided they are of sufficient extent, are observed as low backscatter patches in SAR images.

For instance, an increase of the viscosity due to oil notably reduces the roughness of the sea surface (already noticed by Benjamin Franklin in 1774 [172]), which is the source of the electromagnetic backscattering (see Figure 111). Hence, an oil spill is characterized by low-backscattered energy and appears as a dark patch in a SAR image. More specifically, according to Marangoni's theory, slick damps gravity-capillary waves, because the oil on the water surface reduces surface tension and friction between wind and liquid [173] [174] [175]. This results in a modification of the ocean spectrum. When the introduction of an external element alters the wave balance, the system reacts by spreading uniformly the energy through its whole spectrum in order to recover equilibrium. In fact, the waves transfer part of their energy to the peak of damping produced around the Marangoni resonant wavelength.

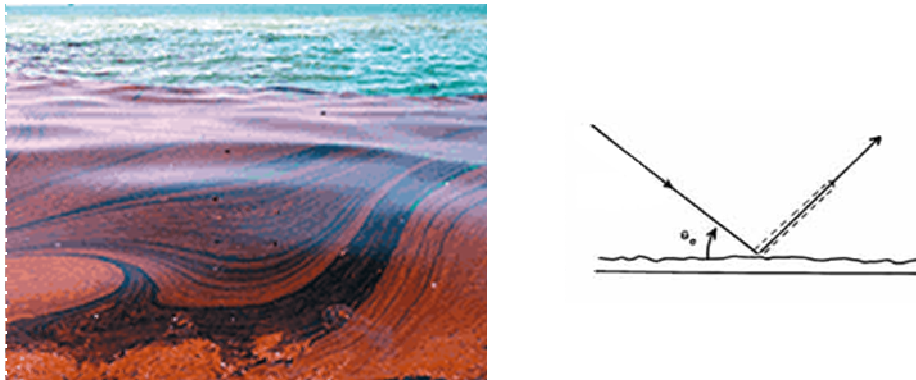


Figure 111. Backscattering as a function of sea surface roughness, in the presence of an oil spill.

Even if SAR systems have already proven to be well suited for the monitoring of oil spills in the sea surface, the visibility of the slicks in the SAR images is subject to parameters related to the radar configuration, as well as to meteorological and maritime conditions and characteristics of the spill.

More specifically, according to the radar frequency band, several experiments assisted by the results of numerical simulations have proven that C, X and Ku bands favor the contrast between the spills and the sea background [176] [177] [178] [179] [180]. According to the literature, the effect of the polarization on the slick detection capability is not fully assessed [181] [182] [183]. For the incidence angle, since the Bragg reflection is the dominant mechanism for a 20° - 70° incidence angle, this region is preferred. By taking also into account the wind constraints, incidence angles from 20° to 45° are especially well suited.

The wind has a meaningful impact for slick imaging purposes with SAR sensors. According to the literature, the interval of wind speeds more propitious for the detection of surface films at C-band frequency goes from $2\text{-}3$ to $10\text{-}14 \text{ m.s}^{-1}$ [175] [182]. Lower wind speeds do not produce surface roughness in the sea and, as a consequence, they appear as dark patches in SAR images. For instance, in the context of spill detection, low wind areas constitute a major source of false alarms. On the contrary, a higher wind speeds roughens the sea surface even in the presence of viscous films. Under these circumstances, slick areas produce a backscatter similar to that induced by the background sea. As a consequence, contrast decreases and discrimination is thus more difficult. On the other hand, high winds have two effects that difficult the capability of SAR systems of detection of the slick: they spread the slick very quickly and they produce high clutter [184] [185].

Furthermore, the aspect of the oil spill in the SAR image also depends on the characteristics of the spill. The damping produced in the wave backscattered to the radar depends on the viscosity and elasticity properties of the slick [175] [186].

6.3.2 Main drawbacks for segmentation and state of the art

As seen in previous sections, the presence of an oil spill in the sea surface is noticeable in the SAR image as a dark patch. The main difficulty for segmentation is the fact that oil spills are not the only phenomena producing a reduction of backscattered energy to the SAR sensor and hence a dark area in the resulting image. Apart from the absence of wind as already introduced in previous section, the presence of phytoplankton, of algae, rain cells, grease ice and internal waves constitute possible sources of ambiguity [187] [188] [189].

The two main difficulties of performing an efficient discrimination of oil spills and look alikes can be observed in Figure 112 and in Figure 113. On the one hand, essentially due to the evolution of the slick when interacting with the wind in the sea surface and currents, the appearance of oil spills in SAR images is subject to a great diversity. As a consequence, the assumption of a priori models is not efficient, the training of algorithms based on neural networks is time consuming and techniques exclusively based on morphological features are not robust. On the other hand, oil spills and look alikes can present remarkable similarities.

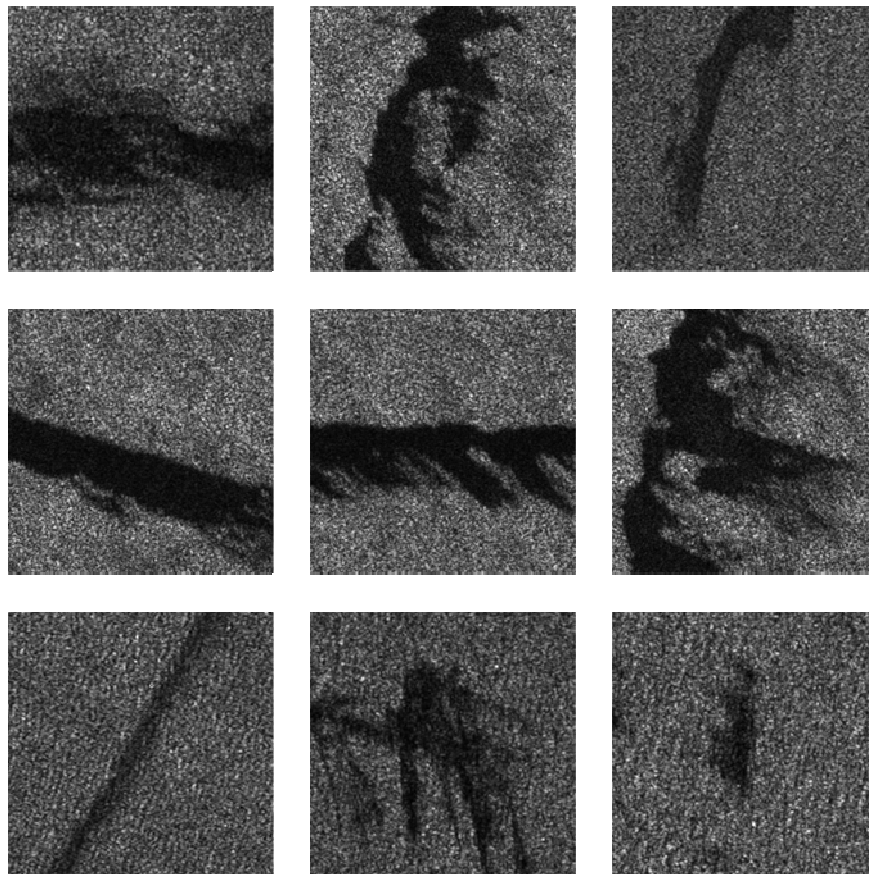


Figure 112. Examples of oil spills in the sea surface.

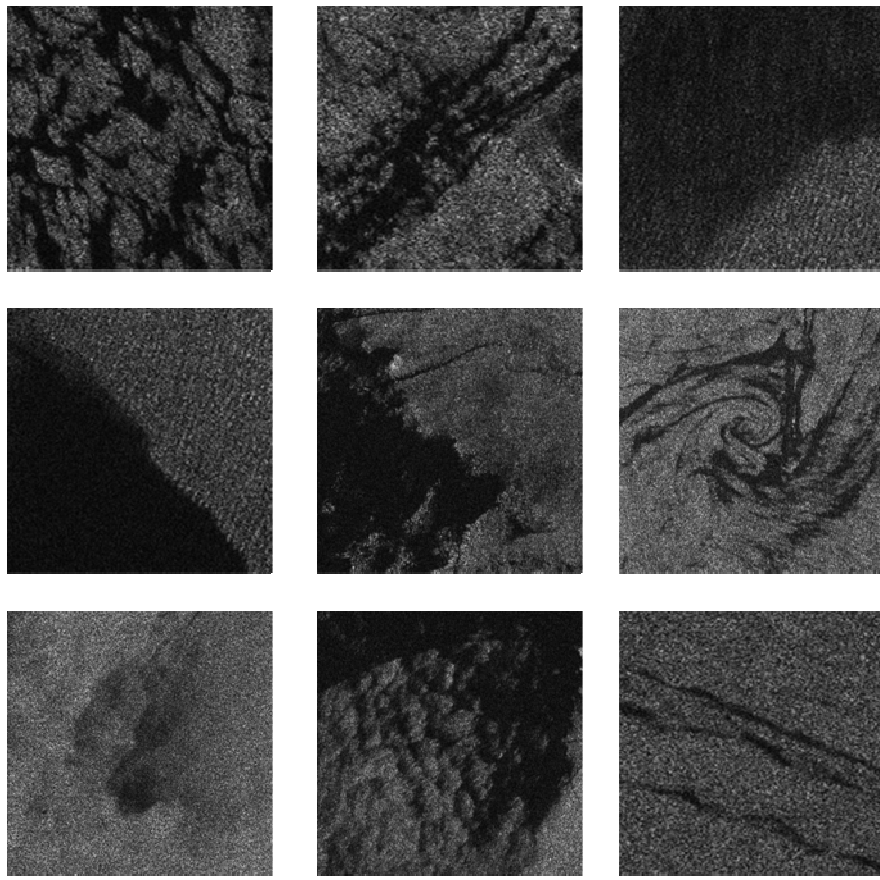


Figure 113. Examples of look-alikes in the sea surface.

Several semi automatic approaches have been proposed in the last years, but a reference method does not exist yet. In general, they are based on three steps: the detection of dark areas, the extraction of statistical parameters of dark formations and the comparison of these set of features with predefined ones determined through phenomenological considerations and statistical assessments [170]. More specifically, a first set of works are based on thresholding techniques to detect oil spill candidates [190] [191]. Another series of papers [192] [193] [194] [195] [196] proposes methods for the semi-automatic probabilistic discrimination of oil spills and look alikes, based on the consideration of contextual information such as the presence of point targets (vessels or offshore platforms) in the vicinity of the oil spill candidate, wind speed in the sea surface and visual observation of the slick surroundings. More recently, in [197] a system for segmentation and feature extraction of oil spills is proposed based on digital image processing techniques, such as filters, gradients and mathematical morphology. In [198], a stand-alone application which offers the user the oil spill candidates with an estimation of their likeliness based on a fuzzy classifier is presented. In [199], a classification technique is designed based on the estimation of a number of parameters and fuzzy logic. Multiscale approaches have also been considered [200] [201] [202] and in [203] a strategy is presented based on the segmentation of the shape of the local sea-surface wave spectrum.

As already shown, the decrease of intensity is the most significant effect of oil slick presence on SAR images. However, other factors, more subtle, can hold the key in the discrimination of oil spills and look-alikes.

For instance, in [204], an experimental study has been carried out considering, apart from the intensity of the image, the normalized intensity moments defined as

$$NIM = \frac{I_n}{(I_1)^n} \text{ where } I_n = \int x^n f(x) dx \quad (6.23)$$

where $f(x)$ is the probability density function of x . These measures provide information of the pixel intensity distribution around the mean value. It has been empirically observed that higher order moments significantly differ between an oil-free area (even in low wind conditions) and a polluted one. Conceptually, this may constitute an interesting observation. Nonetheless, from a practical point of view, a precise estimation of the intensity moments in an image requires considering a large number of samples (and the higher the moment to estimate, the larger the amount of samples to consider). Since oil spills are not usually extended over a large number of pixels, the estimation of the intensity moments in **¡Error! No se encuentra el origen de la referencia.** is not feasible.

On the other hand, natural and artificial slicks in the ocean surface exhibit different fractal characteristics [203]. In fact, sea surface exhibits self similarity at all radar reflectivity levels, whereas artificial oil spills present lower fractal dimensions. This assumption stands both for the contour of the slick as for the surface roughness.

6.3.3 Experimental results

6.3.3.1. Validation through simulated images

The multiscale algorithm proposed for texture analysis and represented in Figure 114 has first been tested on a series of simulated signals.

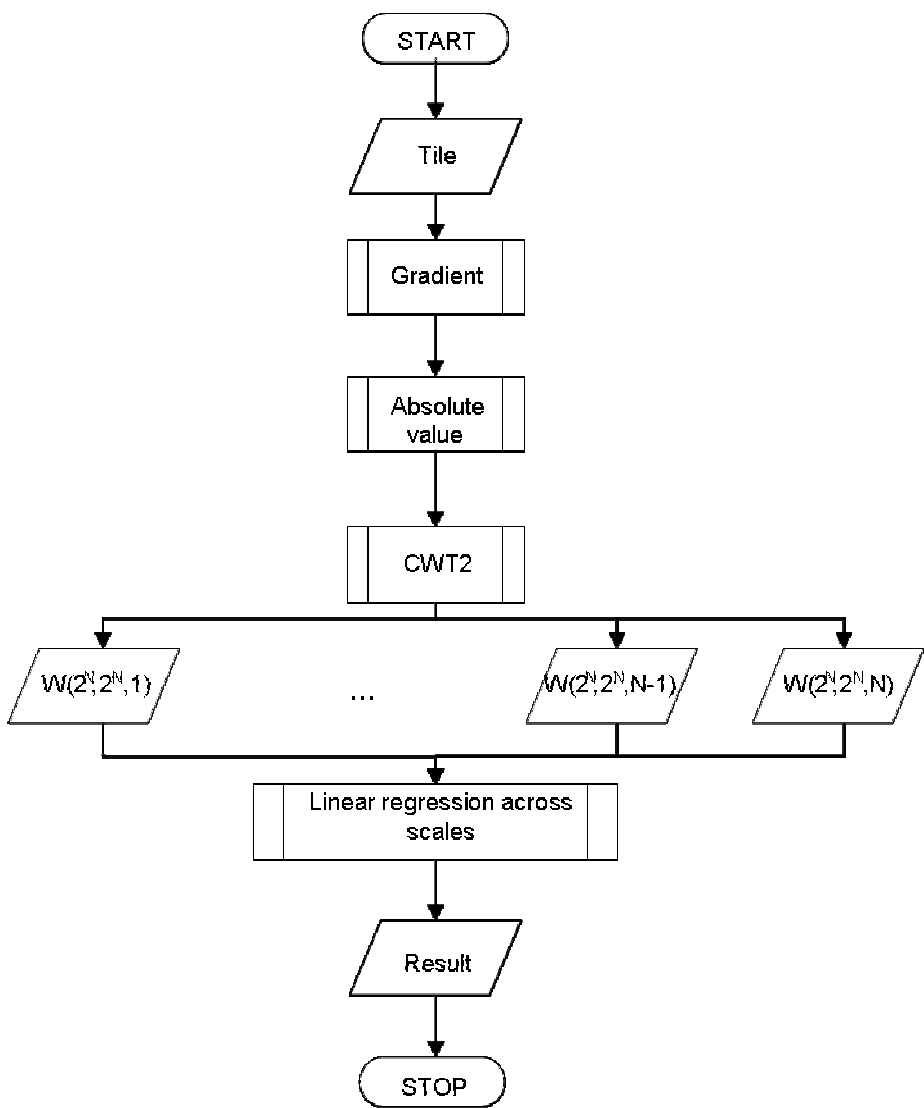


Figure 114. Flowchart of the algorithm for the local estimation of the regularity.

The first test is carried out on a set of simulated speckle matrices. The objective is to verify that the technique proposed is not dependent on the intensity of the image. A 512×512 pixel speckle matrix is synthesized and its regularity is retrieved with the multiscale method proposed (see Figure 115). Then, the intensity of the input signal is increased through multiplication with a constant value. As expected, the same regularity is retrieved in both cases.

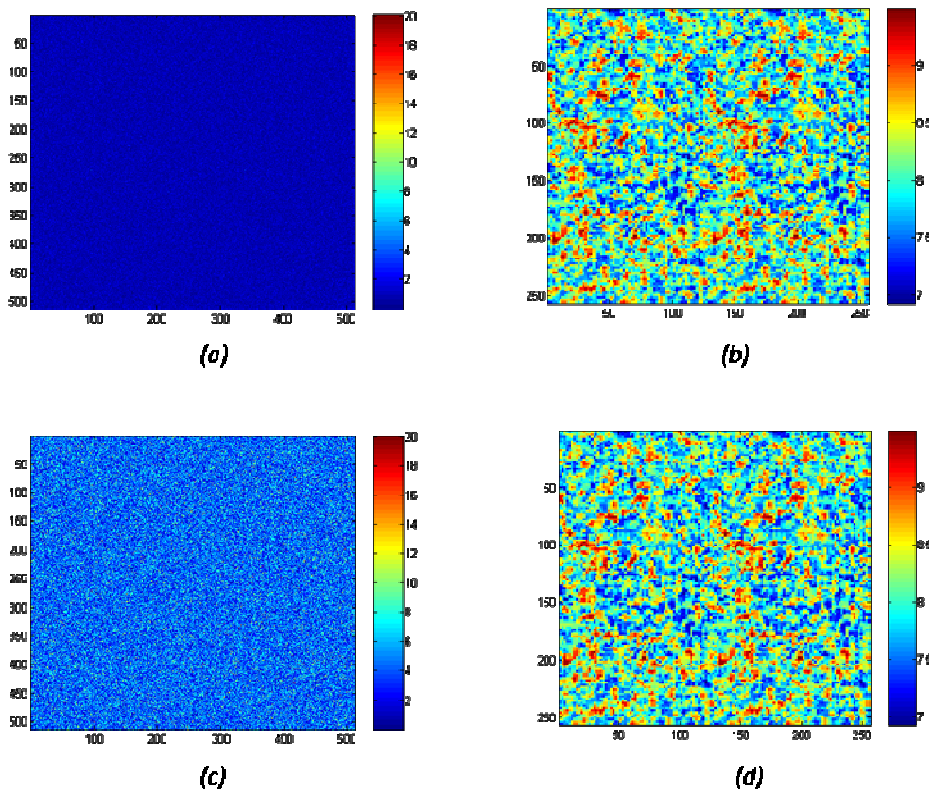


Figure 115. Independency of the algorithm on the intensity of the input image. (a) Simulated sea surfaces and (b) corresponding local fractal dimension. (c) Simulated surface increased by pointwise multiplication with a constant value and (d) corresponding local fractal dimension.

On a second step of the validation with simulated data, fractional Brownian motion surfaces with a given, non homogeneous Hölder exponent have been synthesized. The method proposed has been applied to these simulated signals to retrieve a local estimation of the regularity. An example is shown in Figure 116. It can be observed that the Hölder exponent estimated matches the original Hölder one precisely.

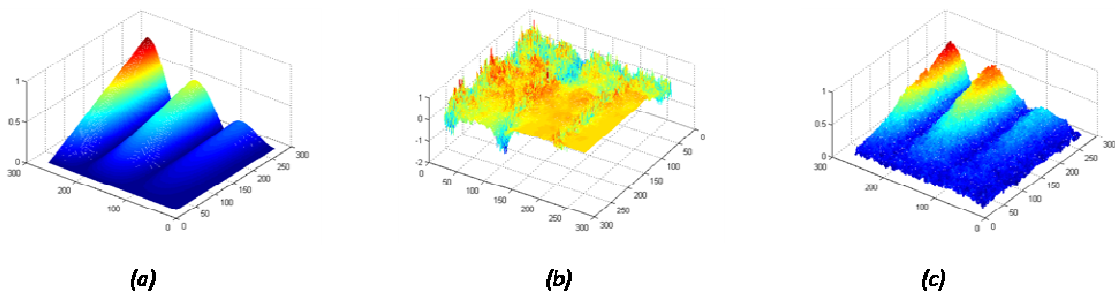


Figure 116. Retrieval of the Hölder exponent of a fractional Brownian motion process. (a) Input Hölder exponent. (b) Fractional Brownian motion surface. (c) Hölder exponent retrieved.

Then, the technique is tested on simulated images resulting from a SAR signal simulator, which is able to reproduce SAR images relative to ocean surfaces covered by oil slicks [204]. The simulator relies on a sound physical model that allows evaluating the SAR return starting from knowledge of sea state and oil properties. It is based on an oceanographic model that predicts sea surface modifications caused by an oil layer [175]. The simulator then generates the SAR model taking into account the ocean dynamics and the electromagnetic wave-ocean surface interaction.

The fractal dimension of the simulated images is estimated with the techniques introduced in previous sections. Two results are shown in Figure 117. The first example corresponds to a simulation of a calm sea surface with several oil spills with different shapes. The second example exhibits as well a calm sea surface with two low intensity areas. The one in the upper left corner corresponds to an oil spill, whereas the one in the lower right corner corresponds to a low wind area. It can be observed that the fractal dimension retrieved in the simulated oil spill is lower than that in the clean sea surface. This result matches the qualitative theoretical hypothesis stating that the presence of a fresh artificial spill decreases the fractality of the sea surface. Moreover, it can be noticed that in spite a lower backscattered energy in the low wind area, the technique applied retrieves correctly the same fractal dimension for the sea surface and for the look-alike. As a consequence, this test proves the robustness of the algorithm in front of false alarms.

Nevertheless, from a quantitative point of view, it is worth noting that the expected fractal dimension values are slightly higher than those retrieved. For instance, according to the literature [205] [206] [207], the value of the fractal dimension in the artificial oil spill should be around 2.1, whereas the fractal dimension in the sea surface is expected to be 2.4 approximately. The experimental results obtained on the set of simulated data by the SAR signal simulator of the University of Naples give a mean value of 1.9 for oil spills and of 2.2 for the sea surface and this with a very low standard deviation.

At last, it is worth observing the local peaks of fractality produced by the edges of the spills. Our hypothesis is that they are produced by the way of generating the spills in the simulator which provides very sharp edges. As it will be seen in following section, these border effects do not appear in the results with real data.

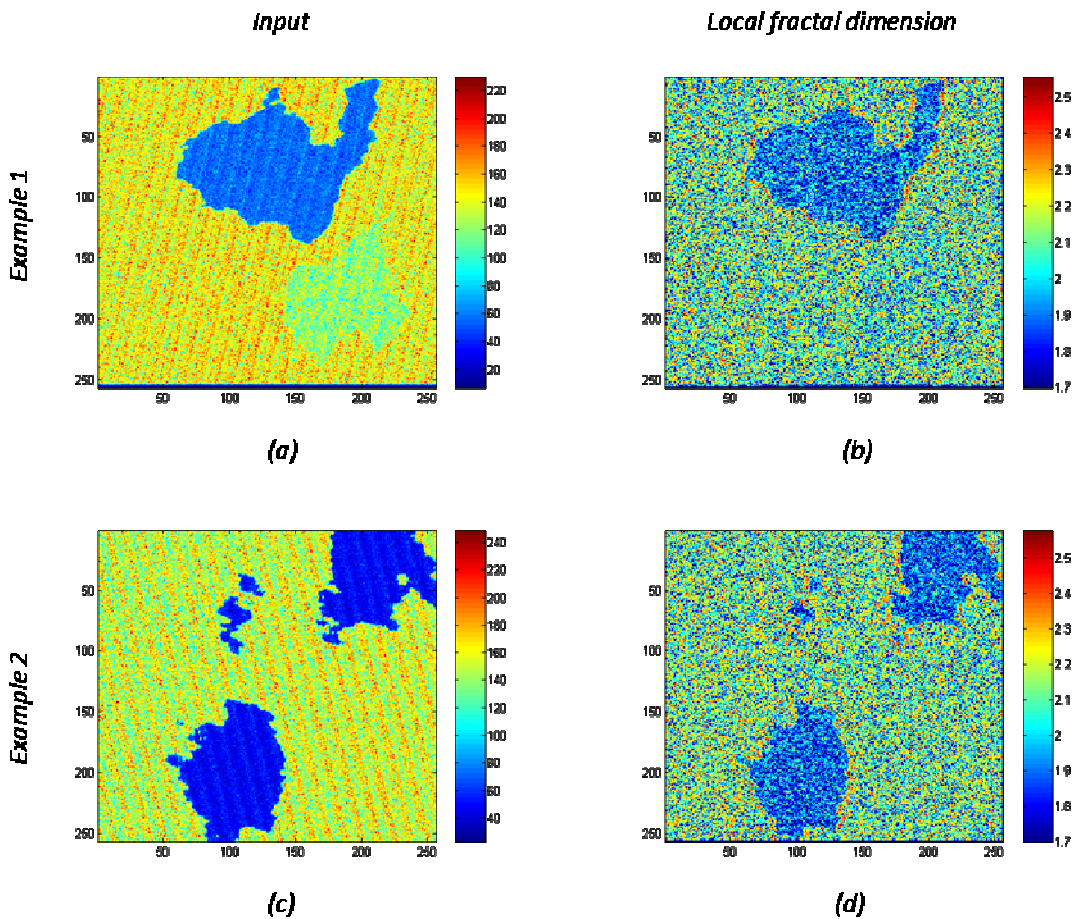


Figure 117. Two examples of retrieval of the local fractal dimension in images generated by a SAR simulator. Example 1: (a) Input image and (b) corresponding local fractal dimension. Example 2: (c) Input image and (d) corresponding local fractal dimension.

6.3.3.2. Validation through real data

A second step of the validation consists of the application of the multiscale algorithm developed to SAR images. In front of simulated data, real scenarios present a great diversity of unpredictable heterogeneities, impossible to cover by simulations. Nonetheless, the counterpart of the processing of real data in front of simulated ones is the habitual lack of ground truth. Apart from a limited number of experiments with controlled spills in the open ocean ([181] [208] among others), the nature of the eventual spills in the images is usually unknown. As a consequence, the validation is usually performed through visual inspection. The manual discrimination by an experienced operator between an oil spill and a look alike is reliable in most of the situations, but not infallible: in some cases, the operator can not decide.

A dataset constituted by ten ERS and ENVISAT images, acquired at different dates, at different places, will be tested. In these images, one may find artificial oil spills, as well as look alikes of diverse natures. As an example,

Figure 118 shows two of the images employed. The first one corresponds to an ERS, PRI image of the area of Barcelona (Spain). Several dark areas due to natural maritime phenomena are present. They will be useful to analyze the behavior of the techniques proposed in front of false alarms. The second one corresponds as well to an ERS PRI image of an area in the Mediterranean Sea, near to the Egyptian coast. One may observe a number of oil spills in a homogeneous calm sea surface.

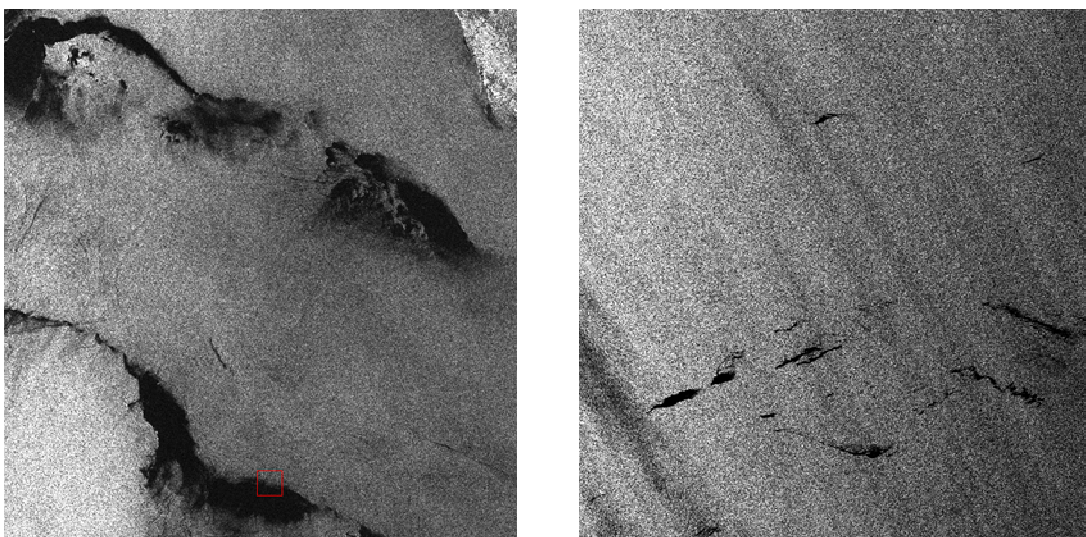


Figure 118. Two examples of SAR maritime images in the presence of oil spills and look-alikes.

The local regularity of the images has been estimated by means of the multiscale techniques exposed in previous sections. The method of gradient modulus projection (see 6.2.2) is preferred over the method of the WT modulus maxima followed by the subsequent definition of ridges (see 6.2.1). Results obtained are quantitatively similar, but the later produces a non dense representation and its computational cost is noticeably higher. As a consequence, results presented in this chapter, unless otherwise stated, have been obtained by the method of gradient projection, with five scales and a Mexican hat family of wavelet functions.

On the one hand, Figure 119 recaps results obtained over imagettes presenting oil spills. As hypothesized, local fractality in the oil spill is significantly lower than in the clean sea surface. It can be observed that this feature is independent on the intensity values of the input image and that the presence of the oil spill appears neatly enhanced in the representation of the local regularity of the image. On the contrary, natural patterns producing dark areas in the input images appear as blurred in the result image (see for example dark areas in the lower right corner of the first row in Figure 119). From the point of view of the resolution of the result, it can be observed that the estimation of the regularity is retrieved independently at every single

pixel, i.e., leading to the same resolution in the result than in the input image: no low pass effects due to a loss of resolution are noticeable; the edges are sharp, not blurred. An example of the good resolution capabilities of the method is the first case of Figure 119. The spill appears divided by a narrow band which is effectively reproduced in the result. Moreover, the result is not affected by edge effects which constitute a common drawback when using wavelet tools. Nevertheless, it can be noticed that the shape of the oil spill appears narrower. This is due to the age and history of the spill. If the spill is not fresh, its older parts and its limits have begun to disintegrate and melt with clean water. Thus, these areas rapidly recover the fractality of the sea surface.

On the other hand, Figure 120 presents examples of several images with natural phenomena source of false alarms in the scope of automatic spill detection. In the input images (left column), it can be observed that the look alikes appear as dark areas with a similar overall contrast with respect to the clean sea surface than the oil spills of the examples shown previously in Figure 119. As it can be observed in the representations of the local regularity retrieved, these natural slicks slightly lower the fractal dimension of the sea surface. However, in views of automatic segmentation of oil spills and natural slicks, the key point is that the fractal dimension of a natural slick is usually higher than that of a fresh oil spill.

Specifically, from a quantitative point of view, for the entire set of images considered, the mean fractal dimension obtained in the oil spill is of 2.05, of 2.24 for the natural look alikes and of 2.40 in the sea surface. These values are very similar to those hypothesized in [205]: 2.45 for the clean sea surface and 2.15 for the artificial oil spill. Moreover, the hypothesis stated in [206] [207] has also been verified: the fractal dimension on the oil spill is lower than the fractal dimension in the natural oil slick.

For automatic segmentation purposes, since the deviation from these mean values is low, the retrieval of the local regularity by means of the multiscale techniques proposed can be used to detect the presence of oil spills and to discard eventual sources of false alarms.

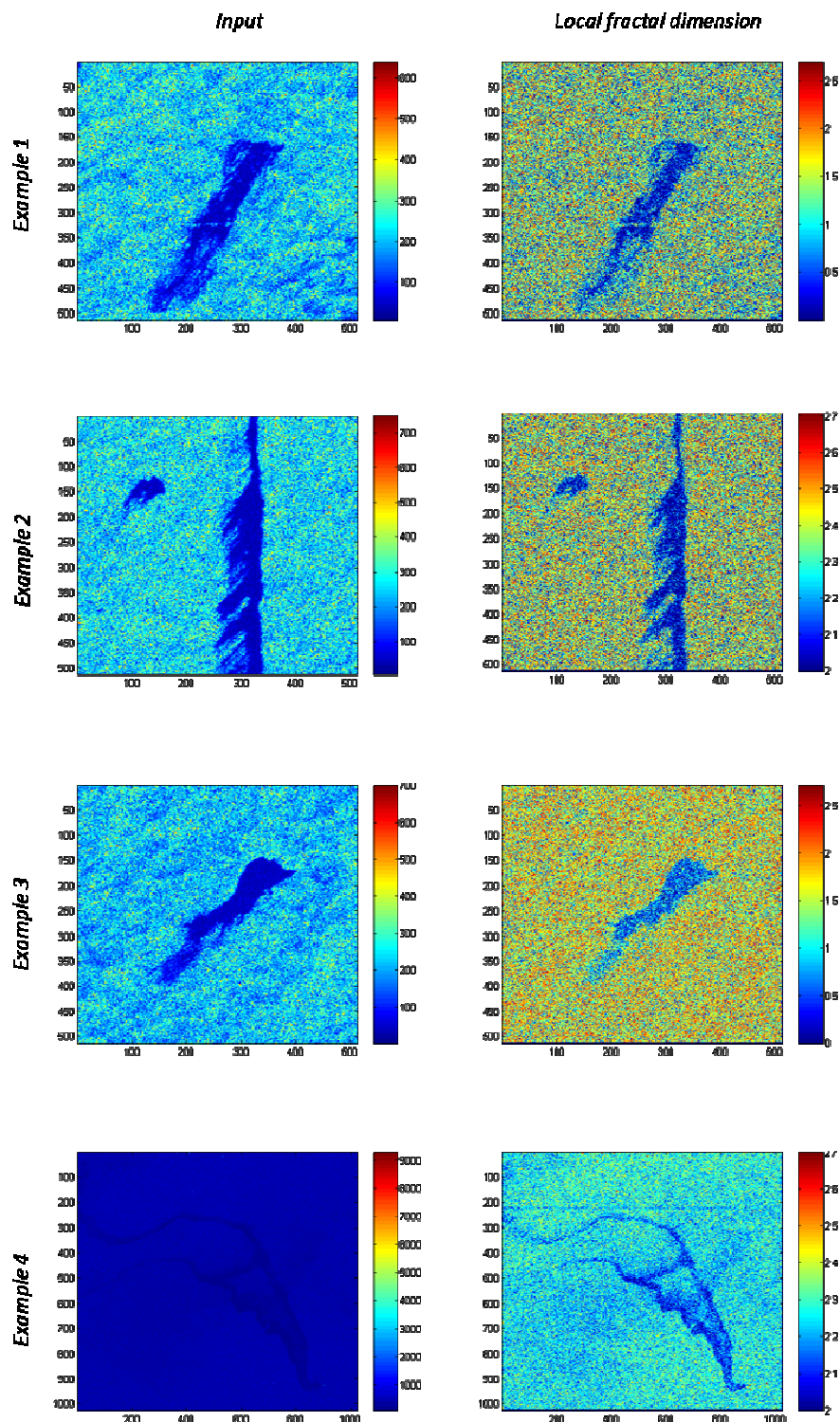


Figure 119. Examples of automatic retrieval of the local fractal dimension in maritime SAR images with oil spills.

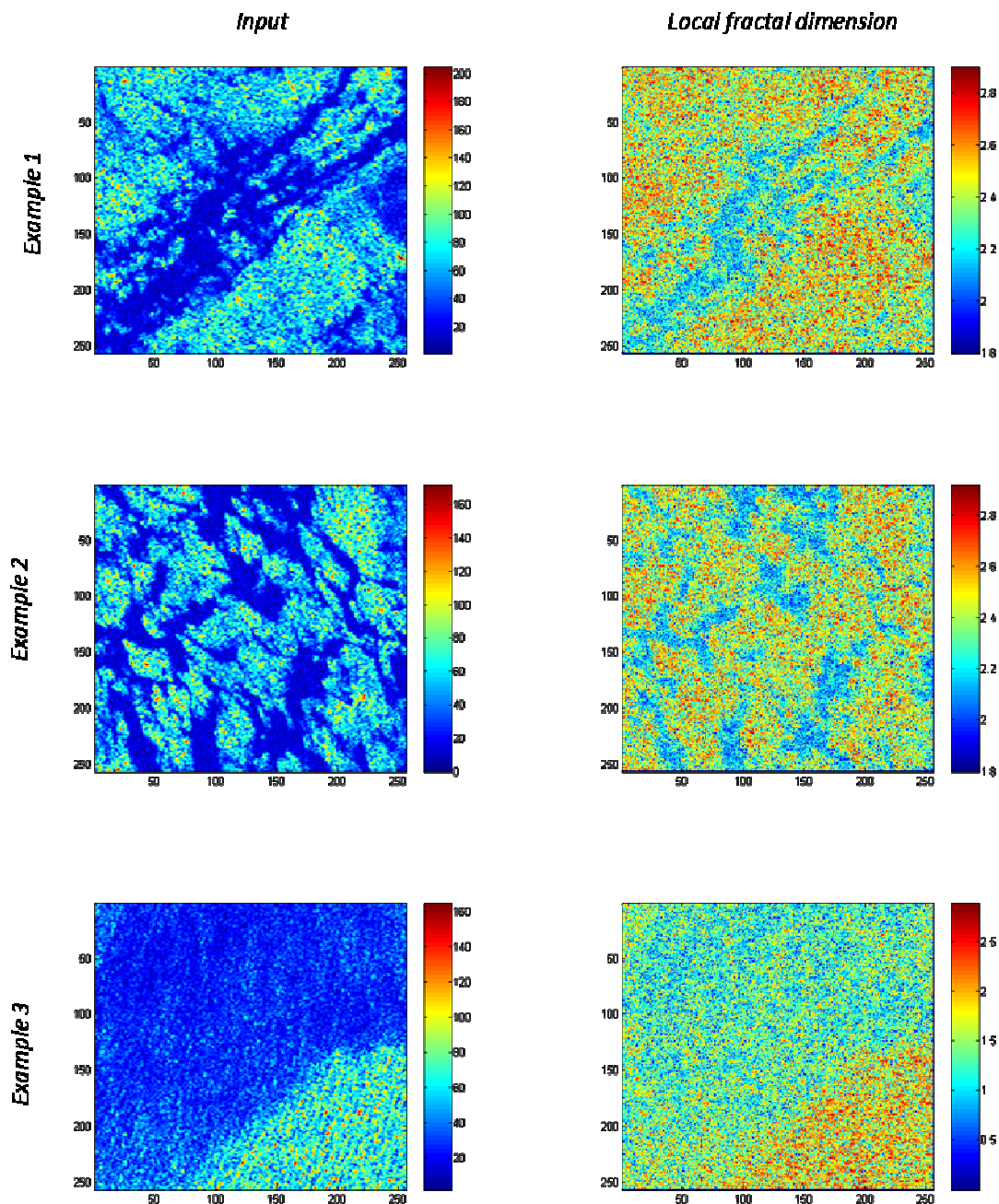


Figure 120. Examples of automatic retrieval of the local fractal dimension in maritime SAR images with look alikes.

6.4 Conclusions

This Chapter has been devoted to discuss the retrieval of an estimation of the local regularity of maritime SAR images. In particular, a technique based on the evaluation of the Hölder or Lipschitz exponent has been proposed and further extended to the estimation of a measure of the local fractal dimension. Following the framework in which this dissertation is inscribed, the algorithms employed are based on multiscale wavelet analysis which has shown to overcome the flexibility of other methods for fractality measurement such as box counting. The algorithm has been validated through simulated images and SAR data. Nonetheless, the validation of the technique is at a preliminary phase, due to the non availability of a large enough dataset and to the lack of groundtruth.

The usefulness of the estimation of the local regularity for automatic oil spill detection in SAR images has been evaluated. Experimental results match the theoretical hypothesis stating that, provided it is fresh, an artificial oil spill lowers noticeably the fractality of the sea surface where it is poured. Moreover, most of the natural slicks or other natural phenomena, even if they appear in the image as dark patches with similar intensities than the oil spills, have a fractal dimension considerably higher than that of an oil spill. As a consequence, this feature may be employed to automatically detect oil spill candidates and to discard false alarms produced by natural phenomena. This method is simple and robust and it is well suited for an unsupervised scheme since it does not present degrees of freedom apart from the number of scales and the nature of the wavelet functions employed which are not critical. This is particularly useful in front of neural network solutions since due to the diversity of scenarios, training is difficult and not efficient.

Nevertheless, oil spill detection in the ocean with SAR sensors is highly dependent on the wind velocity. It is considered that SAR sensors are only sensitive to the presence of an oil spill in the sea surface provided a wind velocity in the sea surface within the range of 3-10 m/s. Moreover, if the spill is not recent, its visibility diminishes and automatic algorithms reduce their performances. As a consequence, an operational system for oil spill detection exclusively based on SAR systems is not completely viable yet.

Even if out of the scope of this dissertation, the algorithms developed for the retrieval of local regularity in maritime SAR images have been applied to more general scenarios. Due to their characteristics, they can be useful in coastal and inland applications as well. An example is given in Figure 121. It corresponds to a semi urban scene. A small town is surrounded by agricultural fields. The output image retrieves the local fractal dimension of this scene. The different elements in the scene can be easily identified, as the technique has good resolution capabilities. As expected, the lower fractal dimensions correspond to man-made features. Moreover, it can be observed that fine regularity variations are effectively captured by the method.

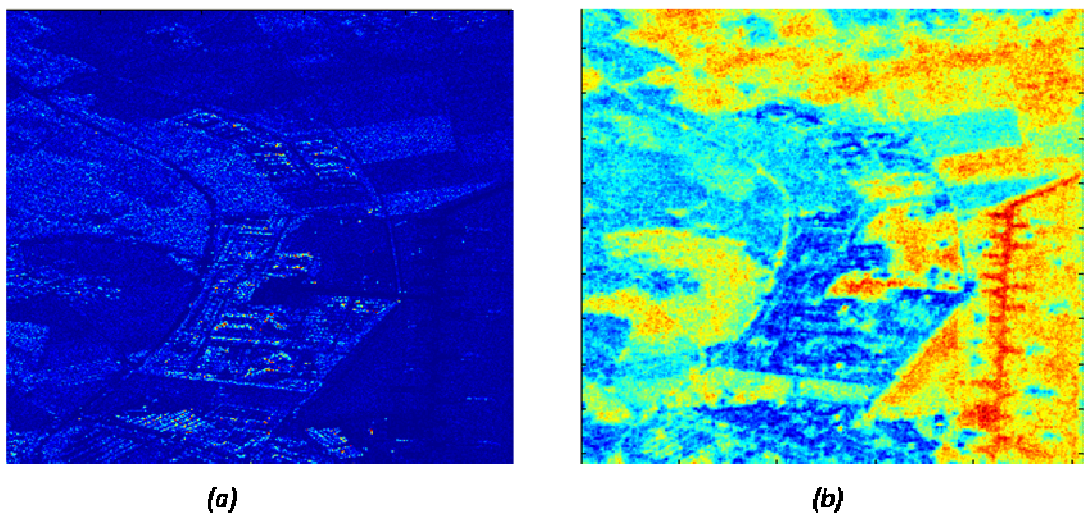


Figure 121. Automatic retrieval of the local fractal dimension in an inland SAR image. (a) SAR image of the area of Oberpfaffenhofen in Germany and (b) corresponding local fractal dimension.

Chapter 7. Conclusions

The ocean is a vulnerable environment, subject to exploitative activities and it is one of the principal agents involved in climate change. In the last years, governments and industry parties have taken conscience of the urge of continuous observation of oceanic parameters at a global scale. In that sense, remote sensing tools constitute a powerful monitoring solution. Among the different remote sensing tools, spaceborne SAR sensors present a series of distinctive capabilities which make them useful for a large coverage observation with independence on the day – night cycle and on the weather conditions. Nonetheless, fully operational services with SAR images are difficult to establish, mainly due to the fact that unsupervised post processing techniques in SAR data are not always available and efficient. The main purpose of this dissertation has been to investigate the feasibility of automatic ocean monitoring in SAR imagery and proposing unsupervised post processing methods specific for this purpose.

A general recap of the ensemble of the present dissertation is briefly sketched hereafter. The introduction in Chapter 1 goes through the framework of interests in a series of civilian applications of remote sensing in oceanic scenarios giving rise to the questions addressed in this thesis.

Chapter 2 is devoted to review the mechanisms involved in the formation of a SAR image. This analysis permits understanding how the information contained in the observed scene is reflected in the SAR image and it establishes the basis necessary for a consistent interpretation. Then, through a succinct survey of several applications in which the use of SAR is especially interesting, the need of developing unsupervised methods for data interpretation is justified. The main drawback is that the SAR system of data acquisition and processing induces intrinsic features in the SAR images that render their automatic interpretation difficult.

These particularities are analyzed in order to establish a signal processing framework suitable for their treatment. Attending to this analysis, the suitability of a multiscale space – scale approach is justified in Chapter 3. Mathematical basics of time – frequency decomposition methods and, in particular, of the WT are given. Once the theoretical formalism exposed, the objective has been to obtain a framework for the qualitative and complete extraction of information from SAR images, going from high entropy elements to low entropy ones, just like the operation of the mammal visual system. This is the most efficient way to manage the information contained in a scene, whatever its nature.

As a consequence, spots are the first features addressed (Chapter 4). The notion of spot has been deeply discussed. In particular, it has been observed that the intuitive concept is difficult to translate into a mathematical one and that no useful theoretical model can be established in that case. As a consequence, unsupervised spot detection has to be addressed with no a priori information, apart from, eventually, a range of scale of the dimensions of the spots to be detected. However, even if a mathematical model is difficult to establish, it has been shown that the presence of a spot is noticeable by a local maximum in the spatial correlation. Besides, it has been observed and justified that the presence of a local peak of spatial correlation can be enhanced by a suitable combination of wavelet coefficients at a same scale, due to the fact that the WT is not a perfect whitening process, leaving a residual correlation, often neglected, between subbands both within a same scale and at different scales. Within a scale, the usual isometric distribution of pixels belonging to a spot provokes a co-occurrence of similar values in the bandpass subbands of the wavelet decomposition, at the location of the spot. Taking advantage on this property, an Unsupervised Spot Enhancement Algorithm (USEA) has been proposed. Even if it is also valid for its use on optical imagery, it has primarily been developed to deal with speckled SAR images. It is based on the combination by means of a pointwise product of wavelet subbands within the same scale. Contrarily to conventional methods, it provides a qualitative result directly in the wavelet domain, thus resulting in an enhanced contrast between the target and the homogeneous background due to sparsity of the WT, further increased by the intrascale product. Besides, it is worth noting that the contrast achieved in the wavelet domain depends on the spatial correlation in the original domain and not exclusively on its intensity values. This is a distinctive property of USEA compared to the algorithms most commonly employed for automatic spot detection. After the spot enhancement phase, the final decision phase consists on simple thresholding. The automatic evaluation of a threshold is usually a delicate issue, which effectiveness is directly related to the existing contrast between the target and the background. In that sense, the main advantage of USEA is that it provides a high contrast that makes this operation straightforward

in most of the cases, enhancing detection rates. USEA has been tested on a set of RADARSAT and ENVISAT SAR images in the scope of ship detection, which is treated as a particular case of spot detection with a high practical interest. It has been confirmed that automatic ship detection from SAR images can be performed with high performance rates. The most difficult situation of detection is the one that involves small vessels with a low reflectivity, in heterogeneous backgrounds. In that case, the sea surface can present spot like features with characteristics very close or even identical to the ones of ships. This situation can not produce an unambiguous detection: unavoidably, it will lead to a false miss or to a false alarm. USEA has been designed considering that a false miss is more problematic than a false alarm and it presents thus a high sensitivity, which makes it suitable for targets of reduced dimensions and low contrast with respect to the background.

An interesting discussion nowadays is to assess the benefits of multipolarization for ship detection purposes. USEA has been extended to multichannel data and it has been tested on ENVISAT dual polarized data and on RADARSAT-2 fully polarimetric images. It has been shown that the availability of polarimetric diversity improves ship detection capability. It has been confirmed that ships are dominated by dihedral like mechanisms and it has been observed that the main drawback for ship detection by means of conventional polarimetric decompositions is the ambiguity of vessels with sea spikes presenting as well a dihedral behavior. For ship detection purposes, USEA overcomes the polarimetric entropy parameter. Comparing the performance of USEA in single, dual and full pol data, it has been verified that an enhancement of contrast of about 30 – 50 dBs is obtained when employing the polarimetric diversity with respect to the single channel case. Nonetheless, the contrast achieved in the single channel case is largely enough in most of the cases for a further automatic decision step. As a consequence, it should be carefully analyzed if polarimetric data obtained at the expenses of a reduction of the swath width is necessary for ship detection purposes.

After spots, edges are the elements with the highest entropy in an image. Hence, automatic edge detection in SAR images is addressed in Chapter 5. First, the notion of edge has been explored. An edge is usually considered as a frontier between two adjacent solid regions but, once again, the translation of the intuitive concept to machine interpretable terms is cumbersome and no mathematical unambiguous model can be defined to assist the detection. Besides, since the edge depends on the range of dimensions considered for the adjacent regions, the notion of edge has to be understood from a multiscale perspective. Hence, a multiscale framework for edge enhancement is established, based on the WT. It is shown that the presence of an edge induces an important peak in the spatial correlation of wavelet subbands sharing the same orientation at different scales, whereas features due to speckle tend to be uncorrelated between scales. Taking advantage of this property, an Unsupervised Edge Enhancement Algorithm (UEEA) is proposed. It is essentially based on the pointwise product of wavelet coefficients at different scales and it provides a qualitative result directly in the wavelet domain. The main properties of UEEA compared to other methods for edge enhancement is simplicity and robustness. After the edge enhancement phase assumed by UEEA, a final decision step is applied, based on a Geodesic Active Contour approach. Then, the technique has been applied to perform coastline detection in SAR images and its effectiveness has been verified in different types of scenarios. In particular, the awkward situation presented

by images with a high presence of topography has been addressed. It has been shown that the technique performs successfully. The extracted coastline matches very closely the real one.

It is worth mentioning that the edge enhancement phase is essential in SAR images: the direct application of the Geodesic Active Contour to the gradient of the image or even after smoothing by means of a speckle filter is unable to capture the relevant edges in the scene.

As a consequence, the complementary application of USEA and UEEA is able to extract the most relevant structural information of a maritime SAR scene, in an unsupervised way. This process is completely self-contained; it does not require a priori hypothesis and settings, nor external information.

Once the structure of an image revealed, a finest segmentation requires texture analysis. This is addressed in Chapter 6 in the specific scope of maritime SAR images. Texture can be understood as the spatial distribution of relationships between samples' amplitudes. Thus, in order to preserve as much as possible spatial resolution, this Chapter proposes the estimation of the local regularity of an image through the evaluation of the Lipschitz exponent for each position of the input image. This is done by studying the evolution of wavelet coefficients across scales. A series of features in the ocean surface, both of natural and man-made nature, modulate the sea surface roughness and consequently the radar cross section. As a consequence, they can be discriminated in SAR data by means of adequate post processing texture analysis techniques. In particular, in the scope of this dissertation, local regularity has been calculated for oil spill detection in the sea surface. The main drawback of this application is the difficult disambiguation between oil spills and look-alikes, produced essentially by low wind areas. A precise measure of the fractality of the sea surface based on the Lipschitz exponent has been proposed to solve this ambiguity. It has been empirically confirmed that an oil spill lowers noticeably the fractality of the sea surface where it is poured in a different amount than the absence of wind or a natural slick. Hence, a measure of the fractality in the sea surface may be employed to identify artificial oil spills with acceptable success rates, while reducing the amount of false positives with respect to other conventional methods exclusively based on the point to point intensity. Despite the high ecological interest in this application, an intensive validation of oil spill detection methods is difficult to carry out due to the lack of ground truth data. Nonetheless, spaceborne SAR sensors constitute a useful tool for this purpose. However, a critical issue to be considered is when the amount of signal backscattered to the sensor is lower than the noise of the system, due to the smoothness of the surface. In that extreme situation, methods have to be aware that they are dealing with a situation of "no signal" in an area. As a consequence, the retrieval of parameters such as the local regularity is meaningless in this area. Other alternative aspects should be explored in that particular case, such as morphological ones.

Moreover, the sensitivity to the surface roughness both of the acquisition system and of the post-processing technique proposed may be employed in other applications, not yet explored. As an example, it would be interesting to identify the amount and extension of seasonal plankton blooms in the oceans by means of spaceborne SAR sensors. Besides, future work should be oriented at testing the usefulness of the techniques presented for texture analysis in inland or ice-covered surfaces. The span of applications is wide.

The contributions of this dissertation range in two main directions: multiscale signal processing and SAR data interpretation. From the point of view of signal processing, a different way of employing space – scale (similarly time - frequency) decompositions is explored. In fact, in image processing applications, multiscale decompositions and, in particular the WT, are commonly used as filters: input data is projected into the time – frequency space and a threshold is then applied in order to reduce the effects of low value coefficients which are associated to noise. Finally, the inverse transform is applied in order to recover a filtered version of the input image. This filtering technique has been widely used and it has proven its efficiency in different applications. Nevertheless, in some cases, low value coefficients in the projected domain may not be exclusively associated to noise and the thresholding of coefficients is delicate, since meaningful information can be erased. Besides, the inversion of low amplitude coefficients may produce artifacts in the output image. Moreover, this filtering procedure is usually employed independently of the nature of the input image and of the application involved. In order to employ more efficiently the information provided by the projection according to the application concerned and to the type of input data and to avoid drawbacks related to the inversion process, this dissertation suggests instead performing the segmentation directly in the transformed domain. It is worth noting that this approach is only valid for qualitative applications, such as the ones considered in this work. Another distinctive aspect of the methods proposed in this dissertation is that they take advantage of residual intrascale and interscale correlations which are usually neglected since the WT is commonly treated as a whitening process. However, it has been shown that accounting for these residual dependencies is a simple, robust and effective way of enhancing the structure of an image. This leads to simple and robust techniques for unsupervised spot and edge enhancement and for the estimation of local regularity in an image.

From the point of view of SAR data interpretation, a framework for the unsupervised interpretation of maritime SAR images has been proposed and it is planned to be developed in an operational way in the near future. Techniques for automatic vessel detection, for the extraction of the coastline and for the detection of oil spills in the sea surface have been designed and largely tested on simulated and real images. Even if extensions to multichannel data have been proposed and tested, the algorithms mainly rely on single channel information. Their efficiency has been proven and, whenever possible, it has been compared to other existing approaches. In that sense, due to the lack in the literature of common parameters for the evaluation and further comparison of the goodness of methods, several quantitative indexes have been defined for this purpose. The algorithms proposed are well suited for operational applications since they are not computationally costly, they are self-contained and they require neither the use external data, nor a previous adjustment to input data. As a consequence, they are sufficiently flexible to adapt to different types of input SAR images and they are suitable to be integrated in automatic chains of post-processing. Moreover, even if usually treated separately, the oceanic applications considered in this dissertation are very closely related to each other and numerous contributive interactions can be found. For example, coastline extraction is necessary for the landmask step previous to ship detection. When looking for oil spills, since the objective is to prosecute responsibilities, ship detection is required. Hence, the most efficient exploitation of oceanic SAR images implies a simultaneous use of the algorithms designed for different but complementary applications. As a consequence, this dissertation proposes a combined exploitation of oceanic SAR images. A

more reliable segmentation is obtained through an interpretation simultaneously based on three output layers: result of spot detection, result of edge extraction and result of texture analysis. From the point of view of practical implementation, the three methods developed are based on combinations of coefficients in the wavelet domain. Therefore, the application of the WT is a common step to all of them. As a consequence, a combined application of the three algorithms augments the overall efficiency.

As future work, intensive validation of a fully operational combination of the algorithms designed in this dissertation is to be carried out. Furthermore, the algorithms should be applied to the data provided by new sensors, with enhanced resolution and polarimetric capabilities.

Besides, it would be interesting to extend the tool to the evaluation of other parameters related to the sea surface, such as wind speed, surface currents or sea ice monitoring among others. Their analysis through a multiscale framework would probably offer new capabilities. Moreover, the availability of this information would be extremely useful to assist the applications already addressed.

From the point of view of signal processing, a closer insight on wavelet coefficient dependencies through Hidden Markov Models would probably help in revealing different possibilities of combinations of coefficients to enhance different types of information content. Besides, the establishment of Hidden Markov Model trees would allow the extrapolation of the signal to subpixel level. This may lead to new possibilities in the use of the wavelet framework for analysis purposes, specifically for the understanding of SAR images. In particular, a deep analysis of the speckle concept in SAR images could be considered. New sensors with very high resolution capabilities suggest a revision of the current treatment of speckle in SAR post processing issues.

References

- [1] ESA webpage: www.esa.int
- [2] GMES webpage: www.gmes.info
- [3] GeoEye webpage: www.geoeye.com
- [4] Spotimage webpage: www.spotimage.com
- [5] Digital Globe webpage: <http://www.digitalglobe.com/>
- [6] LandSat webpage: <http://landsat.gsfc.nasa.gov/>
- [7] SMOS webpage: <http://www.esa.int/esaLP/LPsmos.html>
- [8] ERS webpage: <http://earth.esa.int/ers/>
- [9] ENVISAT webpage: <http://envisat.esa.int/>
- [10] RADARSAT 2 webpage: <http://www.radarsat2.info/>
- [11] SEASAT webpage: <http://southport.jpl.nasa.gov/scienceapps/seasat.html>
- [12] RADARSAT webpage: <http://www.asc-csa.gc.ca/eng/satellites/radarsat1/default.asp>

- [13]PALSAR webpage: <http://www.eorc.jaxa.jp/ALOS/en/about/palsar.htm>
- [14]TERRASAR-X webpage: <http://www.dlr.de/desktopdefault.aspx/tabcid-4219/>
- [15]SMAP webpage: <http://smap.jpl.nasa.gov/>
- [16]Sentinel webpage: http://www.esa.int/esaLP/SEMZHM0DU8E_LPgmes_0.html
- [17]Aquarius webpage: <http://aquarius.nasa.gov/>
- [18]Curlander, J.C.; McDonough, R.N.; "Synthetic Aperture Radar: Systems and Signal Processing" John Wiley & Sons, New York, 1991.
- [19]Bamler, R.; Hartl, P. Synthetic Aperture Radar Interferometry. Inverse Problems, 1998, R1 – R 54.
- [20]Massonet, D.; Rabaute, R. "Radar Interferometry: Limits and Potential", IEEE Transactions on Geoscience and Remote Sensing, Vol. 31, No. 2, pp. 455 - 464, March 1993.
- [21]Ulaby, F.T.; Elachi, C. *Radar Polarimetry for Geoscience Applications*, Artech House, Norwook, MA, 1990.
- [22]Lee, J.S.; Pottier, E. *Polarimetric Radar Imaging: from Basics to Applications*, CRC Press, 2009.
- [23]Van Zyl, J.J.; Zebker, H.A., "Imaging Radar Polarimetry", Progress in Electromagnetics Research, PIER 03, pp. 277 – 326, 1990.
- [24]Boerner, W. M.; Yan, W.L.; Xi, A.Q.; Yamaguchi, Y. "On the Principles of Radar Polarimetry: The Target Characteristic Polarization State Theory of Kennaugh, Huynen's Polarization Fork Concept, and its Extension to the Partially Polarized Case", *IEEE Proceedings, Special Issue on Electromagnetic Theory*, Vol. 79, No. 10, pp. 1538-1550, October, 1991.
- [25]Levanon, N.; Mozeson, E.; *Radar Signals*, IEEE Press, Wiley Interscience, Hoboken, New Jersey, 2004.
- [26]Soumekh, M. *Synthetic Aperture Radar Signal Processing*. A Wiley-Interscience Publication. John Wiley & Sons, Inc., New York, 1999.
- [27]Barnard, E.; Odendaal, J.W.; Pistorius, C.W.I.; Two Dimensional Superresolution Radar Imaging Using the MUSIC Algorithm", IEEE Transactions on Antennas and Propagation, Vol. 42, No. 10, pp. 1386-1391, 1994.
- [28]Yildirim, I.; Tezel, N.S.; Erer, I.; Yazgan, B.; "A comparison of non-parametric spectral estimators for SAR imaging", Proceedings of the International Conference on Recent Advances in Space Technologies, 2003. 20-22 November 2003, pp. 369-374.
- [29]Tello, M.; López-Dekker, P.; Mallorqui, J.J.; "A Novel Strategy for Radar Imaging Based on Compressive Sensing", International Geoscience and Remote Sensing Symposium IGARSS 2008, Boston, U.S.A., July 2008.

- [30] Ferrazzoli, P.; "SAR for Agriculture: Advances, Problems and Prospects", in Proceedings of the 3rd International Symposium Retrieval Bio- Geophysical Parameters from SAR Data for Land Applications, Sheffield, UK, ESA SP-475, 2002, pp. 47-56.
- [31] Miller, R.J.; Wright, P.A.; Anderson, C.; "SAR for Agriculture and Forestry (SAFE): Technical Requirements", Retrieval of Bio- and Geo- Physical Parameters from SAR Data for Land Applications Workshop ESTEC, 21-23 October 1998.
- [32] Kühbauch, W.; Hawlitschka, S.; "Remote Sensing – A Future Technology in Precision Farming", Proceedings in Pol-InSAR 2003, Frascati, Italy, January 2003.
- [33] McNairn, H.; Brown, R.J.; McGovern, M.; Huffman, T.; Ellis, J.; "Integration of Multipolarized SAR Data and High Spatial Optical Imagery for Precision Farming"; Proceedings of the 22nd Canadian Symposium on Remote Sensing, Victoria, B.C.; August 21-24, 2000.
- [34] Gaveau, D.L.A.; Balzter, H.; Plummer, S.; "Forest Woody Biomass Classification with Satellite-based Radar Coherence over 900 000 km² in Central Siberia", Forest Ecology and Management, Vol. 174, 17 February 2003, pp. 65-75(11).
- [35] Rauste, Y.; "Multi-temporal JERS SAR Data in Boreal Forest Biomass Mapping", Remote Sensing of Environment, Vol. 97, Issue 2, 30 July 2005, pp. 263-275.
- [36] Imhoff, M.L.; "Radar Backscatter and Biomass Saturation: Ramifications for Global Biomass Inventory", IEEE Transactions on Geoscience and Remote Sensing, vol. 33, n°. 2, pp. 511-518, March 1995.
- [37] Thiel, C.; Drezet, P.; Weise, C.; Quegan, S.; Schmullius, C.; "Radar Remote Sensing for the Delineation of Forest Cover Maps and the Detection of Deforestation", Institute of Chartered Foresters, 2006.
- [38] Hoekman, D.H.; Vissers, M.A.M.; Sugardiman, R.A.; Vargas, J. "ENVISAT Forest Monitoring in Indonesia", NRSP-2 Report 01, December 2001.
- [39] Pedroso, E.C.; de Miranda, F.P.; Bannerman, K.; HenriqueBeisl, C.; Rodriguez, M.H.; Caceres, R.G.; "A Multi-sensor Approach and Ranking Analysis Procedure for Oil Seeps Detection in Marine Environments", Proceedings on the Geoscience and Remote Sensing Symposium 2007, 23-28 July 2007, pp. 865-870.
- [40] Zebker, H.A.; Goldstein, R.M.; "Topographic Mapping from Interferometric Synthetic Aperture Radar Observations", International Journal of Remote Sensing, Vol. 9, Nº5, pp. 857-872, 1988.
- [41] Kerbaoul, V.; Collard, F.; "SAR-Derived Coastal and Marine Applications: from Research to Operational Products", IEEE Journal of Oceanic Engineering, Vol. 30, Nº3, July 2005.
- [42] Langenberg, K.; Brandfass, M.; Mayer, K.; Kreutter, T. "Principles of microwave imaging and inverse scattering", Advances in Remote Sensing, (2), pp. 163 – 186, 1993.
- [43] Goodman, J.W. Speckle Phenomena in Optics: Theory and Applications, Roberts & Company, 2007.

- [44]Goodman, J.W. Some Fundamental Properties of Speckle. *J. Opt. Soc. Am.*, 1976, Vol. 66, pp. 1145 – 1149.
- [45]Lee, J.S. “Speckle Analysis and Smoothing of Synthetic Aperture Radar Images”. *Computer Graphics and Image Processing*, Vol. 17, Issue 1, September 1981, pp. 24 – 32.
- [46]Lee, J.S.; “Refined Filtering of Image Noise Using Local Statistics”, *Computer Vision, Graphics and Image Processing*, Vol. 15, pp.380-389, 1981.
- [47]Kuan, D.T.; Sawchuck, A.A.; Strand, T.C.; Chavel, P.; “Adaptive restoration of images with speckle”, *IEEE Trans. on Acoustics, Speech and Signal Processing*, Vol. 35, March 1987, pp. 373-383.
- [48]Evans, A. N.; “A Gamma Filter for Multi-look Synthetic Aperture Radar Images”, *Proceedings on ISSPA*, 1996.
- [49]Touzi, R.; “A review of speckle filtering in the context of estimation theory”, *IEEE Trans. on Geoscience and Remote Sensing*, Vol. 40, Nov. 2002, pp. 2392 – 2404.
- [50]Oliver, C.; Quegan, S.; *Understanding Synthetic Aperture Radar Images*, Artech House Publishers, 1998.
- [51]Arsenault, H.; April, G.; “Properties of speckle integrated with a finite aperture and logarithmically transformed”, *Journal of Optics*, Vol. 66, No. 11, November 1976, pp. 1160-1163.
- [52]Fung, A.K.; Lee, K.K. “A semi-empirical sea-spectrum model for scattering coefficient estimation”, *IEEE J. Oceanic Engin.*, vol. OE-7, Oct. 1982.
- [53]Wright, J.W. “A new model for sea clutter”, *IEEE Trans. on Antennas Propagation*, vol. AP-16, pp. 217-223, March 1968.
- [54]Hara, T.; Plant, W.J. “Hydrodynamic modulation of short wind-wave spectra by long waves and its measurement using microwave backscatter”, *J. Geophys. Res.*, vol. 99, no. C5, pp. 9767 – 9784.
- [55]Hasselmann, K.; Hasselmann, S. “On the nonlinear mapping of an ocean wave spectrum into a synthetic aperture radar image spectrum and its inversion”, *J. Geophys. Res.*, vol. 99, no. C6, pp. 10713 - 10729, 1991.
- [56]Greidanus, H., “Findings of the DECLIMS project – Detection and classifications of marine traffic from space”, *Proceedings on SEASAR 2006*.
- [57]Blakemore, C.; Campbell, F.W. “On the existence of neurons in the human visual system selectively sensitive to the orientation and size of retinal images”. *J. Physiol.*, Vol. 203, pp. 237 – 260, 1969.
- [58]Bradley, A.; Skottun, B.C.; Ohzawa, I.; Sclar, G.; Freeman, R.D. “Visual orientation and spatial frequency discrimination: a comparison of single neurons and behavior”. *J. Neurophysio.*, Vol. 57, Issue 3, pp. 755 – 772, 1987.

- [59]Field, D.J.; Hayes, A.; Hess, R.F. "Contour Integration by the Human Visual System: Evidence for a Local "Association Field""", *Vision Res.*, Vol. 33, №2, pp. 173 – 193, 1993.
- [60]Heisenberg, W. "Über den Anschaulichen Inhalt der Quantentheoretischen Kinematik und Mechanik". *Zeitschrift für Physik*, 43, 127, 1927.
- [61]Boashash, B. *Time Frequency Advances in Modern Spectrum Analysis and Array Processing*, Ed. S. Haykin, Prentice Hall, 1990.
- [62]Guanghua, C.; Shiwei, M.; Ming, L.; Jingming, Z.; Weimin, Z.: "Wigner-Ville distribution and cross Wigner-Ville distribution of noisy signals", *Journal of Systems Engineering and Electronics*, Vol. 19, Issue 5, August 2008, pp. 1053 – 1057.
- [63]Donoho, D., Johnstone, I. "Adapting to unknown smoothness via wavelet shrinkage", *J. Amer. Stat. Assoc.*, Vol. 90, pp. 1200-1224, Dec. 1995.
- [64]Pesquet, J.C., Krim, H., Hamman, E. "Bayesian approach to best basis selection", *IEEE Int. Conf. Acoust., Speech, Signal Process. ICASSP*, Atlanta, GA, 1996, pp. 2634-2637.
- [65]Chipman, H., Kolaczyk, E., McCulloch, R. "Adaptive Bayesian Wavelet Shrinkage", *J. Amer. Stat. Assoc.*, vol. 92, 1997.
- [66]Lee, N., Huynh, Q., Schwarz, S. "New methods of linear time-frequency analysis for signal detection", in *Proc. IEEE Int. Symp. Time-Frequency, Time-Scale Anal.*, 1996.
- [67]Shapiro, J., "Embedded image coding using zerotrees of wavelet coefficients", *IEEE Trans. Signal Processing*, vol. 41, pp. 3445-3462, December 1993.
- [68]Basseville, M. et al. "Modeling and estimation of multiresolution stochastic processes", *IEEE Trans. Inform. Theory*, vol. 38, pp. 766-784, March 1992.
- [69]Flandrin, P., "Wavelet analysis and synthesis of fractional Brownian motion", *IEEE Trans. Inform. Theory*, vol. 38, pp. 910-916, March 1992.
- [70]Hambaba, A. Nonstationary statistical tests in time-scale space. *Aerospace Conference Proceedings* 2000.
- [71]Mallat, S. *A Wavelet Tour on Signal Processing*. Academic Press, London, 1999.
- [72]Nason, G.P.; Silverman, B.W. "The stationary wavelet transform and some statistical applications", *Lecture Notes in Statistics*, Vol. 103, pp. 281-299, 1995.
- [73]Chen et al. Coding system for reducing redundancy. United States Patent, nº4,698,672. October 6, 1987.
- [74]Abramovich, F., Sapatinas, T., Silverman, B.W. "Wavelet thresholding via a bayesian approach", *J. R. Statis. Soc. B*, Vol. 60, pp. 725-749, 1998.
- [75]Luettgen, M.R., Karl, W.C., Willsky, A.S., Tenney, R.R., "Multiscale representations of Markov random fields", *IEEE Trans. Signal Processing*, vol. 41, pp. 3377-3395, Dec. 1993.

- [76]Chou, K.C., Heck, L.P. "A multiscale stochastic modeling approach to the monitoring of mechanical systems", Proc. IEEE Int. Symp. Time-Freq. Time-Scale Anal., 1994.
- [77]Simoncelli, E.P., Adelson, E.H. "Noise removal via Bayesian wavelet coring", Proc. IEEE Int. Conf. Image Processing, ICIP, Sept. 1996.
- [78][Orchard, M.T., Ramchandran, K. "An investigation of wavelet-based image coding using an entropy constrained quantization framework", Proc. Data Compression Conf., Snowbird, UT, 1994, pp. 341-350.
- [79]Mallat, S., Zhong, S. "Characterization of signals from multiscale edges", IEEE Trans. Pattern Anal. Machine Intell., vol. 14, pp. 710-732, July 1992.
- [80]Mallat, S., Hwang, W. "Singularity detection and processing with wavelets", IEEE Trans. Inform. Theory, Vol. 38, pp. 617-643, 1992.
- [81]Azimifar, Z., Fieguth, P., Jernigan, E. "Modeling the correlation structure of images in the wavelet domain", Canadian Conference on [Electrical and Computer Engineering](#). Volume 2, n 13-16 May 2001 Page(s): 1123 - 1127 vol.2.
- [82]Crouse, M.S., Nowak, R.D., Baraniuk, R.G., "Wavelet-based statistical signal processing using hidden markov models", IEEE Trans. on Signal Processing, Vol. 46, pp. 886-902, 1998.
- [83]Portilla, J., Simoncelli, E., "Image denoising via adjustment of wavelet magnitude correlation", Proceedings of the 7th International Conference on Image Processing, Vancouver, BC, Canada, 2000.
- [84]Ulaby, F.; Moore, R.; Fung, A.; *Microwave Remote Sensing. Active and Passive*, Artech House Publishers, 1982.
- [85]B. Zheng, W. Quian and L.P. Clarke, Digital mammography: mixed feature neural network with spectral entropy decision for detection of microcalcifications, *IEEE Trans Med Imag* **15** (1996), 589-597
- [86]Liebe, C.C., "Pattern recognition of star constellations for spacecraft applications", IEEE Aerospace and Electronic Systems Magazine, Vol. 8, Issue 1, Jan. 1993, pp. 31-39.
- [87]Nagarajan, R. "Intensity-based segmentation of Microarrays images," IEEE Trans. Medical Imag., vol. 22, July 2003, pp. 882–889.
- [88]Ferretti, A., Prati, C., Rocca, F., "Permanent scatterers in SAR interferometry", IEEE Trans. Geoscience and Remote Sensing, Vol. 39, Issue 1, Jan. 2001, pp. 8-20.
- [89]Hansen, V.G.; "Constant false alarm rate processing in search radars", Proceedings of the IEEE International Radar Conference, London, 1973, pp. 325-332.
- [90]Achim, A.; Loza, A.; Bull, D.; Canagarajah, N.; Statistical Modeling for Wavelet Domain Image Fusion, *Image Fusion. Algorithms and Applications*, Academic Press, 2008.

- [91]Lee, J.S.; "Refined Filtering of Image Noise Using Local Statistics", Computer Vision, Graphics and Image Processing, Vol. 15, pp. 380-389, 1981.
- [92]Greidanus, H. et al., "Assessing the operationality of ship detection from space", Proceedings on EURISY, New space services for maritime users, Feb. 2005.
- [93]Vessel Monitoring System (VMS) Information Website: <http://www.glf.dfo-mpo.gc.ca/fm-gp/cp-cp/vms-ssn/index-e.jsp>.
- [94]Kourtzi, N.; Shepherd, I. Marine Surveillance Case Study – Integrating Active and Passive Satellite Based Technologies to Improve European Fisheries Monitoring and Control. http://www.rsi.ca/rsic/marine/mar_euro_jrc1.asp
- [95]Greidanus, H. et al., "Benchmarking Operational SAR ship detection", Proceedings on IGARSS, 2004.
- [96]Crisp, D. J. The State of the Art in Ship Detection in Synthetic Aperture Radar Imagery. DSTO-RR-0272, DSTO Information Sciences Laboratory, May 2004.
- [97]Henschel, M.D.; Hoyt, R.B.; Sotckhausen, J.H.; Vachon, P.W.; Rey, M.T.; Campbell, J.W.M.; Edel, H.R. Vessel Detection with Wide Area Remote Sensing. Sea Technology, 39(9), pp. 63-68, 1998.
- [98]Vachon, P.W.; Adlakha, P.; Edel, H.; Henschel, M.; Ramsay, B.; Flett, D.; Rey, M.; Staples, G.; Thomas, S. Canadian Progress toward Marine and Coastal Applications of Synthetic Aperture Radar. Johns Hopkins APL Technical Digest, 21 (1), pp. 33-40, 2000.
- [99]Pichel, W.F., Clemente-Colon, P. NOAA CoastWatch SAR Applications and Demonstration. Johns Hopkins APL Technical Digest, 21(1): 49-57, 2000.
- [100]Wackerman, C.C.; Friedman, K.S., Pichel, W.G., Clemente-Colon, P., Li, X. Automatic detection of ships in RADARSAT-1 SAR Imagery. Canadian Journal of Remote Sensing, 27(5), pp. 568-577, 2001.
- [101]Schwartz, G.; Alvarez, M.; Varfis, A.; Kourtzi, N. Elimination of false positives in vessels detection and identification by remote sensing. In IEEE 2002 International Geoscience and Remote Sensing Symposium (IGARSS'02), vol. 1, pp. 116-118, 2002.
- [102]Kourtzi, N.; Shepherd, I., Verborgh, J. Fishing boat detection by using SAR imagery. In Ship Detection in Coastal Waters Three Day Workshop, 2000.
- [103]Kourtzi, N.; Shepherd, I.; Schwartz, G.; Pavlakis, P. Integrating spaceborne SAR imagery into operational systems for fisheries monitoring. Canadian Journal of Remote Sensing, 27 (4): 291-305, 2001.
- [104]Arnesen, T.N. and Olsen, R.B., *Literature review on vessel detection*, FFI/RAPPORT-2004/02619, 2004.
- [105]Lin, I.I.; Khoo, V. Computer based algorithm for ship detection from ERS-XSAR imagery. Proceedings of the 3rd ERS Scientific Symposium, Florence, Italy, 17-21, March 1997.

- [106] Lin, I.I.; Leong Keong Kwoh, Yuan-Chung Lin, Khoo, V. Ship and Ship wake detection in the ERS SAR imagery using computer based algorithms. IEEE International Geoscience and Remote Sensing Symposium (IGARSS'97), pp. 151-153, 1997.
- [107] Gagnon, L.; Oppenheim, H.; Valin, P. R&D Activities in Airborne SAR Image Processing / Analysis at Lockheed Martin Canada. Proceedings of SPIE, vol. 3491, pp. 998-1003, 1998.
- [108] Lombardo, P.; Sciotti, M. Segmentation-based technique for ship detection in SAR images. IEE Proceedings: Radar, Sonar & Navigation, 148 (3): 147-159, 2001.
- [109] Sciotti, M.; Lombardo, P. Ship Detection in SAR images: a segmentation-based approach. Proceedings of the 2001 IEEE Radar Conference (RADAR'01), pp. 81-86, 2001.
- [110] Yeremy, M.; Geling, G.; Rey, M.; Plache, B.; Henschel, M. Results from the CRUSADE Ship Detection Trial: Polarimetric SAR. IEEE 2002 International Geoscience and Remote Sensing Symposium (IGARSS'02), 2002.
- [111] Benelli, G.; Garzelli, A.; Mecocci A. Complete Processing System that uses Fuzzy Logic for Ship Detection in SAR Images. IEE Proceedings on Radar, Sonar & Navigation, 141(4), pp. 181-186, 1994.
- [112] Argenti, F.; Benelli, G.; Garzelli, A.; Mecocci, A. Automatic Ship Detection in SAR Images. IEE International Conference Radar 92, pp. 465-468, 1992.
- [113] Askari, F.; Zerr, B. Automatic Approach to Ship Detection in Spaceborne Synthetic Aperture Radar Imagery: An Assessment of Ship Detection Capability Using RADARSAT. Technical Report SACLANTCEN-SR-338, SACLANT Undersea Research Centre, La Spezia (Italy), December 2000.
- [114] Osman, H.; Blostein, S.D. Probabilistic Winner-Take-All Segmentation of Images with Application to Ship Detection. IEEE Transactions on Systems, Man and Cybernetics, Part B: Cybernetics, 30 (3), pp. 485-490, 2000.
- [115] Ouchi, K.; Tarnaki, S.; Yaguchi, H.; Ichihara, M.; "Ship Detection based on Coherence Images Derived from Cross Correlation of Multilook SAR Images", IEEE Geoscience and Remote Sensing Letters, Vol. 1, Issue 3, July 2004, pp.: 184-187.
- [116] Yeremy, M.; Livingstone, C.; Mattar, K.; Gallop, L.; Lang, J. Polarimetric Interferometry Experimental Trials for Years 2001 and 2002: Experiment Design, Ground Truthing, Data Quality and Analysis. Technical Report DRDC Ottawa TM 2003-142-DRDC Ottawa, Canada, September 2003.
- [117] Yeremy, M.; Campbell, J.W.M.; Mattar, K.; Potter, T. Ocean Surveillance with Polarimetric SAR. Canadian Journal of Remote Sensing, 27 (4), pp. 328-344, 2001.
- [118] Sanden, J.J.; Ross, S.G. Applications Potential of RADARSAT-2: A Preview. Report, Canada Centre for Remote Sensing, 2001. Available at: http://www.ccrs.nrcan.gc.ca/ccrs/rd/rd_e.html.

- [119] Touzi, R.; Charbonneau, F.; Hawkins, R.K.; Murnaghan, K.; Kavoun, X. Ship-Sea Contrast Optimisation when Using Polarimetric SARs. IEEE 2001 International Geoscience and Remote Sensing Symposium (IGARSS'01), vol. 1, pp. 426-428, 2001.
- [120] Touzi, R.; Charbonneau, F.; Hawkins, R.K.; Vachon, P.W. Ship Detection and Characterization Using Polarimetric SAR. Canadian Journal of Remote Sensing, 2003.
- [121] Cloude, S.R.; Pottier, E. A Review of Target Decomposition Theorems in Radar Polarimetry. IEEE Transactions on Geoscience and Remote Sensing, vol. 34., pp. 498-518, 1996.
- [122] GMV website: <http://www.gmv.es/>
- [123] Margarit, G.; Mallorqui, J.J.; Rius, J.M.; Sanz-Marcos, J.; "On the Usage of GRECOSAR, an Orbital Polarimetric SAR Simulator of Complex Targets, to Vessel Classification Studies", IEEE Transactions on Geoscience and Remote Sensing, Vol. 44, Issue 12, December 2006, pp. 3517-3526.
- [124] Corbane, C. et al. "A complete processing chain for ship detection using optical satellite imagery", International Journal of Remote Sensing, 2010, to appear.
- [125] Pratt, W.K. Digital Image Processing. New York, Wiley, 1978.
- [126] Pavlidis, T. Algorithms for Graphic and Image Processing, Computer Science Press, 1982.
- [127] Prewitt, J.M.S. "Object Enhancement and Extraction", Picture Processing and Psychopictorics, B.S. Lipkin and A. Rosenfeld, Eds. New York, Academic Press, 1970, pp. 75-149.
- [128] Canny, J. "A computational approach to edge detection". IEEE Trans. Patt. Anal. and Match. Intell., 36, pp. 961-1005, September 1986.
- [129] Mallat, S. A *Wavelet Tour on Signal Processing*. Academic Press, London, 1999.
- [130] Sadler, B.M.; Swami, A; "Analysis of multiscale products for step detection and estimation" IEEE Transactions on Information Theory, Vol. 45, Issue 3, April 1999 pp. 1043 – 1051.
- [131] Cuartero, G.; Meas-Yedid, V.; Galy, V.; Nehrbass, U.; Olivo-Marine, J.-C.; "Three dimensional spot detection by multiscale analysis", International Conference on Image Processing, Vol. 1, 7-10 Oct. 2001 pp. 317 - 320.
- [132] Kuo, J.; Chen, K.-S.; "The application of wavelets correlator for ship wake detection in SAR images", IEEE Transactions on Geoscience and Remote Sensing, Vol. 41, Issue 6, Part 2, June 2003 pp. 1506 – 1511.
- [133] Yansun Xu; Weaver, J.B.; Healy, D.M.; Jian Lu; "Wavelet transform domain filters: a spatially selective noise filtration technique", IEEE Transactions on Image Processing, Vol. 3, Issue 6, Nov. 1994 pp. 747 – 758. gar, I.; Fombellida, J.; Gomez, J.; Seijas, J. "Edge detection algorithms in intensity SAR images: Empirical comparison of

performances and proposed improvements". Proceedings of the WAC'08, September 2008, pp.: 1-7.

- [134] Touzi, R.; "A review of speckle filtering in the context of estimation theory", IEEE Trans. on Geoscience and Remote Sensing, Vol. 40, Nov. 2002, pp. 2392 – 2404.
- [135] White, R.G.; Oliver, C.J.; "Change Detection in SAR imagery", IEEE International Radar Conference, pp. 217-222, May 1990.
- [136] Oliver, C.J.; Blacknell, D.; White, R.G. "Optimum edge detection in SAR", IEEE Proceedings on Radar, Sonar and Navigation, Vol. 143, pp.: 31-40, February 1996.
- [137] Fjortoft, R.; Lopes, A.; Marthon, P.; Cubero-Castan, E. "An optimal multiedge detector for SAR image segmentation", IEEE Transactions on Geoscience and Remote Sensing, Vol. 36, pp. 793-802, May 1998.
- [138] Romaneessen, E.; Niedermeier, A.; Winkel, N.; Lehner, S. "Improved bottom topography in the Elbe estuary using wavelet and active contour methods on SAR images". Proceedings on IGARSS'99, vol. 3, july 1999, pp.: 1674-1676.
- [139] Madchakham, S.; Thitimajshima, P.; Ragsanseri, Y. "Edge Detection in Speckled SAR Images using Wavelet Decomposition", Proceedings on ACRS 2001, Vol. 2, pp. 1842-1844, May 1996.
- [140] Arsenault, H.; April, G.; "Properties of speckle integrated with a finite aperture and logarithmically transformed", Journal of Optics, Vol. 66, No. 11, November 1976, pp. 1160-1163.
- [141] Freeman, A.; SAR calibration: an overview, IEEE Transactions on Geoscience and Remote Sensing, Vol. 30, Issue 6, Nov. 1992, pp.: 1107-1121.
- [142] Caselles, V., Kimmel, R., Sapiro, G.; "Geodesic Active Contours", International Journal of Computer Vision 22 (1), 61-79, 1997.
- [143] Chen, Y.G., Giga, Y., Goto, S. Uniqueness and existence of viscosity solutions of generalized mean curvature flow equations, J. Differential Geometry, 33: 749-786, 1991.
- [144] Oliver, C.; Quegan, S.; *Understanding Synthetic Aperture Radar Images*, Artech House Publishers, 1998.
- [145] Mandelbrot, B.B. *The Fractal Geometry of Nature*, W.H. Freeman & C., New York, 1993.
- [146] Andreoli, G.; Berizzi, F.; Dalle Mese, E.; Pinelli, G. "A two-dimensional fractal model of the sea surface and sea spectrum evaluation", IEE International Radar Conference, Edinburgh, Scotland, pp. 189-193, 1997.
- [147] Berizzi, F.; Gamba, P.; Garzelli, A.; Monorchio, A. "Fractal analysis and validation of a sea-surface fractal model for SAR imagery", SPIE Proc., pp. 612-621, 1999.

- [148] Berizzi, F.; Dell'Acqua, F.; Gamba, P.; Garzelli, A.; Martorella, M. "On the fractal behavior of SAR images of ocean sea surface", IEEE Trans. on IGARSS'01, July 2001, Vol. 4, pp. 1729 – 1731.
- [149] Franceschetti, G.; Migliaccio, M.; Riccio, D. "On ocean SAR raw signal simulation", IEEE Trans. Geosci. Remote Sensing, Vol. 36, pp. 84-100, Jan. 1998.
- [150] Kasilingam, D.P.; Shemdin, O.H. "The validity of the composite surface model and its application to the modulation of the radar backscatter", Int. J. Remote Sens., Vol. 13, pp. 2079-2104, 1994.
- [151] Ulaby, F.T.; Moore, R.K.; Fung, A.K. "Microwave Remote Sensing: Active and Passive", MA Addison – Wesley, 1982.
- [152] Berizzi, F.; Dalle Mese, E. "Fractal analysis of the signal scattered from the sea surface", IEEE Trans. on Antennas and Propagation, vol. 47 (2), 1999.
- [153] Franceschetti, G.; Iodice, A.; Migliaccio, M.; Riccio, D. "Scattering from natural rough surfaces modeled by fractional Brownian motion two-dimensional processes", IEEE Trans. Antennas Prop., vol. 47, pp. 1405 – 1415, 1999.
- [154] Ruello, G.; Blanco, P.; Iodice, A.; Mallorqui, J.J.; Riccio, D.; Broquetas, A.; Franceschetti, G. "Electromagnetic Scattering Measurements on a Fractal Surface", Proc. on IGARSS'04, September 2004, Vol. 1, pp. 425 – 427.
- [155] Turiel, A., Mato, G., Parga, N., Nadal, J.P. "The self-similarity properties of natural images resemble those of turbulent flows, Phys. Rev. Lett. 80 (1998), pp. 1098-1101.
- [156] Farge, M.; Kevlahan, N.K.R.; Perrier, V. "Turbulence analysis, modeling and computing using wavelets", *Wavelets in Physics*, pp. 117-200. Cambridge University Press, London, 1999.
- [157] Turiel, A., Parga, N., "The multifractal structure of contrast changes in natural images: from sharp edges to textures, Neural Comput. 12 (2000) 763-793.
- [158] Perrier, V.; Philipovitch, T.; Basdevant, C. "Wavelet spectra compared to Fourier spectra", J. Math. Phys., 36 (3), pp. 1506 – 1519, 1995.
- [159] Jaffard, S.; Some mathematical results about multifractal formalism for functions, *Wavelets: Theory, Algorithms and Applications*, eds. C. K. Chui, L. Montefusco and L. Puccio, pp. 1 – 37, 1994.
- [160] Turiel, A., Pérez-Vicente, C., Grazzini, J. "Numerical methods for the estimation of multifractal singularity spectra on sampled data: a comparative study", Journal of Computational Physics, December 2005, pp. 362-390.
- [161] Mercier, G., Girard-Ardhuin, F. "Partially Supervised Oil-Slick Detection by SAR Imagery Using Kernel Expansion", IEEE Transactions on Geoscience and Remote Sensing, Vol. 44, No. 10, October 2006, pp. 2839 – 2846.

- [162] Mallat, S., Zhong, S. "Characterization of signals from multiscale edges", IEEE Trans. Pattern Anal. Mach. Intelligence 14, 1992, pp. 710-732.
- [163] Mallat, S., Hwang, W.L. "Singularity detection and processing with wavelets", IEEE Trans. Info. Theory, 38 (2), pp. 617-643, March 1992.
- [164] Platonov et al. SAR observations of vortical structures and turbulence in the oceans, Models, Experiments and computation in turbulence, 2007.
- [165] Mallat, S. "A theory for multiresolution signal decomposition: the wavelet representation", IEEE Trans. Pattern Anal. Mach. Intelligence 11, 1989, pp. 674-693.
- [166] Muzy, J.F., Bacry, E., Arneodo, A. "Wavelets and multifractal formalism for singular signals: application to turbulence data, Phys. Rev. Lett. 67, 1991, pp. 3515-3518.
- [167] Fingas, M.F.; C.E. Brown; J.V. Mullin. A Comparison of the Utility of Airborne Oil Spill Remote Sensors and Satellite Sensors. Proceedings, Fifth Conference on Remote Sensing for Marine and Coastal Environment Environmental Research Institute of Michigan, Ann Arbor, MI, 1998, 1, I- 171-I-178.
- [168] Girard-Ardhuin, F., Mercier, G., Collard, F., Garello R. "Operational oil slick characterization by SAR imagery and synergistic data" IEEE J. Ocean Eng., vol. 30, no. 3, pp. 487-495, Jul. 2005.
- [169] Nand Jha, M.; Levy, J.; Gao, Y. "Advances in Remote Sensing for Oil Spill Disaster Management: State of the Art Sensors Technology for Oil Spill Surveillance, Sensors, 2008, vol. 8, pp. 236-255.
- [170] Topouzelis, K. "Oil Spill detection by SAR images: Dark Formation Detection, Feature Extraction and Classification Algorithms", Sensors, 2008, Vol. 8, pp. 6642-6659.
- [171] Brekke, C., Solberg, A. Oil spill detection by satellite remote sensing, Remote Sensing of Environment, March 2005, vol. 95, n° 1, pp. 1-13.
- [172] Franklin, B. "Of the stilling of waves by means of oil", Philos. Trans., vol. 64, pt. 1, pp. 445-460, 1774.
- [173] Marangoni, C. "Sul principio della viscosità superficiale dei liquidi stabilito dal Sig. J. Plateau", Nuovo Cim. Ser. 2, vol. 5/6, pp. 239-273, 1872.
- [174] W. Alpers, H. Hüfnerfuss, "Radar signatures of oil films floating on the sea surface and the Marangoni effect", J. Geophysic. Res., vol. 93, no. C4, pp. 3642-3648, 1988.
- [175] W. Alpers, H. Hüfnerfuss, "The damping of ocean waves by surface films: a new look at an old problem", J. Geophys. Res., vol. 94, no. C5, pp. 6251-62655, 1989.

- [176] Hühnerfuss, H., Alpers, W., Cross, A., Garret, W.D., Keller, W.C., Lange, P.A., Plant, W.J., Chlude, F., Schuler, D.L. "The modification of X and L-band radar signals by monomolecular sea slicks", *J. Geophys. Res.* Vol. 88, no. C14, pp. 9817-9822, 1983.
- [177] Hühnerfuss, H., Alpers, W., Garret, W.D., Lange, P.A., Stolte, S. "Attenuation of capillary and gravity waves at sea by monomolecular organic surface films", *J. Geophys. Res.*, Vol. 88, no. C14, pp. 9809-9816, 1983.
- [178] Wismann, V. "Radar signatures of mineral oil spills measured by an airborne multi-frequency radar and the ERS-1 SAR", *Proc. IGARSS*, Tokyo, Japan, Aug. 18-21, 1993, pp. 940-942.
- [179] Pavlakis, P., Sieber, A., Alexandry, S. "On the optimization of spaceborne SAR capacity in oil spill detection and the related hydrodynamic phenomena", *Spill Sci. Technol. Bull.*, vol. 3, no. ½, pp. 33-40, 1996.
- [180] Gade, M., Alpers, W., Hühnerfuss, H., Masuko, H., Kobayashi, T. "Imaging of biogenic and anthropogenic ocean surface films by the multifrequency/multipolarization SIR-C/X-SAR", *J. Geophy. Res.*, vol. 103, no. C9, pp. 18851-18866, 1998.
- [181] Wismann, V., Gade, M., Alpers, W., Hühnerfuss, H. "Radar signatures of marine mineral oil spills measured by an airborne multi-frequency radar", *Int. J. Remote Sensing*, vol. 19, no. 18, pp. 3607-3623, 1998.
- [182] Singh, K.P., Gray, A.L., Hawkins, R.K., O'Neil, R.A., "The influence of surface oil on C- and Ku- band ocean backscatter", *IEEE Trans. Geosci. Remote Sens.*, vol. GRS-24, no. 5, pp. 738-744, sept. 1986.
- [183] Masuko, H., Kobayashi, T., Okamoto, K., Alpers, W. "Observation of artificial slicks with SIR-C/X-SAR around Japan", in *Proc. IGARSS*, Florence, Italy, Jul. 10-14, 1995, Vol. 1, pp. 227-229.
- [184] Ermakov, E.A.; Sergievskaya, I.A.; Zuikova, E.H.; Goldbet, V.Y.; Scott, J.C. "Field studies of natural slicks due to internal waves", *Proc. IGARSS 1999*, Hamburg, Germany, Vol. 3, pp. 167-169.
- [185] Lu, J.; Lim, H.; Liew, S.C.; Bao, M.; Kwoh, L.K. "Ocean oil pollution mapping with ERS SAR imagery", *Proc. IGARSS 1999*, Hamburg, Germany, Vol. 3, pp. 212-214.
- [186] Hühnerfuss, W., Alpers, W., Jones, W.L., "Measurements at 13.9 GHz of the radar backscattering cross section of the North Sea covered with an artificial surface film", *Radio Sci.*, Vol. 13, no. 6, pp. 979-983, 1978.
- [187] Scott, J.C. "Ocean surface slicks – Pollution, productivity, climate and life saving", in *Proc. IGARSS*, June 1999, Hamburg, Germany, Vol. 3, pp. 1463 – 1465.
- [188] Alpers, W. et al. "The damping of ocean surface waves by monomolecular sea slicks measured by airborne multifrequency radars during the saxon-fpn experiment",

Proc. International Geoscience and Remote Sensing Symposium (IGARSS'91), Helsinki, Finland, 1991, pp. 1987-1990.

- [189] Hovland, H.A.; Johannessen, J.A.; Digranes, G. "Slick detection in SAR images", Proc. International Geoscience and Remote Sensing Symposium (IGARSS 94), Pasadena, CA, USA, 1994, pp. 2038-2040.
- [190] M. Gade, J. Scholz, C. Von Viebahn, "On the detectability of marine oil pollution in European marginal waters by means of ERS SAR imagery", in Proc. IGARSS, Honolulu, HI, Jul. 24-28, 2000, vol. 6, pp. 2510-2512.
- [191] K.W. Bjerde, A.H.S. Solberg, "Oil spill detection in SAR imagery", in Proc. IGARSS, Tokyo, Japan, Aug. 18-21, 1993, vol. 3, pp. 943-945.
- [192] Solberg, A.; Storvik, G.; Solberg, R.; Volden, E. "Automatic Detection of Oil Spills in ERS SAR Images", IEEE Trans. on Geosci. and Remote Sensing, 1999, vol. 37, pp. 1916-1924.
- [193] Del Frate, F.; Petrocchi, A.; Lichtenegger, J.; Calabresi, G. "Neural networks for oil spill detection using ERS-SAR data", IEEE Trans. Geosci. Remote Sens. 2000, vol. 5, pp. 2282-2287.
- [194] Espedal, H.A.; Wahl, T. "Satellite SAR oil spill detection using wind history information". Int. Journal of Remote Sensing, 1999, vol. 20, pp. 49-65.
- [195] Espedal, H.A.; Johannessen, J.A. "Detection of oil spills near offshore installations using synthetic aperture radar (SAR)", Int. Journal of Remote Sensing, 2000, vol. 11, pp. 2141-2144.
- [196] Fiscella, B.; Giancaspro, A.; Nirchio, F.; Trivero, P. "Oil Spill detection using marine SAR images". Int. J. Remote Sens. 2000, vol. 20, pp. 49-65.
- [197] De Souza, D.; Neto, A.; Da Mata, W. "Intelligent System for Feature Extraction of Oil Slicks in SAR images: Speckle Filter Analysis. Lecture Notes in Computer Science, Vol. 4233, 13th International Conference, ICONIP 2006, Hong Kong, China.
- [198] Keramitsoglou, I.; Cartalis, C.; Kiranoudis, C. "Automatic identification of oil spills on satellite images", Environ. Model. Software, 2006, Vol. 21, pp. 640-652.
- [199] Karathanassi, V.; Topouzelis, K.; Pavlakis, P.; Rokos, D. "An object-oriented methodology to detect oil spills". Int. J. Remote Sens., 2006, Vol. 27, pp. 5235-5251.
- [200] Mercier, G., Derrode, S., Pieczynski, W, Le Caillec, J. M., Garello, R. "Multiscale oil slick segmentation with Markov chain model", Proc. IGARSS, Toulouse, France, Jul. 21-25, 2003, pp. 3501-3503.
- [201] Mercier, G., Girard-Ardhuin, F. "Oil slick detection by SAR imagery using support vector machines", Proc. IEEE Oceans – Europe, Brest, France, Jun. 20-23, 2005, pp. 90-95.

- [202] Mercier, G., Girard-Ardhuin, F. Partially Supervised Oil-Slick Detection by SAR Imagery using Kernel Expansion, IEEE Transactions on Geoscience and Remote Sensing, Vol. 44, no. 10, october 2006, pp. 2839-2846.
- [203] Platonov et al. SAR observations of vortical structures and turbulence in the oceans, Models, Experiments and computation in turbulence, 2007.
- [204] Franceschetti, G.; Iodice, A.; Riccio, D.; Ruello, G.; Siviero, R. "SAR Raw Signal Simulation of Oil Slicks in Ocean Environments", IEEE Trans. on Geoscience and Remote Sensing, Vol. 40, no. 9, September 2002.
- [205] Benelli, G.; Garzelli, A. "Oil-spills detection in SAR images by fractal dimension estimation", Proceedings on IGARSS'99, Vol. 1., pp. 218-220.
- [206] Berizzi, F.; Martorella, M.; Bertini, G.; Garzelli, A.; Nencini, F.; Dell'Acqua, F.; Gamba, P. "Sea SAR image analysis by fractal data fusion", Proceedings on IGARSS'04, Vol 1., pp. 93-96.
- [207] Redondo, J.M.; Platonov, A.K.; Grau, J. "Application of multi-fractal feature analysis to the sea surface", Fluxes and Structures in Fluids 2003, RAS. Moscow, 2000.
- [208] Sandven, S.; Kudriavtsev, V.; Malinovsky, V.; Stanovoy, V. "Development of Oil Spill Monitoring System for the Black Sea, Caspian Sea and the Barents/Kara Seas (DEMOSS)", Proceedings on SEASAR 2008.